

学位論文

Observation of the phase differences of
near-threshold high-order harmonics
generated in atoms and molecules

(原子および分子から発生する高次高調波の
イオン化限界近傍における位相差の観測)

平成26年7月博士(理学)申請

東京大学大学院理学系研究科
物理学専攻
加藤 康作

Abstract

High-order harmonic generation from aligned molecules can be used as a unique tool for imaging molecular electronic structures with unprecedented spatial and temporal resolutions. Though a wide range of harmonics is needed for molecular orbital imaging, studies on the lower-order harmonics are less extensive than those on higher-order harmonics. Especially, information about the phase of the harmonic components is quite limited in the energy region near the ionization threshold. In this thesis, we present the experimental results of the phase differences $\Delta\phi_{\text{HH}}^{(2n)}$ between adjacent high-order harmonics generated in atoms and molecules in the near-threshold region.

As a method to observe the phase differences of high-order harmonics, we employ a technique called RABBIT (reconstruction of attosecond beating by interference of two-photon transitions). In this method, we observe the signal of two-color two-photon ionization of rare-gas atoms produced by high-order harmonics to be measured and the fundamental pulse for probe. The phase differences between adjacent harmonics are evaluated by analyzing the dependence of the photoelectron signals on the delay time between the high-order harmonics and the probe pulse.

For the RABBIT method, the high-order harmonics have to be focused on the rare-gas jet. We have constructed a RABBIT apparatus equipped with a newly developed chamber to focus the high-order harmonics with a gold-coated toroidal mirror. We measure the kinetic energy distributions of the produced photoelectrons with the velocity-map imaging technique. To extract the phase differences from the obtained signals, we devise a new analysis method based on the theory of two-color two-photon ionization.

We observed the phase differences $\Delta\phi_{\text{HH}}^{(2n)}$ between adjacent high-order harmonics generated in Ar, N₂, Kr, and CO₂. The observed $\Delta\phi_{\text{HH}}^{(2n)}$'s increase as a function of the sideband order $2n$, which is reproduced by a model calculation based on the strong-field approximation. However, we find that in the results of Ar and CO₂, $\Delta\phi_{\text{HH}}^{(12)}$ is almost the same as $\Delta\phi_{\text{HH}}^{(14)}$, whereas they differ by ~ 0.5 rad in the results of N₂. For high-order harmonics generated in Kr, we note that the difference between $\Delta\phi_{\text{HH}}^{(12)}$ and $\Delta\phi_{\text{HH}}^{(14)}$ depends on the intensity of the driving laser field. These results cannot be explained by the model calculation. As an origin of these phenomena, we discuss the effects of the excited states or those of the Coulomb potential, both of which are neglected in the strong-field approximation.

Acknowledgments

The research presented in this thesis could not be conducted without kindness and support from many people. Firstly I express my deep appreciation to my supervisor, Professor Hirofumi Sakai for giving me a wonderful opportunity to study in his laboratory with great experimental environment. I also thank him for his persistence and enthusiasm, which strongly stimulate me to propel the research. I am extremely grateful to Dr. Shinichirou Minemoto, the Assistant Professor in the laboratory, for teaching me the basics of experiment and various measurement techniques, and for maintaining lasers and experimental apparatuses. I am also thankful to him for a lot of invaluable advice he gave to me. I gratefully acknowledge Mr. Yusuke Sakemi, one of the collaborator of the presented study, for assisting the setup of the apparatus and the measurement of data, and for many fruitful discussions with him. I would like to thank Mr. Je-Hoi Mun for his useful advice on experiments and numerical simulation. I give heartfelt thanks to Mr. Kei Nakagawa for his contribution in the early part of the experiment, and I also feel grateful that his study on the ellipticity dependence of the high-order harmonics calls my attention to the near-threshold harmonics. I am grateful to Mr. Yo Iida for helping our experiment and for insightful discussions with him. I thank all the former members and visiting researchers of the laboratory, especially to Dr. Tsuneto Kanai, Dr. Ryo Yamashiro, Dr. Hiraku Matsukuma, Dr. Tomoya Mizuno, Dr. Kyo Nakajima, Mr. Masahiro Muramatsu, Mr. Akihisa Goban, Mr. Keita Oda, Mr. Gentaro Watanabe, Mr. Masafumi Hita, Mr. Midai Suzuki, Mr. Tetsuro Hoshino, and Mr. Daisuke Takei. I genuinely indebted to them for their kindness and support. I express deep gratitude to Professor Jiro Itatani, Chief of the thesis defence committee, and Professor Yohei Kobayashi, Professor Satoshi Yamamoto, Professor Kenichi Ishikawa, and Professor Ryo Shimano, the members of the thesis defence committee, for a lot of valuable advice and comments on the thesis. I greatly appreciate the members of the machine shop of the physics department for their excellent technical supports. I would also like to thank the secretaries for their clerical supports. This work was supported by Grant-in-Aid for Specially Promoted Research No. 21000003 from MEXT and the Photon Frontier Network Program of MEXT. I am grateful for the financial support from the Global COE Program “Physical Sciences Frontier,” MEXT, Japan, Grant-in-Aid for JSPS Fellows No. 12J10272. I also thank to the financial aid from the University of Tokyo and the scholarship from Japan Student Services Organization. Finally, I would like to thank my family for their warm support and encouragement.

Contents

Abstract	iii
Acknowledgments	v
1 Introduction	1
1.1 Imaging molecular orbitals by high-order harmonics	1
1.2 The phase of harmonics	7
1.3 Beyond strong field approximation	8
1.4 Purpose of this study	11
1.5 Content of the thesis	12
2 Theoretical background of high-order harmonic generation	13
2.1 The Lewenstein model of high-order harmonic generation process with strong-field approximation	13
2.1.1 Strong-field approximation	14
2.1.2 Saddle-point approximation	15
2.1.2.1 Integral over p	16
2.1.2.2 Integral over t	17
2.1.2.3 Removing unphysical paths	18
2.1.3 Quantum path selection by phase matching	20
2.1.4 Relation to tomographic imaging	21
2.2 Spectral phase of high-order harmonics	21
2.2.1 Spectral structure of high-order harmonics	22
2.2.2 The effect of phase differences on the temporal structure	24
2.3 Detection of the phase difference by using two-color two-photon ionization	25
2.3.1 Overview of the RABBIT method	26
2.3.2 Two-color two-photon ionization	27
2.3.3 Atomic phase	29
3 Experimental setup and techniques	31
3.1 Laser and optical system	32
3.1.1 Ti:sapphire based chirped pulse amplification system	32

3.1.1.1	Ti:sapphire laser	32
3.1.1.2	Oscillator	33
3.1.1.3	Amplifier	33
3.1.2	Optical system after the amplifier	35
3.1.3	Focusing high-order harmonics into the detection gas	35
3.1.3.1	Reflection on metals	36
3.1.3.2	Focusing by a toroidal mirror	37
3.1.4	Grating spectrometer	38
3.2	Vacuum system and molecular beam	38
3.2.1	Harmonic generation chamber	40
3.2.2	Refocusing chamber	41
3.2.3	Detection-gas source chamber	41
3.2.4	Velocity map imaging chamber	41
3.2.5	The chamber of the grating spectrometer	42
3.3	Velocity map imaging technique	42
3.3.1	Imaging velocity distributions of photoproducts by using a time-of-flight chamber	42
3.3.2	Principle of the velocity map imaging method	43
3.3.3	Setup of the velocity map imaging apparatus	43
3.3.3.1	Configuration	46
3.3.3.2	Wiring of high-voltage circuit	47
3.3.3.3	Noise shielding	47
3.3.4	Blob detection	49
3.3.5	Reconstruction of three-dimensional velocity distribution	49
3.3.5.1	Inverse Abel transform	50
3.3.5.2	Fourier-Hankel method	51
3.3.5.3	BASEX method	51
3.3.5.4	Example	53
3.3.6	Getting radial distribution with a distortion correction	55
3.4	Signal flow	56
3.5	Nonadiabatic alignment of molecules with strong laser pulses	57
3.5.1	Overview	57
3.5.2	Principle of the nonadiabatic alignment	57
4	Results	63
4.1	Extracting phase differences	63
4.1.1	Calibration of the delay between the harmonics and the probe pulse	63
4.1.2	Normalization and fitting of sideband intensities	65
4.2	Results of the measurement of phase differences	69
4.2.1	Ar	71

CONTENTS

4.2.2	N ₂	72
4.2.3	Kr	74
4.2.4	CO ₂	75
4.2.5	Intensity of the harmonics	77
5	Discussions	79
5.1	Comparison with the results of model calculation	79
5.2	Two possible reasons for the day-by-day difference	82
5.2.1	Effect of the dispersion of the gas	82
5.2.2	Effect of the misalignment	84
5.2.3	Comparison among the measurements performed in series	84
5.3	The anomaly of the phase differences at the near-threshold region	86
5.3.1	Summary of the differences between $\Delta\phi_{\text{HH}}^{(12)0}$ and $\Delta\phi_{\text{HH}}^{(14)0}$	86
5.3.2	Ionization	89
5.3.3	Propagation	89
5.3.4	Recombination	90
5.3.5	Errors caused by the fluctuations of experimental conditions	93
5.4	Summary of the discussions	93
6	Conclusion	95
6.1	Summary of the experiment	95
6.2	Summary of the results and discussions	95
6.3	Outlook	96
A	Appendix	97
A.1	Detailed calculations in the saddle-point approximation	97
A.1.1	saddle points on t and t'	97
A.1.2	The saddle point approximation around the stationary points of the time	98
A.1.3	Calculation of the determinant of the Hessian matrix $\det \Theta''_{(\pm)}$	100
A.2	Derivation of the expression for the probability of two-color two-photon ionization	101
A.3	Calculation of the atomic phase	105
A.3.1	Separation of the radial part and the angular part	105
A.3.2	Summation over all the intermediate states	106
A.4	Matrix elements of spherical harmonics, $\cos \theta$ and $\cos^2 \theta$	108
A.5	Calculation of the density matrix of molecules at the thermal equilibrium	109
A.6	Calculation of the Abel transform of the basis in the BASEX method	112
A.7	Note on classical trajectory Monte Carlo method	112
A.7.1	classical theory	113
A.7.2	Wigner distribution with cutoff	113
A.7.3	Scaling	116
A.7.4	Softcore potential	116

CONTENTS

A.8	Calculation of the recombination transition dipole moment of atoms	116
A.8.1	The stationary continuum state	117
A.8.2	The transition dipole moment from a continuum state to a bound state	117

Chapter 1

Introduction

1.1 Imaging molecular orbitals by high-order harmonics

In the early twentieth century, researches by scientists greatly advanced the understanding of the quantum nature [1–3]. They revealed that most of common matters around us are made of electrons and nuclei, and their behavior is described by the quantum mechanics: the state of the particles is described by the wavefunction which obeys the Schrödinger equation, and the probability of the position where the particles are found is determined by the modulus squared of its spatial representation. A molecule has more than one electrons, which are interacting and correlating with each other. In general it is very hard to calculate the exact many-electron wavefunction of a molecule and, even if it is possible, difficult to understand the molecular property directly from the complicated exact many-electron wavefunction. To describe the electronic structure of a molecule, it is convenient to use the “molecular orbital”, that is, a one-electron wavefunction which approximately describes the state of an electron in a molecule and approximately constitutes the many-electron wavefunction. The concept of molecular orbitals is useful not only for determination of molecular structure by calculation or spectroscopy, but also for understanding chemical reactions [4, 5].

Since molecular orbitals are only approximation derived from the exact many-electron wavefunction, their functional form cannot be defined uniquely. There are several kinds of definitions of molecular orbitals [6], among which two approximations are vast prevailing. One of the well-known molecular orbitals is the one obtained by Hartree-Fock approximation [7, §§2–3]. Let us consider a molecule with N_e electrons whose coordinates are designated by $\{\mathbf{x}\}_{N_e} = \mathbf{x}_1, \mathbf{x}_2, \dots, \mathbf{x}_{N_e}$ (\mathbf{x} is a set of the space coordinate \mathbf{r} and the spin coordinate s). In the Hartree-Fock approximation the many-electron wavefunction of the ground state $\Psi_0(\{\mathbf{x}\}_{N_e})$ is replaced by one Slater determinant which is composed of N_e orbitals,

$$\Psi_0(\{\mathbf{x}\}_{N_e}) \simeq \Psi_0^{\text{HF}}(\{\mathbf{x}\}_{N_e}) \equiv \frac{1}{\sqrt{N_e!}} \begin{vmatrix} \psi_1^{\text{HF}}(\mathbf{x}_1) & \psi_2^{\text{HF}}(\mathbf{x}_1) & \cdots & \psi_{N_e}^{\text{HF}}(\mathbf{x}_1) \\ \psi_1^{\text{HF}}(\mathbf{x}_2) & \psi_2^{\text{HF}}(\mathbf{x}_2) & \cdots & \psi_{N_e}^{\text{HF}}(\mathbf{x}_2) \\ & & \ddots & \\ \psi_1^{\text{HF}}(\mathbf{x}_{N_e}) & \psi_2^{\text{HF}}(\mathbf{x}_{N_e}) & \cdots & \psi_{N_e}^{\text{HF}}(\mathbf{x}_{N_e}) \end{vmatrix}, \quad (1.1)$$

1.1 Imaging molecular orbitals by high-order harmonics

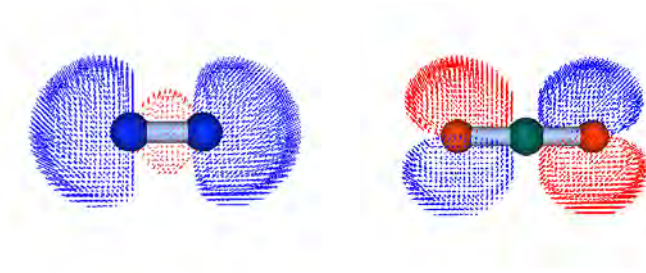


Figure 1.1: Examples of molecular orbitals. left: highest-occupied molecular orbital of N_2 . right: that of CO_2 . The color shows the sign of the wavefunction. They are obtained by using the density functional theory with B3LYP functionals and 6311+G(d) basis sets. Calculation was made by Firefly package [9], which is partially based on the GAMESS (US) [10] source code, and the figures are drawn by Facio [11, 12].

and the molecular orbitals are determined so that the total energy of the molecule is minimized under the orthonormal condition $\int d\mathbf{x} \psi_i^{\text{HF}*}(\mathbf{x}) \psi_j^{\text{HF}}(\mathbf{x}) = \delta_{ij}$. Hartree-Fock orbitals are widely used in quantum chemistry calculations, but due to the approximation (1.1) the correlation of the motion of electrons is neglected except for the exchange effect. To cover this drawback several methods have been invented such as multiconfiguration self-consistent field method [7, §4.5]. The other approach is based on the density functional theory, in which it is probed that all the electronic properties of the ground-state are determined by the electron density $\rho(\mathbf{r})$ [8]. According to this theory, the true electron density $\rho(\mathbf{r})$ can be found by considering that the density is sum of the modulus squared N_e orbitals $\rho(\mathbf{r}) = \sum_{i,s} \psi_i^{\text{KS}}(\mathbf{r}, s)$ and solving the so-called Kohn-Sham equations [8, §7.2],

$$\left[-\frac{1}{2} \nabla^2 + v_{\text{eff}} \right] \psi_i^{\text{KS}}(\mathbf{x}) = \epsilon_i \psi_i^{\text{KS}}(\mathbf{x}), \quad (1.2)$$

$$v_{\text{eff}}(\mathbf{r}) = v(\mathbf{r}) + \int \frac{\rho(\mathbf{r}')}{|\mathbf{r} - \mathbf{r}'|} d\mathbf{r}' + v_{\text{xc}}(\mathbf{r}), \quad (1.3)$$

where $v(\mathbf{r})$ is the potential due to the nuclei and $v_{\text{xc}}(\mathbf{r})$ is a function called the exchange-correlation potential. In general the exact form of $v_{\text{xc}}(\mathbf{r})$ is not known so that an approximation is used in the calculations. Both the Hartree-Fock orbitals and Kohn-Sham orbitals can be obtained by using quantum chemistry calculation packages. Figure 1.1 shows the examples of molecular orbitals of N_2 and CO_2 molecules by using a density functional theory.

There are other types of orbitals, one of which is the Dyson orbital [13, 14] defined by

$$\psi^{\text{D}}(\mathbf{x}_{N_e}) = \sqrt{N_e} \int d\mathbf{x}_1 d\mathbf{x}_2 \dots d\mathbf{x}_{N_e-1} \Psi_{\text{ion}}^*(\{\mathbf{x}\}_{N_e-1}) \Psi_0(\{\mathbf{x}\}_{N_e}), \quad (1.4)$$

where $\Psi_{\text{ion}}(\{\mathbf{x}\}_{N_e-1})$ is the wavefunction of a molecular ion made by removing one electron from the molecule. This orbital is difficult to obtain by calculation compared to the above-mentioned two types of orbitals. One of the most useful features of Dyson orbitals is that the spatial distribution can in principle be obtained experimentally, since both the ion state $\Psi_{\text{ion}}(\{\mathbf{x}\}_{N_e-1})$ and the neutral

1 Introduction

state $\Psi_0(\{\mathbf{x}\}_{N_e})$ really exist. This is in contrast to Hartree-Fock and Kohn-Sham orbitals, which are introduced for computational convenience.

One of the major methods to experimentally investigate the Dyson orbitals is the electron momentum spectroscopy or $(e, 2e)$ spectroscopy [13, 15, 16], which was devised around 1970. In the electron momentum spectroscopy a high-energy (~ 1 keV or above) electron beam hits the sample atom, molecule or solid M , and the ionization reaction $e^- + M \rightarrow M^+ + e^- + e^-$ is induced. The momentum of both the scattered and ejected electrons are observed. By using several approximations the differential cross section of ionization is related to the Dyson orbital in momentum space defined by $\psi^D(\mathbf{x}) = (2\pi)^{-3/2} \int d^3q e^{i\mathbf{r}\cdot\mathbf{q}} \tilde{\psi}^D(\mathbf{p})$ as [13, §3.3]

$$\frac{d^5\sigma}{d\Omega_f d\Omega_s dE_f} \simeq (2\pi)^4 \frac{k_f k_s}{k_0} f_{ee} \sum |\tilde{\psi}^D(\mathbf{p})|^2, \quad (1.5)$$

where $\Omega_{f/s}$ and $k_{f/s}$ are the solid angle and momentum of the faster/slower outgoing electron, E_f is the energy of the faster electron, k_0 is the momentum of the incident electron, f_{ee} is a factor depending on the momenta of incident and outgoing electrons (electron-electron collision factor), and the sum is taken over all final states. Information about the Dyson orbital can be obtained from the measurement of the differential cross section.

The electron momentum spectroscopy has a drawback that since the directions of molecular axes are not fixed in gas phase the results are averaged on the orientation of the molecules [13, §3.3.2]. The orbital of a fixed molecule was observed by using a scanning tunneling microscope [17–19]. A scanning tunneling microscope observes the tunneling current between the sample and the tip of the probe, which depends on the electronic state of the sample. This method, however, also has a limitation: to observe the orbital of gaseous molecules they have to be adsorbed on the surface on a substrate, which may change their electronic state from that of free molecule. In 2004, Itatani *et al.* reported an image of the highest occupied molecular orbital (HOMO) of gaseous N_2 molecules [20–22]. The image of the orbital obtained in their experiment shows a significant agreement with that obtained by calculation, including the change of the sign. Their success comes from the following three points: first, the direction of the gaseous molecules was pre-fixed by using nonadiabatic alignment method [23] (see § 3.5). Secondly, they probed the molecules by using intense laser pulses whose duration ~ 30 fs is sufficiently shorter than the duration ~ 0.1 ps when molecular alignment is maintained (on the other hand, it is difficult to make such short electron pulses required for the electron momentum spectroscopy). Finally, the image of the orbital is reconstructed from the spectra of high-order harmonics generated by the laser pulses, as we describe below.

Studies on high-order harmonics generated in gaseous media started in the late 1980s with the development of high-intensity lasers [24, §13.6]. An example of the spectra of high-order harmonics is shown in Fig. 1.2. Despite its high-nonlinearity, it was indicated in 1993 [25] that the spectra of high-order harmonics are well explained by the following simple three step model (see Fig. 1.3): (1) an atom or molecules is ionized by an intense laser field and an electron is released from the potential. (2) the released electron is driven and accelerated by the laser field and returned to the parent ion. (3) the returning electron recombines with the parent ion and its kinetic energy is transferred to a high-energy photon. Further theoretical investigations based on quantum mechanics such as Refs. [26–30]

1.1 Imaging molecular orbitals by high-order harmonics

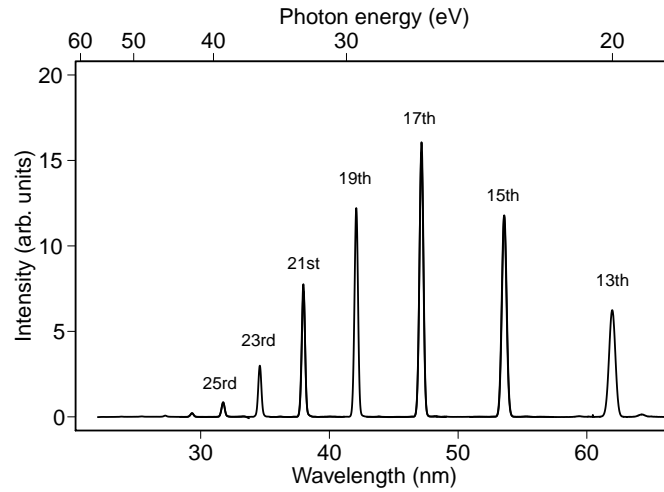


Figure 1.2: A typical example of the spectrum of high-order harmonics observed in our experimental setup. The harmonics were generated in Ar by outputs from a Ti:sapphire amplifier with the center wavelength of ~ 800 nm and detected by a flat-field grating spectrometer equipped with an x-ray CCD camera.

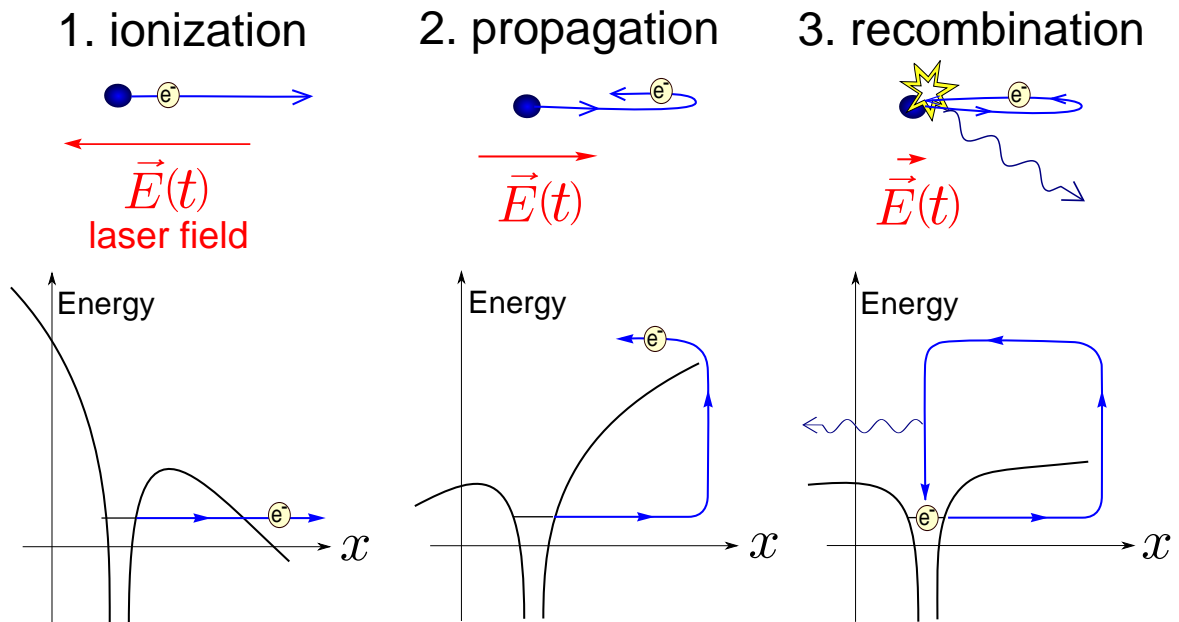


Figure 1.3: The three step model [25]. (1) An electron is tunnel-ionized from atoms or molecules through the laser-modulated potential barrier. (2) It is driven by the laser electric field and return to the parent ions. (3) It recombines when it returns in the vicinity of the parent ion and a high-energy photon is emitted as the sum of the electron kinetic energy E and the ionization potential of atoms or molecules I_p .

1 Introduction

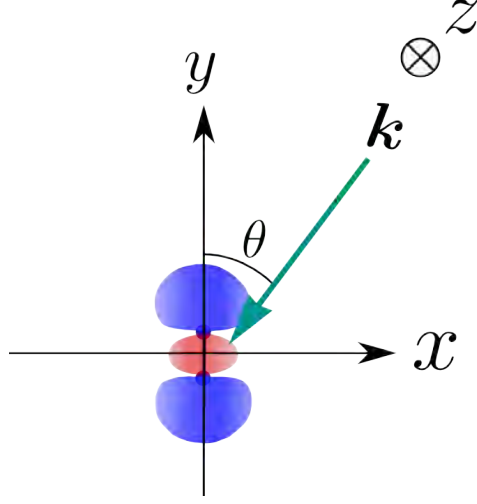


Figure 1.4: Geometry in the molecular orbital imaging. Molecules are aligned along the y axis. The probe light is linearly-polarized and propagates along the z axis.

validated this model, and revealed that each component of the harmonics $E_{\text{HH}}(\omega)$ is approximately related to the transition dipole moment between the returning electron $|\mathbf{k}\rangle$ and the orbital from which the electron is ionized $|\psi^{\text{D}}\rangle$ as (see §2.1 for detail)

$$E_{\text{HH}}(\omega) \propto \omega^2 \mathbf{D}(\omega) \sim \omega^2 a(\mathbf{k}) \mathbf{d}^*(\mathbf{k}), \quad (1.6)$$

$$\mathbf{d}(\mathbf{k}) \equiv \langle \mathbf{k} | \mathbf{r} | \psi^{\text{D}} \rangle, \quad (1.7)$$

where ω is the angular frequency of the high-order harmonics, \mathbf{k} is the wavevector of the returning electron de Broglie wave, and $a(\mathbf{k})$ stands for the amplitude of the returning electron wave packet with wavevector \mathbf{k} . By using this relationship the image of the orbital of N_2 was obtained in Ref. [20] as follows: **(1)** first, molecules are aligned by means of laser-induced nonadiabatic alignment technique [23] (§ 3.5). **(2)** the high-order harmonic spectra generated in target molecules are measured with varying the angle θ between the laser polarization and the molecular axis (Fig. 1.4). **(3)** the transition dipole moment $\mathbf{d}(\mathbf{k})$ is calculated from the obtained spectra and Eq. (1.6). In Ref. [20], the coefficient $a(\mathbf{k})$ is estimated from the high-order harmonic spectra generated from Ar, whose ionization potential is almost the same as that of N_2 . **(4)** the transition dipole moment $\mathbf{d}(\mathbf{k}) \equiv \langle \mathbf{k} | \mathbf{r} | \psi^{\text{D}} \rangle = \int d\mathbf{r}^3 \mathbf{r} \psi^{\text{D}}(\mathbf{r}) \exp(-i\mathbf{k} \cdot \mathbf{r})$ is the Fourier transform of the complex conjugate of the orbital multiplied by the position. We set the coordinate system as shown in Fig. 1.4. If \mathbf{d} 's for all wavenumbers k could be measured, the wavefunction could be obtained by 3D inverse Fourier transformation:

$$\psi^{\text{D}}(\mathbf{r}) = \frac{1}{(2\pi)^3 r_i} \int dk^3 d_i(\mathbf{k}) \exp(i\mathbf{k} \cdot \mathbf{r}), \quad (1.8)$$

where $i = x, y, z$ represents the component of the vector. In experiments, however, the direction of the wavevector \mathbf{k} is confined to the plane perpendicular to the direction of probe light propagation (the xy plane in Fig. 1.4) and difficult to obtain the 3D image. Instead, in Ref. [20] the “tomographic image”

1.1 Imaging molecular orbitals by high-order harmonics

was calculated as

$$\begin{aligned} \int dz \psi^D(\mathbf{r}) &= \frac{1}{y} \int dz y \psi(\mathbf{r}) = \frac{1}{y} \frac{1}{(2\pi)^2} \int dk^2 d_y(k_x, k_y, 0) \exp(ik_x \cdot x) \exp(ik_y \cdot y) \\ &= \frac{1}{y} \frac{1}{(2\pi)^2} \int_0^{+\infty} k dk \int_0^\pi d\theta d_y(k \cos \theta, k \sin \theta, 0) \exp[ik(x \cos \theta + y \sin \theta)]. \end{aligned} \quad (1.9)$$

The point is that the scale of de Broglie wavelength of the returning electron wave packet in high-order harmonic generation is angstrom or sub-angstrom, which is the same scale as the structure of molecular orbitals. Therefore, the molecular orbital structure is reflected sensitively in the quantum interference between the returning electron and the ground-state molecule, and thus in the generated high-order harmonics.

The excellent advantage of the imaging by high-order harmonics is its ultrahigh time resolution [21]. The three steps of high-order harmonic generation occurs within half cycle of the fundamental laser field, which is ~ 1.3 fs for outputs from a Ti:sapphire laser (wavelength ~ 800 nm) used in Ref. [20]. In fact, according to the studies by Niikura *et al.* [31], the duration of the returning electron wave packet is ~ 1 fs. In addition, the returning electron wave packet is chirped, that is, the time of recombination differs depending on the kinetic energy [32, 33]. Therefore, the duration of wave packet corresponding to each harmonic is even shorter. This short duration of returning electron enables us to probe the change of electronic states accompanying nuclear motion, because the typical timescale for nuclear motion is femtosecond [34]. It was demonstrated that high-order harmonics can probe the change in the configuration of atoms caused by photoionization [33], vibrational excitation [35], and photodissociation [36].

Since the first demonstration in 2004 [20], many researchers have investigated the tomographic imaging of molecular orbitals with high-order harmonics. For example, Haessler *et al.* [37] closely examined the tomographic image of N_2 by measuring not only the intensities of the harmonics but also the phase differences between their adjacent orders. They confirmed the phenomena reported in Ref. [38] that when the laser field to generate harmonics is intense enough the second highest-occupied molecular orbital (HOMO-1) as well as HOMO contribute to the high-order harmonics generated in N_2 . The image they obtained shows the superposition of HOMO and HOMO-1. Since an ion which release an electron from HOMO-1 has a different energy from that from HOMO, the superposition of these two states will oscillate in a frequency corresponding to the energy difference [39, §IV.10]. Therefore, the image they obtained is a “snapshot” of the electronic state moving dynamically. Another example is the tomographic imaging of the orbital of a CO_2 molecule by Vozzi *et al.* [40]. The phases of the high-order harmonics generated in CO_2 changes rapidly in a certain energy range when the angle between the laser polarization and the molecular axis is changed. This comes from the destructive interference effect found by Kanai *et al.* [41]. In Ref. [40], Vozzi *et al.* succeeded in imaging the HOMO of a CO_2 molecule by reconstructing the harmonic phases from the modulation of harmonic intensities depending on the angular distribution of molecules. As demonstrated by these two examples, the measurement of the phases of high-order harmonics is one of the bases for the development of tomographic imaging. In the next section we describe the phases of high-order harmonics and their measurements.

1 Introduction

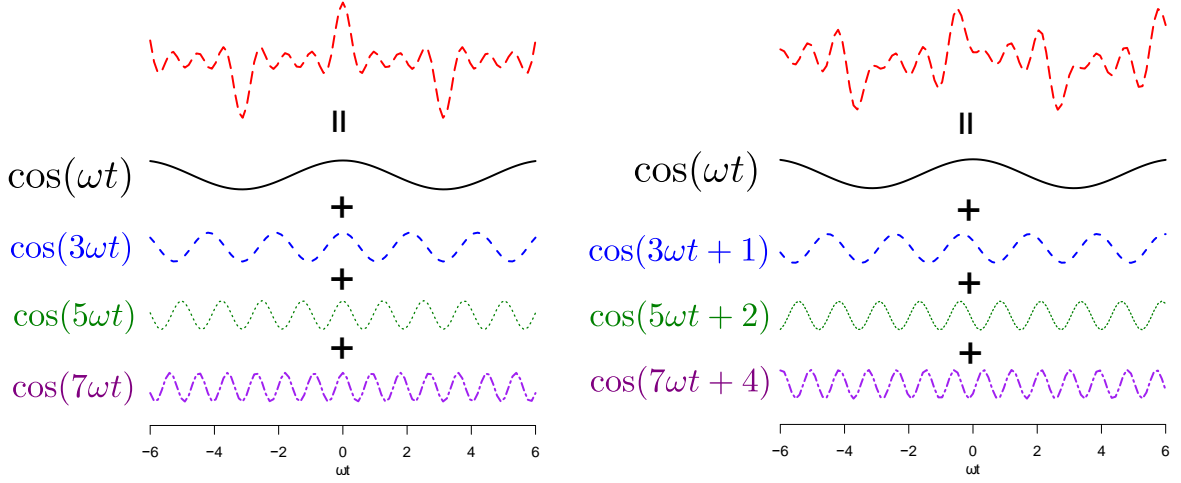


Figure 1.5: Effect of the phase on the temporal structure of the field. The top waveforms of the left and right panels have components of the same amplitude but different phase. Though the waveforms are quite different, one cannot distinguish these two wave from their components without measuring their phase.

1.2 The phase of harmonics

The component of the electric field $E_{\text{HH}}(\omega)$ appeared in Eq. (1.6) is derived from its temporal waveform $E_{\text{HH}}(t)$ by Fourier expansion as

$$E_{\text{HH}}(t) = \sum_{\omega} E_{\text{HH}}(\omega) e^{-i\omega t} + \text{c.c.}, \quad (1.10)$$

where c.c. stands for complex conjugate. The component $E_{\text{HH}}(\omega)$ is in general a complex value and has a phase ϕ_{ω} as well as an amplitude A_{ω} :

$$E_{\text{HH}}(\omega) = A_{\omega} e^{i\phi_{\omega}} \quad (1.11)$$

Substituting Eq. (1.11) into Eq. (1.10), we obtain

$$E_{\text{HH}}(t) = 2 \sum_{\omega} A_{\omega} \cos(\omega t - \phi_{\omega}). \quad (1.12)$$

This expression shows that the phase ϕ_{ω} determines the shift between each component of the electric field (see Fig. 1.5).

The phase of each harmonic plays an important role in the imaging by high-order harmonics. This can be seen, for example, from Eq. (1.9), in which the transition dipole \mathbf{d} is integrated over the wavevector \mathbf{k} of the electron wave. The transition dipole \mathbf{d} is a complex value and its phase as well as its amplitude depends on \mathbf{k} . Here, the wavevector \mathbf{k} of the electron is proportional to its momentum and therefore is related to the photon energy $\hbar\omega$ of the high-order harmonics, whereas the transition dipole \mathbf{d} is related to the component of the electric field $E_{\text{HH}}(\omega)$ by Eq. (1.6). Therefore, it is desirable to observe both the amplitude and phase of $E_{\text{HH}}(\omega)$. The phase ϕ_{ω} of the electric field, however, cannot be detected by an ordinary spectrometer with a grating.

In 2001, Paul *et al.* demonstrated the detection of the phase difference between adjacent high-order harmonics [42]. They irradiated rare gas atoms simultaneously with the high-order harmonics to be measured and its fundamental, and extracted the phase difference from the photoelectron signal produced by two-color two-photon ionization (see §2.3 for detail). Their method was later named “reconstruction of attosecond beating by interference of two-photon transitions” (RABBIT) ¹. This technique was originally developed in order to clarify the temporal structure of the high-order harmonics, and this goal was achieved successfully by the work [42] and subsequent studies such as Refs. [32, 45, 49, 50]. Later, the RABBIT technique was employed to investigate high-order harmonic generated in molecules [37, 48, 51]. One of the most important results is the above-mentioned work by Haessler *et al.* [37], in which the RABBIT method was applied to the tomographic imaging of molecular orbitals. They reconstructed the two highest occupied molecular orbital of N₂ by using the characteristic that the difference in the symmetry of the HOMO and HOMO-1 causes the $\pi/2$ difference in the harmonic phase.

There are other methods to obtain information about spectral phases. The mixed-gas method first demonstrated by Kanai *et al.* [52] observes high-order harmonics generated in the mixed gas of target molecules and reference atoms. The contributions from the target and reference interfere with each other, and phase difference between them can be extracted by comparing their spectra with that generated in pure gas. In the transient grating method [53], the target molecules are first irradiated by two pump pulses which are spatially separated before focusing and make an interference fringe at the focus, which serves as a grating. The high-order harmonics diffracted by this grating is the superposition of the contributions from the pumped media and that without being pumped, and one can obtain the phase difference between them. These methods do not require the observation of photoelectrons, so their experimental setup can be simple compared to that for RABBIT method. On the other hand, the RABBIT method has the advantage that it can obtain the phase difference between adjacent harmonic orders without “reference” (reference atoms for mixed-gas method, un-pumped media in the transient grating method). This advantage is valuable when we investigate the situation where no medium can be used as a reference.

1.3 Beyond strong field approximation

Equation (1.6) plays the central role in the molecular orbital imaging by high-order harmonics. As stated in §2.1, this equation is derived by using so-called strong field approximation, which includes the following three approximations:

approximation (1) The contributions of all bound states except the ground state are neglected.

approximation (2) The depletion of the ground state is neglected.

approximation (3) In the continuum state, the electron can be treated as a free particle moving in the electric field without effect of Coulomb potential of the parent ion.

¹There are several acronyms for this technique: RABBITT [43, 44], RABITT [37, 45], or RABBIT [46–48]. In this thesis we use RABBIT for it.

1 Introduction

The strong-field approximation successfully clarifies properties of high-order harmonics and is widely used. On the other hand, it has been reported that this approximation is too coarse to quantitatively compare the experimental results with the results of calculations. Many attempts have been proposed to improve the calculation by correcting each of the above three approximations. For example, the approximation (1) can be corrected by considering the contribution of excited states as well as the ground state [37, 38], though the accurate structure of the excited states is very difficult to obtain because it cannot be calculated without including effects of the electron correlation. Corrections for the approximation (2) can be made by calculating the rate of ionization which causes the ground-state depletion [26, 54]. Compared to these two approximations, it is not clear how to correct the approximation (3). A proper correction for the approximation (3) is important because the failure of the approximation (3) is frequently pointed out as follows: in the calculation with the approximation (3), the continuum states are expanded by plane waves without considering the effects of the Coulomb potential (§2.1.1). However, it is well-known in the scattering theory that the Coulomb potential can influence a charged particle in a faraway place due to its slow falloff [55, §14]. Moreover, in the recombination process the electron must approach the parent ion and the effect of the Coulomb interaction is inevitable. Therefore it is unrealistic to neglect the Coulomb potential. In fact, it is shown that the calculation in which the returning electron is assumed as a plane wave cannot reproduce the position of the minimum in the high-order harmonic spectra from H_2^+ which the time-dependent Schrödinger equation predicts, and a heuristic correction is needed for its reproduction [56]. Several theories have been proposed to correctly add the effects of the Coulomb potential to the strong-field approximation. In the theory of Ivanov *et al.* [57], each factor in the three step model, the ionization, propagation, and recombination, is first calculated within the strong-field approximation, and then is corrected for the Coulomb potential individually. This approach was further improved in works such as Refs. [58–60], among which the “quantitative rescattering theory” proposed by Le *et al.* [59] is one of the most commonly-used methods. In the quantitative rescattering theory it is assumed that the induced dipole D , which generates high-order harmonics, can be written as the product of the returning electron wave packet W and the photorecombination transition dipole moment d . Then, it is found that the calculation with the strong-field approximation can reproduce the structure of the wave packet W which agrees very well with that obtained by solving a time-dependent Schrödinger equation. Therefore, one can obtain a reasonably accurate induced dipole D^{QRS} by first calculating the induced dipole D^{SFA} with the strong-field approximation and then replacing its photorecombination transition dipole moment d^{SFA} to the exact one d^{Coulomb} : $D^{\text{QRS}} = (D^{\text{SFA}}/d^{\text{SFA}})d^{\text{Coulomb}}$.²

Experimentally, the first clear evidence for the failure of the strong-field approximation was found in the high-order harmonics around the ionization thresholds of the medium, that is, the energy range which is near the ionization potential of the medium. This makes sense because in the three-step model an electron with a lower kinetic energy remains closer to the parent ion and is expected to be

²To be precise, this is the explanation of the method called “QRS1” in Ref. [59]. [59] also introduces the “QRS2”, in which the returning electron wave packet is obtained by solving a time-dependent Schrödinger equation for a simple reference atom like a scaled hydrogen.

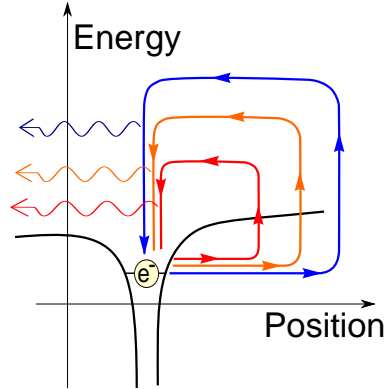


Figure 1.6: Relation between the energy of the high-order harmonics and the Coulomb potential. In the three-step model, an electron with a lower kinetic energy remains closer to the parent ion and is expected to be more affected by the Coulomb potential (see also Footnote 3).

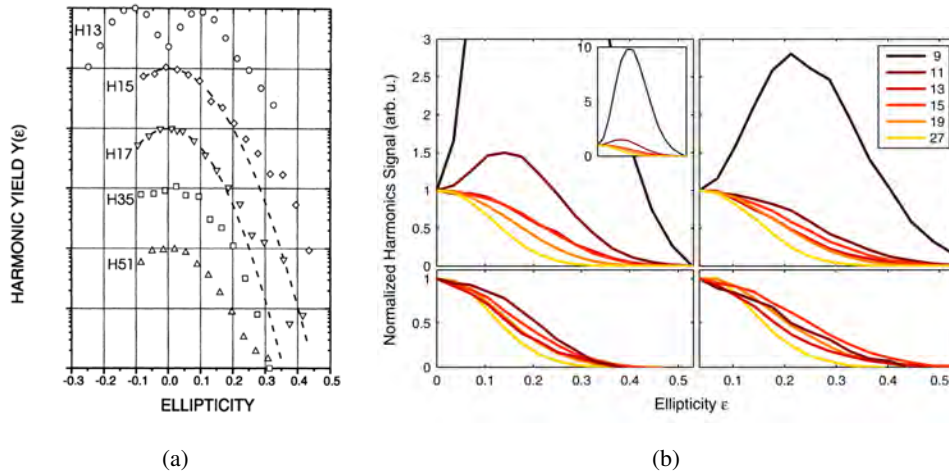


Figure 1.7: (a) Ellipticity dependence of the high-order harmonics generated in Ne reported in Ref. [61]. The 13th harmonic intensity is higher when the driving pulse has a finite value of the ellipticity than that generated with a linearly-polarized pulse. Reprinted figure with permission from N. H. Burnett, C. Kan, and P. B. Corkum, *Phys. Rev. A* **51**, R3418 (1995). Copyright (1995) by the American Physical Society. (b) Ellipticity dependence of the high-order harmonics generated in aligned O_2 molecules reported in Ref. [62]. Molecules are aligned parallel (left) and perpendicular (right) to the the major axis of the polarization ellipse, and short (top) and long (bottom) trajectories are selected. Reprinted figure with permission from H. Soifer, P. Botheron, D. Shafir, A. Diner, O. Raz, B. D. Bruner, Y. Mairesse, B. Pons, and N. Dudovich, *Phys. Rev. Lett.* **105**, 143904 (2010). Copyright (2010) by the American Physical Society.

1 Introduction

more affected by the Coulomb potential (Fig. 1.6).³ It was reported in 1995 that the 13th harmonic intensity generated in Ne is higher when the driving pulse has a finite value of the ellipticity than that generated with a linearly-polarized pulse [61, 63] (Fig. 1.7(a)). This result seems conflicting with approximation (3) of the strong-field approximation, because if the Coulomb potential is neglected, the high-order harmonics become weaker when the driving field is elliptically polarized, which deviates the returning electron from the parent ion and prevents the recombination process. In the theory of Ivanov *et al.* [57], this anomaly is attributed to the interference between the contributions from different electron trajectories. However, recently similar phenomena were found even when the path of the electron is selected by using phase-matching (§2.1.3): Soifer *et al.* [62] investigated the intensity of the high-order harmonics from molecules around their ionization thresholds with the selected electron trajectories. They found that the 9th and 11th harmonics from aligned O₂ molecules are maximized at a finite value of the ellipticity of the probe pulse when shorter trajectories are selected, but they are maximized at linear polarization when longer trajectories are selected (Fig. 1.7(b)). In addition, in Ref. [62] they also found the phenomena which suggest the failure of approximation (1). They observed that the 11th harmonic generated in N₂ shows a different behavior from higher-order harmonics when the molecules are aligned. According to their analysis, this anomaly indicates that some excited bound states of N₂ may contribute to the high-order harmonic spectra, which is against approximation (1).

1.4 Purpose of this study

The studies introduced above suggest that in the near-threshold region the strong-field approximation cannot be applied and Eq. (1.6) needs corrections when used in applications. In fact, in the experiments introduced above [20, 37] they used 17th and higher harmonics for tomographic imaging of N₂. Lower harmonics corresponds to an electron with lower kinetic energy and thus with larger de Broglie wavelength. Therefore, if we can use lower harmonics properly for imaging it will improve the resolution for larger structure. This is considered to be important when one obtains the image of larger molecules than N₂.

Experimental studies on the near-threshold harmonics is not so extensive compared to those for higher-orders. Further accumulation of knowledge is essential for developing proper treatments of them. Especially, the measured data about the phase of near-threshold harmonics are mostly limited to those generated in rare-gas atoms [32, 50]. We are interested in the phase of the near-threshold harmonics generated in molecules. The phase differences between adjacent orders are closely related to the time when the returning electron recombines with the parent ion (§2.2). Thus, when the Coulomb potential affects the trajectory of the electrons its effect will appear in the phase difference. In addition, at the recombination the electron with low energy undergoes a phase shift depending on the shape of the potential, and this shift is reflected in the phase of the harmonics [59]. In this

³Strictly speaking, this is true only for the “short paths” introduced in §2.1.2.3. The “long paths” for the near-threshold harmonics tend to go farther away from the parent ion than the short paths. This is consistent with the results by Soifer *et al.* [62] that the anomaly in the ellipticity dependence is found only when the short trajectories are selected.

thesis, we report the experimental results of the phase differences between adjacent orders of 11th–19th harmonics generated in atoms and molecules. We employ the RABBIT technique for the phase measurement. As stated in §1.2, the RABBIT method can directly access the phase differences between the adjacent harmonic orders, and unlike the mixed gas method or transient grating method, the RABBIT does not need a reference system to compare the phase. This feature is desirable for our study because the understanding of the near-threshold harmonics is not sufficient and no system can be used as a reference. We find some interesting differences between the result of atoms and those of molecules. We discuss the reason of these differences with the help of a theoretical model.

1.5 Content of the thesis

This thesis is organized as follows: In Chapter 2, we review the theoretical background on the high-order harmonic generation. Chapter 3 presents the details of our experimental setup and techniques. In Chapter 4, we present the experimental results and the analysis on them. The origins of our findings are discussed in Chapter 5. In Chapter 6, we summarize the results of our study and discuss the outlook.

Throughout this thesis, equations are written in atomic units [64], in which the Dirac constant \hbar , the mass of the electron m_e , and the charge of an electron q_e are all set equal to unity. The sign of the charge of an electron $q_e = -e$ is chosen as $+1$.⁴ The speed of light in vacuum is denoted by c . When considering the interaction between a light and an atom or a molecule, we assume that the wavelength of the light is so long compared to the size of atoms/molecules that its electric field can be considered uniform (dipole approximation [67, §5.1.2]). We choose the length gauge, in which the interaction potential \hat{V}_I between an electron at \boldsymbol{x} and an electric field \boldsymbol{E} is $\hat{V}_I = -\boldsymbol{E} \cdot \boldsymbol{x}$ [68].

⁴Note that in some references such as Refs. [65, 66], the electron charge is defined as -1 .

Chapter 2

Theoretical background of high-order harmonic generation

In this chapter, we review basic theories about high-order harmonics and measurements of their phase difference. In §2.1 we introduce a quantum mechanical model of the high-order harmonics, and show that by using several approximations the model can be written as a sum of the contributions from several “trajectories” of electrons. This will clarify why the simple three-step model can describe the property of high-order harmonics so well. In §2.2 we explain that the phase difference between adjacent high-order harmonics can be related to the moment when the harmonics are emitted. In §2.3 we describe how to detect the phase difference by using two-color two-photon ionization.

2.1 The Lewenstein model of high-order harmonic generation process with strong-field approximation

Let us consider an electron which is bound to an atom or a molecule by the Coulomb potential $V(x)$. When the electron is driven by the laser field $\mathbf{E}(t)$, its state $|\Psi(t)\rangle$ will evolve according to the time-dependent Schrödinger equation as

$$i\frac{\partial}{\partial t}|\Psi(t)\rangle = \left(\frac{1}{2}\mathbf{p}^2 + V(\mathbf{x}) - \mathbf{E} \cdot \mathbf{x}\right)|\Psi(t)\rangle, \quad (2.1)$$

where \mathbf{x} and \mathbf{p} are the position and the momentum operator, respectively. The resultant oscillation of the electric dipole moment causes the emission of high-order harmonics. Below we introduce the theory developed by Lewenstein *et al.* [26]. They showed that based on two approximations, the strong-field approximation (§2.1.1) and the saddle-point approximation (§2.1.2), the major contribution to the electric dipole moment can be extracted as a sum of several terms. Each of these terms corresponds to a trajectory of the electron. The paths are further selected by using phase matching, which we describe in §2.1.3. For simplicity, we consider the motion of only one electron (single active electron approximation) in most of the discussions in this section, but in §2.1.4 we introduce some theories about the multielectron effect.

2.1 The Lewenstein model of high-order harmonic generation process with strong-field approximation

2.1.1 Strong-field approximation

In Ref. [26] Lewenstein *et al.* introduced the following approximations: **(1)** As the bound state, only the ground state $|0\rangle$ is considered and the contributions from all other bound states are neglected. **(2)** The depletion of the ground state by ionization is neglected. **(3)** In the continuum state, the effect of the Coulomb potential of the parent ion is neglected and the electron is treated as a plane wave. They showed that under these approximation the differential equation (2.1) can be integrated as

$$|\Psi(t)\rangle = e^{iI_P t} |0\rangle + \int d^3 \mathbf{p}' e^{iI_P t} b(\mathbf{p}, t) |\mathbf{p}'\rangle, \quad (2.2)$$

$$b(\mathbf{p}, t) = i \int_{t_0}^t dt' \mathbf{E}(t') \cdot \mathbf{d} \left(\mathbf{p} - \int_{t'}^t \mathbf{E}(s) ds \right) \exp \left[-i \int_{t'}^t \left(\frac{\left(\mathbf{p} - \int_{t'}^s \mathbf{E}(s) ds \right)^2}{2} + I_P \right) dt'' \right], \quad (2.3)$$

where $|\mathbf{p}\rangle$ is the continuum state wavefunction with momentum \mathbf{p} , I_P is the ionization potential of the atom or molecule and

$$\mathbf{d}(\mathbf{p}) \equiv \langle \mathbf{p} | \mathbf{x} | 0 \rangle = (2\pi)^{-3/2} \int_{-\infty}^{+\infty} d^3 \mathbf{x} e^{-i\mathbf{p}\cdot\mathbf{x}} \mathbf{x} \langle \mathbf{x} | 0 \rangle \quad (2.4)$$

is the bound-free transition dipole. When continuum-continuum transition is neglected, the dipole moment $\mathbf{x}(t) \equiv \langle \Psi(t) | \mathbf{x} | \Psi(t) \rangle$ is expressed as

$$\mathbf{x}(t) = i \int d^3 \mathbf{p} \int_{t_0}^t dt' [\mathbf{E}(t') \cdot \mathbf{d}(\mathbf{p} - \mathbf{A}(t'))] \exp \{-iS(\mathbf{p}, t, t')\} \mathbf{d}^*(\mathbf{p} - \mathbf{A}(t)) + \text{c.c.}, \quad (2.5)$$

where $\mathbf{A}(t)$ and $S(\mathbf{p}, t, t')$ are defined by

$$\mathbf{A}(t) \equiv - \int_0^t dt' \mathbf{E}(t'), \quad (2.6)$$

$$S(\mathbf{p}, t, t') \equiv \int_{t'}^t \left[\frac{(\mathbf{p} - \mathbf{A}(t''))^2}{2} + I_P \right] dt''. \quad (2.7)$$

The detailed derivation of Eqs. (2.2)–(2.5) is described in App.B of Ref. [69]. Each factor in the integrand of Eq. (2.5) corresponds to the three steps of the classical model introduced in §1.1: $\mathbf{d}(\mathbf{p} - \mathbf{A}(t'))$ is the ionization amplitude at time t' , $S(\mathbf{p}, t, t')$ in the exponential function corresponds to the phase the freed electron acquires during the propagation from t' to t , and $\mathbf{d}^*(\mathbf{p} - \mathbf{A}(t))$ is the recombination amplitude at time t . The relation between Eq. (2.5) and the three-step model becomes clearer when the saddle-point approximation is applied. Before that, we show some preparatory calculations.

In the following, we only consider the case when the laser field is linearly polarized along the z -axis. From Eq. (2.5), the z -component of the dipole $x_z(t)$ is

$$x_z(t) = i \int d^3 \mathbf{p} \int_{t_0}^t dt' [\mathbf{E}(t') \cdot \mathbf{d}(\mathbf{p} - \mathbf{A}(t'))] \exp \{-iS(\mathbf{p}, t, t')\} d_z^*(\mathbf{p} - \mathbf{A}(t)) + \text{c.c.}, \quad (2.8)$$

where d_z is the z component of the bound-free transition dipole (2.4). The electric field $E_{\text{HH},z}(t)$ emitted by the oscillation of the electron is proportional to the acceleration of the dipole moment as

$$E_{\text{HH},z}(t) \propto \ddot{x}_z(t - D/c), \quad (2.9)$$

2 Theoretical background of high-order harmonic generation

where D is the distance from the electron to the detector and c is the speed of light. The Fourier transform of the electric field of high-order harmonics $\tilde{E}_{\text{HH},z}(\omega)$ is then

$$\tilde{E}_{\text{HH},z}(\omega) \equiv \int_{-\infty}^{+\infty} dt e^{+i\omega t} E_{\text{HH},z}(t) \propto \int_{-\infty}^{+\infty} dt e^{+i\omega t} \ddot{x}_z(t - D/c) \propto \int_{-\infty}^{+\infty} dt e^{+i\omega t} \ddot{x}_z(t). \quad (2.10)$$

By using integration by parts, the most right-hand side of Eq. (2.10) becomes

$$\begin{aligned} \int_{-\infty}^{+\infty} dt e^{+i\omega t} \ddot{x}_z(t) &= e^{+i\omega t} \dot{x}_z(t) \Big|_{t \rightarrow -\infty}^{t \rightarrow +\infty} - i\omega \int_{-\infty}^{+\infty} dt e^{+i\omega t} \dot{x}_z(t) \\ &= e^{+i\omega t} \dot{x}_z(t) \Big|_{t \rightarrow -\infty}^{t \rightarrow +\infty} - i\omega e^{+i\omega t} x_z(t) \Big|_{t \rightarrow -\infty}^{t \rightarrow +\infty} - \omega^2 \tilde{x}_z(\omega), \end{aligned} \quad (2.11)$$

where

$$\tilde{x}_z(\omega) \equiv \int_{-\infty}^{+\infty} dt e^{+i\omega t} x_z(t) \quad (2.12)$$

is the Fourier transform of $x_z(t)$. We assume that at $t = -\infty$, when molecules are not driven by the laser pulses yet, $\dot{x}_z(t = -\infty) = 0$ and $x_z(t = -\infty) = 0$. If the envelope of laser pulses varies slowly enough and the degree of ionization is negligible, $\dot{x}_z(t = +\infty)$ and $x_z(t = +\infty)$ can be regarded as zero, and the first two terms of Eq. (2.11) can be neglected:

$$\int_{-\infty}^{+\infty} dt e^{+i\omega t} \ddot{x}_z(t) \simeq -\omega^2 \tilde{x}_z(\omega). \quad (2.13)$$

By adopting this approximation to Eq. (2.10), we find that the Fourier transform of the harmonic field can be approximately proportional to that of the dipole moment times the square of the frequency:

$$\tilde{E}_{\text{HH},z}(\omega) \propto \omega^2 \tilde{x}_z(\omega). \quad (2.14)$$

2.1.2 Saddle-point approximation

From Eqs. (2.5), (2.12) and (2.14), the spectrum of the high-order harmonics can be obtained by calculating the Fourier transform of the dipole moment:

$$\begin{aligned} \tilde{x}_z(\omega) &= \int_{-\infty}^{+\infty} dt e^{+i\omega t} \left\{ i \int d^3 \mathbf{p} \int_{t_0}^t dt' \right. \\ &\quad \left. \times [\mathbf{E}(t') \cdot \mathbf{d}(\mathbf{p} - \mathbf{A}(t'))] \exp \{-iS(\mathbf{p}, t, t')\} d_z^*(\mathbf{p} - \mathbf{A}(t)) + \text{c.c.} \right\} \\ &= i \int_{-\infty}^{+\infty} dt \int_{t_0}^t dt' \int d^3 \mathbf{p} [\mathbf{E}(t') \cdot \mathbf{d}(\mathbf{p} - \mathbf{A}(t'))] \exp \{-i[S(\mathbf{p}, t, t') - \omega t]\} d_z^*(\mathbf{p} - \mathbf{A}(t)) \\ &\quad - i \int_{-\infty}^{+\infty} dt \int_{t_0}^t dt' \int d^3 \mathbf{p} [\mathbf{E}(t') \cdot \mathbf{d}^*(\mathbf{p} - \mathbf{A}(t'))] \exp \{i[S(\mathbf{p}, t, t') + \omega t]\} d_z(\mathbf{p} - \mathbf{A}(t)). \end{aligned} \quad (2.15)$$

The form of Eq. (2.15), multidimensional integral with phase term, reminds us of Feynman's path integral [70]: in the path integral formulation, the probability that a particle goes from a point x_a at time t_a to a point x_b at time t_b is the absolute square of the quantity $K(b, a)$ defined by

$$K(b, a) = \int_a^b \exp(iS[b, a]) \mathcal{D}x(t) \equiv \lim_{N \rightarrow +\infty} \frac{1}{A^N} \int dx_1 \int dx_2 \cdots \int dx_{N-1} \exp(iS[b, a]), \quad (2.16)$$

2.1 The Lewenstein model of high-order harmonic generation process with strong-field approximation

where $S[b, a]$ is the ‘‘action’’ or time integral of the Lagrangian, $x_1, x_2 \dots x_{N-1}$ is a set of partition points between x_a and x_b , and $1/A^N$ is a normalization factor. In the integral the major contribution comes from the vicinity of paths where $S[b, a]$ is stationary because otherwise the exponential function $\exp(iS[b, a])$ will oscillate rapidly and interfere destructively to each other. In the same sense, the five-dimensional integral (2.15) is considered to be dominated by the contributions around the stationary points of the phase factor $[S(\mathbf{p}, t, t') \pm \omega t]$ in the exponential function. Below we extract these dominant contributions by using saddle-point approximation [71, §7.3] as presented in Refs. [26–29, 72].

2.1.2.1 Integral over \mathbf{p}

First we calculate the stationary value of the \mathbf{p} , which is denoted by \mathbf{p}_{st} . Since

$$\begin{aligned} \frac{\partial}{\partial \mathbf{p}} [S(\mathbf{p}, t, t') \pm \omega t] &= \frac{\partial}{\partial \mathbf{p}} S(\mathbf{p}, t, t') \stackrel{(2.7)}{=} \frac{\partial}{\partial \mathbf{p}} \int_{t'}^t \left[\frac{(\mathbf{p} - \mathbf{A}(t''))^2}{2} + I_p \right] dt'' \\ &= (t - t')\mathbf{p} - \int_{t'}^t \mathbf{A}(t'') dt'' \end{aligned} \quad (2.17)$$

is zero at the stationary value, \mathbf{p}_{st} is determined as:

$$\mathbf{p}_{\text{st}}(t'; t) \equiv \frac{1}{t - t'} \int_{t'}^t \mathbf{A}(t'') dt''. \quad (2.18)$$

Next, we expand the phase factor $S(\mathbf{p}, t, t') \pm \omega t$ using Taylor series around \mathbf{p}_{st} to the second order [73, §3.8]:

$$\begin{aligned} S(\mathbf{p}, t, t') \pm \omega t &= \sum_{n=0}^{+\infty} \frac{1}{n!} \left[(\mathbf{p} - \mathbf{p}_{\text{st}}(t'; t)) \cdot \frac{\partial}{\partial \mathbf{p}'} \right]^n \left[S(\mathbf{p}', t, t') - \omega t \right] \Big|_{\mathbf{p}' = \mathbf{p}_{\text{st}}(t'; t)} \\ &\simeq S(\mathbf{p}_{\text{st}}(t'; t), t, t') \pm \omega t + (\mathbf{p} - \mathbf{p}_{\text{st}}(t'; t)) \cdot \frac{\partial}{\partial \mathbf{p}'} S(\mathbf{p}', t, t') \Big|_{\mathbf{p}' = \mathbf{p}_{\text{st}}(t'; t)} \\ &\quad + \frac{1}{2} (\mathbf{p} - \mathbf{p}_{\text{st}}(t'; t)) \cdot \frac{\partial}{\partial \mathbf{p}'} \left[(\mathbf{p} - \mathbf{p}_{\text{st}}(t'; t)) \cdot \frac{\partial}{\partial \mathbf{p}'} S(\mathbf{p}', t, t') \right] \Big|_{\mathbf{p}' = \mathbf{p}_{\text{st}}(t'; t)} \\ &= S(\mathbf{p}_{\text{st}}(t'; t), t, t') \pm \omega t + \frac{1}{2} (t - t') (\mathbf{p} - \mathbf{p}_{\text{st}}(t'; t))^2. \end{aligned} \quad (2.19)$$

By employing this approximation in Eq.(2.15) and by integrating it over \mathbf{p} , we obtain

$$\begin{aligned} &\tilde{x}_z(\omega) \\ &= i \int_{-\infty}^{+\infty} dt \int_{t_0}^t dt' \left(\frac{\pi}{i(t - t')/2} \right)^{3/2} [\mathbf{E}(t') \cdot \mathbf{d}(\mathbf{p}_{\text{st}}(t'; t) - \mathbf{A}(t'))] e^{-i[S_{\text{st}}(t'; t) - \omega t]} d_z^*(\mathbf{p}_{\text{st}}(t'; t) - \mathbf{A}(t)) \\ &\quad - i \int_{-\infty}^{+\infty} dt \int_{t_0}^t dt' \left(\frac{\pi}{-i(t - t')/2} \right)^{3/2} [\mathbf{E}(t') \cdot \mathbf{d}^*(\mathbf{p}_{\text{st}}(t'; t) - \mathbf{A}(t'))] e^{i[S_{\text{st}}(t'; t) + \omega t]} d_z(\mathbf{p}_{\text{st}}(t'; t) - \mathbf{A}(t)), \end{aligned} \quad (2.20)$$

2 Theoretical background of high-order harmonic generation

where

$$\begin{aligned}
S_{\text{st}}(t'; t) &\equiv S(\mathbf{p}_{\text{st}}(t'; t), t, t') \\
&= \int_{t'}^t \left[\frac{1}{2} (\mathbf{p}_{\text{st}}(t'; t) - \mathbf{A}(t''))^2 + I_{\text{P}} \right] dt'' \\
&= \frac{t-t'}{2} \mathbf{p}_{\text{st}}^2(t'; t) - \mathbf{p}_{\text{st}}(t'; t) \cdot \left[\int_{t'}^t \mathbf{A}(t'') dt'' \right] + \frac{1}{2} \left[\int_{t'}^t \mathbf{A}^2(t'') dt'' \right] + I_{\text{P}}(t-t') \\
&\stackrel{(2.18)}{=} -\frac{t-t'}{2} \mathbf{p}_{\text{st}}^2(t'; t) + \frac{1}{2} \left[\int_{t'}^t \mathbf{A}^2(t'') dt'' \right] + I_{\text{P}}(t-t').
\end{aligned} \tag{2.21}$$

Due to the factor $\{\pi/[i(t-t')/2]\}^{3/2}$, the integrand of Eq. (2.20) diverges unphysically at $t-t' = 0$. This divergence does not occur when the \mathbf{p} -dependence of $\mathbf{d}(\mathbf{p})$ is also taken into account. In order to remove the unphysical singularity at $t-t' = 0$, $\{\pi/[i(t-t')/2]\}^{3/2}$ in Eq. (2.20) is replaced by $\{\pi/[i(t-t')/2 + \epsilon]\}^{3/2}$, where ϵ is a small value [26, 74]:

$$\begin{aligned}
\tilde{x}_z(\omega) &= i \int_{-\infty}^{+\infty} dt \int_{t_0}^t dt' \left(\frac{\pi}{i(t-t')/2 + \epsilon} \right)^{3/2} \\
&\quad \times [\mathbf{E}(t') \cdot \mathbf{d}(\mathbf{p}_{\text{st}}(t'; t) - \mathbf{A}(t'))] e^{-i[S_{\text{st}}(t'; t) - \omega t]} d_z^*(\mathbf{p}_{\text{st}}(t'; t) - \mathbf{A}(t)) \\
&\quad - i \int_{-\infty}^{+\infty} dt \int_{t_0}^t dt' \left(\frac{\pi}{-i(t-t')/2 + \epsilon} \right)^{3/2} \\
&\quad \times [\mathbf{E}(t') \cdot \mathbf{d}^*(\mathbf{p}_{\text{st}}(t'; t) - \mathbf{A}(t'))] e^{i[S_{\text{st}}(t'; t) + \omega t]} d_z(\mathbf{p}_{\text{st}}(t'; t) - \mathbf{A}(t)).
\end{aligned} \tag{2.22}$$

2.1.2.2 Integral over t

Next we search the stationary points on t and t' . Since the calculation is somewhat cumbersome, most part of the derivation is omitted here and described in Appendix A.1.1.

For shorthand notation let us define $\Theta_{(\pm)}(t'; t)$ as

$$\Theta_{(\pm)}(t'; t) \equiv \omega t \pm S_{\text{st}}(t'; t). \tag{2.23}$$

With this notation Eq. (2.22) becomes

$$\begin{aligned}
\tilde{x}_z(\omega) &= i \int_{-\infty}^{+\infty} dt \int_{t_0}^t dt' \left(\frac{\pi}{i(t-t')/2 + \epsilon} \right)^{3/2} e^{+i\Theta_{(-)}(t'; t)} [\mathbf{E}(t') \cdot \mathbf{d}(\mathbf{p}_{\text{st}}(t'; t) - \mathbf{A}(t'))] d_z^*(\mathbf{p}_{\text{st}}(t'; t) - \mathbf{A}(t)) \\
&\quad - i \int_{-\infty}^{+\infty} dt \int_{t_0}^t dt' \left(\frac{\pi}{-i(t-t')/2 + \epsilon} \right)^{3/2} e^{+i\Theta_{(+)}(t'; t)} [\mathbf{E}(t') \cdot \mathbf{d}^*(\mathbf{p}_{\text{st}}(t'; t) - \mathbf{A}(t'))] d_z(\mathbf{p}_{\text{st}}(t'; t) - \mathbf{A}(t)).
\end{aligned} \tag{2.24}$$

We assume that the major contribution to the integral over t and t' in Eq. (2.24) comes from the stationary point of $\Theta_{(\pm)}(t'; t)$, denoted by $\mathbf{t}_{\text{st}}^{(\pm)} \equiv (t_{\text{st}}^{(\pm)}, t'_{\text{st}}^{(\pm)})$. These stationary points are the solution

2.1 The Lewenstein model of high-order harmonic generation process with strong-field approximation

of the following simultaneous equations (see Appendix A.1.1):

$$\frac{[\mathbf{p}_{\text{st}}(t_{\text{st}}^{(\pm)}; t_{\text{st}}^{(\pm)}) - \mathbf{A}(t_{\text{st}}^{(\pm)})]^2}{2} + I_P \pm \omega = 0, \quad (2.25)$$

$$\frac{[\mathbf{p}_{\text{st}}(t_{\text{st}}^{(\pm)}; t_{\text{st}}^{(\pm)}) - \mathbf{A}(t_{\text{st}}^{(\pm)})]^2}{2} + I_P = 0. \quad (2.26)$$

In view of the interpretation described after Eq. (2.7), $t_{\text{st}}^{(\pm)}$ and $t_{\text{st}}^{(\pm)}$ correspond to the time of ionization and recombination of the electron, respectively. By using the saddle point approximation around $(t_{\text{st}}^{(\pm)}, t_{\text{st}}^{(\pm)})$, in Eq. (2.24), we have (See Appendix A.1.2)

$$\begin{aligned} \tilde{x}_z(\omega) \simeq & \sum_{(t_{\text{st}}^{(-)}, t_{\text{st}}^{(-)})} \frac{+i2\pi}{\sqrt{-\det \Theta''_{(-)}}} \left(\frac{\pi}{+i(t_{\text{st}}^{(-)} - t_{\text{st}}^{(-)})/2 + \epsilon} \right)^{3/2} e^{+i\Theta_{(-)}(t_{\text{st}}^{(-)}; t_{\text{st}}^{(-)})} \\ & \times [\mathbf{E}(t_{\text{st}}^{(-)}) \cdot \mathbf{d}(\mathbf{p}_{\text{st}}(t_{\text{st}}^{(-)}; t_{\text{st}}^{(-)}) - \mathbf{A}(t_{\text{st}}^{(-)}))] d_z^*(\mathbf{p}_{\text{st}}(t_{\text{st}}^{(-)}; t_{\text{st}}^{(-)}) - \mathbf{A}(t_{\text{st}}^{(-)})) \\ & + \sum_{(t_{\text{st}}^{(+)}, t_{\text{st}}^{(+)})} \frac{-i2\pi}{\sqrt{-\det \Theta''_{(+)}}} \left(\frac{\pi}{-i(t_{\text{st}}^{(+)} - t_{\text{st}}^{(+)})/2 + \epsilon} \right)^{3/2} e^{+i\Theta_{(+)}(t_{\text{st}}^{(+)}; t_{\text{st}}^{(+)})} \\ & \times [\mathbf{E}(t_{\text{st}}^{(+)}) \cdot \mathbf{d}^*(\mathbf{p}_{\text{st}}(t_{\text{st}}^{(+)}; t_{\text{st}}^{(+)}) - \mathbf{A}(t_{\text{st}}^{(+)}))] d_z(\mathbf{p}_{\text{st}}(t_{\text{st}}^{(+)}; t_{\text{st}}^{(+)}) - \mathbf{A}(t_{\text{st}}^{(+)})), \end{aligned} \quad (2.27)$$

where $\Theta''_{(\pm)}$ is a Hessian matrix of $\Theta_{(\pm)}(t'; t)$ at $t = t_{\text{st}}^{(\pm)}$, the determinant of which can be calculated as (see Appendix A.1.3)

$$\begin{aligned} \det \Theta''_{(\pm)} = & \frac{4I_P [I_P \pm \omega]}{(t_{\text{st}}^{(\pm)} - t_{\text{st}}^{(\pm)})^2} - \frac{2 [I_P \pm \omega]}{t_{\text{st}}^{(\pm)} - t_{\text{st}}^{(\pm)}} \mathbf{E}(t_{\text{st}}^{(\pm)}) \cdot [\mathbf{p}_{\text{st}}(t_{\text{st}}^{(\pm)}; t) - \mathbf{A}(t_{\text{st}}^{(\pm)})] \\ & + \frac{2I_P}{t_{\text{st}}^{(\pm)} - t_{\text{st}}^{(\pm)}} \mathbf{E}(t_{\text{st}}^{(\pm)}) \cdot [\mathbf{p}_{\text{st}}(t_{\text{st}}^{(\pm)}; t) - \mathbf{A}(t_{\text{st}}^{(\pm)})] \\ & - \left\{ \mathbf{E}(t_{\text{st}}^{(\pm)}) \cdot [\mathbf{p}_{\text{st}}(t_{\text{st}}^{(\pm)}; t) - \mathbf{A}(t_{\text{st}}^{(\pm)})] \right\} \left\{ \mathbf{E}(t_{\text{st}}^{(\pm)}) \cdot [\mathbf{p}_{\text{st}}(t_{\text{st}}^{(\pm)}; t) - \mathbf{A}(t_{\text{st}}^{(\pm)})] \right\} \\ & - \frac{\left\{ [\mathbf{p}_{\text{st}}(t_{\text{st}}^{(\pm)}; t) - \mathbf{A}(t_{\text{st}}^{(\pm)})] \cdot [\mathbf{p}_{\text{st}}(t_{\text{st}}^{(\pm)}; t) - \mathbf{A}(t_{\text{st}}^{(\pm)})] \right\}^2}{(t_{\text{st}}^{(\pm)} - t_{\text{st}}^{(\pm)})^2}. \end{aligned} \quad (2.28)$$

2.1.2.3 Removing unphysical paths

Though Eqs. (2.25) and (2.26) have many solutions, some of them are unphysical and must be rejected. First of all, in Eq. (2.25) the term $[\mathbf{p}_{\text{st}}(t_{\text{st}}^{(\pm)}; t_{\text{st}}^{(\pm)}) - \mathbf{A}(t_{\text{st}}^{(\pm)})]^2/2$ corresponds to the kinetic energy of the electron at the recombination and thus it should be positive¹. Therefore, for positive (negative) ω , the solution is acceptable only when plus-minus sign \pm is minus (plus). and $|\omega| > I_P$. Since the dipole moment is real, the Fourier component $\tilde{x}_z(\omega)$ satisfies the condition $\tilde{x}_z(-\omega) = \tilde{x}_z^*(\omega)$

¹ Equation (2.26) shows that $[\mathbf{p}_{\text{st}}(t_{\text{st}}^{(\pm)}; t_{\text{st}}^{(\pm)}) - \mathbf{A}(t_{\text{st}}^{(\pm)})]^2/2$, which corresponds to the kinetic energy of the electron at the ionization, is negative. This makes sense because the ionization process occurs by tunneling the potential barrier, where the kinetic energy is negative [27].

2 Theoretical background of high-order harmonic generation

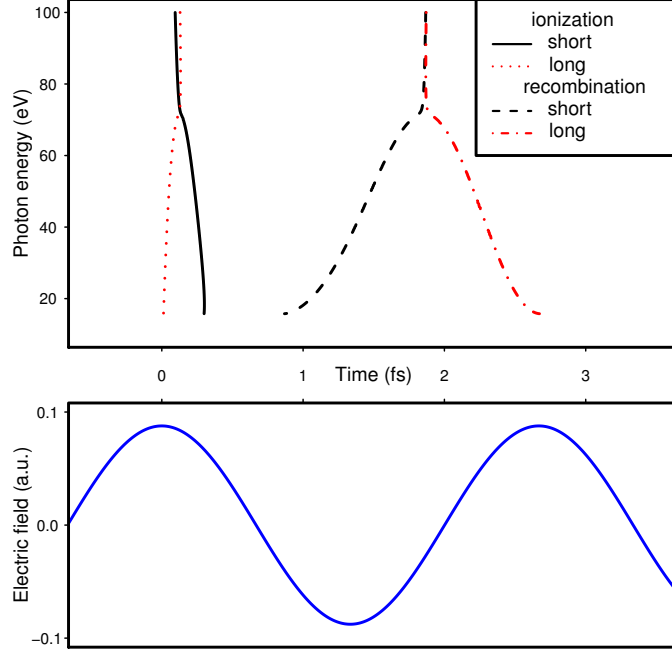


Figure 2.1: Short and long paths (upper panel) of an electron ionized by an electric field with intensity $I = 2.7 \times 10^{14}$ W/cm² (lower panel). The real parts of the ionization time $t_{\text{st}}^{(-)}$ and the recombination time $t_{\text{st}}^{\prime(-)}$ are plotted. The equations (2.29) and (2.30) are solved by using the `gsl_multirroot_fsolver_hybrids` solver provided in the GNU Scientific Library (GSL) [75, §35].

[71, §15.3]. Thus we only need to calculate paths for $\omega > 0$. To summarize, what we have to solve is a pair of nonlinear equations

$$\frac{[\mathbf{p}_{\text{st}}(t_{\text{st}}^{\prime(-)}; t_{\text{st}}^{(-)}) - \mathbf{A}(t_{\text{st}}^{(-)})]^2}{2} + I_{\text{P}} - \omega = 0, \quad (2.29)$$

$$\frac{[\mathbf{p}_{\text{st}}(t_{\text{st}}^{\prime(-)}; t_{\text{st}}^{(-)}) - \mathbf{A}(t_{\text{st}}^{\prime(-)})]^2}{2} + I_{\text{P}} = 0, \quad (2.30)$$

where $\mathbf{p}_{\text{st}}(t'; t)$ and $\mathbf{A}(t)$ are defined by Eqs. (2.18) and (2.6) respectively, and the dipole moment can be calculated by substituting the solutions $(t_{\text{st}}^{\prime(-)}, t_{\text{st}}^{(-)})$ into

$$\begin{aligned} \tilde{x}_z(\omega) \simeq & \sum_{(t_{\text{st}}^{\prime(-)}, t_{\text{st}}^{(-)})} \frac{+i2\pi}{\sqrt{-\det \Theta''_{(-)}}} \left(\frac{\pi}{+i(t_{\text{st}}^{(-)} - t_{\text{st}}^{\prime(-)})/2 + \epsilon} \right)^{3/2} e^{+i\Theta_{(-)}(t_{\text{st}}^{\prime(-)}, t_{\text{st}}^{(-)})} \\ & \times [\mathbf{E}(t_{\text{st}}^{(-)}) \cdot \mathbf{d}(\mathbf{p}_{\text{st}}(t_{\text{st}}^{\prime(-)}; t_{\text{st}}^{(-)}) - \mathbf{A}(t_{\text{st}}^{\prime(-)}))] d_z^*(\mathbf{p}_{\text{st}}(t_{\text{st}}^{\prime(-)}; t_{\text{st}}^{(-)}) - \mathbf{A}(t_{\text{st}}^{(-)})). \end{aligned} \quad (2.31)$$

Equations (2.29) and (2.30) still have infinite solutions, but the contribution from paths whose recombination time $t_{\text{st}}^{\prime(-)}$ is too far from the ionization time $t_{\text{st}}^{(-)}$ will be small due to the quantum diffusion of the electron [27]. If we limit the paths which recombine within one cycle, there are two solutions: One of the two paths ionizes later and recombines earlier and is called the “short path”,

2.1 The Lewenstein model of high-order harmonic generation process with strong-field approximation

because the flight time of the electron is shorter than the other (“long path”). The example of short and long paths is shown in the upper panel of Fig. 2.1. This figure shows the relation between the real parts of the ionization and the recombination time of a trajectory (horizontal axis) and the energy of the photon produced by the relevant trajectory (vertical axis), in the same way as Fig. 3 of Ref. [72]. The solutions for the short and the long trajectories merge at ~ 70 eV, which corresponds to the sum of the maximum kinetic energy of the electron and the ionization potential I_P [see Eq. (2.29)]. After the merging point the solutions still run vertically toward high-energy region. In reality, however, in this energy region the imaginary part of the solutions grows rapidly, which make the solutions unphysical [27]. In this thesis we do not use solutions in such high-energy region for discussions.

2.1.3 Quantum path selection by phase matching

In general, the efficiency of harmonic generation is very low unless the phase matching condition is satisfied [24, §2.3]. The phase matching condition for high-order harmonics is important for their application and has been studied in many works such as Refs. [27, 29, 76–79]. To clarify the property of the phase of high-order harmonics, we rewrite the phase $\Theta_{(-)}$ [Eq. (2.23)] of the dipole moment \tilde{x}_z [Eq. (2.31)] by using Eqs. (2.21), (2.18) and (2.6) as

$$\begin{aligned}\Theta_{(-)}(t'; t) &= \omega t + \frac{t-t'}{2} \mathbf{p}_{\text{st}}^2(t'; t) + \frac{1}{2} \left[\int_{t'}^t \mathbf{A}^2(t'') dt'' \right] + I_P(t-t') \\ &= \omega t + \frac{1}{2(t-t')} \left(\int_{t'}^t \mathbf{A}(t'') dt'' \right)^2 + \frac{1}{2} \left[\int_{t'}^t \mathbf{A}^2(t'') dt'' \right] + I_P(t-t') \\ &= \omega t + \frac{1}{2(t-t')} \left(\int_{t'}^t dt'' \int_0^{t''} d\tilde{t} \mathbf{E}(\tilde{t}) \right)^2 + \frac{1}{2} \left[\int_{t'}^t \left(\int_0^{t''} d\tilde{t} \mathbf{E}(\tilde{t}) \right)^2 dt'' \right] + I_P(t-t').\end{aligned}\quad (2.32)$$

When the fundamental field is continuous and expressed as $\mathbf{E}(\tilde{t}) = \mathbf{E}_0 \cos \omega_0 \tilde{t}$, we obtain

$$\begin{aligned}\Theta_{(-)}(t'; t) &= \omega t + \frac{|\mathbf{E}_0|^2}{2(t-t')} \left(\int_{t'}^t dt'' \int_0^{t''} d\tilde{t} \cos \omega_0 \tilde{t} \right)^2 \\ &\quad + \frac{|\mathbf{E}_0|^2}{2} \left[\int_{t'}^t \left(\int_0^{t''} d\tilde{t} \cos \omega_0 \tilde{t} \right)^2 dt'' \right] + I_P(t-t') \\ &= \omega t + \left(I_P + \frac{|\mathbf{E}_0|^2}{4\omega_0^2} \right) \tau - \frac{|\mathbf{E}_0|^2}{2\omega_0^4 \tau} (1 - \cos(\omega_0 \tau)) \\ &\quad - \frac{|\mathbf{E}_0|^2}{4\omega_0^3} \left[\sin \omega_0 \tau - \frac{4}{\omega_0 \tau} \sin^2(\omega_0 \tau / 2) \right] \cos [2\omega_0(t - \tau/2)],\end{aligned}\quad (2.33)$$

where $\tau \equiv t - t'$ is the flight time of the electron, that is, the time interval between ionization and recombination². Since $\tau \equiv t - t'$ is usually considerably larger than the atomic unit of time (24.2 attoseconds), the dominant term in Eq. (2.33) is

$$\Theta_{(-)}(t'; t) \simeq \omega t + \left(I_P + \frac{|\mathbf{E}_0|^2}{4\omega_0^2} \right) \tau. \quad (2.34)$$

² The quantity $\frac{|\mathbf{E}_0|^2}{4\omega_0^2}$ which appears in Eq. (2.33) equals to the averaged kinetic energy of an electron in an oscillating electric field, and is called ponderomotive energy [24, §13.5].

2 Theoretical background of high-order harmonic generation

Equation (2.34) shows that the phase of the harmonics has a term that is proportional to the intensity of the fundamental field $|E_0|^2$ times the flight time τ . This fact makes us deduce the following two things: first, the position of the harmonic generation with respect to the focal point of the fundamental pulse is important for phase-matching because the intensity of the focused beam depends on the position. Secondly, due to the dependence on τ , the phase matching condition differs between the contribution of short trajectories and that of long trajectories. In addition to these two factors, one must take into account the phase change induced by focusing the laser light [80, §4.7] (this phase change appears for a geometrical reason and is called Gouy phase [81]). In this way, the phase-matching problem of high-order harmonics is very complicated. Fortunately, Antoine *et al.* [77] found a simple rule: when the laser pulse is focused before the medium position, the contribution from the short paths is dominant. When the focus is located around the medium, the contribution of the long trajectories are mainly selected. By utilizing this rule, we can select only one dominant trajectory per one half cycle.

2.1.4 Relation to tomographic imaging

As stated in §2.1.2.3, the term $[\mathbf{p}_{\text{st}}(t_{\text{st}}^{(\pm)}; t_{\text{st}}^{(\pm)}) - \mathbf{A}(t_{\text{st}}^{(\pm)})]^2/2$ in Eq. (2.25) corresponds to the kinetic energy of the electron. Thus $\mathbf{p}_{\text{st}}(t_{\text{st}}^{(-)}; t_{\text{st}}^{(-)})$ appeared in d_z^* of Eq. (2.31) corresponds to the momentum of the electron at the recombination. In atomic units the momentum is equal to the wavevector \mathbf{k} . Therefore, Eq. (2.31) gives the relation

$$\tilde{x}_z(\omega) \sim a(\mathbf{k})d_z^*(\mathbf{k}), \quad (2.35)$$

which is used in the tomographic imaging (Eq. (1.6) in §1.1).

So far we only consider one electron in a molecule. More rigorous treatments including multi-electron effects are presented in Refs. [14, 30, 82]. According to the study of Patchkovskii *et al.* [30], $d^*(\mathbf{k}) = \langle 0 | \mathbf{x} | \mathbf{k} \rangle$ defined in Eq. (2.4) is replaced by $\sqrt{2}(\langle \psi^{\text{D}} | \mathbf{x} | \mathbf{k} \rangle + \mathbf{d}_2)$, where $|\psi^{\text{D}}\rangle$ is the Dyson orbital (see §1.1) corresponding to the one-electron ground state $|0\rangle$ and \mathbf{d}_2 is a term defined in Ref. [30], which comes from the exchange correlation [7, §2.3.6]. When the effect of \mathbf{d}_2 is relatively small like N_2 [30], the dipole becomes the one presented in §1.1 [Eq. (1.7)]. In the case where the exchange effect is important, the correction based on Refs. [14, 30, 82] will be needed.

2.2 Spectral phase of high-order harmonics

In this section, we discuss the relation between the phase of the harmonics and its temporal structure, and present the physical meaning of the phase difference between adjacent orders of high-order harmonics. In §2.2.1 we show the structure of high-order harmonic spectrum by using the result obtained in the previous subsection. Next in §2.2.2 we describe the effect of harmonic phase difference on the temporal structure of high-order harmonics.

2.2.1 Spectral structure of high-order harmonics

From Eqs. (2.14), (2.23) and (2.31) in the previous subsection, we see that the Fourier component of the electric field of high-order harmonics can be written as a sum of the contributions of several trajectories:

$$\tilde{E}_{\text{HH}}(\omega) \propto \sum_{(t'_{\text{st}}(-), t_{\text{st}}(-))} f(t'_{\text{st}}(-), t_{\text{st}}(-)) e^{+i\omega t_{\text{st}}(-)}, \quad (2.36)$$

where

$$\begin{aligned} f(t'_{\text{st}}(-), t_{\text{st}}(-)) &\simeq \omega^2 \frac{+i2\pi}{\sqrt{-\det \Theta''_{(-)}}} \left(\frac{\pi}{+i(t_{\text{st}}(-) - t'_{\text{st}}(-))/2 + \epsilon} \right)^{3/2} e^{-iS(t'_{\text{st}}(-); t_{\text{st}}(-))} \\ &\times \left[\mathbf{E}(t'_{\text{st}}(-)) \cdot \mathbf{d}(\mathbf{p}_{\text{st}}(t'_{\text{st}}(-); t_{\text{st}}(-)) - \mathbf{A}(t'_{\text{st}}(-))) \right] d_z^*(\mathbf{p}_{\text{st}}(t'_{\text{st}}(-); t_{\text{st}}(-)) - \mathbf{A}(t_{\text{st}}(-))). \end{aligned} \quad (2.37)$$

Below we consider the situation that the fundamental field \mathbf{E} for generating high-order harmonics has constant angular frequency ω_0 . In addition, we assume that by phase matching (§2.1.3) only one trajectory is selected per one half cycle of the fundamental field.

For the periodicity of the generating field, the ionization and recombination will occur periodically. When $T \equiv 2\pi/\omega_0$ denotes the cycle of the fundamental field, the ionization time $t'_{\text{st}}(-)$ and the recombination time $t_{\text{st}}(-)$ can be written respectively by using integer n as

$$\begin{cases} t'_{\text{st}}(-) = t_i + nT/2, \\ t_{\text{st}}(-) = t_i + nT/2 + \tau, \end{cases} \quad (2.38)$$

where t_i is one of the ionization time satisfying $0 \leq t_i < T/2$, and τ is the flight time of the electron (see Fig. 2.2). Substituting these to Eqs. (2.36) and (2.37), we obtain

$$\tilde{E}_{\text{HH}}(\omega) \propto \sum_n f_n(\omega) e^{+i\omega(t_i+\tau)} e^{+in\omega T/2}, \quad (2.39)$$

where

$$\begin{aligned} f_n(\omega) &\equiv f(t_i + \frac{nT}{2}, t_i + \frac{nT}{2} + \tau) \\ &\simeq \omega^2 \frac{+i2\pi}{\sqrt{-\det \Theta''_{(-)}(t_i + \frac{nT}{2}, t_i + \frac{nT}{2} + \tau)}} \left(\frac{\pi}{+i\tau/2 + \epsilon} \right)^{3/2} e^{-iS_{\text{st}}(t_i + \frac{nT}{2}; t_i + \frac{nT}{2} + \tau)} \\ &\times \left[\mathbf{E}(t_i + \frac{nT}{2}) \cdot \mathbf{d}(\mathbf{p}_{\text{st}}(t_i + \frac{nT}{2}; t_i + \frac{nT}{2} + \tau) - \mathbf{A}(t_i + \frac{nT}{2})) \right] d_z^*(\mathbf{p}_{\text{st}}(t_i + \frac{nT}{2}; t_i + \frac{nT}{2} + \tau) - \mathbf{A}(t_i + \frac{nT}{2} + \tau)). \end{aligned} \quad (2.40)$$

Again, because of the periodicity of the fundamental field \mathbf{E} , \mathbf{p}_{st} [(2.18)] and \mathbf{A} [(2.6)] are also periodic with period T , and so $\mathbf{p}_{\text{st}}(t_i + \frac{nT}{2}; t_i + \frac{nT}{2} + \tau) = (-1)^n \mathbf{p}_{\text{st}}(t_i; t_i + \tau)$, $\mathbf{A}(t_i + \frac{nT}{2}) = (-1)^n \mathbf{A}(t_i)$, $\mathbf{A}(t_i + \frac{nT}{2} + \tau) = (-1)^n \mathbf{A}(t_i + \tau)$. In addition, from the definitions of $\det \Theta''_{(-)}$ [(2.28)], and S_{st} [(2.21)], they do not depend on n . Therefore,

$$\begin{aligned} f_n(\omega) &= \omega^2 \frac{+i2\pi}{\sqrt{-\det \Theta''_{(-)}(t_i, t_i + \tau)}} \left(\frac{\pi}{+i\tau/2 + \epsilon} \right)^{3/2} e^{-iS_{\text{st}}(t_i; t_i + \tau)} \\ &\times [(-1)^n \mathbf{E}(t_i) \cdot \mathbf{d}((-1)^n [\mathbf{p}_{\text{st}}(t_i; t_i + \tau) - \mathbf{A}(t_i)])] d_z^*((-1)^n [\mathbf{p}_{\text{st}}(t_i; t_i + \tau) - \mathbf{A}(t_i + \tau)]). \end{aligned} \quad (2.41)$$

2 Theoretical background of high-order harmonic generation

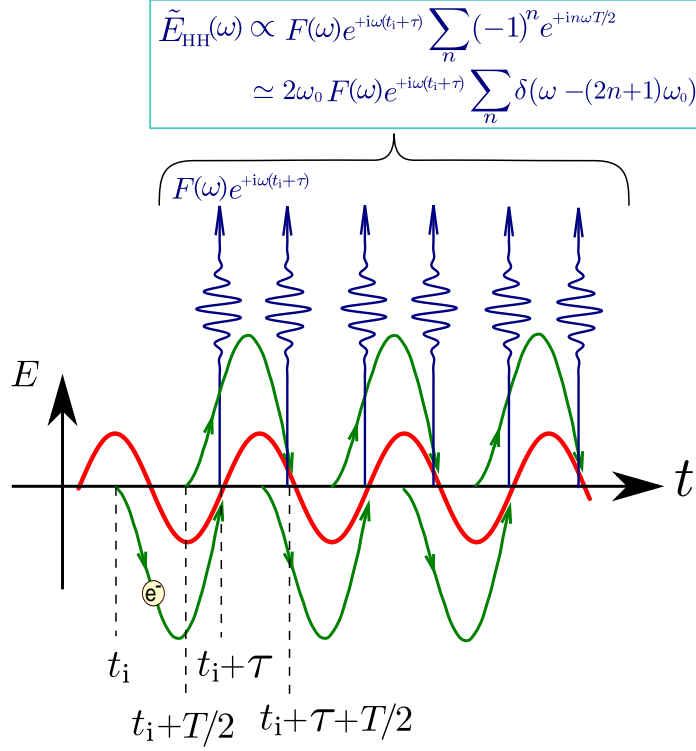


Figure 2.2: The periodic structure of the high-order harmonics. The ionization time $t_{\text{st}}^{(-)}$ and the recombination time $t_{\text{st}}^{(-)}$ can be written by using integer n as $t_{\text{st}}^{(-)} = t_i + nT/2$ and $t_{\text{st}}^{(-)} = t_i + nT/2 + \tau$, respectively.

Here, the transition dipole \mathbf{d} in Eq. (2.41) is defined as $\mathbf{d}(\mathbf{p}) = (2\pi)^{-3/2} \int_{-\infty}^{+\infty} d^3\mathbf{x} e^{-i\mathbf{p}\cdot\mathbf{x}} \mathbf{x} \langle \mathbf{x} | 0 \rangle$ [Eq. (2.4)]. If the system has inversion symmetry $\langle \mathbf{x} | 0 \rangle = \langle -\mathbf{x} | 0 \rangle$, then $\mathbf{d}(\mathbf{p})$ becomes an odd function of \mathbf{p} because

$$\mathbf{d}(-\mathbf{p}) = (2\pi)^{-3/2} \int_{-\infty}^{+\infty} d^3\mathbf{x} e^{+i\mathbf{p}\cdot\mathbf{x}} \mathbf{x} \langle \mathbf{x} | 0 \rangle = -(2\pi)^{-3/2} \int_{-\infty}^{+\infty} d^3\mathbf{x} e^{-i\mathbf{p}\cdot(-\mathbf{x})} (-\mathbf{x}) \langle -(-\mathbf{x}) | 0 \rangle = -\mathbf{d}(\mathbf{p}). \quad (2.42)$$

In this case, f_n in Eq. (2.41) becomes

$$f_n(\omega) = (-1)^n F(\omega), \quad (2.43)$$

where

$$\begin{aligned}F(\omega) &= \omega^2 \frac{+i2\pi}{\sqrt{-\det \Theta''_{(-)}(t_i, t_i+\tau)}} \left(\frac{\pi}{+i\tau/2 + \epsilon} \right)^{3/2} e^{-iS_{\text{st}}(t_i; t_i+\tau)} \\ &\quad \times [\mathbf{E}(t_i) \cdot \mathbf{d}(\mathbf{p}_{\text{st}}(t_i; t_i + \tau) - \mathbf{A}(t_i))] d_z^* (\mathbf{p}_{\text{st}}(t_i; t_i + \tau) - \mathbf{A}(t_i + \tau)).\end{aligned} \quad (2.44)$$

By using these equations in Eq. (2.39) we get a simple form of $\tilde{E}_{\text{HH}}(\omega)$ as

$$\tilde{E}_{\text{HH}}(\omega) \propto \sum_n (-1)^n F(\omega) e^{+i\omega(t_i+\tau)} e^{+in\omega T/2} = F(\omega) e^{+i\omega(t_i+\tau)} \sum_n (-1)^n e^{+in\omega T/2}. \quad (2.45)$$

If n runs from $-\infty$ to $+\infty$,

$$\begin{aligned}
 \tilde{E}_{\text{HH}}(\omega) &\propto F(\omega)e^{+i\omega(t_1+\tau)} \sum_{n=-\infty}^{+\infty} (-1)^n e^{+in\omega T/2} \\
 &= F(\omega)e^{+i\omega(t_1+\tau)} \left[2 \sum_{n=-\infty}^{+\infty} e^{+2in\omega T/2} - \sum_{n=-\infty}^{+\infty} e^{+in\omega T/2} \right] \\
 &= F(\omega)e^{+i\omega(t_1+\tau)} \left[\frac{4\pi}{T} \sum_{n=-\infty}^{+\infty} \delta(\omega - n2\pi/T) - \frac{4\pi}{T} \sum_{n=-\infty}^{+\infty} \delta(\omega - n4\pi/T) \right] \\
 &= 2\omega_0 F(\omega)e^{+i\omega(t_1+\tau)} \sum_{n=-\infty}^{+\infty} \delta(\omega - (2n+1)\omega_0).
 \end{aligned} \tag{2.46}$$

Here, we use the equation $(1/a) \sum_{n=-\infty}^{+\infty} e^{+i(2n\pi/a)x} = \sum_{n=-\infty}^{+\infty} \delta(x - na)$ [83, §2.10]. This result shows that when high-order harmonics are generated in a system with inversion symmetry their spectra have peaks at only odd multiples of the frequency of the fundamental, and that the envelope of the spectra is given by $F(\omega)$ defined by Eq. (2.44), which corresponds to the spectra generated in one ionization–recombination process. In practice, since the driving pulses have finite duration, the range of n in Eq. (2.45) is limited and thus the peaks of the spectra are not delta-function-like but have a finite width.

2.2.2 The effect of phase differences on the temporal structure

In this section we discuss the relation among the harmonic phase, the recombination time of the electron, and the emission time of each harmonic, based on the study by Mairesse *et al.* [32]. From the expression of the spectra (2.46), the phase $\phi_{\text{HH}}^{(2n+1)}$ of the $(2n+1)$ th order harmonics can be written as

$$\phi_{\text{HH}}^{(2n+1)} = \phi_F^{(2n+1)} + (2n+1)\omega_0 t_r^{(2n+1)}, \tag{2.47}$$

where $\phi_F^{(2n+1)}$ is the phase of $F(\omega)$ at $\omega = (2n+1)\omega_0$ and $t_r^{(2n+1)}$ is the recombination time $t_1 + \tau$ at $\omega = (2n+1)\omega_0$. The phase difference $\Delta\phi_{\text{HH}}^{(2n)}$ between $(2n+1)$ th and $(2n-1)$ th harmonics is then

$$\Delta\phi_{\text{HH}}^{(2n)} \equiv \phi_{\text{HH}}^{(2n+1)} - \phi_{\text{HH}}^{(2n-1)} = \phi_F^{(2n+1)} - \phi_F^{(2n-1)} + (2n+1)\omega_0 t_r^{(2n+1)} - (2n-1)\omega_0 t_r^{(2n-1)}. \tag{2.48}$$

If $\phi_F^{(2n+1)} \simeq \phi_F^{(2n-1)}$ and $t_r^{(2n+1)} \simeq t_r^{(2n-1)}$, we get

$$\Delta\phi_{\text{HH}}^{(2n)} \simeq 2\omega_0 t_r, \tag{2.49}$$

where $t_r \simeq t_r^{(2n+1)} \simeq t_r^{(2n-1)}$. Therefore, the phase difference $\Delta\phi_{\text{HH}}^{(2n)}$ between adjacent harmonic orders is related to the time of recombination of the electron. Note that Eq. (2.49) is not valid if $\phi_F^{(2n+1)}$ has a rapid change of the harmonic order. For example, a phase jump is observed in high-order harmonics generated in CO₂ molecules [51, 84, 85], which is attributed to the sign change of the transition dipole \mathbf{d} in $F(\omega)$ [Eq. (2.44)] due to the destructive interference effect [41].

From the three-step model introduced in §1.1, the recombination time t_r is expected to correlate with the time of the emission of each harmonic. This expectation is reinforced as follows³. Let us

³In Ref. [32] the relation of the group delay $t_e = d\phi/d\omega$ [80, §8.6.4] is used with the approximation $d\phi/d\omega \simeq \Delta\phi_{\text{HH}}^{(2n)}/(2\omega_0)$. Here we present an explanation without this approximation.

2 Theoretical background of high-order harmonic generation

consider the high-order harmonics

$$E_{\text{HH}}(t) = \sum_n A^{(2n+1)} \cos \left[(2n+1)\omega_0 t - \phi_{\text{HH}}^{(2n+1)} \right], \quad (2.50)$$

generated by a fundamental field

$$E^{\text{driving}}(t) = E_0^{\text{driving}} \cos [\omega_0 t]. \quad (2.51)$$

Equation (2.50) can be rewritten as

$$\begin{aligned} E_{\text{HH}}(t) &= \sum_n (A^{(2n)} + A^{(2n+2)}) \cos \left[(2n+1)\omega_0 t - \phi_{\text{HH}}^{(2n+1)} \right] \\ &= \sum_n A^{(2n)} \left\{ \cos \left[(2n+1)\omega_0 t - \phi_{\text{HH}}^{(2n+1)} \right] + \cos \left[(2n-1)\omega_0 t - \phi_{\text{HH}}^{(2n-1)} \right] \right\} \\ &= \sum_n 2A^{(2n)} \cos \left[2n\omega_0 t - \frac{\phi_{\text{HH}}^{(2n+1)} + \phi_{\text{HH}}^{(2n-1)}}{2} \right] \cos \left\{ \omega_0 \left[t - \frac{\Delta\phi_{\text{HH}}^{(2n)}}{2\omega_0} \right] \right\}, \end{aligned} \quad (2.52)$$

where $A^{(2n)} + A^{(2n+2)} = A^{(2n+1)}$ with $A^{(0)} = 0$. This result shows that the superposition of odd-order harmonics [Eq.(2.50)] is equivalent to the superposition of trains of wave packets with carrier frequency $2n\omega_0$ whose maxima of the envelope lag behind those of the fundamental field [Eq.(2.51)] by

$$t_e \simeq \frac{\Delta\phi_{\text{HH}}^{(2n)}}{2\omega_0}. \quad (2.53)$$

When Eq. (2.49) is valid, we finally get

$$t_e \simeq \frac{\Delta\phi_{\text{HH}}^{(2n)}}{2\omega_0} \simeq t_r. \quad (2.54)$$

In this way, the emission time of harmonics t_e corresponds to the recombination time t_r and both are related to the phase difference $\Delta\phi_{\text{HH}}^{(2n)}$ of harmonics between adjacent orders.

2.3 Detection of the phase difference by using two-color two-photon ionization

In this section we describe the theoretical background of the RABBIT method introduced in §1.2. First in §2.3.1 a brief overview of the RABBIT method is provided. Next in §2.3.2, we derive the probability of two-color two-photon ionization by using second-order time-dependent perturbation theory. By using this result we show the expression of the photoelectron signal from which the phase difference is obtained. In §2.3.3 we give a note on the so-called ‘‘atomic phase’’, which must be taken into account when we extract phase differences from the RABBIT result.

2.3 Detection of the phase difference by using two-color two-photon ionization

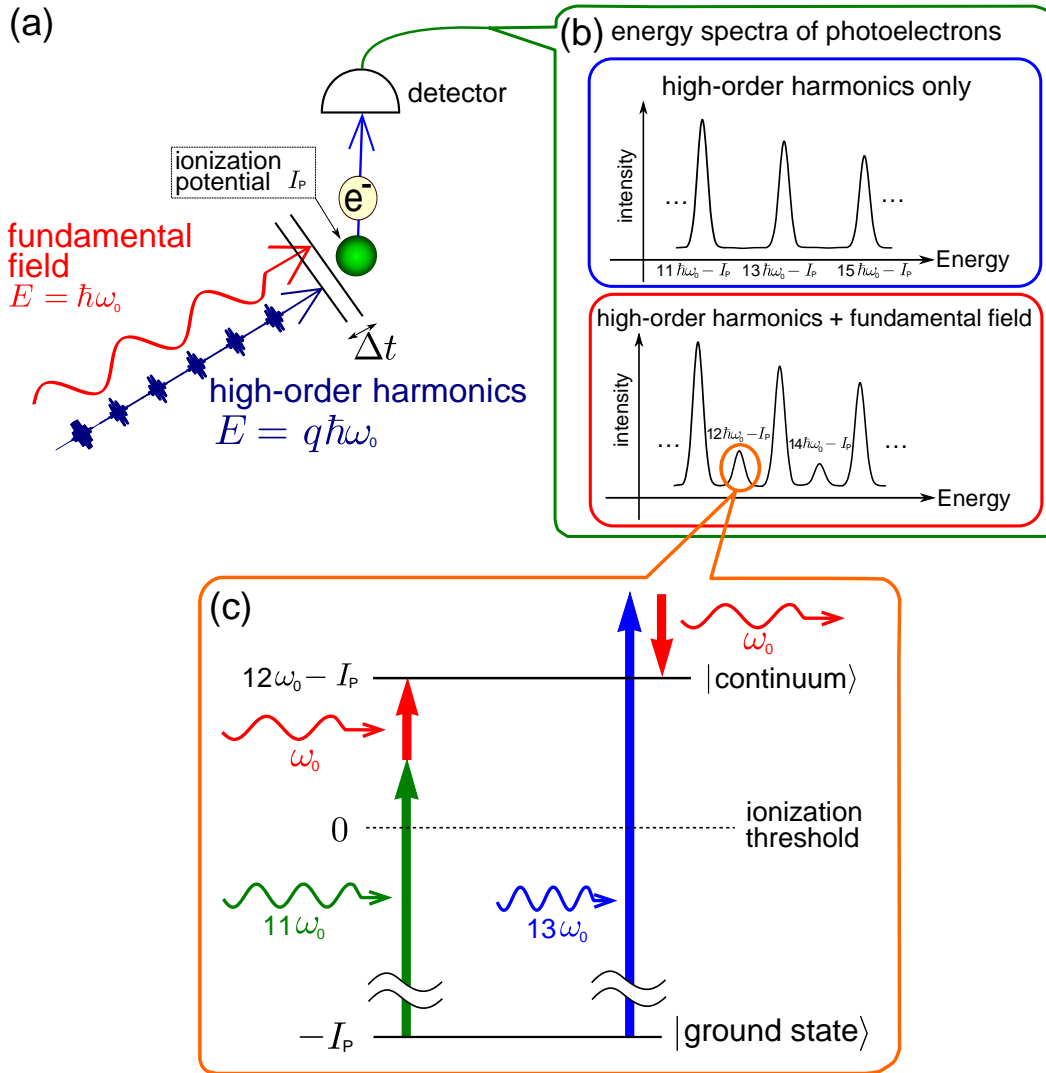


Figure 2.3: The principle of the RABBIT technique. See text for details

2.3.1 Overview of the RABBIT method

The schematic of RABBIT technique is illustrated in Fig. 2.3. In this method we irradiate rare-gas atoms with the high-order harmonics to be measured and the fundamental near-infrared pulse for probe, and obtain the energy spectrum of photoelectrons produced from the atoms (Fig. 2.3(a)). The energy of photons in harmonics is odd multiple of that in fundamental field (§2.2.1). If the fundamental field does not exist, the produced photoelectrons have energies $(2n - 1)\omega_0 - I_p$, where n is an integer, ω_0 is the photon energy of the fundamental field, and I_p is the ionization potential of the rare-gas atom (upper panel of Fig. 2.3(b)). When the probe pulse is introduced together with the high-order harmonics, the two-color two-photon ionization process with one high-order harmonic photon and one fundamental photon produces additional sidebands between single-photon ionization signals (lower panel of Fig. 2.3(b)). For the two-photon signal $(2n$ -th sideband) between the signals from $(2n - 1)$ th and $(2n + 1)$ th harmonics, two processes can contribute: (1) absorption of one photon of

2 Theoretical background of high-order harmonic generation

the $(2n - 1)$ th harmonic and one photon of the fundamental pulse, and (2) absorption of one photon of the $(2n + 1)$ th harmonic and stimulated emission of one photon of the fundamental pulse (Fig. 2.3(c)). These two processes can interfere with each other and as a result the intensity of the $2n$ -th sideband changes as a function of the delay Δt between high-order harmonics and the probe pulse. As shown below, the phase differences between adjacent harmonics are evaluated by analyzing the dependence of the photoelectron signals on Δt .

2.3.2 Two-color two-photon ionization

To reveal the relationship between the phase of harmonics and the signal of two-color two-photon ionization, we first review the theory of two-photon ionization. Let us write the electric field of high-order harmonics and probe pulse as

$$E_X(t) = \sum_n \mathcal{E}_X^{(2n+1)} e^{-i(2n+1)\omega_0 t} + \text{c.c.}, \quad (2.55)$$

$$E_I(t) = \mathcal{E}_I e^{-i\omega_0 t} + \text{c.c.}, \quad (2.56)$$

respectively. Note that $\mathcal{E}_X^{(q)}$ and \mathcal{E}_I are in general complex numbers and can be written as

$$\mathcal{E}_X^{(2n+1)} = \mathcal{A}_X^{(2n+1)} e^{i\phi_{\text{HH}}^{(2n+1)}} \quad (2.57)$$

$$\mathcal{E}_I = \mathcal{A}_I e^{i\phi_{\text{IR}}}, \quad (2.58)$$

where \mathcal{A}_X , \mathcal{A}_I , $\phi_{\text{HH}}^{(2n+1)}$, ϕ_{IR} are real numbers. For simplicity, let us suppose that both $E_X(t)$ and $E_I(t)$ has constant amplitudes when $t_i < t < t_f$, and are zero when $t < t_i$ or $t_f < t$. The combined electric field is

$$E(t) = \begin{cases} E_X(t) + E_I(t) & (t_i < t < t_f), \\ 0 & (t < t_i \text{ or } t_f < t). \end{cases} \quad (2.59)$$

Since both the high-order harmonics and the probe pulse have wavelength much longer than the size of rare gas atoms, the electric field can be considered homogeneous in space, and the matrix element of the interaction potential can be represented as

$$V_{ba}(t) = -\langle b | E(t) \cdot z | a \rangle = -\langle b | z | a \rangle E(t). \quad (2.60)$$

We assume that the intensities of both harmonics and probe pulse are sufficiently weak and we can calculate the ionization probability by using the second order perturbation theory.

Let us consider the probability $W_{i \rightarrow f}$ that the atom which was in the state i at time t_i makes transition to the state f at time $t_f = t_i + T$. To the second order of perturbation calculation, $W_{i \rightarrow f}$ is given by [39, §XVII.2]

$$W_{i \rightarrow f} = \left| \sum_{j=1}^{+\infty} \langle f | U^{(j)} | i \rangle \right|^2 \simeq \left| \langle f | U^{(1)} | i \rangle + \langle f | U^{(2)} | i \rangle \right|^2, \quad (2.61)$$

2.3 Detection of the phase difference by using two-color two-photon ionization

where $U^{(j)}$ is the j th order term of the time-evolution operator:

$$\langle f | U^{(1)} | i \rangle = \frac{1}{i} \int_{t_i}^{t_f} d\tau \left[e^{-iE_f^0(t_f-\tau)} V_{fi}(\tau) e^{-iE_i^0(\tau-t_i)} \right], \quad (2.62)$$

$$\langle f | U^{(2)} | i \rangle = \frac{1}{(i)^2} \sum_m \int_0^{t_f} d\tau \int_0^\tau d\tau' \left[e^{-iE_f^0(t_f-\tau)} V_{fm}(\tau) e^{-iE_m^0(\tau-\tau')} V_{mi}(\tau') e^{-iE_i^0(\tau'-t_i)} \right]. \quad (2.63)$$

The intermediate state $|m\rangle$ in Eq.(2.63) runs all of the eigenstate of the atom, and \sum_m means sum if $|m\rangle$ is bound state and integration if $|m\rangle$ is continuum state. The probability $W_{i \rightarrow f}$ for the interaction (2.60) can be approximated as (see Appendix A.2 for the derivation)

$$\begin{aligned} W_{i \rightarrow f} \simeq & 2\pi T \sum_n |\langle f | z | i \rangle|^2 \mathcal{A}_X^{(2n+1)^2} \delta(E_f^0 - E_i^0 - (2n+1)\omega_0) \\ & + 2\pi T \sum_n \left[\left| \mathcal{E}_I \mathcal{E}_X^{(2n-1)} \left(M_{(f,i)}^{(2n-1)} + M_{(f,i)}^{(+1)} \right) + \mathcal{E}_I^* \mathcal{E}_X^{(2n+1)} \left(M_{(f,i)}^{(2n+1)} + M_{(f,i)}^{(-1)} \right) \right|^2 \right. \\ & \left. \times \delta(E_f^0 - E_i^0 - 2n\omega_0), \right. \end{aligned} \quad (2.64)$$

where

$$M_{(f,i)}^{(q)} \equiv \sum_m \frac{\langle f | z | m \rangle \langle m | z | i \rangle}{E_i^0 + q\omega_0 - E_m^0}. \quad (2.65)$$

From Eq. (2.64), we find that the strength of the side-band which appears between $(2n-1)$ th and $(2n+1)$ th harmonics is proportional to

$$S_{2n} \equiv \sum_{i,f} \left| \mathcal{E}_I \mathcal{E}_X^{(2n-1)} \left(M_{(f,i)}^{(2n-1)} + M_{(f,i)}^{(+1)} \right) + \mathcal{E}_I^* \mathcal{E}_X^{(2n+1)} \left(M_{(f,i)}^{(2n+1)} + M_{(f,i)}^{(-1)} \right) \right|^2. \quad (2.66)$$

Let us define $\tilde{M}_{(f,i,\pm)}^{(2n\pm 1)}$ as

$$\tilde{M}_{(f,i,\pm)}^{(2n\pm 1)} \equiv M_{(f,i)}^{(2n\mp 1)} + M_{(f,i)}^{(\pm 1)}. \quad (2.67)$$

By using Eqs. (2.57), (2.58) and (2.67), Eq. (2.66) can be rewritten as

$$\begin{aligned} S_{2n} &= \sum_{i,f} \left| e^{i\phi_{IR}} e^{i\phi_{HH}^{(2n-1)}} \mathcal{A}_I \mathcal{A}_X^{(2n-1)} \tilde{M}_{(f,i,+)}^{(2n+1)} + e^{-i\phi_{IR}} e^{i\phi_{HH}^{(2n+1)}} \mathcal{A}_I \mathcal{A}_X^{(2n+1)} \tilde{M}_{(f,i,-)}^{(2n-1)} \right|^2 \\ &= \mathcal{A}_I^2 \mathcal{A}_X^{(2n-1)^2} \sum_{i,f} \left| \tilde{M}_{(f,i,+)}^{(2n+1)} \right|^2 + \mathcal{A}_I^2 \mathcal{A}_X^{(2n+1)^2} \sum_{i,f} \left| \tilde{M}_{(f,i,-)}^{(2n-1)} \right|^2 \\ &\quad + \mathcal{A}_I^2 \mathcal{A}_X^{(2n-1)} \mathcal{A}_X^{(2n+1)} \left[e^{i(2\phi_{IR} + \phi_{HH}^{(2n-1)} - \phi_{HH}^{(2n+1)})} \sum_{i,f} \tilde{M}_{(f,i,+)}^{(2n+1)} \left(\tilde{M}_{(f,i,-)}^{(2n-1)} \right)^* + \text{c.c.} \right] \\ &= \mathcal{A}_I^2 \mathcal{A}_X^{(2n-1)^2} A_+^{(2n+1)} + \mathcal{A}_I^2 \mathcal{A}_X^{(2n+1)^2} A_-^{(2n-1)} \\ &\quad + \mathcal{A}_I^2 \mathcal{A}_X^{(2n-1)} \mathcal{A}_X^{(2n+1)} A_{\text{atom}}^{(2n)} \cos \left(2\phi_{IR} + \phi_{HH}^{(2n-1)} - \phi_{HH}^{(2n+1)} + \Delta\phi_{\text{atom}}^{(2n)} \right), \end{aligned} \quad (2.68)$$

2 Theoretical background of high-order harmonic generation

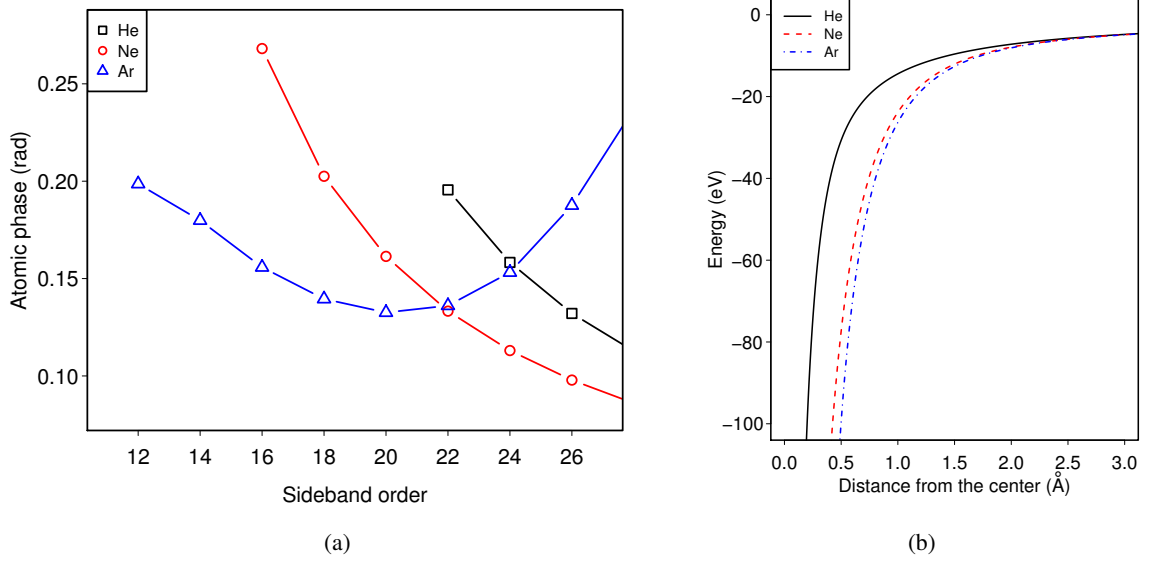


Figure 2.4: (a) The atomic phase calculated by using second-order perturbation theory [86]. square, circle, and triangle symbols show the results about He, Ne, and Ar, respectively. (b) The effective potentials used in the calculation of Fig. 2.4(a). They are given in Refs. [87], [88], and [89], for He, Ne, and Ar, respectively.

where

$$A_{\pm}^{(2n\pm 1)} = \sum_{i,f} \left| \tilde{M}_{(f,i,\pm)}^{(2n\pm 1)} \right|^2, \quad (2.69)$$

$$A_{\text{atom}}^{(2n)} = 2 \left| \sum_{i,f} \tilde{M}_{(f,i,+)}^{(2n+1)} \left(\tilde{M}_{(f,i,-)}^{(2n-1)} \right)^* \right|, \quad (2.70)$$

$$\Delta\phi_{\text{atom}}^{(2n)} = \arg \left(\sum_{i,f} \tilde{M}_{(f,i,+)}^{(2n+1)} \left(\tilde{M}_{(f,i,-)}^{(2n-1)} \right)^* \right). \quad (2.71)$$

2.3.3 Atomic phase

The interference term in Eq. (2.68) is proportional to

$$\cos \left(2\phi_{\text{IR}} + \phi_{\text{HH}}^{(2n-1)} - \phi_{\text{HH}}^{(2n+1)} + \Delta\phi_{\text{atom}}^{(2n)} \right). \quad (2.72)$$

Here, the phase of the probe pulse ϕ_{IR} can be controlled by changing the delay between the harmonics and probe pulse Δt :

$$\phi_{\text{IR}} = \omega_0 \Delta t + \phi_{\text{IR}}^{(\Delta t=0)}. \quad (2.73)$$

So we can get $\phi_{\text{HH}}^{(2n-1)} - \phi_{\text{HH}}^{(2n+1)} + \Delta\phi_{\text{atom}}^{(2n)}$ by observing the dependence of the sideband intensity on Δt . In order to retrieve the phase difference $\Delta\phi_{\text{HH}}^{(2n)} \equiv \phi_{\text{HH}}^{(2n+1)} - \phi_{\text{HH}}^{(2n-1)}$, the value of $\Delta\phi_{\text{atom}}^{(2n)}$ is needed. This value is called ‘‘atomic phase’’. This term appears because the time delays of the photoelectron

2.3 Detection of the phase difference by using two-color two-photon ionization

wave packet in the photoionization process are different depending on their kinetic energies [90, 91]: $\Delta\phi_{\text{atom}}^{(2n)}$ is related to the sum of the two delays, τ_{W} and τ_{cc} , as

$$-\Delta\phi_{\text{atom}}^{(2n)}/(2\omega_0) = \tau_{\text{W}} + \tau_{\text{cc}}. \quad (2.74)$$

Here, τ_{W} is the delay for escaping from the potential by one-photon ionization and τ_{cc} is the delay due to the continuum-continuum transition in the Coulomb potential. Since τ_{cc} does not depend on the short range potential [90], Eq. (2.74) shows that the smaller the atomic phase $\Delta\phi_{\text{atom}}^{(2n)}$, the longer the delay τ_{W} needed to escape from the potential.

We calculate $\Delta\phi_{\text{atom}}^{(2n)}$ within the second-order perturbation theory and the single-active-electron approximation, by using the method of Toma and Muller [86]. Figure 2.4(a) shows the calculated results of $\Delta\phi_{\text{atom}}^{(2n)}$ about the photoionization from He, Ne and Ar. In this calculation we use effective potentials given in Refs. [87], [88], and [89], for He, Ne, and Ar, respectively [Fig. 2.4(b)]. The detailed calculations are presented in Appendix A.3. The atomic phase $\Delta\phi_{\text{atom}}^{(2n)}$ of Ne is smaller than that of He. This is reasonable because the charge of the nuclei of Ne is larger than that of He and thus the short-range potential is deeper, which makes the delay τ_{W} longer. However, at the high-energy region $\Delta\phi_{\text{atom}}^{(2n)}$ of Ar becomes larger than that of both Ne and He, though the nuclear charge of Ar is largest. This is thought to be due to the phase shift accompanying the so-called Cooper minimum [92] around ~ 50 eV [91].

Chapter 3

Experimental setup and techniques

In this chapter, we present the setup of our experiment. A schematic diagram of the experimental setup is shown in Fig. 3.1. Intense femtosecond 800-nm pulses are delivered from the chirped pulse amplification system (§3.1.1). The output of the amplifier is separated into a “driving pulse” for high-order harmonic generation and a “probe pulse” of the RABBIT method (§3.1.2). They are focused into a supersonic gas jet of molecules in the vacuum chamber. The generated harmonics are re-focused into another supersonic gas jet and produce photoelectrons (§3.1.3). At the same time, high-order harmonics are spectrally resolved by a flat-field vacuum spectrometer and detected by a charge coupled device (CCD) camera (§3.1.4). High-order harmonics and photoelectrons are generated in a vacuum chamber (§3.2). The velocity distribution of the produced photoelectrons are observed by using the velocity-map imaging technique (§3.3). The laser, gas jet, and the detectors are synchronized by the trigger signal based on the repetition rate of the Ti:sapphire oscillator (§3.4). When we investigate the harmonics from aligned molecules, we irradiate the sample with a “pump pulse” to impulsively align the molecules (§3.5). The details are described in the following sections.

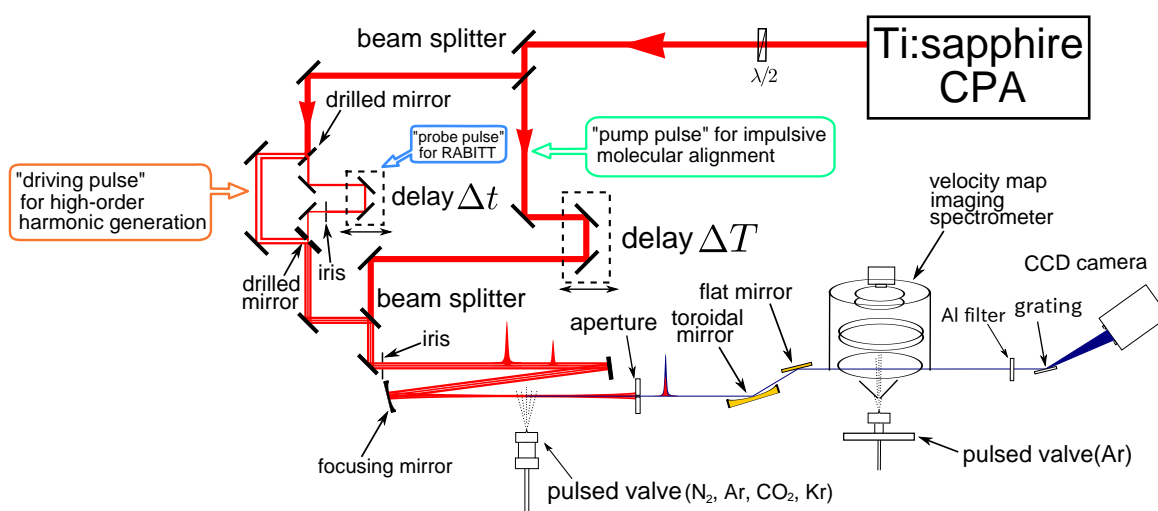


Figure 3.1: Schematic diagram of the experimental setup.

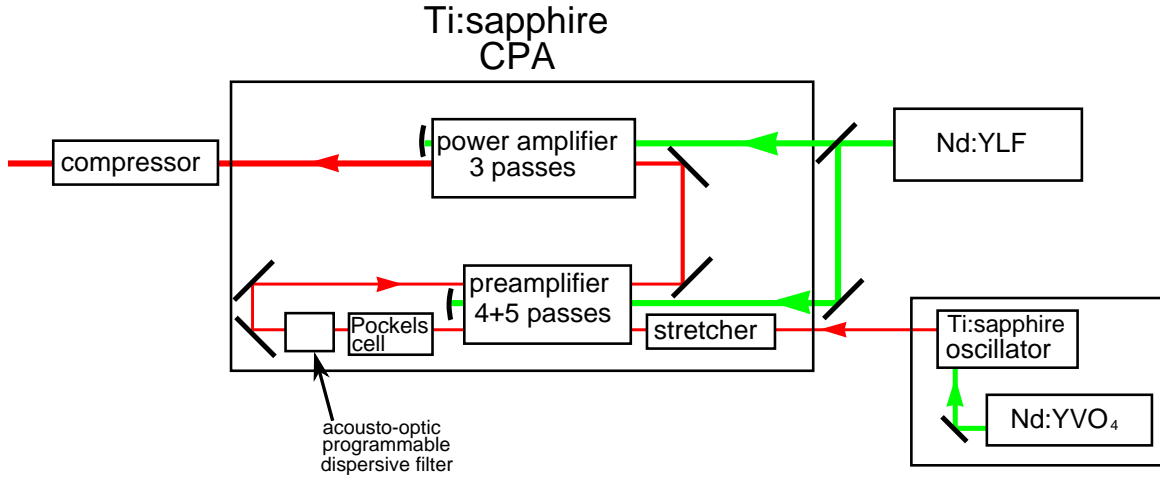


Figure 3.2: A schematic diagram of the laser system used in our experiment.

Procedures about the analysis of acquired data are summarized in Chapter 4.

3.1 Laser and optical system

In this section we describe the setup concerning the laser and optical system. In §3.1.1 we describe the amplifier system to produce femtosecond pulses. The output of the laser is separated and controlled both spatially and temporally, which is described in §3.1.2. In the RABBIT method, we have to focus the generated high-order harmonics in the rare-gas jet. In §3.1.3 we provide information about it. In §3.1.4 we briefly mention the grating spectrometer.

3.1.1 Ti:sapphire based chirped pulse amplification system

To generate intense femtosecond laser pulses, we use Ti:sapphire based chirped pulse amplification system. The schematic diagram of the laser system is shown in Fig. 3.2. First we introduce the property of Ti:sapphire, the active media of our oscillator and amplifier. After that we describe the components of the laser system.

3.1.1.1 Ti:sapphire laser

Ti:sapphire (or $\text{Ti:Al}_2\text{O}_3$) is widely used as an active medium of femtosecond or tunable lasers [80, § 9.2.8]. In Ti:sapphire crystals a Ti^{3+} ion is surrounded by six O^{2-} ions like Fig 3.3(a), and the octahedral crystal field splits the energy levels of the $3d$ electron of a Ti^{3+} ion into lower states (2T_2) and upper states (2E). Because of the interaction between $3d$ electron and the crystal field, the equilibrium point of the distance between a Ti^{3+} ion and its nearest-neighbor O^{2-} ion ($R_{\text{Ti-O}}$) is larger for the upper states than that for the lower states (Fig 3.3(b)). The laser action takes place in a four-level laser scheme as follows: The system is first pumped by light with wavelength ~ 500 nm from the lowest vibrational level of the lower state to a vibrationally-excited level in the upper state

3 Experimental setup and techniques

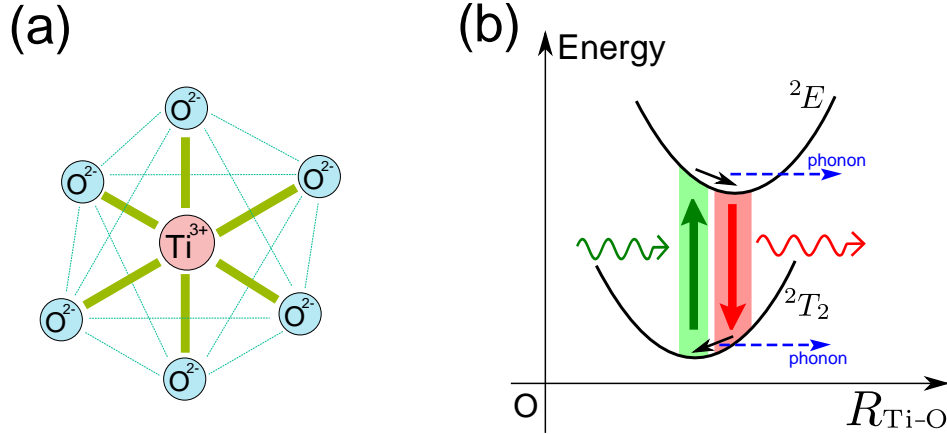


Figure 3.3: Mechanism of Ti:sapphire lasers [80, § 9.2.8]. (a) configuration of a Ti^{3+} ion in the Ti:sapphire crystal. (b) energy diagram of Ti:sapphire. The horizontal axis shows the distance between a Ti^{3+} ion and its nearest-neighbor O^{2-} ion.

where the $R_{\text{Ti-O}}$ is near to the equilibrium distance of the ground state (Frank-Condon principle [93, § 11.4]). Next, the crystal transforms so that $R_{\text{Ti-O}}$ reaches the equilibrium of the upper state, by emitting phonons and decaying to the lowest vibrational level. The upper state emits a photon with wavelength ~ 800 nm and makes transition to some vibrational levels of the lower state, again obeying the Frank-Condon principle. Finally the system return to the ground level of the lower state by phonon decay. Since a lot of vibrational levels are involved, Ti:sapphire has very large bandwidth of the laser transition (~ 100 THz).

3.1.1.2 Oscillator

We use a Ti:sapphire oscillator with outputs of sub-10 fs, ~ 2.5 nJ and repetition rate of ~ 78 MHz (Femtolasers, Rainbow). In this oscillator the output from a frequency-doubled Nd:YVO₄ laser (Coherent, Verdi-V6) pumps a Ti:sapphire crystal in a cavity. The cavity dispersion [80, §8.6.4] is compensated by using chirped multilayer dielectric mirrors [94, 95], which enables the generation of sub-10 fs pulses through Kerr lens mode-locking [80, §8.6.3]. This oscillator also serves as a generator of the trigger signals used in the experiments (see §3.4).

3.1.1.3 Amplifier

The output of the oscillator is used as a seed of a Ti:sapphire chirped-pulse amplification (CPA) system [96, 97]. The principle of CPA is explained in Fig. 3.4. First, the input pulse is stretched by giving it a linear positive chirp. This process lowers the peak intensity of the pulse with its pulse energy almost unchanged, and enables us to amplify energetic pulses without damaging the amplifier. Since the linearity of the chirp is maintained after the amplification, the amplified pulse can be compressed by providing a suitable amount of negative chirp to it.

The CPA system we use (Femtolasers, FEMTOPOWER PRO V CEP) is comprised of the 9-pass

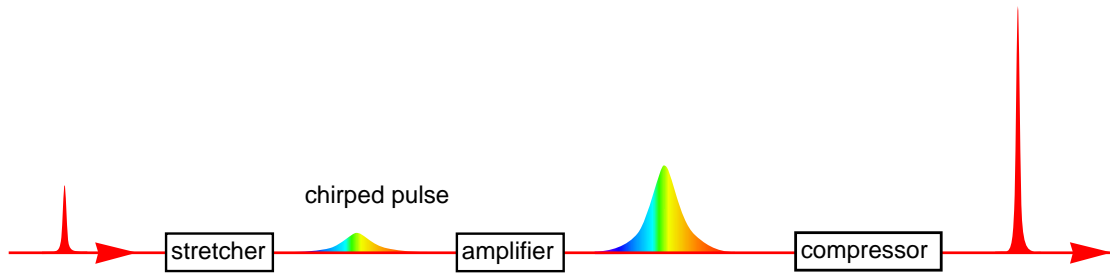


Figure 3.4: The method of chirped-pulse amplification [96, 97]. The input pulse is first stretched with a linear chirp before amplification to lower the peak intensity. The amplified pulse is then compressed by its chirp compensation.

preamplifier and 3-pass power amplifier, both of which are pumped by the output of a frequency-doubled Nd:YLF laser (Photonics Industries, DM60-527). The output pulses of the oscillator are stretched by passing through glass blocks and amplified by the preamplifier. In the middle of preamplification process (after the 4th pass over the Ti:sapphire crystal) the pulse enters a Pockels cell [98, § 8.11], which divides the frequency of the pulse train to ~ 1 kHz. The passed pulses are next modified by acousto-optic programmable dispersive filter (FASTLITE, Dazzler) [99] to shape its spectrum and to compensate the high-order dispersion, and then enter the remaining preamplification and the main amplification processes. The amplified pulse are finally compressed by a grating compressor [100] to ~ 25 fs. In the present experiment the pulse energy after the compressor is ~ 1.8 mJ.

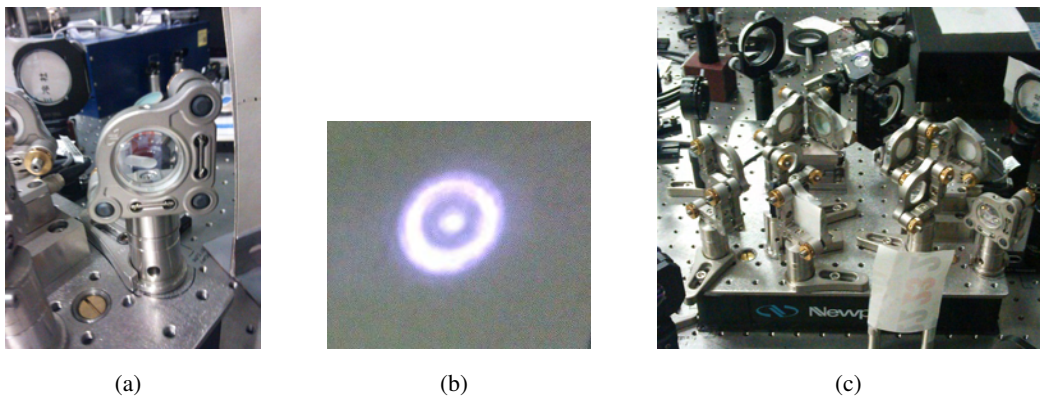


Figure 3.5: (a) A photograph of the drilled mirror. A hole with diameter of 4 mm is drilled at the center of the mirror at 45° to the surface of the mirror. (b) A profile of the driving beam (outer) and probe beam (inner) before focusing. (c) A photo of the breadboard on which the driving and probe pulses are separated and recombined.

3 Experimental setup and techniques

3.1.2 Optical system after the amplifier

An output from the CPA is split into two pulses by a beamsplitter. One is used as a “pump pulse” to impulsively align molecules [23]. We describe this molecular alignment technique in §3.5. The other is spatially divided by a drilled mirror (Fig. 3.5(a)) into an outer annular beam and an inner small beam. The outer beam (8 mm diam. with a hole of 4 mm diam.) is used as a “driving pulse” for high-order harmonic generation. The inner part is further made smaller by an iris to 2 mm diam. and used as a “probe pulse” of the RABBIT method. The pulse energies of the driving and the probe pulses are ~ 0.2 mJ and ~ 0.02 mJ, respectively. In addition, since the beam radius of the probe pulse is smaller than that of the driving pulse, the probe pulse is more loosely focused than the driving pulse. Therefore, at the focus the intensity of the probe pulses (estimated as $\sim 10^{12}$ W/cm²) is much weaker than that of the driving pulses ($\sim 10^{14}$ W/cm²). The effect of the probe pulse on the harmonic generation process is discussed later in §4.1. The delay Δt between the driving and the probe pulses is controlled by a closed-loop piezoelectric positioning stage with position resolution 10 nm (SIGMA KOKI Co. Ltd., SFS-H60X(CL)). After that, the two pulses are made collinear by another drilled mirror. Figure 3.5(b) shows a profile of the recombined beam. To reduce the disturbance of Δt by vibration, the separation and the recombination of the two pulses are done on a breadboard (Newport, M-RG-11-2-ML) with short optical mounts (Fig. 3.5(c)).

The temporal overlap of three pulses is checked by observing the second harmonic generated in a β -BaB₂O₄ crystal. Since the driving pulse and the probe pulse are spatially separated before focusing, they do not interfere even if the delay Δt is zero. Therefore, we use pump pulse as a reference, that is, we first overlap pump and probe pulses, and next overlap pump and driving pulses. The pump, driving, and probe pulses are spatially overlapped by seeing the focused profile of the beams with a beam profiler (Ophir, SP620U). Figure 3.6(a) shows a typical profile of the driving pulse at the focus. Though the beam of the driving pulse is annular before focusing, the intense part of the focused beam is concentrated at the center of the profile.

The pulses are introduced into the vacuum chamber and focused by a concave mirror (focal length = 300 mm) at an atomic or molecular gas jet, in which high-order harmonics are generated. The position of the focus is set before the gas jet to select the contribution from the short trajectory (see § 2.1.3). Before focusing the harmonics and the probe pulse in rare-gas atoms for RABBIT measurement, the driving pulse has to be removed because it has the same wavelength as that of the probe pulse and thus interfere with the probe. Since the driving pulse returns to annular beam after focusing but the generated harmonics propagate along the center of the driving pulse, we can separate high-order harmonics from the driving pulse with an aperture [101]. In our setup, the driving pulse is blocked by an aperture located ~ 400 mm after the focus, while the generated harmonics and the inner probe pulse pass through the aperture (Fig. 3.6(b)).

3.1.3 Focusing high-order harmonics into the detection gas

To implement the RABBIT measurement, it is necessary to focus high-order harmonics, vacuum ultraviolet light with various wavelengths, onto the rare gas for detection. This is a difficult task for

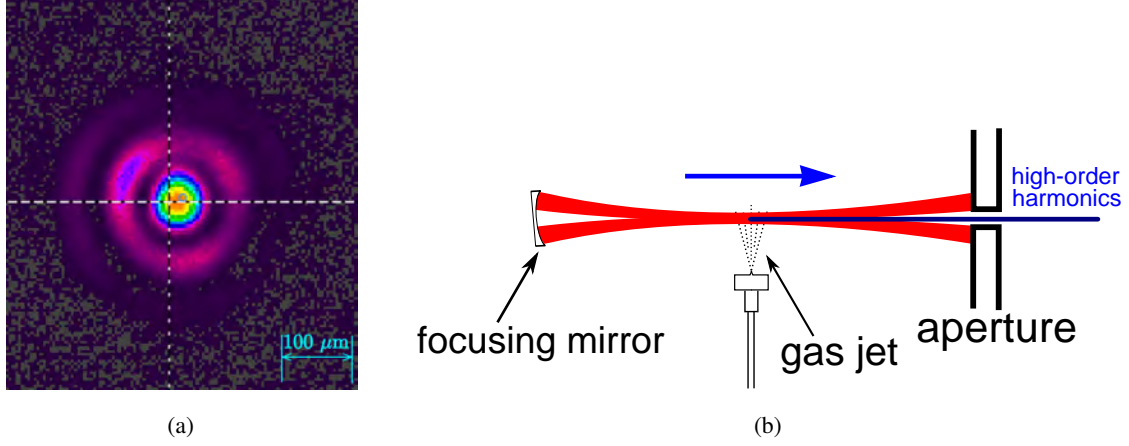


Figure 3.6: (a) Focused profile of the driving pulse observed by a beam profiler (Ophir, SP620U). (b) The driving pulse is blocked by an aperture, while the generated XUV harmonics and the probe pulse pass through the aperture [101].

transmitting optics like lenses or multilayer optics, and metallic mirrors at glazing incidence are often used [102, § 9.1]. In this subsection, we describe the property of reflection and focusing by a metallic mirror.

3.1.3.1 Reflection on metals

While multilayer dielectric mirrors reflect light by the interference of wave scattered at each interface between layers, the reflection by metals occurs due to the presence of free electrons: when an electromagnetic wave enters a conductor, free electric charges are driven to oscillate and emit lights which result in reflected light. This mechanism gives high reflectivity in a wide range of wavelength. On the other hand, in the course of oscillation some of the energy of electrons is dissipated as Joule heat. These effects of free electric charges can be included in optical theory by extending the refractive index to a complex value: [103, § 14.1]

$$\hat{n}(\omega) \equiv n(\omega) [1 + i\kappa(\omega)], \quad (3.1)$$

where n and κ are real functions of the frequency of the light. κ shows how much the propagating light is attenuated and is called the attenuation index. If the complex refractive index is given, the reflection coefficients can be calculated by using generalized Fresnel equations with generalized Snell's law [103, § 14.2]:

$$r_S = -\frac{\sin(\theta_i - \theta_t)}{\sin(\theta_i + \theta_t)} = -\frac{\tan \theta_i - \tan \theta_t}{\tan \theta_i + \tan \theta_t}, \quad (3.2)$$

$$r_P = \frac{\tan(\theta_i - \theta_t)}{\tan(\theta_i + \theta_t)} = \frac{(\tan \theta_i - \tan \theta_t)(1 - \tan \theta_i \tan \theta_t)}{(\tan \theta_i + \tan \theta_t)(1 + \tan \theta_i \tan \theta_t)} = -r_S \frac{1 - \tan \theta_i \tan \theta_t}{1 + \tan \theta_i \tan \theta_t}, \quad (3.3)$$

$$\frac{\sin \theta_i}{\sin \theta_t} = \hat{n}, \quad (3.4)$$

3 Experimental setup and techniques

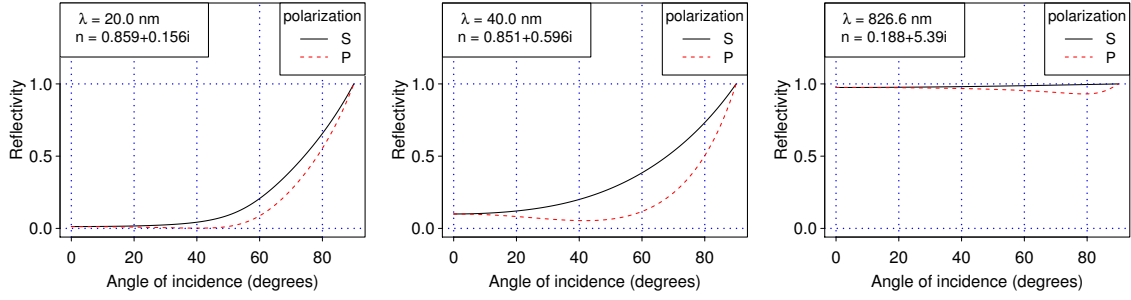


Figure 3.7: Calculated reflectivity of a gold mirror. The complex refractive indices are obtained from Ref. [104].

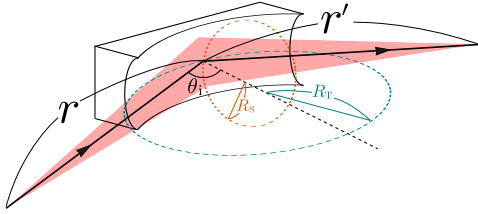


Figure 3.8: Parameters about focusing by a toroidal mirror.



Figure 3.9: A photograph of the toroidal mirror.

where r_s and r_p are the reflection coefficients for light whose polarization direction is perpendicular (S-polarized) and parallel (P-polarized) to the plane of incidence, respectively¹. θ_i stands for the angle of incidence, whereas θ_t does not simply mean the angle of transmission since its value is complex².

Three panels in Fig. 3.7 show the reflectivity of Au as a function of the incidence angle for the light with wavelength 20 nm, 40 nm, and 826.6 nm. The complex refractive indices are obtained from Ref. [104]. Note that reflectivity of ultraviolet light is very small except at the grazing angle. Also note that the reflectivity for S-polarized light is larger than that for P-polarized light. We therefore use lights in S polarization. Because of the reflectivity dependence on the polarization, the reflection on the metal acts like a polarizer of VUV light. This property has been utilized, for example, in the measurement of ellipticity of the high-order harmonics [105, 106] and in the tomographic imaging [37].

3.1.3.2 Focusing by a toroidal mirror

A usual spherical mirror cannot correctly focus light that enters obliquely, because the focal point of the light rays in the plane containing the optical axis and the normal to the mirror (tangential plane) is in general different from that in the plane including the optical axis and perpendicular to the tangential plane (sagittal plane). To focus the grazing-incidence light, we use a “toroidal mirror”,

¹ ‘S’ and ‘P’ is the initial of the word Senkrecht and Parallele, German for perpendicular and parallel, respectively.

² In metals, the surfaces of constant amplitude and those of constant phase in general propagate toward different directions, so the angle of transmission cannot be defined in a simple manner. See [103, § 14.2].

which has different curvatures between the direction of the tangential plane and that of the sagittal plane. When a light is emitted at a distance r from the center of the mirror and is reflected by the mirror with the incidence angle θ_i , the image distance for rays in the tangential plane r'_T and that for rays in the sagittal plane r'_S are obtained by the following relations known as “the Coddington equations for a spherical reflector” [102, § 9.5]:

$$\frac{1}{r} + \frac{1}{r'_T} = \frac{2}{R_T \cos \theta_i}, \quad (3.5)$$

$$\frac{1}{r} + \frac{1}{r'_S} = \frac{2 \cos \theta_i}{R_S}, \quad (3.6)$$

where R_T and R_S are the radius of curvature of the mirror in the tangential and sagittal plane, respectively (see Fig. 3.8). To focus the light properly, R_T and R_S must be chosen so that the image distance for the tangential and sagittal plane coincides.

Figure 3.9 shows a photograph of the toroidal mirror we use in the experiment, which was manufactured by Kiyohara Optics Inc. The tangential radius R_T and sagittal radius R_S are designed so that the light emitted from the distance $r = 450$ mm and hit the mirror with incident angle $\theta_i = 78^\circ$ is focused into the point at $r' = 450$ mm away from the mirror (we choose $r' = r$ because otherwise the aberration becomes worse [102, § 9.5.4.2]). From Eqs. (3.5) and (3.6), we determined R_T and R_S as 2164 mm and 93.6 mm, respectively. In practice, fine tuning of the position and orientation of the toroidal mirror is needed for good focusing. We control the toroidal mirror by using a rotation stage (SIGMA KOKI Co. Ltd., VSGSP-60YAW) and two linear stages (Newport, AG-LS25V6) as well as by tuning the inclination of the chamber. To control the path of the focused light, the light is reflected right after the toroidal mirror by a flat gold mirror whose optical mount (Newport, AG-M100NV6) can be driven from the outside of the chamber.

3.1.4 Grating spectrometer

In addition to the phase measurement by RABBIT method, the spectra of the high-order harmonics are observed by a flat-field grating spectrometer (vacuum&optical instruments, XUV-640). This spectrometer has an aberration-corrected concave grating with grooves of 1200 per mm (Hitachi, 001-0640). Spectrally-resolved light is detected by a charge-coupled device (CCD) camera (Andor Technology, DO420-BN) and the acquired spectra are transferred to a personal computer through a controller card (Andor Technology, CCI-010). An aluminum filter (Luxel Corporation, with thickness of 1500 Å) is placed before the spectrometer to suppress the fundamental and lower-order harmonics.

3.2 Vacuum system and molecular beam

The system after the high-order harmonic generation is maintained in a vacuum, because high-order harmonics have the wavelength of vacuum ultraviolet and are easily absorbed by air [108, §9]. In this section we describe the vacuum system in our experiment. We also mention the atomic and molecular beam source for generating high-order harmonics and photoelectrons.

3 Experimental setup and techniques

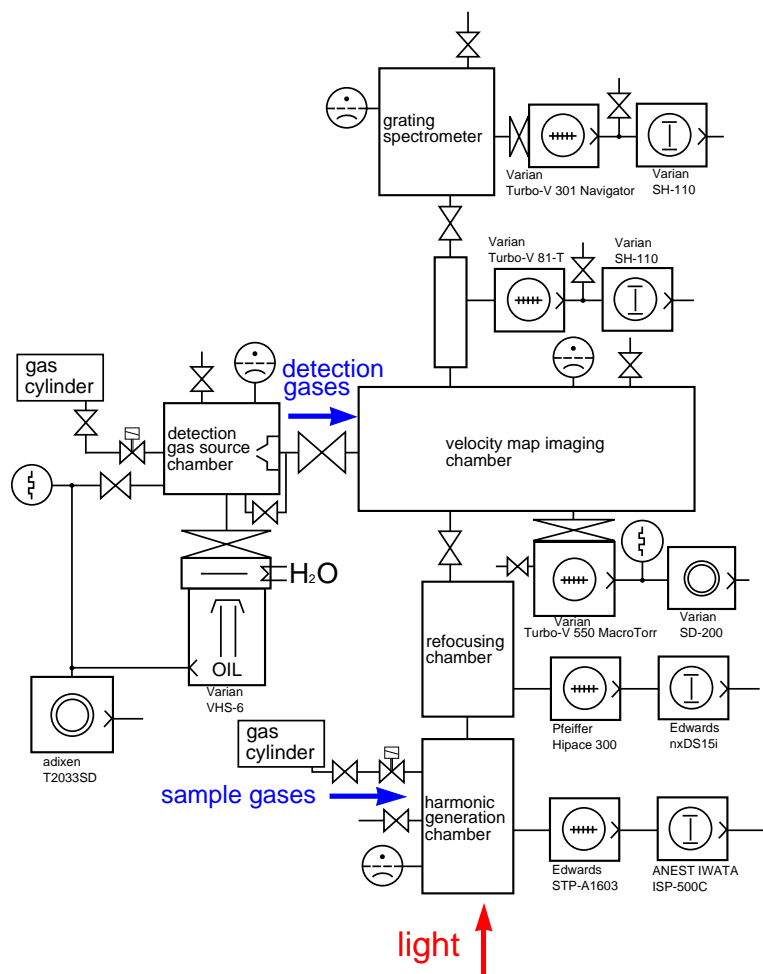


Figure 3.10: Schematic diagram of the vacuum system of the velocity map imaging apparatus. Symbols for vacuum components are defined in, for example, Ref. [107].



Figure 3.11: A photograph of the chambers used in the experiment. Left: harmonic generation chamber. Middle: refocusing chamber. Right: detection gas source chamber (far side) and velocity map imaging chamber (near side). The grating spectrometer is not shown.



Figure 3.12: A photograph of the nozzle of the pulsed valve for sample gases.

3.2 Vacuum system and molecular beam

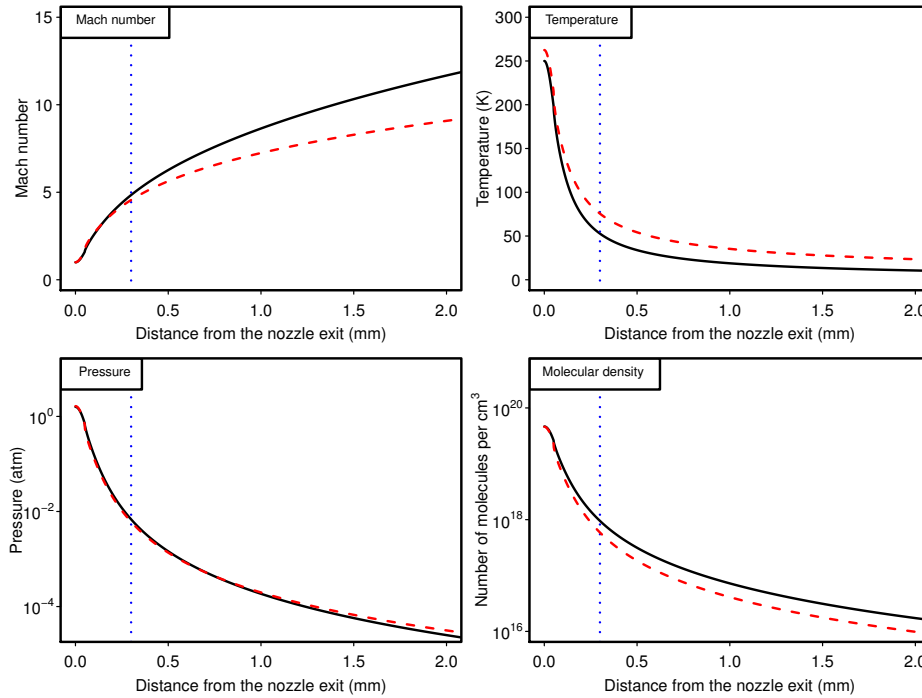


Figure 3.13: Properties of the supersonic flow calculated with the model presented in Ref. [109, §2]. Results for diatomic and triatomic molecules are represented by solid and dashed lines, respectively. Vertical blue dotted lines show the estimated distance between the nozzle exit and the focus of the laser pulse in our experiment (0.3 mm).

Figure 3.10 shows the configuration of our vacuum system. The vacuum system consists of a source chamber of the medium for harmonic generation, a differential chamber with a toroidal mirror to focus high-order harmonics, a source chamber for providing a rare gas beam for RABBIT measurement, a RABBIT chamber for velocity-map imaging, and a grating spectrometer. Figure 3.11 is a photograph of these chambers (the spectrometer is not shown). Each of the five chambers are described in the following.

3.2.1 Harmonic generation chamber

In this chamber, the gas jet for generating high-order harmonics is introduced through a pulsed valve (Parker-Hannifin, 009-1670-900) with orifice diameter 0.1 mm. The nozzle of the valve is modified to make a conical form around the orifice in order to avoid blocking the laser beam by its flange (Fig. 3.12). The pulsed valve is driven with a repetition rate of 100 Hz by the controller (Parker-Hannifin, IOTA-ONE). The chamber is evacuated to $\sim 10^{-2}$ Pa by a turbomolecular pump (Edwards, STP-A1603C, ~ 1600 L/s) backed by a dry scroll pump (ANEST IWATA, ISP-500C, ~ 500 L/min).

When molecules are introduced from a nozzle into the vacuum, they are accelerated by the pressure difference and the adiabatic expansion occurs, during which the temperature of the molecule is cooled down [110]. Figure 3.13 shows the calculated values of Mach number (the ratio of the moving

3 Experimental setup and techniques

speed to the local speed of sound), temperature, pressure, and the number of molecules per cubic centimeter, as a function of the distance from the nozzle exit. The Mach number is calculated with the model given in Table 2.2 of Ref. [109, §2.2.3], and from the Mach number the other properties are obtained by using thermodynamic laws for ideal gas [109, §2.1.2]. In the calculation an orifice diameter $d = 0.1$ mm, a room temperature $T_0 = 300$ K, and a backing pressure $P_0 = 3$ atm are assumed. Results for diatomic and triatomic molecules are represented by solid and dashed line, respectively. Figure 3.13 shows that we can obtain a molecular ensemble with lower temperature as the distance from the nozzle becomes farther. As stated in §3.5 low temperatures are desirable for the molecular alignment technique³. The intensity of the high-order harmonics, however, get weaker with increasing the distance from the nozzle because the density of the medium becomes lower. To generate high-order harmonics with sufficient intensities, the distance between the nozzle exit and the focus of the laser pulse is set to ~ 0.3 mm in our experiment (shown in Fig. 3.13 by vertical blue dotted lines). From Fig. 3.13, the temperature of the molecules is estimated to be $50 \sim 60$ K for diatomic molecules (N_2) and $70 \sim 80$ K for triatomic molecules (CO_2).

3.2.2 Refocusing chamber

The toroidal mirror (see § 3.1.3.2) is set in this chamber to focus the high-order harmonics and the fundamental. This chamber is pumped by a turbomolecular pump (Pfeiffer, Hipace 300, ~ 260 L/s), backed by a dry scroll pump (Edwards, nxDS15i, ~ 285 L/min). Small apertures are set at the both ends of the refocusing chamber so that this chamber also serves as a differential pumping section between the harmonic-generation chamber and the velocity-map imaging chamber.

3.2.3 Detection-gas source chamber

This chamber provides a beam of rare gas atoms which is used for observing the phase differences by the RABBIT technique. The gas is introduced by an Even-Lavie valve [111] and the atomic beam is extracted from the free molecular flow region by a skimmer (Beam Dynamics, No. 50.8, 3 mm diam.). The atomic beam then goes from this chamber into the velocity map imaging apparatus. The source chamber is evacuated by a diffusion pump (Varian, VHS-6, ~ 2400 L/s) with water-cooled baffle (Varian, 336), backed by an oil-sealed rotary vane pump (adixen, T2033SD, ~ 500 L/min).

3.2.4 Velocity map imaging chamber

In this chamber the high-order harmonics and the probe pulses are focused on the atomic beam and the produced photoelectrons are detected. A high degree of vacuum is required for this chamber because the electrons from background gaseous molecules contaminate the signal. This chamber is evacuated to $\sim 10^{-7}$ Pa by a turbomolecular pump (Varian, Turbo-V 550 MacroTorr, ~ 550 L/s) backed by an oil-sealed rotary vane pump (Varian, SD-200, ~ 170 L/min).

³ To be precise, the translation, vibration and rotational temperatures are in general not the same. It is because the number of collisions decreases during the expansion and the internal energy relaxation tends to stop before the system reaches thermal equilibrium [109, §2.3.6]

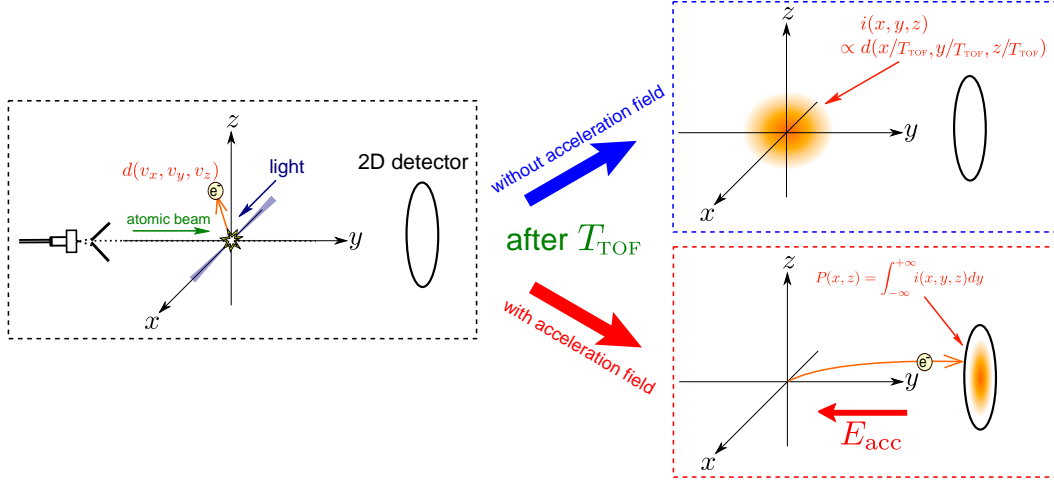


Figure 3.14: The method to obtain the image of the velocity distribution of photoproducts by using a time-of-flight (TOF) chamber and a phosphor screen.

3.2.5 The chamber of the grating spectrometer

The chamber of the grating spectrometer (§ 3.1.4) is evacuated by a turbomolecular pump (Varian, Turbo-V 301 Navigator, ~ 250 L/s) backed by a dry scroll pump (Varian, SH-110, ~ 90 L/min). The chamber for velocity map imaging and the spectrometer are connected by a differential pumping section, which is evacuated by another turbomolecular pump (Varian, Turbo-V 81-T, ~ 77 L/s) and a dry scroll pump (Varian, SH-110).

3.3 Velocity map imaging technique

In our experiments, the electron energy spectra are obtained by using the velocity map imaging technique [112]. In this section, we describe the principle of the velocity map imaging method, the setup of our apparatus, and the procedure for getting the energy distribution of photoelectrons from the image.

3.3.1 Imaging velocity distributions of photoproducts by using a time-of-flight chamber

Suppose that in a coordinate system of Fig. 3.14 a group of ions or electrons has an initial velocity distribution $d(v_x, v_y, v_z)$ at the origin. If the acceleration field does not exist, after some time T the charged particles make a spatial distribution $i(x, y, z; T)$ which can be approximately related to $d(v_x, v_y, v_z)$ as

$$i(x, y, z; T) \propto d(x/T, y/T, z/T). \quad (3.7)$$

When the acceleration field is applied parallel to the y axis, the charged particles are driven by the field, and after some flight time T_{TOF} they reach the detector. If the acceleration field is sufficiently

3 Experimental setup and techniques

high and nearly parallel, T_{TOF} is almost the same for all particles, and the detected distribution $P(x, z)$ at the detector will be the projection of the distribution without acceleration field:

$$P(x, z) = \int_{-\infty}^{+\infty} i(x, y, z; T_{\text{TOF}}) dy. \quad (3.8)$$

Therefore, if $i(x, y, z; T_{\text{TOF}})$ in Eq. (3.8) can be reconstructed from its projection $P(x, z)$, the initial velocity distribution $d(v_x, v_y, v_z)$ can be obtained through Eq. (3.7).

3.3.2 Principle of the velocity map imaging method

The imaging method described in § 3.3.1 was first demonstrated in 1987 by Chandlar and Houston [116]. As the configuration of acceleration electrodes, they adopted the Wiley and McLaren setup [113] used for time-of-flight detection, which is shown in Fig. 3.15(a) (details are shown in Ref. [117]). The acceleration system consists of three electrodes called repeller, extractor, and ground. The electrodes toward which ions flight (extractor and ground) have fine wire grids in order to make the acceleration field homogeneous, and both of them were grounded in the imaging experiments [116] (while in the time-of-flight experiment the voltage of the extractor is set to an appropriate value to improve mass resolution [113]). The structure shown in Figs. 3.15(a) has a problem that the obtained images become blurred due to the finite size of the interaction region and the distortion of the electric field around the wire mesh. In addition, a part of photofragments are captured by the mesh, which lowers the signal-to-noise ratio. To reduce the effect of meshes, a configuration with one ground mesh (Fig. 3.15(b)) was also used by some experiments [118], but the above-mentioned problems still remained.

In 1997 Eppink and Parker presented another configuration [114], shown in Fig. 3.15(c). They removed the meshes from the extractor and the ground of the Wiley and McLaren setup (Fig. 3.15(a)). The electric field is then distorted. However, by adjusting the ratio of the voltage of the extractor to that of the repeller appropriately, the distorted field can act as an electrostatic lens which focuses electrons with the same initial momentum into almost the same position on the screen, independent of their initial positions. This method is named “velocity map imaging”. Figure 3.16 shows a simulation of our velocity map imaging setup, calculated with SIMION 8.0 [115]. Blue curves show contour lines of the electric potential, whose interval is 250 V. Black and red curves show the trajectories of electrons produced at the z -coordinate +2 mm or -2 mm, respectively. One can see that the electrons are focused at the screen depending on the initial kinetic energy (5 eV or 10 eV).

3.3.3 Setup of the velocity map imaging apparatus

We use the chamber which was used in the past in the experiments of molecular alignment and orientation. Since a part of the electrical setup and the CCD camera are in use for other experiments, they were newly prepared for this experiment by reference to Refs. [119, 120].

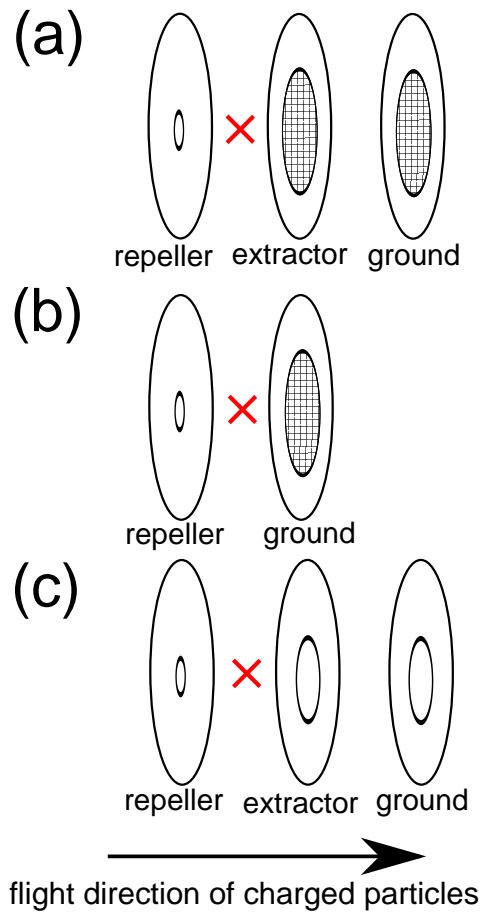


Figure 3.15: Comparison of the electrode configurations used in imaging methods. (a) Wiley–McLaren configuration [113]. (b) Simple structure. (c) Velocity-map imaging [114].

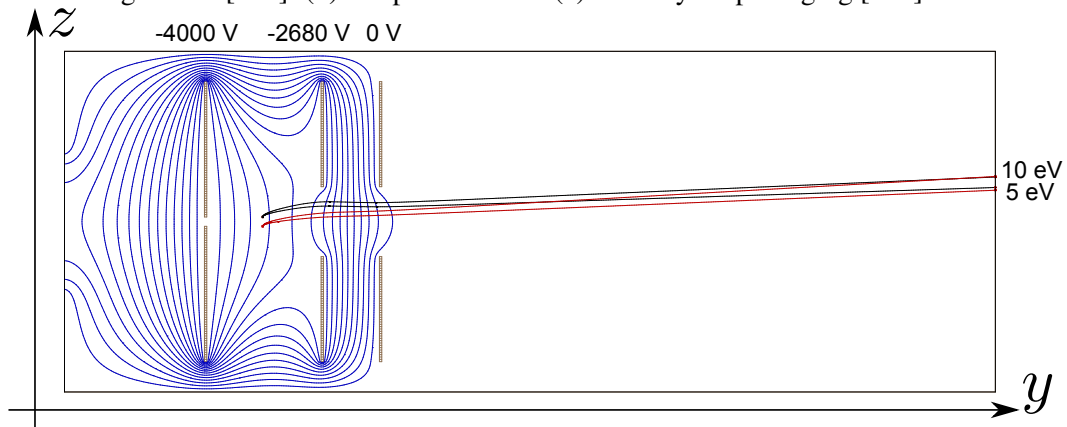


Figure 3.16: Example of the trajectories of electrons in a velocity-map apparatus. This figure is drawn by using SIMION 8.0 [115]. Electrons with initial energy 5 eV and 10 eV are emitted toward z direction at the z -coordinate +2 mm (black trajectories) and -2 mm (red trajectories). At the screen they are focused depending on their initial momenta. Blue curves indicate contour lines of the potential, whose interval is 250 V.

3 Experimental setup and techniques

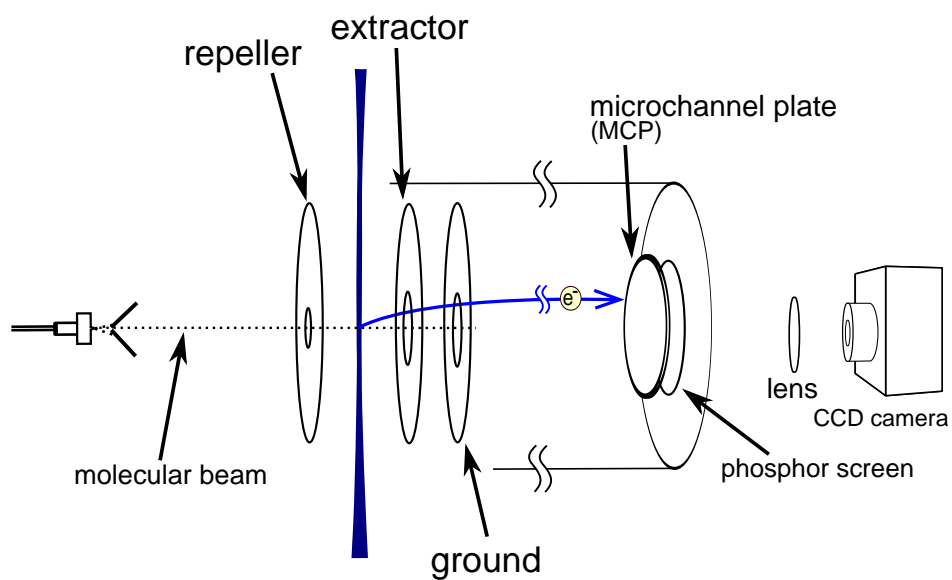


Figure 3.17: Schematic diagram of the setup of our velocity map imaging apparatus.

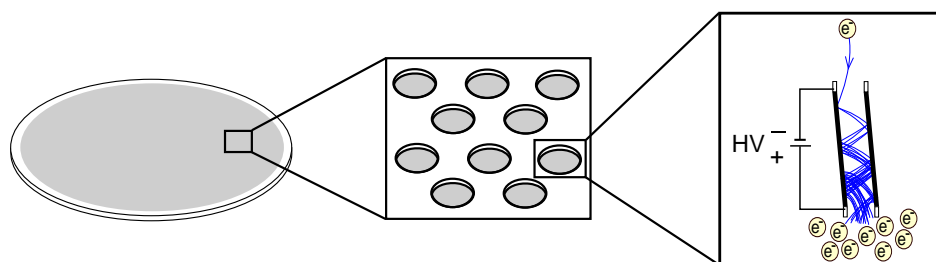


Figure 3.18: The principle of multiplying electrons in a microchannel plate (MCP). When a charged particle hits the inner wall of the channel, secondary electrons are emitted repeatedly and the number of electrons is rapidly increased.

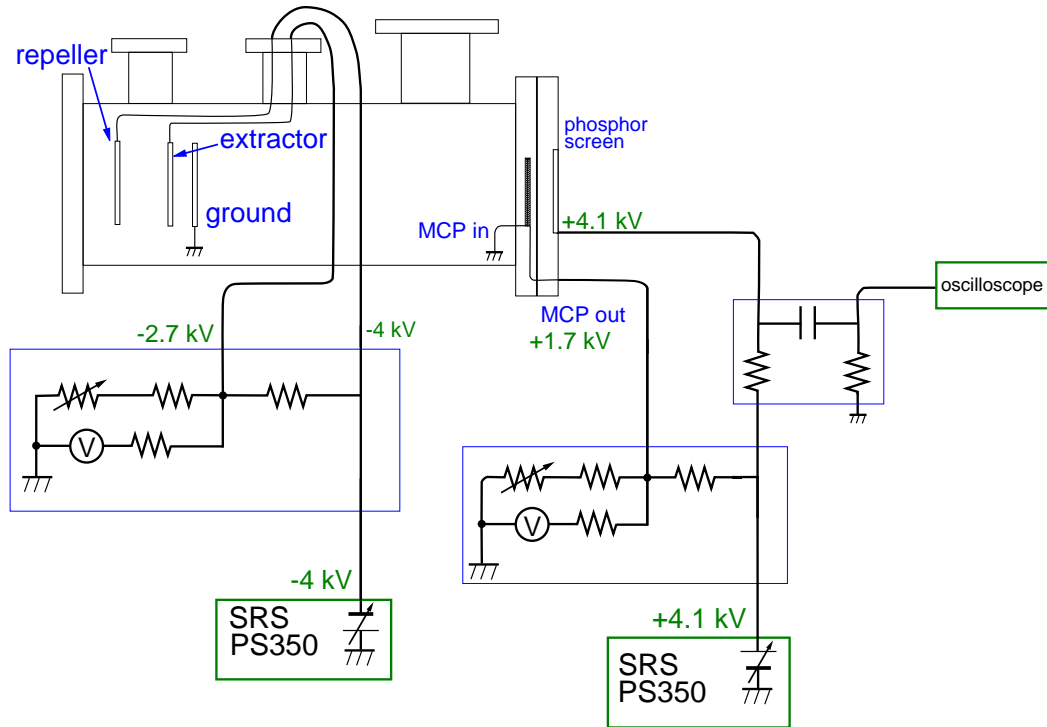


Figure 3.19: Schematic diagram of the electrical setup of the velocity map imaging apparatus.

3.3.3.1 Configuration

The setup of our velocity map imaging apparatus is shown in Fig. 3.17. The beam of the detection gas and the beam of the light intersect between the repeller and the extractor. Produced photoelectrons are accelerated by the electric field created by the electrodes and hit the two-dimensional detector (HAMAMATSU PHOTONICS, F2226-24PF132). This detector has 2 stages of MCP (F1942-04, effective area $\phi 77$ mm, channel diameter $25 \mu\text{m}$, channel pitch $31 \mu\text{m}$) and a phosphor screen. An MCP (or microchannel plate) [121, 122] is a plate with a lot of channels and is used with high voltage applied between the two sides (Fig. 3.18). When a charged particle enters the plate and hits the inner wall, secondary electrons are emitted. They are accelerated by the high-voltage potential, hit the channel wall, and produce further secondary electrons. Repeating these processes multiplies the number of electrons exponentially. The flood of output electrons are then accelerated and strike the phosphor screen, and the impact site produces fluorescence. The light from the phosphor screen is focused by a lens with focal length of 50 mm on the CCD camera (Basler, avA2300-30km, 2330×1750 pixels). The image is transferred to a personal computer with a frame grabber (Euresys, GrabLink Base). The position where the electrons hit the screen is recorded as a “blob” in images. We describe in §§3.3.4–3.3.6 the analysis of the obtained images.

3 Experimental setup and techniques



Figure 3.20: A photograph of the baffle at the exit of the velocity map imaging chamber.

3.3.3.2 Wiring of high-voltage circuit

Figure 3.19 shows the cabling to the velocity map apparatus. We use two high-voltage power supplies (Stanford Research Systems, PS350), one for the acceleration electrodes and the other for two-dimensional detector. The output of each power supply is divided by home-built voltage dividers, where the divided voltages are monitored by a voltmeter (AKIZUKI DENSHI TSUSHO, K-00025). The voltage of the acceleration electrodes are -4000 V, -2680 V and 0 V for the repeller, extractor, and ground, respectively. These voltages are determined by first simulating with SIMION 8.0 and finally checking the convergence of experimental images. The entrance side of the MCP is grounded and $+1700$ V is applied to its exit side. The voltage of the phosphor screen is set at $+4100$ V. The line between the phosphor screen and the power supply is coupled by a capacitor and the current is monitored by an oscilloscope (Tektronix, TDS3052B).

3.3.3.3 Noise shielding

The noise in the photoelectron signal mainly results from the photoionization from background gas. To reduce the flow of the sample gas for harmonic generation, we set small apertures at the exit of harmonic generation chamber and the entrance of the velocity-map imaging chamber, which makes the chamber for the toroidal mirror act as a differential chamber (§3.2.2). In addition, we find a vacuum leak around the entrance of the grating spectrometer and this was hard to remove. To block the effect of this leak we add another differential pumping section (§3.2.5). Between the velocity map imaging chamber and the differential pumping section we set a baffle like Fig. 3.20, which suppresses the gas flow from the vacuum leakage and whose shape reduces the light from reflected back to the velocity map imaging chamber. To decrease the outgassing from the surface of the chamber we bake out the velocity map imaging chamber and some components around this before the experiment.

Noise photoelectrons also come from the metal composing the apparatus when it is irradiated with high-order harmonics. Therefore, we carefully manipulate the path of the light and the position of the chamber so that the high-order harmonics does not hit the chamber.

3.3 Velocity map imaging technique

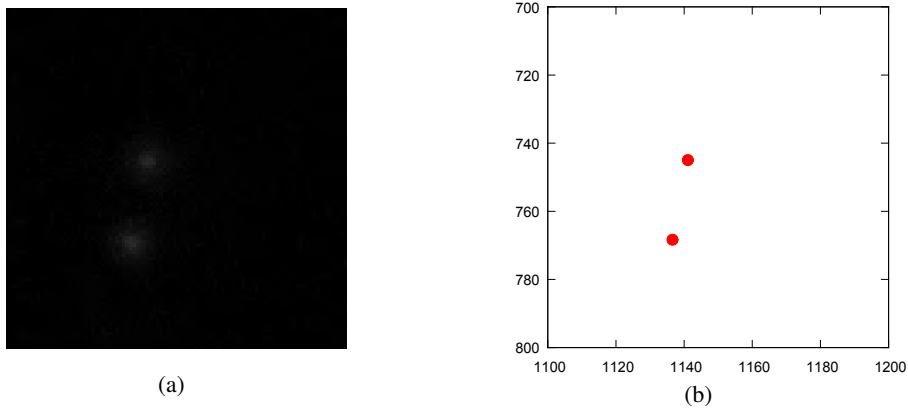


Figure 3.21: An example of the blob detection process. (a) an enlarged image of blobs obtained by the CCD camera. (b) extracted centroids of the blobs.

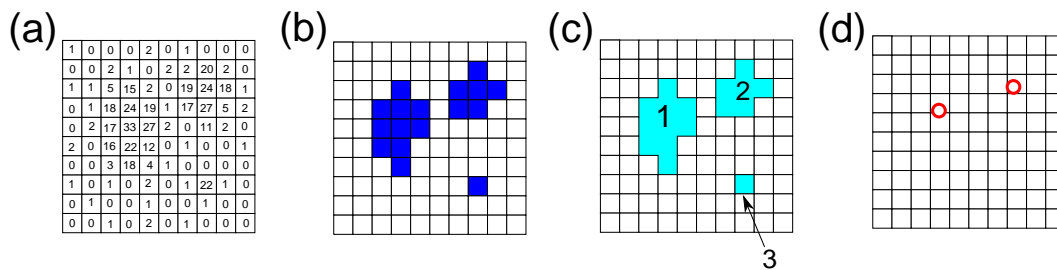


Figure 3.22: The procedure for extracting the positions of blobs. Data obtained by the CCD camera (a) are first binarized (b) and then clustered with “cluster labeling” algorithm [123] (c). The centroids of clusters are obtained with noises excluded (d).

3 Experimental setup and techniques

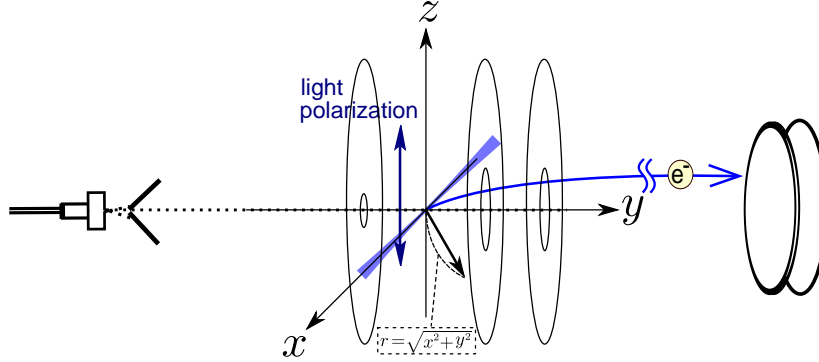


Figure 3.23: Coordinate system in §3.3.5.

3.3.4 Blob detection

The point where the photoelectron hits the detector appears like the gray blobs in Fig. 3.21(a). With the help of Ref. [119] we extract the positions of these blobs by the following procedure: the image obtained by the CCD camera is saved as a series of 8-bit numbers (Fig. 3.22(a)). The data series is first binarized by setting a threshold which is higher than the background noise level but lower than the signal (Fig. 3.22 (b)). Next, the above-threshold pixels adjacent to each other are grouped into one blob, by using the “cluster labeling” algorithm described in Ref. [123] (Fig. 3.22(c)). Clusters with too small size (like cluster 3 in Fig. 3.22(c)) are thought of as noises and are excluded. Finally, the centroids of each cluster are calculated and recorded as a position where a charged particle hits the detector (Fig. 3.22 (d)). For example, the position of two blobs in Fig. 3.21(a) are extracted as shown by circles in Fig. 3.21(b).

The number of blobs per one image is $10 \sim 60$. The rate of the detection process is ~ 17 Hz, which is not so bad compared to the operation rate of our CCD camera without any detection processing (~ 24 Hz). Although the data acquisition rate can be faster by integrating the image directly without blob detection (integration mode), the use of blob detection process provides the following advantages [112, §2.4.5.7]: first, while in the integration mode the resolution of the position of the photoelectron is determined by the size of blobs (typically $\sim 10 \times 10$ pixels on our CCD, which corresponds to $\sim 300 \mu\text{m} \times 300 \mu\text{m}$ on the screen), calculating the centroid of the blobs greatly improves the resolution to the channel pitch of the MCP ($31 \mu\text{m}$ for our MCP). Secondly, the blob detection process can effectively get rid of the noise by setting an appropriate threshold value of the intensity and the size of the blobs. Last but not least, unlike the integration mode, the use of the blob detection process can avoid the effects of large fluctuations in the size and the intensity of the blobs and the inhomogeneity in the detection efficiency of the two-dimensional detector.

3.3.5 Reconstruction of three-dimensional velocity distribution

As discussed in §3.3.1, the two-dimensional image obtained by the velocity map imaging is a projection of the three-dimensional velocity distribution. It is proved that when the system has cylindrical symmetry one can reconstruct the three-dimensional distribution from the projected image. In this

subsection, we present mathematical representation of this reconstruction procedure and two methods for its implementations.

3.3.5.1 Inverse Abel transform

Let us consider photoelectrons which are produced from rare-gas atoms by a pulse with linear polarization along z axis and accelerated to the direction of y axis (see Fig. 3.23). When the speed of the rare-gas atoms is small enough compared to that of photoelectrons⁴, the initial velocity distribution of the electrons before projection can be regarded as cylindrically symmetric around z axis, so $i(x, y, z; T_{\text{TOF}})$ in Eq. (3.8) can be written as

$$i(x, y, z; T_{\text{TOF}}) = I(r, z), \quad (3.9)$$

where $r = \sqrt{x^2 + y^2}$. Then,

$$P(x, z) \stackrel{(3.8)}{=} \int_{-\infty}^{+\infty} I(r, z) dy = 2 \int_0^{+\infty} I(r, z) dy = 2 \int_{|x|}^{+\infty} I(r, z) \frac{dy}{dr} dr = 2 \int_{|x|}^{+\infty} \frac{rI(r, z)}{\sqrt{r^2 - x^2}} dr. \quad (3.10)$$

The integral transform which appears in this equation is known as Abel transform⁵. Its inverse transform can be obtained analytically as [124]

$$I(r, z) = -\frac{1}{\pi} \int_r^{+\infty} \frac{dP(x, z)/dx}{\sqrt{x^2 - r^2}} dx. \quad (3.12)$$

This analytical form is, however, not suitable for reconstruction from experimental data because of the singularity of the integrand at $x = r$ and the derivative dP/dx which will enhance experimental noises. To overcome these difficulties, many kinds of reconstruction methods are devised [112, § 3]. Below we introduce two of them: the Fourier-Hankel method and the BASEX method.

⁴ The speed v_{jet} of the Ar jet with temperature $T_0 = 300$ K is estimated as $v_{\text{jet}} \sim 6 \times 10^2$ m/s from the relation $v_{\text{jet}} \approx \sqrt{\frac{2R}{W} \left(\frac{\gamma}{\gamma-1}\right) T_0}$ (§2.1.2 of [109]), where R , W , γ are a molar gas constant, molar weight, and the heat capacity ratio, respectively. On the other hand, the speed of electron with kinetic energy of 1 eV is $\sim 6 \times 10^5$ m/s, which is much faster than that of the jet. Therefore, in the energy range for our measurement (1 eV – 15 eV) the initial velocity distribution of photoelectrons can be assumed to have cylindrical symmetry.

⁵ For small Δr , Eq. (3.10) can be approximated as

$$\begin{aligned} P(x, z) &= 2 \int_{|x|}^{+\infty} \frac{rI(r, z)}{\sqrt{r^2 - x^2}} dr \simeq 2 \sum_{k=\min\{k \in \mathbb{Z} | k\Delta r \geq |x|\}}^{+\infty} \int_{k\Delta r}^{(k+1)\Delta r} \frac{rI(r, z)}{\sqrt{r^2 - x^2}} dr \\ &\simeq 2 \sum_{k=\min\{k \in \mathbb{Z} | k\Delta r \geq |x|\}}^{+\infty} I(k\Delta r, z) \int_{k\Delta r}^{(k+1)\Delta r} \frac{r}{\sqrt{r^2 - x^2}} dr \\ &\simeq 2 \sum_{k=\min\{k \in \mathbb{Z} | k\Delta r \geq |x|\}}^{+\infty} I(k\Delta r, z) \sqrt{r^2 - x^2} \Big|_{r=k\Delta r}^{(k+1)\Delta r}. \end{aligned} \quad (3.11)$$

3 Experimental setup and techniques

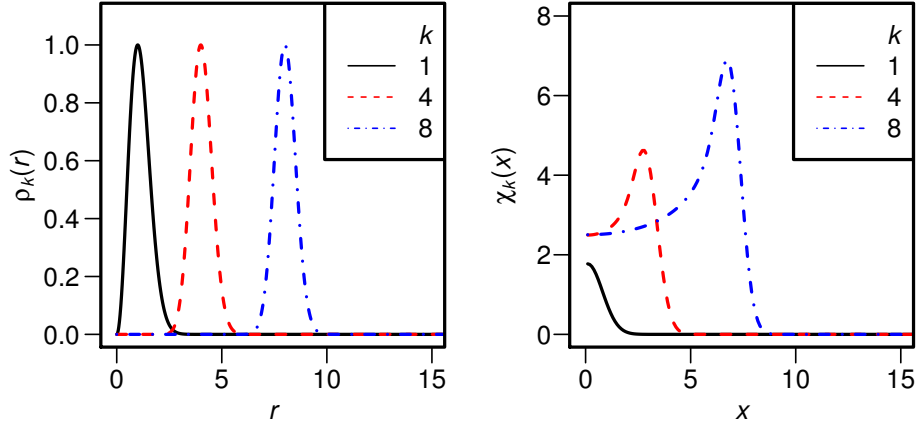


Figure 3.24: Examples of the basis $\rho_k(r)$ used in BASEX method [Eq. (3.16)] (left) and their Abel transform $\chi_k(x)$ [Eq. (3.19)] (right).

3.3.5.2 Fourier-Hankel method

Montgomery Smith *et al.* showed that the inverse Abel transform can be constructed by combining integral transforms [124]. First, the Fourier transform on the x axis of the projection is

$$\begin{aligned}\tilde{P}(k, z) &\equiv \int_{-\infty}^{\infty} dx P(x, z) e^{-ikx} = \int_{-\infty}^{\infty} dx \int_{-\infty}^{+\infty} dy I(r, z) e^{-ikx} \\ &= \int_0^{\infty} r dr \int_0^{2\pi} d\theta I(r, z) e^{-ikr \cos \theta} \\ &= 2\pi \int_0^{\infty} r I(r, z) J_0(kr) dr.\end{aligned}\quad (3.13)$$

The integral transform $F(k) = \int_0^{\infty} r f(r) J_\nu(kr) dr$ in Eq. (3.13) is called Hankel transform [71, § 15.1]. By using the closure equation of the Bessel functions $\int_0^{\infty} J_\nu(kr) J_\nu(kr') k dk = \delta(r - r')/r$ [71, § 11.2] it can be proved that the form of inverse Hankel transform is identical to that of forward transform: $f(r) = \int_0^{\infty} k F(k) J_\nu(kr) dk$. Thus,

$$\begin{aligned}I(r, z) &= \frac{1}{2\pi} \int_0^{\infty} k \tilde{P}(k, z) J_\nu(kr) dk \\ &= \frac{1}{2\pi} \int_0^{\infty} k \left[\int_{-\infty}^{\infty} dx P(x, z) e^{-ikx} \right] J_\nu(kr) dk.\end{aligned}\quad (3.14)$$

This representation is free from the singularity stated above. The Fourier transform in Eq.(3.14) can be implemented by the Fast-Fourier transform, which makes this algorithm rapid. This reconstruction technique is called Fourier-Hankel method.

3.3.5.3 BASEX method

Another approach, called the basis set expansion (BASEX) Abel transform method, was reported by Dribinski *et al.* [125]. The idea is that the image is expanded by the basis set which has an analytical

3.3 Velocity map imaging technique

form of its inverse Abel transform. Let us assume that the three-dimensional slice of the velocity distribution $I(r, z)$ can be expanded as

$$I(r, z) = \sum_{k=0}^{K_x-1} \sum_{m=0}^{K_z-1} C_{km} \rho_k(r) \zeta_m(z), \quad (3.15)$$

where

$$\rho_k(r) = \left(\frac{e}{k^2}\right)^{k^2} \left(\frac{r}{\sigma}\right)^{2k^2} e^{-(r/\sigma)^2}, \quad (3.16)$$

$$\zeta_m(z) = \rho_m(z) = \left(\frac{e}{m^2}\right)^{m^2} \left(\frac{z}{\sigma}\right)^{2m^2} e^{-(z/\sigma)^2}. \quad (3.17)$$

$\rho_k(r)$'s for $k = 1, 4, 8$ are plotted in the left panel of Fig. 3.24. The basis function $\rho_k(r)$ has its maximum at $r = k\sigma$. By forward Abel transform, the expansion basis $\rho_k(r)\zeta_m(z)$ is transformed as

$$2 \int_{|x|}^{+\infty} \frac{r \rho_k(r) \zeta_m(z)}{\sqrt{r^2 - x^2}} dr = \left[2 \int_{|x|}^{+\infty} \frac{r \rho_k(r)}{\sqrt{r^2 - x^2}} dr \right] \zeta_m(z) \equiv \chi_k(x) \zeta_m(z), \quad (3.18)$$

where

$$\chi_k(x) \equiv 2 \int_{|x|}^{+\infty} \frac{r \rho_k(r)}{\sqrt{r^2 - x^2}} dr \quad (3.19)$$

is the Abel transform of $\rho_k(r)$. Then $\chi_k(x)$ can be calculated as

$$\chi_k(x) = 2 \sqrt{\pi} \sigma \rho_k(x) \left[1 + \sum_{l=1}^{k^2} \left(\frac{x}{\sigma}\right)^{-2l} \prod_{m=1}^l \frac{(k^2 + 1 - m)(m - 1/2)}{m} \right] \quad (3.20)$$

(see §A.6 for its derivation). $\chi_k(x)$'s for $k = 1, 4, 8$ are plotted in the right panel of Fig 3.24. The projection of $I(r, z)$ can be expanded by χ_k and ζ_m :

$$\begin{aligned} P(x, z) &\stackrel{(3.10)}{\equiv} 2 \int_{|x|}^{+\infty} \frac{r I(r, z)}{\sqrt{r^2 - x^2}} dr \stackrel{(3.15)}{=} 2 \int_{|x|}^{+\infty} \frac{r \sum_{k=0}^{K_x-1} \sum_{m=0}^{K_z-1} C_{km} \rho_k(r) \zeta_m(z)}{\sqrt{r^2 - x^2}} dr \\ &\stackrel{(3.18)}{=} \sum_{k=0}^{K_x-1} \sum_{m=0}^{K_z-1} C_{km} \chi_k(x) \zeta_m(z). \end{aligned} \quad (3.21)$$

Therefore, if the expansion coefficients C_{km} 's from the projection $P(x, z)$ are available, we can retrieve the three-dimensional distribution of the velocity distribution $I(r, z)$ by substituting C_{km} into Eq. (3.15).

In Ref. [125], the expansion coefficients C_{km} 's are obtained from the experimental data as below: The coordinate (x, z) of the projection image $P(x, z)$ obtained by experiments is discretized like

$$x_i = x_0 + i\Delta x, \quad (3.22)$$

$$z_j = z_0 + j\Delta z, \quad (3.23)$$

where $i = 0, 1, \dots$ and $j = 0, 1, \dots$ are integers representing the coordinate. At this discretized coordinate, the projection image $P(x, z)$ and the basis $\chi_k(x)$ and $\zeta_m(z)$ for the expansion (3.21) is

3 Experimental setup and techniques

represented by a matrix form as

$$P_{ij} = P(x_i, z_j), \quad (3.24)$$

$$X_{ki} = \chi_k(x_i), \quad (3.25)$$

$$Z_{mj} = \zeta_m(z_j). \quad (3.26)$$

From Eq. (3.21), the matrices $\mathbf{P} = \{P_{ij}\}$, $\mathbf{X} = \{X_{ki}\}$, $\mathbf{C} = \{C_{km}\}$, and $\mathbf{Z} = \{Z_{mj}\}$ are related by matrix multiplication:

$$\mathbf{P} = \mathbf{X}^T \mathbf{C} \mathbf{Z} \quad (3.27)$$

(superscript T means transposed matrix). It seems that the coefficients C_{km} 's can be obtained by

$$\mathbf{C} = (\mathbf{X}\mathbf{X}^T)^{-1} \mathbf{X}\mathbf{P}\mathbf{Z}^T (\mathbf{Z}\mathbf{Z}^T)^{-1}. \quad (3.28)$$

In practice, the data include experimental noise and errors caused by discretization, which can badly disturb the numerical calculation of the inverse matrix [126, §3]. To stabilize the calculation, Ref. [125] calculate $(\mathbf{X}\mathbf{X}^T + q_1^2 \mathbf{I})^{-1}$ and $(\mathbf{Z}\mathbf{Z}^T + q_2^2 \mathbf{I})^{-1}$ instead of $(\mathbf{X}\mathbf{X}^T)^{-1}$ and $(\mathbf{Z}\mathbf{Z}^T)^{-1}$ (\mathbf{I} stands for an identity matrix). This replacement is known as Tikhonov regularization [126, §4]. By using the calculated $\mathbf{C} = \{C_{km}\}$, the three-dimensional velocity distribution is reconstructed from Eq. (3.15).

The BASEX method tends to be more time-consuming than Fourier-Hankel method. On the other hand, according to the detailed study reported in §3 of Ref. [112], BASEX method is robust over the noise compared to Fourier-Hankel method. We compare the result obtained with the Fourier-Hankel method and that with the BASEX method in the next subsection.

3.3.5.4 Example

Figure 3.25 show an example of the inverse Abel transform. The left panel shows the distribution of the detected photoelectrons produced by irradiating Ar with high-order harmonics. This image is smoothed by a Gaussian filter and the left half and the right half of the data is averaged. The right panel of Fig. 3.25 is the inverse Abel transform obtained by the BASEX method with parameters $\sigma = 1$, $q_1^2 = 1$ and $q_2^2 = 0$. The inverse Abel transform reveals the the ring structure of the velocity distribution, which corresponds to the peaks in the energy spectra of photoelectrons. The lower half of the image is distorted due to the imperfect velocity-map setup and we do not use this area for analysis.

The left and right panels of Fig. 3.26 shows the velocity distribution obtained by Fourier-Hankel method and BASEX method, respectively, reconstructed from the same projected image. Both methods reconstruct the ring structures successfully. However, the area where distribution becomes negative (painted white) is much wider for the image reconstructed by Fourier-Hankel method than that by BASEX method. The true distribution must be positive and the negative area is considered to appear due to experimental noise. Therefore, the result of Fig. 3.26 shows the robustness of BASEX method over the noise. In the following we always use the BASEX method for reconstruction of the velocity distribution.

3.3 Velocity map imaging technique

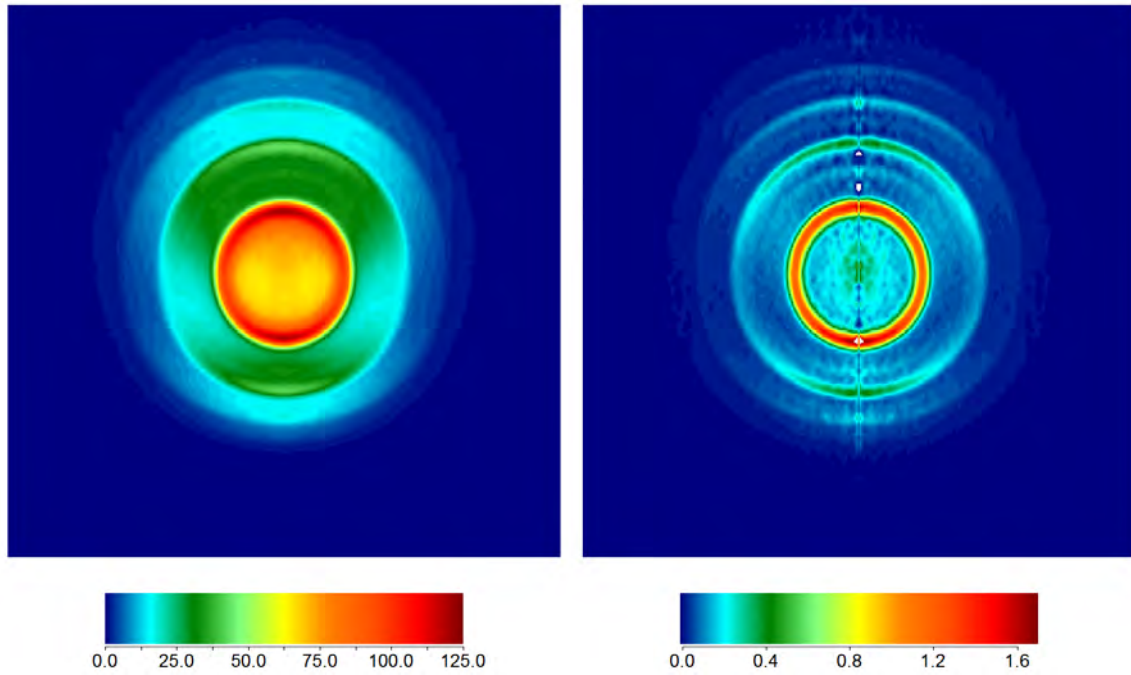


Figure 3.25: An example of the inverse Abel transform. Left: the image of the distribution of the detected photoelectrons produced by irradiating Ar with high-order harmonics generated in Kr and the probe pulses. Right: the inverse Abel transform of the left panel by using the BASEX method.

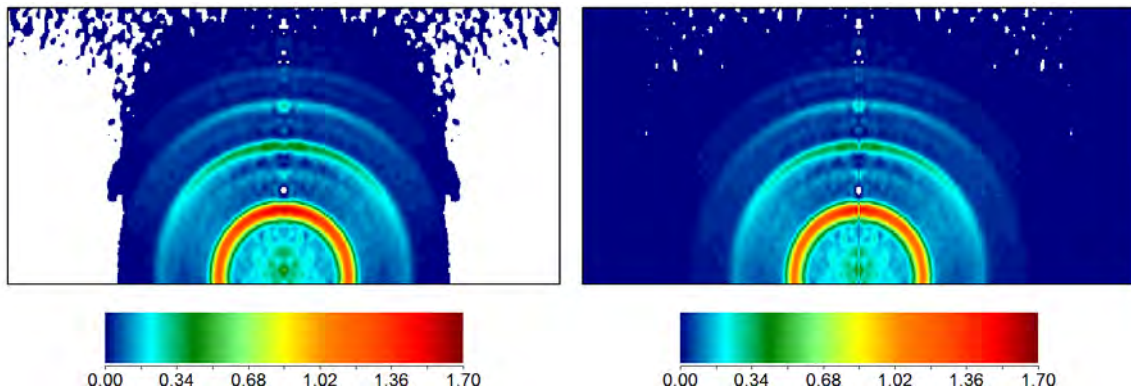


Figure 3.26: Comparison of the reconstructed images obtained by the Fourier-Hankel method (left) and the BASEX method (right). The areas where the values are negative are painted white.

3 Experimental setup and techniques

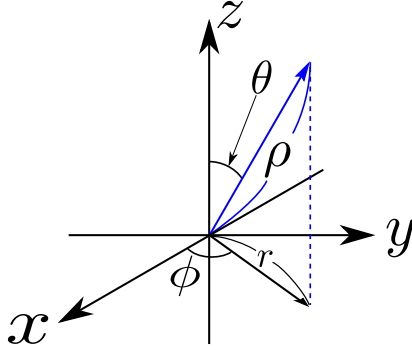


Figure 3.27: The coordinate variables in §3.3.6.

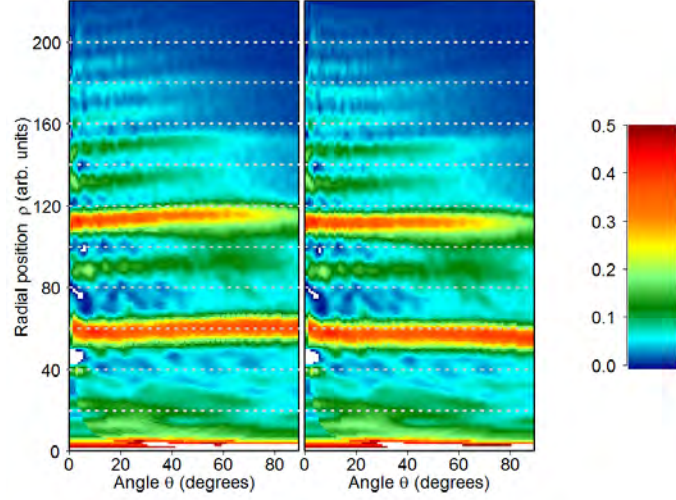


Figure 3.28: An example of the distortion correction. Left: $I(\rho \sin \theta, \rho \cos \theta)$ before correction. Right: after correction.

Noise can be seen along the centerline of both of the images in Fig. 3.26. This comes from the property of the projection [Eq. (3.10)] that the value of the original three-dimensional distribution $I(r, z)$ at $r = r_0$ only contributes to $|x| \leq r_0$ of the projection $P(x, z)$. Thus for small r_0 the information about $I(r_0, z)$ obtained from the projection is limited compared to that for large r_0 , which leads to a bad signal-to-noise ratio near the centerline [125, §IV].

3.3.6 Getting radial distribution with a distortion correction

From Eq. (3.7), the positions (x, y, z) in the reconstructed distribution $I(r, z) = i(x, y, z; T_{\text{TOF}})$ are related to the initial velocities of photoelectrons. Therefore, the energy of the photoelectron corresponds to the distance from the center $\rho = \sqrt{x^2 + y^2 + z^2}$. The signal whose distance from the center is between ρ and $\rho + \Delta\rho$ can be calculated from $I(r, z)$ as (see Fig. 3.27 for coordinate variable)

$$\begin{aligned}
 D(\rho)\Delta\rho &= \int_{\rho}^{\rho+\Delta\rho} \rho^2 d\rho \int_0^{\pi} \sin \theta d\theta \int_0^{2\pi} d\phi I(r, z) = 2\pi \int_{\rho}^{\rho+\Delta\rho} \rho^2 d\rho \int_0^{\pi} \sin \theta d\theta I(\rho \sin \theta, \rho \cos \theta) \\
 &\simeq 2\pi\rho^2 \Delta\rho \int_0^{\pi} \sin \theta d\theta I(\rho \sin \theta, \rho \cos \theta).
 \end{aligned}
 \tag{3.29}$$

The left panel of Fig. 3.28 shows an example of $I(\rho \sin \theta, \rho \cos \theta)$ calculated from $I(r, z)$, with the vertical and horizontal axis ρ and θ , respectively (as stated above we do not use the lower half of the image corresponding to $90^\circ < \theta \leq 180^\circ$). Due to the distortion of the velocity-map setting, the ridges of the signal are slightly inclined. To correct these deformation, we first fit the positions of the peaks made by the 11th and 13th harmonics (the two strongest peaks in Fig. 3.28), which we write as $\rho_{11}(\theta)$

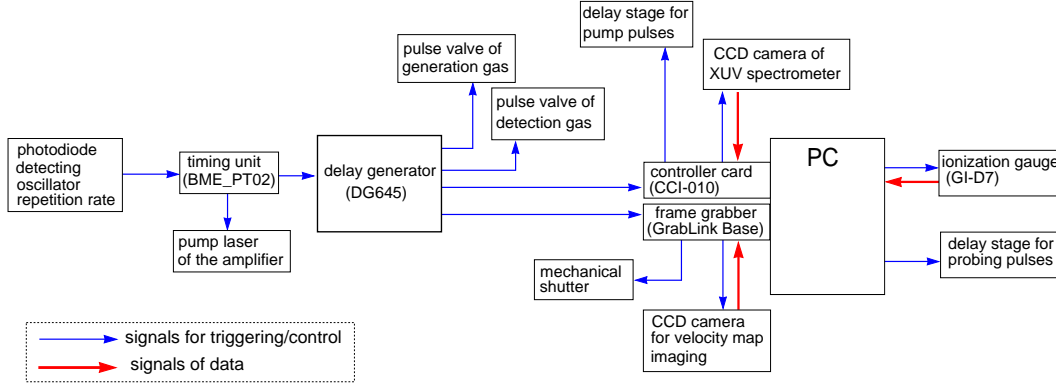


Figure 3.29: Signal-flow diagram of the experiment. See text for details.

and $\rho_{13}(\theta)$ respectively, by a quadratic function of θ as

$$\rho_{11}(\theta) = \rho_{11}(0)(1 + B_{11}\theta + C_{11}\theta^2), \quad (3.30)$$

$$\rho_{13}(\theta) = \rho_{13}(0)(1 + B_{13}\theta + C_{13}\theta^2). \quad (3.31)$$

Then, the r at each θ is scaled to ρ_{new} so that the two peaks come to the same position as that of $\theta = 0$.

$$\rho(\theta) = \rho_{\text{new}}(1 + B(\rho_{\text{new}})\theta + C(\rho_{\text{new}})\theta^2), \quad (3.32)$$

where $B(r)$ and $C(r)$ are a linear function of r satisfying

$$B(\rho_{11}(0)) = B_{11}, \quad B(\rho_{13}(0)) = B_{13}, \quad (3.33)$$

$$C(\rho_{11}(0)) = C_{11}, \quad C(\rho_{13}(0)) = C_{13}. \quad (3.34)$$

The right panel of Fig. 3.28 is the corrected result of the left panel. The ridges of the signal are straightened compared to the left panel. The data with small θ contains noise originated in the inverse Abel transform (§3.3.5.4), so we do not use the data in $0^\circ \leq \theta < 5^\circ$ in the analysis.

3.4 Signal flow

Figure 3.29 shows the flow of the signal for triggering, control, and the obtained data. The experimental system is synchronized by the trigger signal based on the repetition rate of the Ti:sapphire oscillator (§3.1.1.2). A part of the output of the oscillator is detected by a photodiode and its repetition rate (~ 78 MHz) is frequency-divided by a timing unit (Bergmann Messgeraete Entwicklung KG, BME_PT02) into ~ 1 kHz. This signal is used as the trigger of the experiment and is delivered to many apparatuses including the pump laser of the amplifier, pulsed valve, and the CCD camera. The time delay of the pulsed valves and the camera are controlled by a digital delay generator (Stanford Research Systems, DG645). The delay stages for pump and probe pulses, and a mechanical shutter (Suruga Seiki Co. Ltd., model F116) for making pump pulses on/off are controlled automatically with a personal computer. With this computer we collect the data of harmonic spectra and image of photoelectrons and analyze them. We also record the pressure of the harmonic generation chamber (3.2.1) to use as a indicator of the gas flow rate.

3 Experimental setup and techniques

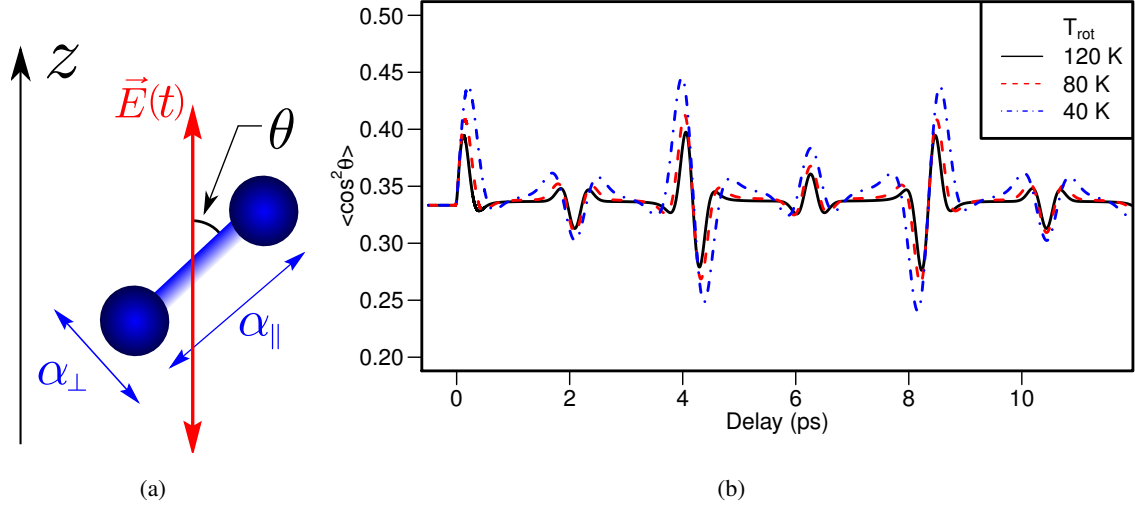


Figure 3.30: (a) Parameters of a rigid-rotor molecule in a linearly-polarized laser field. (b) Calculated time evolution of $\langle \cos^2 \theta \rangle$ for N_2 molecules. The intensity of the pump pulse is $3 \times 10^{13} \text{ W/cm}^2$ and the rotational temperature is 120 K (solid line), 80 K (dashed line), and 40 K (dashed-dotted line).

3.5 Nonadiabatic alignment of molecules with strong laser pulses

Since molecular orbitals are not isotropic, the high-order harmonics generated in molecules are dependent on the direction of their axes. This dependence can be investigated by using laser-induced nonadiabatic alignment technique first demonstrated by Rosca-Pruna and Vrakking [23]. In this section, we present the principle of this technique.

3.5.1 Overview

In the nonadiabatic alignment method [23], we first irradiate sample molecules with a short pump pulse to excite rotational wave packets. When the polar angle between the laser polarization and the molecular axis is denoted as θ (Fig. 3.30(a)), the degree of alignment $\langle \cos^2 \theta \rangle$ changes like Fig. 3.30(b). When the delay time t reaches around $T_{\text{rot}}/2$, where T_{rot} is the rotational period of the molecule, $\langle \cos^2 \theta \rangle$ gets a high value. This means that the molecules are well aligned along the pump pulse polarization. By irradiating the driving pulses at this moment we can observe high-order harmonics generated in aligned molecules.

3.5.2 Principle of the nonadiabatic alignment

In this thesis we consider a linear symmetric molecule. If the molecule can be regarded as a rigid-rotor with the moment of inertia I , its field-free Hamiltonian is given by [39, §XVI.7]

$$\hat{H}_0 = \frac{1}{2} \hat{\mathbf{J}}^2 = B \hat{\mathbf{J}}^2, \quad (3.35)$$

3.5 Nonadiabatic alignment of molecules with strong laser pulses

where \hat{J} is the operator of the rotor's angular momentum and $B \equiv 1/(2I)$ is the rotational constant as angular frequencies⁶. When the molecule interacts with the external electric field $\mathbf{E}(t)$ by the interaction potential $\hat{V}_{\text{int}}(t)$, the time-dependent Schrödinger equation of the rotational state $|\psi(t)\rangle$ becomes

$$i\frac{\partial}{\partial t}|\psi(t)\rangle = (B\hat{J}^2 + \hat{V}_{\text{int}}(t))|\psi(t)\rangle. \quad (3.36)$$

When the molecule has polarizability components α_{\parallel} and α_{\perp} parallel and perpendicular to the molecular axis, respectively (see Figure 3.30(a)), the interaction potential $\hat{V}_{\text{int}}(t)$ can be written as [127]

$$\begin{aligned} \hat{V}_{\text{int}}(t) &= -\frac{1}{2}E_0^2(t)\cos^2(\omega t)(\alpha_{\parallel}\cos^2\theta + \alpha_{\perp}\sin^2\theta) \\ &= -\frac{1}{2}E_0^2(t)\left[\frac{1}{2} + \frac{1}{2}\cos(2\omega t)\right](\alpha_{\parallel}\cos^2\theta + \alpha_{\perp}\sin^2\theta). \end{aligned} \quad (3.37)$$

When the envelope $E_0(t)$ changes much slower than the cycle of laser field $2\pi/\omega$, the rapid oscillations of $\cos(2\omega t)$ in Eq. (3.37) are averaged out and $\hat{V}_{\text{int}}(t)$ becomes

$$\begin{aligned} \hat{V}_{\text{int}}(t) &= -\frac{1}{4}E_0^2(t)(\alpha_{\parallel}\cos^2\theta + \alpha_{\perp}\sin^2\theta) = -\frac{1}{4}E_0^2(t)(\Delta\alpha\cos^2\theta + \alpha_{\perp}) \\ &= -U_{\perp}(t) - U(t)\cos^2\theta, \end{aligned} \quad (3.38)$$

where $\Delta\alpha \equiv \alpha_{\parallel} - \alpha_{\perp}$ is the polarizability anisotropy, $U_{\perp}(t) \equiv \frac{1}{4}E_0^2(t)\alpha_{\perp}$, and $U(t) \equiv \frac{1}{4}E_0^2(t)\Delta\alpha$. By substituting Eq. (3.38) into Eq. (3.36) we get

$$i\frac{\partial}{\partial t}|\psi(t)\rangle = (B\hat{J}^2 - U_{\perp}(t) - U(t)\cos^2\theta)|\psi(t)\rangle, \quad (3.39)$$

The time evolution of one molecule in pure state can be calculated by solving the time-dependent Schrödinger equation (3.39). A molecular ensemble is, in general, not in the pure state but in a mixed states, represented by density operator. Assuming the Boltzmann distribution, the density matrix in thermal equilibrium is written as

$$\hat{\rho}_{\text{eq}}(t=0) = \sum_{J_0=0}^{+\infty} \sum_{M_0=-J_0}^{+J_0} w_{J_0, M_0} |J_0, M_0\rangle \langle J_0, M_0|. \quad (3.40)$$

$$w_{J_0, M_0} = \frac{g_{J_0} \exp[-BJ_0(J_0+1)/(k_B T_{\text{rot}})]}{\sum_{J, M} g_J \exp[-BJ(J+1)/(k_B T_{\text{rot}})]}, \quad (3.41)$$

where g_J is the degeneracy of the rotational level with the energy $BJ(J+1)$, k_B is the Boltzmann constant, and T_{rot} is the rotational temperature. (see Appendix A.5 for the derivation of this expression). The time evolution of the density matrix is determined by the quantum Liouville equation [128, § 3]

$$\frac{\partial \hat{\rho}(t)}{\partial t} = -i[\hat{H}, \hat{\rho}]. \quad (3.42)$$

⁶ In SI units, our rotational constant is represented as $B \equiv \hbar/(2I)$, where the units of \hbar (reduced Planck constant) and I (moment of inertia) are $\text{m}^2 \cdot \text{kg} \cdot \text{s}^{-1}$ and $\text{m}^2 \cdot \text{kg}$, respectively. In some references such as Ref. [93, 10.3], the rotational constant as frequency $B \equiv \hbar/(4\pi I)$ or that as wavenumber $B \equiv \hbar/(4\pi c I)$ are also used.

3 Experimental setup and techniques

We expand the density matrix $\hat{\rho}(t)$ and the Hamiltonian $\hat{H} \equiv \hat{H}_0 + \hat{V}_{\text{int}}$ by rotational states $|J, M\rangle$, which are the eigenstates of \hat{H}_0 :

$$\hat{\rho}(t) = \sum_{J,M} \sum_{J',M'} \rho_{(J,M)}^{(J',M')} |J, M\rangle \langle J', M'|, \quad (3.43)$$

$$\hat{H} = \sum_{J,M} \sum_{J',M'} H_{(J,M)}^{(J',M')} |J, M\rangle \langle J', M'|. \quad (3.44)$$

From Eq. (3.38), matrix elements of the Hamiltonian can be calculated as

$$\begin{aligned} H_{(J,M)}^{(J',M')} &= \langle J, M | \hat{H} | J', M' \rangle \\ &= \langle J, M | B\hat{J}^2 - U_{\perp}(t) - U(t) \cos^2 \theta | J', M' \rangle \\ &= [BJ(J+1) - U_{\perp}(t)] \delta_{J,J'} \delta_{M,M'} - U(t) \langle J, M | \cos^2 \theta | J', M' \rangle \\ &\stackrel{\text{(A.60)}}{=} \left\{ BJ(J+1) - U_{\perp}(t) - U(t) \left[(D_J^M)^2 + (D_{J+1}^M)^2 \right] \right\} \delta_{J,J'} \delta_{M,M'} \\ &\quad - U(t) \left(D_{J+1}^M D_{J+2}^M \delta_{J+2,J'} + D_{J-1}^M D_J^M \delta_{J-2,J'} \right) \delta_{MM'} \\ &\equiv a_{(J,M)} \delta_{J,J'} \delta_{M,M'} + b_{(J+1,M)} \delta_{J+2,J'} \delta_{MM'} + b_{(J-1,M)} \delta_{J-2,J'} \delta_{MM'}, \end{aligned} \quad (3.45)$$

where D_J^M is defined as [129] $D_J^M \equiv \sqrt{\frac{(J-M)(J+M)}{(2J-1)(2J+1)}}$ and

$$a_{(J,M)} \equiv BJ(J+1) - U_{\perp}(t) - U(t) \left[(D_J^M)^2 + (D_{J+1}^M)^2 \right], \quad (3.46)$$

$$b_{(J,M)} \equiv U(t) D_J^M D_{J+1}^M. \quad (3.47)$$

From the quantum Liouville equation (3.42), the matrix element of the density matrix is developed as

$$\begin{aligned} \frac{d\rho_{(J,M)}^{(J',M')}(t)}{dt} &= -i \sum_{J'',M''} \left[H_{(J,M)}^{(J'',M'')} \rho_{(J'',M'')}^{(J',M')} - \rho_{(J,M)}^{(J'',M'')} H_{(J'',M'')}^{(J',M')} \right] \\ &= -i \left[\left(a_{(J,M)} \rho_{(J,M)}^{(J',M')} + b_{(J+1,M)} \rho_{(J+2,M)}^{(J',M')} + b_{(J-1,M)} \rho_{(J-2,M)}^{(J',M')} \right) \right. \\ &\quad \left. - \left(a_{(J',M')} \rho_{(J,M)}^{(J',M')} + b_{(J'-1,M)} \rho_{(J,M)}^{(J'-2,M')} + b_{(J'+1,M)} \rho_{(J,M)}^{(J'+2,M')} \right) \right]. \end{aligned} \quad (3.48)$$

The expectation value of $\cos^2 \theta$ is represented by using the density matrix elements $\rho_{(J,M)}^{(J',M')}$ as

$$\begin{aligned} \langle \cos^2 \theta \rangle &= \text{Tr}(\hat{\rho} \cos^2 \theta) = \sum_{J,M} \langle J, M | \hat{\rho} \cos^2 \theta | J, M \rangle \\ &= \sum_{J,M} \sum_{J',M'} \rho_{(J,M)}^{(J',M')} \langle J', M' | \cos^2 \theta | J, M \rangle \\ &\stackrel{\text{(A.60)}}{=} \sum_{J,M} \sum_{J'} \rho_{(J,M)}^{(J',M')} \left\{ \left[(D_{J'}^M)^2 + (D_{J'+1}^M)^2 \right] \delta_{J',J} + D_{J'+1}^M D_{J'+2}^M \delta_{J'+2,J} + D_{J'-1}^M D_{J'}^M \delta_{J'-2,J} \right\} \\ &= \sum_{J,M} \left\{ \left[(D_J^M)^2 + (D_{J+1}^M)^2 \right] \rho_{(J,M)}^{(J,M)} + D_{J+1}^M D_{J+2}^M \left(\rho_{(J+2,M)}^{(J,M)} + \rho_{(J,M)}^{(J+2,M)} \right) \right\} \end{aligned} \quad (3.49)$$

3.5 Nonadiabatic alignment of molecules with strong laser pulses

□ **Field free case** First we consider the time evolution of $\langle \cos^2 \theta \rangle$ after the irradiation of the pump pulse is finished. Since the laser field is absent, from Eqs. (3.46) and (3.47) $a_{(J,M)} = BJ(J+1)$ and $b_{(J,M)} = 0$, so

$$\begin{aligned} \frac{d\rho_{(J,M)}^{(J',M')}}{dt} &= -i \left[BJ(J+1)\rho_{(J,M)}^{(J',M')} - BJ'(J'+1)\rho_{(J,M)}^{(J',M')} \right] \\ &= -iB(J-J')(J+J'+1)\rho_{(J,M)}^{(J',M')}. \end{aligned} \quad (3.50)$$

The solution of this differential equation is

$$\rho_{(J,M)}^{(J',M')}(t) = e^{-iB(J-J')(J+J'+1)t} \rho_{(J,M)}^{(J',M')}(0). \quad (3.51)$$

Substituting this solution into Eq. (3.49), we obtain

$$\begin{aligned} \langle \cos^2 \theta \rangle &= \sum_{J,M} \left\{ \left[(D_J^M)^2 + (D_{J+1}^M)^2 \right] \rho_{(J,M)}^{(J,M)}(0) \right. \\ &\quad \left. + D_{J+1}^M D_{J+2}^M \left(e^{-2iB(2J+3)t} \rho_{(J+2,M)}^{(J,M)}(0) + e^{2iB(2J+3)t} \rho_{(J,M)}^{(J+2,M)}(0) \right) \right\} \\ &= \sum_{J,M} \left\{ \left[(D_J^M)^2 + (D_{J+1}^M)^2 \right] \rho_{(J,M)}^{(J,M)}(0) \right. \\ &\quad \left. + 2D_{J+1}^M D_{J+2}^M \left| \rho_{(J+2,M)}^{(J,M)}(0) \right| \cos [2iB(2J+3)t + \phi_J] \right\}, \end{aligned} \quad (3.52)$$

where $\phi_J = \arg(\rho_{(J+2,M)}^{(J,M)}(0))$. This equation shows that the time evolution of $\langle \cos^2 \theta \rangle$ is due to the presence of coherence term $\rho_{(J+2,M)}^{(J,M)}(0)$. Next, we consider how this term is developed by the irradiation of pump pulses.

□ **Development of coherence term by short laser pulses** From Eq. (3.48), the coherence term $\rho_{(J,M)}^{(J+2,M)}(0)$ changes in the pump pulse as

$$\begin{aligned} \frac{d\rho_{(J,M)}^{(J+2,M)}(t)}{dt} &= -i \left[\left(a_{(J,M)} \rho_{(J,M)}^{(J+2,M)} + b_{(J+1,M)} \rho_{(J+2,M)}^{(J+2,M)} + b_{(J-1,M)} \rho_{(J-2,M)}^{(J+2,M)} \right) \right. \\ &\quad \left. - \left(a_{(J+2,M)} \rho_{(J,M)}^{(J+2,M)} + b_{(J+1,M)} \rho_{(J,M)}^{(J,M)} + b_{(J+3,M)} \rho_{(J,M)}^{(J+4,M)} \right) \right]. \end{aligned} \quad (3.53)$$

In the thermal equilibrium the coherence term of density matrix (3.40) is zero and $\rho_{(J,M)}^{(J',M')} = w_{J,M} \delta_{J,J'} \delta_{M,M'}$.

Thus, if the laser pulse is short enough, the dominant terms in the right-hand side of Eq. (3.53) are the population terms $\rho_{(J,M)}^{(J,M)}$ and $\rho_{(J+2,M)}^{(J+2,M)}$. If other coherence terms are neglected, Eq. (3.53) becomes

$$\frac{d\rho_{(J,M)}^{(J+2,M)}(t)}{dt} \simeq -ib_{(J+1,M)} \left[\rho_{(J+2,M)}^{(J+2,M)} - \rho_{(J,M)}^{(J,M)} \right] \simeq -ib_{(J+1,M)} \left[w_{J+2,M} - w_{J,M} \right]. \quad (3.54)$$

This shows that large population difference in the equilibrium is necessary for the development of coherence terms $\rho_{(J+2,M)}^{(J,M)}(0)$. The population in the thermal equilibrium is given by Eq. (3.41). Figure 3.31 shows the distribution of the $w_{J,M}$ of N_2 molecules calculated from Eq. (3.41) for the rotational temperatures of 120 K, 80 K, and 40 K. From this result one can see that large $|w_{J+2,M} - w_{J,M}|$ is realized by lowering the rotational temperature T_{rot} . Figure 3.30(b) shows the calculated result of the $\langle \cos^2 \theta \rangle$ for $T_{\text{rot}} = 120$ K, 80 K, and 40 K. The degree of alignment $\langle \cos^2 \theta \rangle$ shows higher value as the rotational temperature gets lower.

3 Experimental setup and techniques

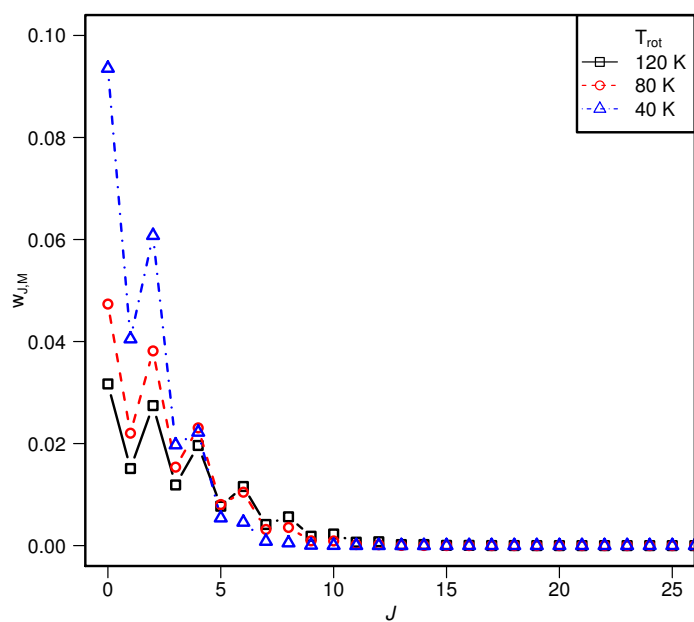


Figure 3.31: The distribution of the $w_{J,M}$ of N_2 molecules, calculated from Eq. (3.41).

3.5 Nonadiabatic alignment of molecules with strong laser pulses

Chapter 4

Results

In this chapter, we present the experimental results obtained by the methods presented in the previous chapter, and the analysis procedure to extract the phase differences between adjacent harmonic orders. First, in §4.1 we show the analyzing method to extract the phase differences between adjacent harmonics from the modulation of sideband intensities. Next, we present in §4.2 the results of the phase differences obtained in our experiments.

4.1 Extracting phase differences

In this section, we describe the process to extract the phase difference of the high-order harmonics from $D(\rho)$ based on the theory of two-color two-photon ionization (§2.3). The problem here is that in the RABBIT method the generation pulse and the probe pulse interfere with each other when focused to generate high-order harmonics. Although the intensity of the probe pulses ($\sim 10^{12}$ W/cm²) are much weaker than that of the generation pulse ($\sim 10^{14}$ W/cm²), their interference causes a modulation of harmonic intensities due to the strong nonlinearity of harmonic generation process. In principle, it is possible to avoid this interference by combining the probe pulses and high-order harmonics *after* the harmonic generation point, as done in Ref. [130]. However, this requires to combine two beams collinearly in a vacuum chamber, which seems too troublesome unless a very large vacuum chamber is available. Instead, we solve the problem accompanied by the effects of the modulation due to the interference by using a new fitting method presented in §4.1.2. This modulation, on the other hand, can be utilized for calibrating the delay Δt between the generation pulse and the probe pulse. We describe this calibration in §4.1.1 before explaining the fitting method.

4.1.1 Calibration of the delay between the harmonics and the probe pulse

The delay Δt between the driving pulse and the probe pulse is controlled by a closed-loop piezoelectric positioning stage with the position resolution 10 nm (§3.1.2). We move the delay stage over 800 nm with the step size of 20 nm. Since the light travels back and forth on the stage, the optical path difference made with this stage is 0–1600 nm by a step of 40 nm, which corresponds to the time difference of 0–5.33 fs by a step of 0.13 fs.

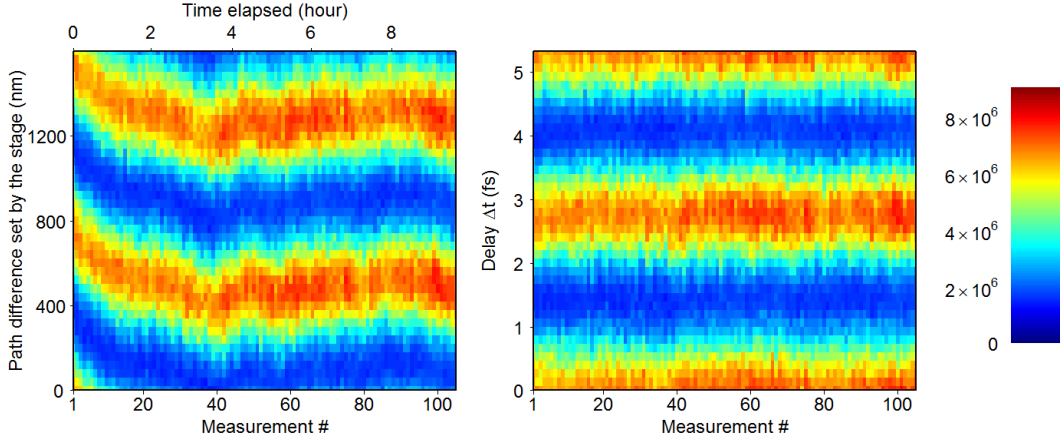


Figure 4.1: Left: the number of blobs at each measurement. The vertical axis stands for the difference in the optical path length set by the positioning stage. Right: the number of blobs reordered by the process describe in §4.1.1. The vertical axis corresponds to the time difference between the driving pulse and the probe pulse.

Due to the interference between the driving pulse

$$E^{\text{driving}}(t) = E_0^{\text{driving}} \cos(\omega_0 t) \quad (4.1)$$

and the probe pulse

$$E^{\text{probe}}(t) = E_0^{\text{probe}} \cos[\omega_0(t - \Delta t)], \quad (4.2)$$

the intensity I of the laser field at the focus for generating high-order harmonics is modulated by changing the delay Δt as

$$\begin{aligned} I(\Delta t) &\propto \overline{|E^{\text{driving}}(t) + E^{\text{probe}}(t)|^2} \\ &= \overline{E_0^{\text{driving}^2} \cos^2(\omega_0 t) + E_0^{\text{probe}^2} \cos^2[\omega_0(t - \Delta t)] + 2E_0^{\text{driving}} E_0^{\text{probe}} \cos(\omega_0 t) \cos[\omega_0(t - \Delta t)]} \\ &= \frac{1}{2} E_0^{\text{driving}^2} + \frac{1}{2} E_0^{\text{probe}^2} + E_0^{\text{driving}} E_0^{\text{probe}} \cos(\omega_0 \Delta t), \end{aligned} \quad (4.3)$$

where the overline stands for time average. Though $|E_0^{\text{probe}}| \ll |E_0^{\text{driving}}|$, the high-order harmonic generation is so nonlinear process that the intensity of the high-order harmonics modulate considerably. The left panel of Fig. 4.1 shows the number of detected photoelectrons which reflects the intensities of the high-order harmonics. The vertical axis of Fig. 4.1 stands for the difference in the optical path length set by the positioning stage and its horizontal axis stands for the measurement number which corresponds to the elapsed time from the start of the measurement. Each measurement shows the modulation in the shape of $\cos(\omega_0 \Delta t)$ appearing in Eq. (4.3), but the positions of the peaks drift slowly as time passes. This drift is considered to be caused by the change of the room temperature and resulting change in optical path difference by the thermal expansion of the system. In fact, the

4 Results

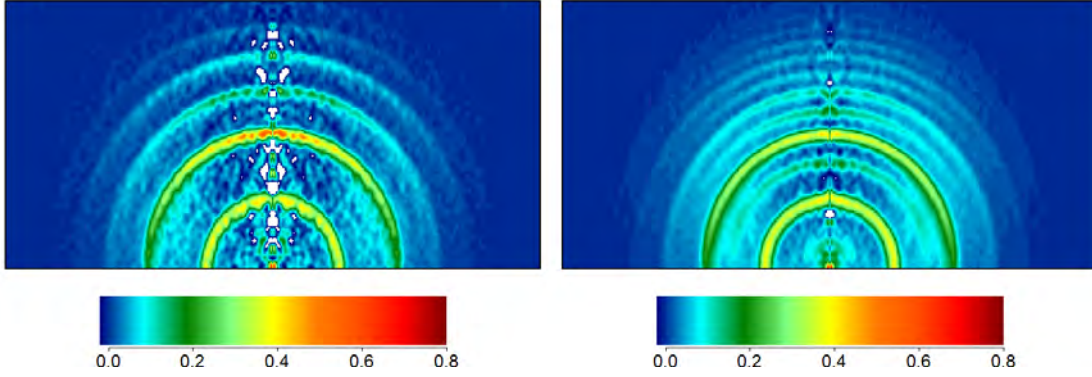


Figure 4.2: Velocity distribution of photoelectrons produced by single-photon ionization with high-order harmonics from Ar (left panel) and by two-color photoionization with high-order harmonics and probe pulses from Ar (right panel). The right panel is the averaged image over all Δt 's.

coefficient of thermal expansion for stainless steel, of which the top of the optical breadboard is made, is $10 \sim 20 \times 10^{-6} \text{ K}^{-1}$ [131, §1.1], and therefore the shift of the temperature by 0.1 K changes the length of a 10 cm-long object of stainless steel by $\sim 100 \text{ nm}$. Since it is difficult to fix the temperature with 0.1 K accuracy throughout the experiment (10 \sim 30 hours), and the variation of the temperature is much slower than the time required in a single measurement (~ 5 minutes), we instead calibrate Δt from the pattern of the modulation in the number of blobs as follows. We define $\Delta t = 0$ as the point where the electric field of the generation pulse and that of the probe pulse is in phase. We Fourier-analyze the number of blobs at each measurement as a function of the time difference $\Delta \tilde{t} = \Delta l/c$, where Δl is the path difference made by the delay stage. The number of blobs is considered to increase with the intensity of the laser field and therefore has a maximum when the two pulses are in phase. Therefore, we rotate the order of each measurement data so that the Fourier component with angular frequency ω_0 has its maximum at $\Delta t = 0$. By this calibration method, the number of blobs in the left panel of Fig. 4.1 is reordered into that in the right panel of Fig. 4.1.

4.1.2 Normalization and fitting of sideband intensities

The left panel of Fig. 4.2 shows an example of the velocity distribution of photoelectrons produced from Ar by high-order harmonics without probe pulses. The ring structure reflects single-photon ionization by the respective-order harmonics. Since the ionization energy of Ar is 15.76 eV [132] and the photon energy of the fundamental light is $\sim 1.55 \text{ eV}$, the most inner ring corresponds to the 11th harmonics. When the probe pulse exists, additional rings between single-photon ionization signals appear like the right panel of Fig. 4.2. They are attributed to the signal of two-color two-photon ionization. Figure 4.3(a) is the photoelectron distribution $D(\rho)$ as a function of the distance ρ from the center [Eq. (3.29)] and the delay Δt of the probe pulse calibrated by the method of §4.1.1. Let us call the signal between the signals from $(2n - 1)$ th and $(2n + 1)$ th harmonics as $2n$ -th sideband. The 14th sideband, for example, in Fig. 4.3(a) is modulated as shown by the circular points in Fig. 4.3(b). We also plot in Fig. 4.3(b) the signals from 13th and 15th harmonics by square and triangular points,

4.1 Extracting phase differences

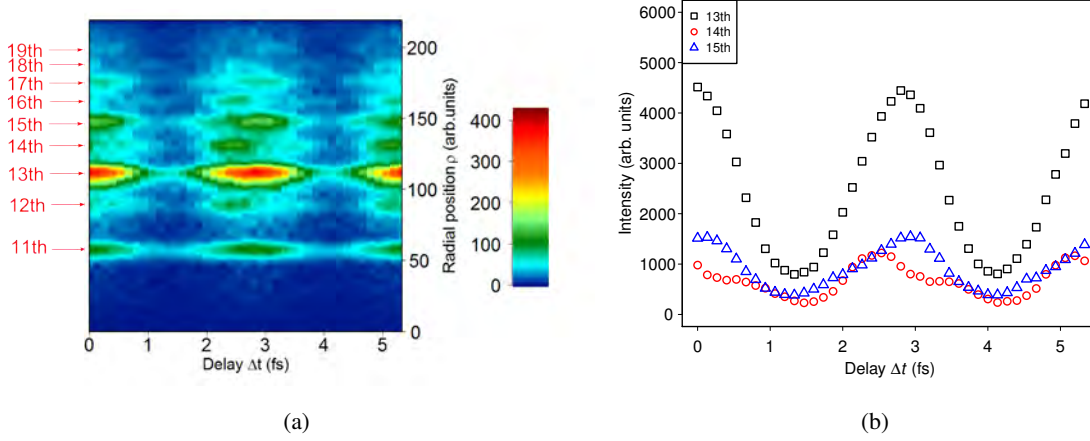


Figure 4.3: (a) An example of the photoelectron distribution $D(\rho)$ produced by the high-order harmonics generated in Ar, as a function of the distance ρ from the center and the delay Δt of the probe pulse. (b) The modulation of the intensity of the 14th sideband as well as the signals produced by the 13th and 15th harmonics, obtained from Fig. 4.3(a).

respectively.

According to Eq. (2.68) in §2.3, the sideband intensity is represented as

$$S_{2n} = \mathcal{A}_I^2 \mathcal{A}_X^{(2n-1)^2} A_+^{(2n+1)} + \mathcal{A}_I^2 \mathcal{A}_X^{(2n+1)^2} A_-^{(2n-1)} + \mathcal{A}_I^2 \mathcal{A}_X^{(2n-1)} \mathcal{A}_X^{(2n+1)} A_{\text{atom}}^{(2n)} \cos(2\phi_{\text{probe}} + \phi_{\text{HH}}^{(2n-1)} - \phi_{\text{HH}}^{(2n+1)} + \Delta\phi_{\text{atom}}^{(2n)}), \quad (4.4)$$

where \mathcal{A}_I and $\mathcal{A}_X^{(2n-1)}$ are the amplitudes of the probe pulse and the $(2n-1)$ th harmonics at the detection point, ϕ_{probe} and $\phi_{\text{HH}}^{(2n-1)}$ are the phases of the probe pulse and the $(2n-1)$ th harmonics at the detection point, and $A_{\pm}^{(2n+1)}$, $A_{\text{atom}}^{(2n)}$ and $\Delta\phi_{\text{atom}}^{(2n)}$ are constants defined in Eqs. (2.69)–(2.71), respectively. When the electric field of the probe pulse is written as Eq. (4.2) and the interval between the point of harmonic generation and that of the detection is denoted by z , the phase ϕ_{probe} of the probe pulse at the detection point becomes

$$\phi_{\text{probe}} = \omega_0 \Delta t + \frac{\omega_0}{c} z \quad (4.5)$$

(see Fig. 4.4) and the sideband intensity S_{2n} [Eq. (4.4)] becomes a function of Δt :

$$S_{2n} = \mathcal{A}_I^2 \mathcal{A}_X^{(2n-1)^2} A_+^{(2n+1)} + \mathcal{A}_I^2 \mathcal{A}_X^{(2n+1)^2} A_-^{(2n-1)} + \mathcal{A}_I^2 \mathcal{A}_X^{(2n-1)} \mathcal{A}_X^{(2n+1)} A_{\text{atom}}^{(2n)} \cos\left(2\omega_0 \Delta t + 2\frac{\omega_0}{c} z + \phi_{\text{HH}}^{(2n-1)} - \phi_{\text{HH}}^{(2n+1)} + \Delta\phi_{\text{atom}}^{(2n)}\right). \quad (4.6)$$

In practice, like the 14th sideband intensity in Fig. 4.3(b), the $\cos(2\omega_0 \Delta t + \phi)$ -shape variation in the sideband is covered by the modulation of the harmonic amplitude $\mathcal{A}_X^{(2n\pm 1)}$. In Refs. [42, 49], the effect of the modulation in harmonic intensities is removed by dividing the sideband intensity at each Δt by the total signal at this delay. Here, we propose another normalizing method based on Eq. (4.6).

When the both side of Eq. (4.6) is divided by $\mathcal{A}_X^{(2n-1)} \mathcal{A}_X^{(2n+1)}$ (the factor before the $\cos(2\omega_0 \Delta t + \phi)$

4 Results

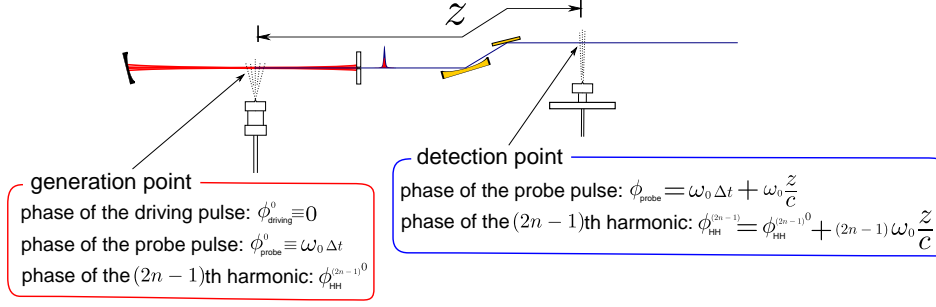


Figure 4.4: The relation between the phases at the generation point and that at the detection point.

term), we get

$$\begin{aligned}
 \tilde{S}_{2n} \equiv S_{2n}/(\mathcal{A}_X^{(2n-1)} \mathcal{A}_X^{(2n+1)}) &= \mathcal{A}_I^2 \frac{\mathcal{A}_X^{(2n-1)}}{\mathcal{A}_X^{(2n+1)}} A_+^{(2n+1)} + \mathcal{A}_I^2 \frac{\mathcal{A}_X^{(2n+1)}}{\mathcal{A}_X^{(2n-1)}} A_-^{(2n-1)} \\
 &+ \mathcal{A}_I^2 A_{\text{atom}}^{(2n)} \cos\left(2\omega_0 \Delta t + 2\frac{\omega_0}{c} z + \phi_{\text{HH}}^{(2n-1)} - \phi_{\text{HH}}^{(2n+1)} + \Delta\phi_{\text{atom}}^{(2n)}\right) \\
 &= \mathcal{A}_I^2 \left[\frac{\mathcal{A}_X^{(2n-1)}}{\mathcal{A}_X^{(2n+1)}} A_+^{(2n+1)} + \frac{\mathcal{A}_X^{(2n+1)}}{\mathcal{A}_X^{(2n-1)}} A_-^{(2n-1)} \right. \\
 &\quad \left. + A_{\text{atom}}^{(2n)} \cos\left(2\omega_0 \Delta t + 2\frac{\omega_0}{c} z + \phi_{\text{HH}}^{(2n-1)} - \phi_{\text{HH}}^{(2n+1)} + \Delta\phi_{\text{atom}}^{(2n)}\right) \right]. \tag{4.7}
 \end{aligned}$$

This normalized sideband intensity \tilde{S}_{2n} is robust over the modulation in harmonic intensities because before the $\cos(2\omega_0 \Delta t + \phi)$ term there is no factor about the harmonic intensities. In addition, the effect of the harmonic intensity modulation on the two terms $\frac{\mathcal{A}_X^{(2n-1)}}{\mathcal{A}_X^{(2n+1)}} A_+^{(2n+1)}$ and $\frac{\mathcal{A}_X^{(2n+1)}}{\mathcal{A}_X^{(2n-1)}} A_-^{(2n-1)}$ is opposite and cancel each other. The normalizing factor $\mathcal{A}_X^{(2n-1)} \mathcal{A}_X^{(2n+1)}$ is estimated from the signal of single photoionization: the probability of single-photoionization is proportional to the intensity of the light, and thus to the square of the amplitude of the electric field (see the first term of the right-hand side of Eq. (2.64)). Therefore, the normalizing factor $\mathcal{A}_X^{(2n-1)} \mathcal{A}_X^{(2n+1)}$ is proportional to the square root of the product of the single-photon ionization signals from $(2n - 1)$ th and $(2n + 1)$ th harmonics.

The square points in Fig. 4.5(a) shows the normalized 14th sideband obtained from the data in Fig.4.3(b) by the square root of the product of the signals from 13th and 15th harmonics. Figure 4.5(b) shows the amplitudes of the Fourier components of the modulation of this normalized sideband as well as those of the raw sideband. The components other than the frequency $2\omega_0$ are successfully reduced by our normalization and the $\cos(2\omega_0 \Delta t + \phi)$ -shape modulation clearly appears in Fig. 4.5(a). However, there still remains the component with frequency ω_0 . From Eq. (4.7), we assume that the remaining component comes from the change in the probe intensity \mathcal{A}_I^2 as a function of Δt . Reference [49] pointed out the possibility that some part of the driving pulse is scattered by the gaseous medium through the aperture for blocking the driving pulse (§3.1.2) and focused on the detecting gas. Another plausible reason is the coupling between the driving pulse and the probe pulse through a nonlinear effect [24, §11.6]. We assume that the probe intensity \mathcal{A}_I^2 varies like $\cos(\omega_0 t + \eta)$

4.1 Extracting phase differences

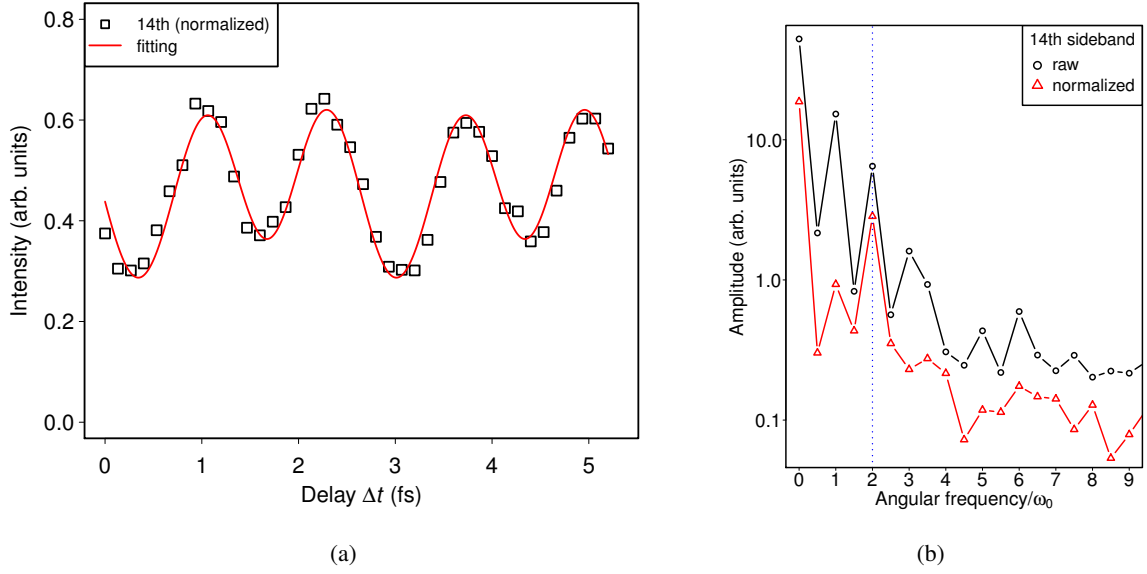


Figure 4.5: (a) An example of the normalized data with the result of fitting. Square points: the normalized 14th sideband obtained from the data in Fig. 4.3(b) by the square root of the product of the signals from 13th and 15th harmonics. Curve: the result of the fitting by Eq. (4.8). (b) Fourier components of the modulations of the raw 14th sideband [Fig. 4.3(b)] and those of the normalized 14th sideband [Fig. 4.5(a)]. Note that the logarithmic scale is used for the vertical axis. The vertical line shows the components with the angular frequency $2\omega_0$.

plus a constant, and the normalized sideband can be fit as

$$A[1 + B \cos(\omega_0 t + \eta)][1 + C \cos(2\omega_0 t + \phi)], \quad (4.8)$$

with A , B , C , η , and ϕ the fitting parameters. In Fig. 4.5(a) we show the result of this fitting for the data points of the normalized 14th harmonics by using Levenberg-Marquardt method [133, §15.5.2]. The function (4.8) fit the data very well.

By comparing Eqs. (4.7) and (4.8), the ϕ of the fitting result is related to the phase of the harmonics as

$$\phi \simeq 2 \frac{\omega_0}{c} z + \phi_{\text{HH}}^{(2n-1)} - \phi_{\text{HH}}^{(2n+1)} + \Delta\phi_{\text{atom}}^{(2n)}. \quad (4.9)$$

Here, $\phi_{\text{HH}}^{(2n\pm 1)}$ is the phase of $(2n \pm 1)$ th harmonics at the detection point. They are related to the phase $\phi_{\text{HH}}^{(2n-1)0}$ at the detection point as

$$\phi_{\text{HH}}^{(2n-1)} = \phi_{\text{HH}}^{(2n-1)0} + \frac{(2n-1)\omega_0}{c} z, \quad (4.10)$$

$$\phi_{\text{HH}}^{(2n+1)} = \phi_{\text{HH}}^{(2n+1)0} + \frac{(2n+1)\omega_0}{c} z \quad (4.11)$$

when the dispersion of the gaseous medium is neglected (see Fig. 4.4). Substituting these relations into Eq. (4.9), we obtain

$$\begin{aligned} \phi &\simeq +\phi_{\text{HH}}^{(2n-1)0} - \phi_{\text{HH}}^{(2n+1)0} + \Delta\phi_{\text{atom}}^{(2n)} \\ &= -(\Delta\phi_{\text{HH}}^{(2n)0} - \Delta\phi_{\text{atom}}^{(2n)}), \end{aligned} \quad (4.12)$$

4 Results

Table 4.1: Ionization potentials of the atoms and molecules we investigated in this study. $\hbar\omega_0 \simeq 1.55$ eV is the photon energy of the fundamental field.

Medium	I_P (eV) [132]	$I_P/\hbar\omega_0$
Ar	15.76	10.2
N ₂	15.58	10.1
Kr	14.00	9.0
CO ₂	13.78	8.9

Table 4.2: Summary of the experimental conditions. The intensities of the driving pulse I_{driving} is estimated from the cutoff of the high-order harmonics generated in the medium in parentheses.

Measurement #	Period	I_{driving} (W/cm ²)	Medium
1	Sep. 26, 2013	$> 1.8 \times 10^{14}$ (Kr) ¹	Kr
2	Jan. 13–16, 2014	2.7×10^{14} (Ar)	N ₂ , Ar, Kr
3	May 14–16, 2014	2.7×10^{14} (Ar)	Ar, N ₂
4	May 20–22, 2014	2.7×10^{14} (Ar)	Kr, Ar, (CO ₂) ²
5	June 4–6, 2014	2.3×10^{14} (CO ₂)	CO ₂ , Kr

where $\Delta\phi_{\text{HH}}^{(2n)0} \equiv \phi_{\text{HH}}^{(2n+1)0} - \phi_{\text{HH}}^{(2n-1)0}$ is the phase difference between the $(2n + 1)$ th and $(2n - 1)$ th harmonics at the generation point. The atomic phase $\Delta\phi_{\text{atom}}^{(2n)}$ is a constant independent of the high-order harmonics and can be obtained by a calculation (see § 2.3.3). Therefore, we can retrieve the phase difference $\Delta\phi_{\text{HH}}^{(2n)0}$ at the generation point by subtracting the calculated atomic phase $\Delta\phi_{\text{atom}}^{(2n)}$ from the ϕ obtained by the fitting and change its sign.

4.2 Results of the measurement of phase differences

In this section we present the experimental results of phase differences $\Delta\phi_{\text{HH}}^{(2n)0}$ between adjacent harmonic orders. We investigate high-order harmonics generated in Ar, N₂, Kr, and CO₂, whose ionization potentials are summarized in Table 4.1. For N₂ and CO₂, we compare the results for high-order harmonics generated in aligned molecules with those generated in randomly-oriented molecules. We do the measurements in the five periods summarized in Table 4.2. Experiments are performed in series in each measurement. Between the measurements the condition of the laser is reasonably considered to be slightly changed mainly due to the maintenance.

4.2 Results of the measurement of phase differences

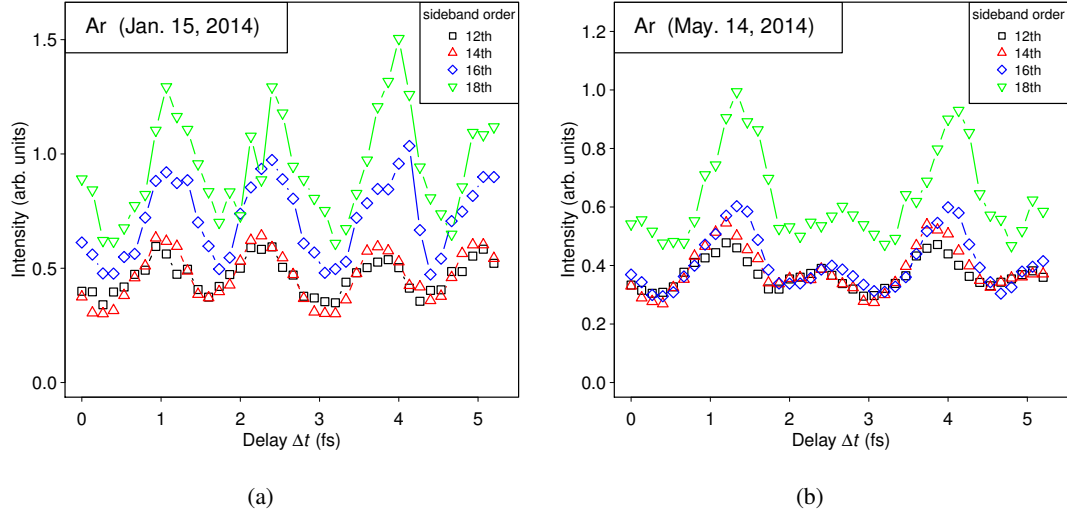


Figure 4.6: (a) Normalized sidebands intensities made by high-order harmonics generated in Ar. These data were taken on January 15, 2014. (b) The same as (a) but taken on May 14, 2014.

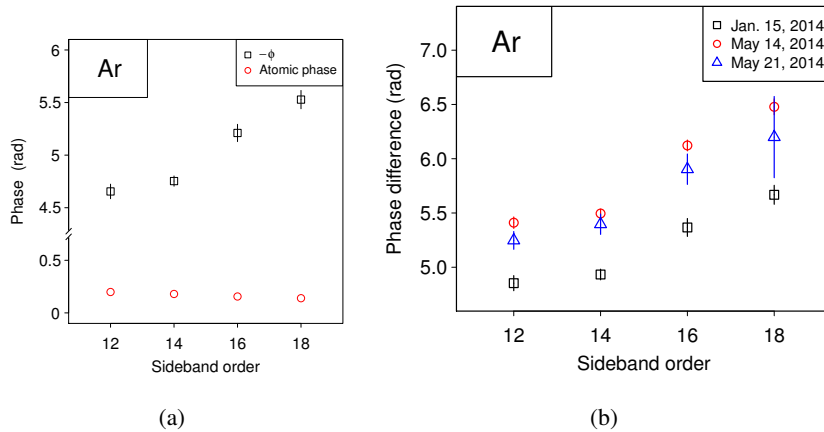


Figure 4.7: (a) The $\phi = -(\Delta\phi_{\text{HH}}^{(2n)0} - \Delta\phi_{\text{atom}}^{(2n)})$ [Eq. (4.12)]. (b) $\Delta\phi_{\text{HH}}^{(2n)0}$ about Ar obtained by fitting the modulation of the sideband intensities. The square, circular, and triangle points show the results obtained by the measurement done on the date shown in the legend. Bars show the errors of the fitting.

4 Results

4.2.1 Ar

First we present the results about high-order harmonics generated in Ar. We perform the measurements for Ar three times. With the grating spectrometer we detect the harmonics up to the 43rd. According to the three-step model [25] introduced in §1.1, the photon energy of the cutoff order $\hbar\omega_{\text{cutoff}}$ becomes

$$\hbar\omega_{\text{cutoff}} \sim 3.17U_{\text{P}} + I_{\text{P}}, \quad (4.13)$$

where U_{P} is the ponderomotive energy [24, §13.5] and I_{P} is the ionization potential of the medium. From this cutoff law we estimate the intensity of the driving pulse as $\sim 2.7 \times 10^{14}$ W/cm².

Figure 4.6(a) shows the intensities of 12th–18th sideband for Ar as a function of the delay Δt of the probe pulse, observed on January 15, 2014. The $2n$ -th sideband intensities are normalized by the square root of the product of the single-photon ionization signals from $(2n - 1)$ th and $(2n + 1)$ th harmonics, as stated in §4.1.2. We fit these normalized intensities by the fitting function (4.8) and obtained fitting parameter ϕ . In Fig. 4.7(a) we plot $-\phi$ together with the atomic phase $\Delta\phi_{\text{atom}}^{(2n)}$ obtained by the calculation (§2.3.3). The phase differences $\Delta\phi_{\text{HH}}^{(2n)0} \equiv \phi_{\text{HH}}^{(2n+1)0} - \phi_{\text{HH}}^{(2n-1)0}$ can be calculated by using Eq. (4.12) as $\Delta\phi_{\text{HH}}^{(2n)0} = -\phi + \Delta\phi_{\text{atom}}^{(2n)}$. Note that the dependence of the atomic phase $\Delta\phi_{\text{atom}}^{(2n)}$ on the sideband order is much slower than that of ϕ and thus has little effect on the sideband-order dependence of $\Delta\phi_{\text{HH}}^{(2n)0}$. The summary of the results is shown in Fig. 4.7(b) by open squares. In this figure we also show the results of other two measurements. The date of the measurement is shown in the legend³. The error bars represent those associated with the least-square fitting.

From the results of Fig. 4.7(b) we can see the following points. First, the phase difference $\Delta\phi_{\text{HH}}^{(2n)0}$ monotonically increase as a function of the sideband order. This is consistent with the experimental results reported by Mairesse *et al.* [32] and Aseyev *et al.* [50] (note that our convention of the sign of the phase difference is the same as that used in Ref. [32] and opposite to that of Ref. [50]). We find another feature that the phase difference $\Delta\phi_{\text{HH}}^{(12)0}$ between 11th and 13th harmonics is almost the same as the difference $\Delta\phi_{\text{HH}}^{(14)0}$ between 13th and 15th harmonics. This feature also appears in the results of Aseyev *et al.* [50], but not clear in those of Mairesse *et al.* [32]. We focus on the difference between $\Delta\phi_{\text{HH}}^{(12)0}$ and $\Delta\phi_{\text{HH}}^{(14)0}$, and find that the degree of the difference varies remarkably depending on the medium in which high-order harmonics are generated, as shown in the following. We discuss the origin of this dependence in the next chapter. The results of the three measurements are similar in shape but the results obtained in May are shifted upward compared to those measured in January. In fact, the sideband modulations observed in May (shown in Figure 4.6(b)) behave differently from those observed in January: the sideband observed in May contains more $\cos(\omega_0 t + \eta)$ component. The reason of these day-by-day difference is also discussed in §5.

¹ By comparison between the cutoff of the high-order harmonics from Kr and those from CO₂ in Measurements #4 and #5, it is likely that the actual intensity is higher than the estimation from the data of Kr. See §4.2.3.

² As stated in §4.2.4, the timing of the pulsed valve for CO₂ was not appropriate in Measurement #4 and thus the results have lower reliability.

³ More precisely, the date in the legend is the one on which the measurement starts. It takes half a day or one day for atoms and two days for molecules to obtain the images which are clear enough to reconstruct the photoelectron distribution by the inverse Abel transform.

4.2.2 N₂

In this subsection, we describe the results of the measurements of high-order harmonics generated in N₂ molecules. The cutoff order of the harmonics is the 43rd, which is the same as that in the case of Ar. Since the ionization potential of N₂ (15.58 eV) is close to that of Ar (15.76 eV) [132], we expect that the intensity of the driving pulse in these measurements is also $\sim 2.7 \times 10^{14}$ W/cm².

To align the molecules we use laser-induced nonadiabatic alignment technique described in §3.5. We first irradiate the sample N₂ molecules with a pump pulse. Figure 4.8 shows the time evolutions of the 13th–19th harmonic intensity from N₂ molecules as a function of the delay time ΔT between the pump and the driving pulses. The intensities in Fig 4.8 are normalized to those generated in randomly-oriented molecules. The driving pulse and the probe pulse are irradiated at $\Delta T = 4.1$ ps, when the molecules are most aligned along the pump pulse polarization around $T_{\text{rot}}/2$ (T_{rot} is the rotational period of the N₂ molecule). The polarization of pump, driving, and probe pulses are parallel to each other. As a reference, we also measure the high-order harmonics generated in randomly-oriented molecules without the pump pulse. Here, when the parameters such as the laser intensity and the gas flow rate fluctuate during the measurement, the resultant change in high-order harmonics can be mistaken as the result of the change of molecular alignment states. To minimize the effect of these fluctuations we measure the high-order harmonics from aligned molecule and those from randomly-oriented molecules alternately, by turning the pump pulse on and off with a mechanical shutter. This technique is also used in Ref. [134]. Unfortunately, because of the lower intensity of the pump pulse, the realized degree of alignment remains very small. To estimate the degree of alignment, we fit the experimental data of the 19th harmonics with the calculated results of the Lewenstein model [26] by changing the degrees of alignment (a red curve in Fig. 4.8). The calculation fits the experimental results well when the intensity and the pulse width of the pump pulse is 0.8×10^{13} W/cm² and 30 fs, respectively, and the rotation temperature of the molecules is 100 K. The obtained degree of alignment is $\langle \cos^2 \theta \rangle \simeq 0.35$, which is nearly the same as that of randomly-oriented molecules, $\langle \cos^2 \theta \rangle \simeq 0.33$. Although we estimate the pump pulse intensity as $\sim 3 \times 10^{13}$ W/cm² at the focus from the energy and the size of the beam waist, the actual intensity at the N₂ gas jet will be weaker because we focus the light before the gas jet to select the short trajectories (§2.1.3), which is consistent with the above estimated intensity. The estimated rotational temperature of 100 K is much higher than the temperature of 50 ~ 60 K expected in §3.2.1. This disagreement may be due to the inaccuracy of the distance between the nozzle exit and the focus of the laser pulse assumed in §3.2.1 and the difference between the translation temperature and the rotational temperature (see Footnote 3 in p. 41), but further discussion is difficult because the calculation model we use here does not have sufficient quantitative accuracy.

In Fig. 4.9 we show the phase differences $\Delta\phi_{\text{HH}}^{(2n)0}$ for aligned and randomly-oriented N₂ molecules by open and filled symbols, respectively. The graph of $\Delta\phi_{\text{HH}}^{(2n)0}$ increases smoothly over the whole observed orders, and $\Delta\phi_{\text{HH}}^{(12)0}$ is significantly lower than $\Delta\phi_{\text{HH}}^{(14)0}$. This is in contrast to the results for Ar. We observed no significant difference between $\Delta\phi_{\text{HH}}^{(12)0}$ of aligned N₂ and that of randomly-oriented N₂. This indicates that the dependence of the phase difference on the molecular direction is

4 Results

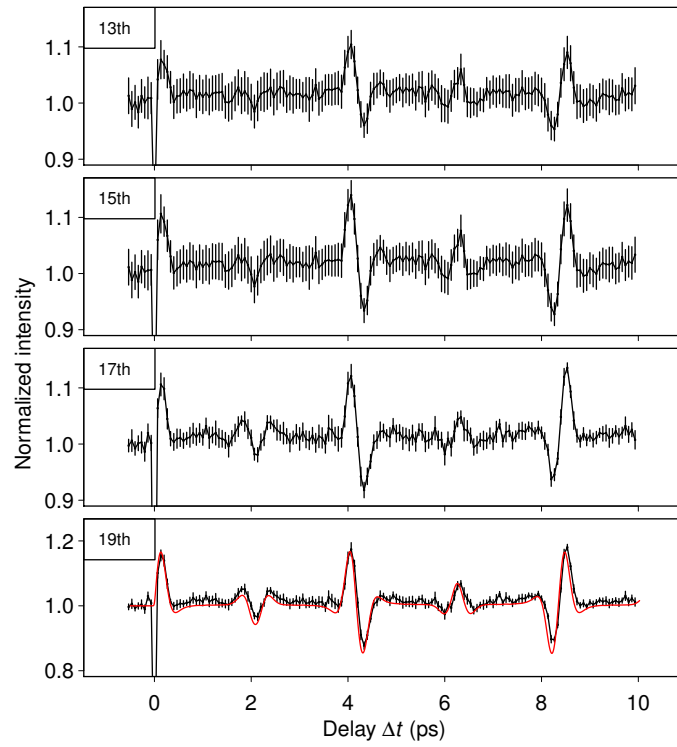


Figure 4.8: Time evolutions of the 13th–19th harmonic intensities from N_2 molecules observed by the grating spectrometer. The intensities are normalized to those generated in randomly-oriented molecules. In the results of the 19th harmonics, we also plot by a red curve the calculated results with the Lewenstein model [26].

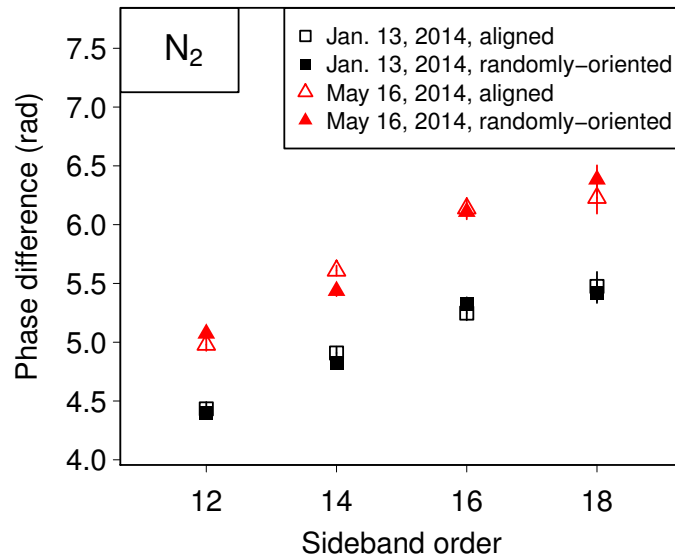


Figure 4.9: The same as Fig. 4.7(b) but for aligned and randomly-oriented N_2 molecules.

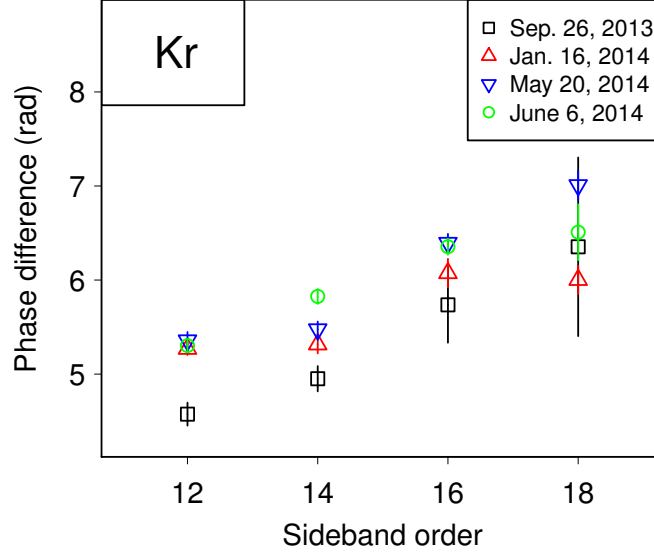


Figure 4.10: The same as Fig. 4.7(b) but for Kr.

not strong for harmonics from N_2 around the observed energy range.

4.2.3 Kr

We measured the $\Delta\phi_{\text{HH}}^{(2n)0}$ four times, when the cutoff orders change as 31st, 37th, 37th, and 33rd depending on the change of the laser intensity. From the cutoff law [Eq. (4.13)] and the ionization potential of the Kr (14.00 eV) [132], the intensity of the driving pulse in each measurement is estimated as $\sim 1.8 \times 10^{14}$ W/cm², $\sim 2.3 \times 10^{14}$ W/cm², $\sim 2.3 \times 10^{14}$ W/cm², and $\sim 1.9 \times 10^{14}$ W/cm², which are rather weak compared to the intensities used in the measurement for Ar and N_2 . However, we find that the cutoff order of the harmonics from Kr is lower than that of CO_2 (§4.2.4), even though the measurements are done in series and the ionization potential is close to each other. It is possible that the cutoff order is changed by the propagation effect [135] and the real intensity might be slightly higher than the above estimations.

Figure 4.10 shows the phase differences $\Delta\phi_{\text{HH}}^{(2n)0}$ for high-order harmonics generated in Kr. The difference between $\Delta\phi_{\text{HH}}^{(12)0}$ and $\Delta\phi_{\text{HH}}^{(14)0}$ is large in the results obtained in September 2013 and in June 2014, but they are almost the same in the results obtained in January 2014 and in May 2014. This phenomenon is discussed again in §5.3.1.

In the experiments for Kr, the fluctuations of the harmonic intensities are larger than those for Ar and N_2 , which results in larger error bars. This fluctuation is considered to be due to larger variations in the density of Kr gas which may come from its relatively large interatomic interaction.

4 Results

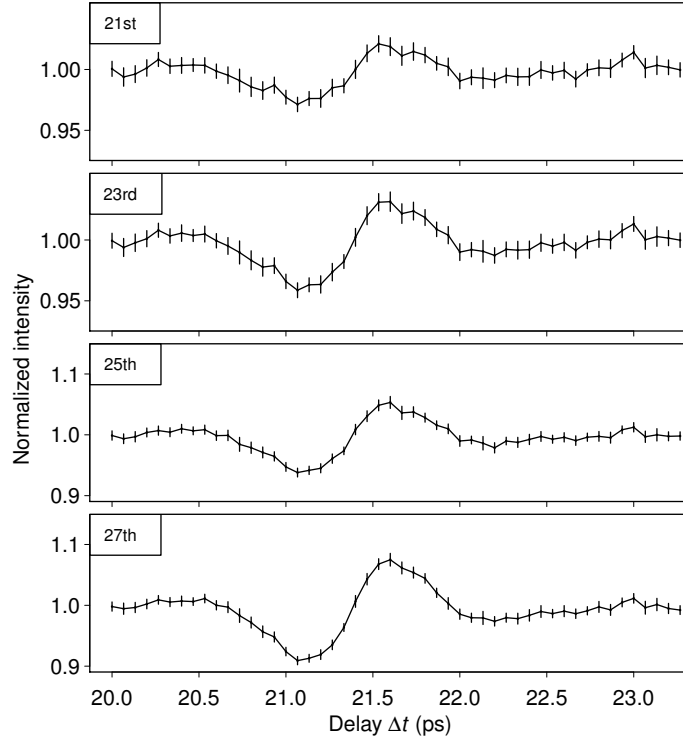


Figure 4.11: Time evolutions of the 21st–27th harmonic intensities from CO₂ molecules observed by the grating spectrometer. The intensities are normalized to those generated in randomly-oriented molecules.

4.2.4 CO₂

We observe high-order harmonics from aligned and randomly-oriented CO₂ molecules in the same way as for N₂ molecules (§4.2.2). Figure 4.11 shows the time evolutions of the 21st–27th harmonic intensities from CO₂ molecules as a function of the delay time ΔT between the pump and the driving pulses. The driving pulse and the probe pulse is irradiated when the molecules are aligned at $\Delta T = T_{\text{rot}}/2 = 21.5$ ps. Note that as reported by Kanai *et al.* in Ref. [41] high-order harmonics generated in CO₂ are suppressed when the molecules are aligned parallel to the polarization of the driving field. When the pump pulse intensity and the rotational temperature is assumed as 0.8×10^{13} W/cm² and 100 K, respectively, the degree of alignment is estimated as $\langle \cos^2 \theta \rangle \simeq 0.35$. The cutoff order is the 41st in the first measurement on May 22, 2014 and the 37th in the second measurement on June 4, 2014. The corresponding laser intensity is calculated with Eq. (4.13) as $\sim 2.6 \times 10^{14}$ W/cm² and $\sim 2.3 \times 10^{14}$ W/cm², respectively. It must be noted that in the measurement in May, the author by mistake set the timing of the pulsed valve for CO₂ shifted from the appropriate value and the density of the gas may be lower than the other experiments.

In Fig. 4.12 we show the phase differences $\Delta\phi_{\text{HH}}^{(2n)^0}$ for aligned and randomly-oriented CO₂ molecules by open and filled symbols, respectively. The results of the measurement in May are ~ 1 rad apart from those measured in June. This may be related to the lower density of the gas in the former ex-

4.2 Results of the measurement of phase differences

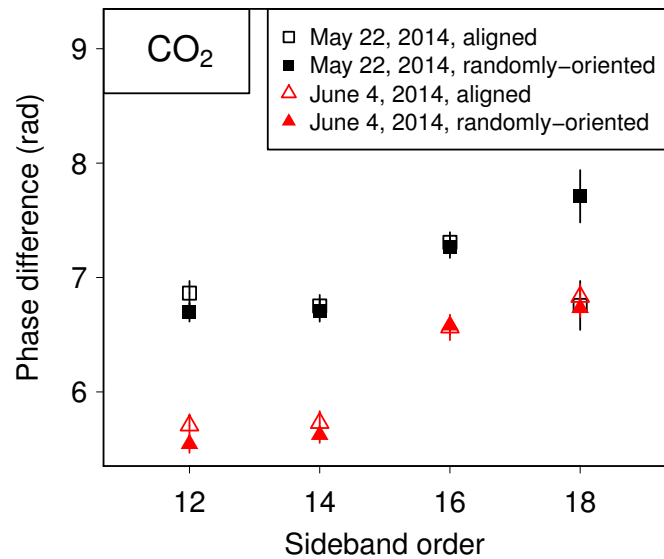


Figure 4.12: The same as Fig. 4.7(b) but for aligned and randomly-oriented CO₂.

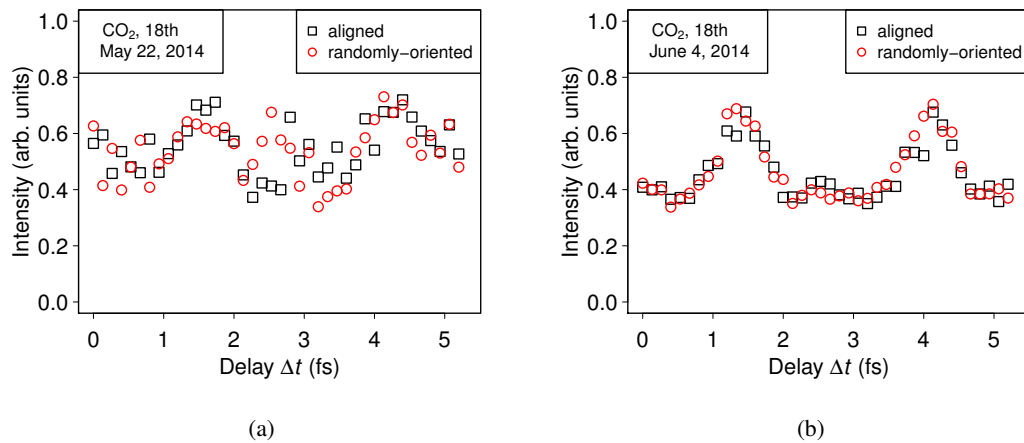


Figure 4.13: (a) Normalized 18th sidebands intensities made by high-order harmonics generated in aligned CO₂ (square points) and randomly-oriented CO₂ (circular points) obtained in May 22, 2014. (b) The same as in (a) but in June 4, 2014.

4 Results

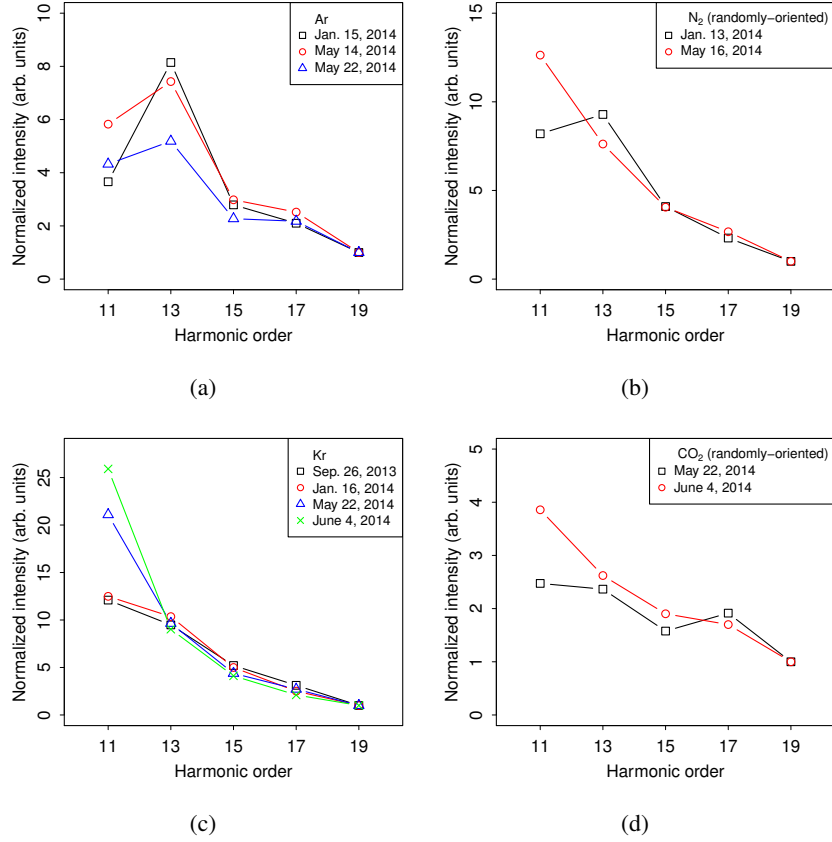


Figure 4.14: Intensities of the high-order harmonics generated in (a) Ar, (b) N₂, (c) Kr, and (d) CO₂, estimated from the signal of one-photon ionization of Ar. They are normalized to the intensity of the 19th harmonics.

periment and we discuss the difference in the next chapter. We also find that the phase difference $\Delta\phi_{\text{HH}}^{(12)0}$ is almost the same as $\Delta\phi_{\text{HH}}^{(14)0}$, which is similar to our results about Ar. The results about the aligned CO₂ and those of randomly-oriented CO₂ is similar, except the large difference of $\Delta\phi_{\text{HH}}^{(18)0}$ in the results obtained in May 22. In Fig. 4.13 we show the modulation of the normalized 18th sideband intensities on May 22 (left) and on June 4 (right). The sideband of the aligned CO₂ and that of randomly-oriented CO₂ behave differently around $\Delta t \sim 2.5$ fs in Fig. 4.13(a). This might be the effect of the phase jump observed by Boutu *et al.* [51], but since the sideband modulation is not so clear (probably due to the large fluctuation in the density of molecules supplied in the wrong timing) this result is not sufficient to conclude.

4.2.5 Intensity of the harmonics

Figures 4.14(a)–4.14(d) show the intensities of the high-order harmonics generated in Ar, N₂, Kr, and CO₂, respectively. Since our grating spectrometer (§3.1.4) cannot observe the 11th harmonic, the intensities shown in Figs. 4.14(a)–4.14(d) are obtained by calibrating the signal of one-photon ionization of Ar taking account of both the photoionization cross-sections given in Ref. [136] and

4.2 Results of the measurement of phase differences

the reflectivity of two Au-coated mirrors calculated in §3.1.3.1. The results are normalized to the intensity of the 19th harmonics. For N₂ and CO₂, the harmonic intensity spectra generated in aligned molecules are almost the same as those generated in randomly-oriented molecules probably due to the low degrees-of-alignment, and here we only show the spectra for randomly-oriented molecules.

It is not clear whether there exists any phenomenon which can be associated with the observed differences in $\Delta\phi_{\text{HH}}^{(2n)0}$. One can see that the shapes of the spectra are dependent on the nonlinear medium, and that the intensities of the 11th harmonic depend on the date of the measurement, but those at the higher harmonic orders are rather robust. This means that the intensity of the high-order harmonics at the near-threshold region is more sensitive to the change of experimental conditions than the higher-order harmonics. We consider that the change of the intensity is mainly caused by the change in the density of the gas, which can greatly affect the phase-matching condition. Later in §5.2.1 we discuss the effect of the change of the medium density on the observed phase differences.

Chapter 5

Discussions

In this chapter, we discuss the results shown in the previous chapter. In §5.1, we compare the experimental results with the results of the model calculation introduced in §2.1. As shown by Mairesse *et al.* [32] this model successfully explains the monotonic increase of $\Delta\phi_{\text{HH}}^{(2n)0}$ as a function of the sideband order. The reason for the shift of the overall results depending on the date of the measurement, shown in Fig. 4.7(b), is discussed in §5.2. In §5.3, we focus on the relation of the phase difference $\Delta\phi_{\text{HH}}^{(12)0}$ between the 11th and 13th harmonics to the phase difference $\Delta\phi_{\text{HH}}^{(14)0}$ between the 13th and 15th harmonics. As presented in §4.2, the observed $\Delta\phi_{\text{HH}}^{(14)0} - \Delta\phi_{\text{HH}}^{(12)0}$ largely depends on the medium. We find that the observed value of $\Delta\phi_{\text{HH}}^{(14)0} - \Delta\phi_{\text{HH}}^{(12)0}$ for Ar and CO₂ is much smaller than that estimated from the model calculation given in §5.1. The energy region of 12th–14th sideband is near the ionization threshold of the medium. As stated in §1.3, the strong-field approximation is not appropriate in this energy region. We discuss in §5.3 the Coulomb potential effect on the three steps of the high-order harmonic generation, that is, the ionization, propagation, and recombination.

5.1 Comparison with the results of model calculation

As shown in §2.2.2, the phase difference $\Delta\phi_{\text{HH}}^{(2n)0}$ at the generation point is related to the recombination time t_r of the returning electron as $\Delta\phi_{\text{HH}}^{(2n)0} \simeq 2\omega_0 t_r$ [Eq. (2.49)] when the dependence of the transition dipole on the frequency is smooth enough¹. The recombination time t_r based on the model introduced in §2.1 can be obtained by solving Eqs. (2.29) and (2.30). Figure 5.1(a) shows the recombination time $t_r = t_{\text{st}}^{(-)}$ obtained by solving these equations for the ionization potentials $I_p = 15.76$ eV, 15.58 eV, 14.00 eV, and 13.78 eV, which correspond to Ar, N₂, Kr and CO₂, respectively [132]². We obtain the phase difference $\Delta\phi_{\text{HH}}^{(2n)0}$ from the recombination time t_r with the relation $\Delta\phi_{\text{HH}}^{(2n)0} = 2\omega_0 t_r$, and the results are shown in Fig. 5.1(b). Note that the ionization potential I_p is the only parameter about

¹ In §2.2.2 we only consider the electric field at the generation point and the superscript 0 on $\Delta\phi_{\text{HH}}^{(2n)}$ is not used. However, it is important in the following discussions to distinguish $\Delta\phi_{\text{HH}}^{(2n)0}$ from the phase difference at the detection point, and we do not omit the superscript 0 in this chapter.

²To be precise, we plot the real part of the solution $t_{\text{st}}^{(-)}$ though $t_{\text{st}}^{(-)}$ is a complex value in general. The imaginary part comes from the tunneling ionization process [27].

5.1 Comparison with the results of model calculation

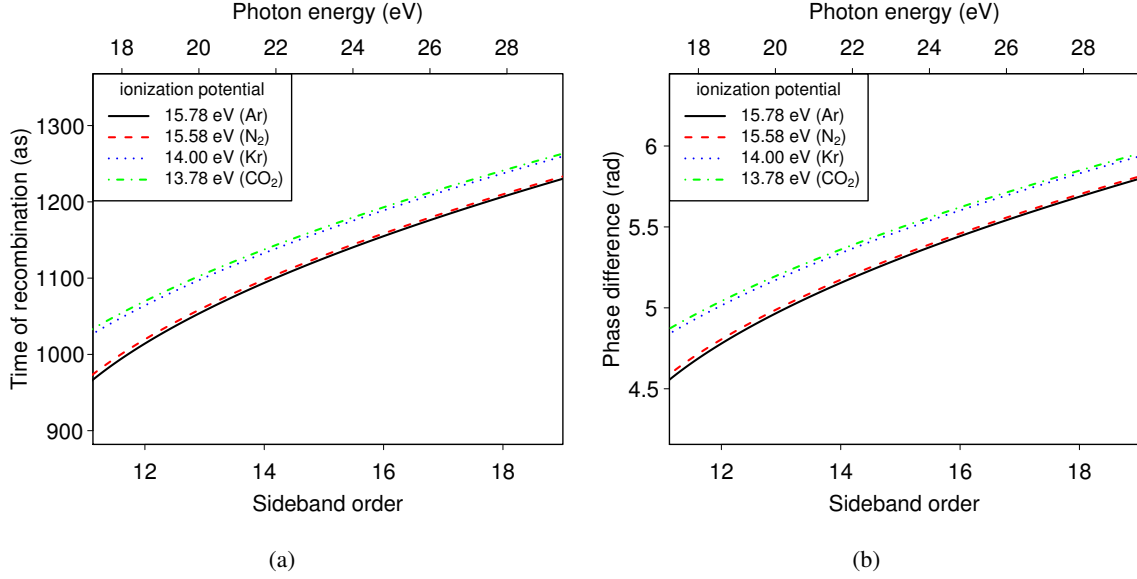


Figure 5.1: (a) The recombination time obtained by solving Eqs. (2.29) and (2.30) in §2.1, with the laser intensity $2.7 \times 10^{14} \text{ W/cm}^2$. (b) The same as Fig. 5.1(a) but the vertical axis is $\Delta\phi_{\text{HH}}^{(2n)0}$, which is related to the recombination time t_r of the returning electron as $\Delta\phi_{\text{HH}}^{(2n)0} \simeq 2\omega_0 t_r$ [Eq. (2.49)].

the medium appearing in Eqs. (2.29) and (2.30). In the experiments we select the short trajectories by focusing the driving pulse before the gas jet (§3.1.2), so the short trajectories are selected in the calculation of Figs. 5.1(a) and 5.1(b). This calculated results show monotonic increase of $\Delta\phi_{\text{HH}}^{(2n)0}$ as a function of the sideband order, which reproduce the tendency of the experimental results. The results so far are consistent with the work by Mairesse *et al.* [32]. However, we find that the model calculation cannot explain the change of the experimental results obtained in different dates. For example, We plot in Fig. 5.2 the experimental results of Ar shown in Fig. 4.7(b) together with the results of model calculation with three laser intensities. The data obtained in January are well fit by the calculated results with the laser intensity $2.7 \times 10^{14} \text{ W/cm}^2$, which is consistent with the estimation from the cutoff order. However, to obtain similar results as the experimental data obtained in May, we have to set the laser intensity in the calculation at $1.5 \times 10^{14} \text{ W/cm}^2$, under which the cutoff order expected from the cutoff law [Eq. (4.13)] is the 29th, which is too low compared to the experimental results. Therefore, we consider that the results of $\Delta\phi_{\text{HH}}^{(2n)0}$ obtained in May is shifted from that obtained in January by other reasons than the change of the laser intensities, which we discuss in the next section. Moreover, the model calculation cannot reproduce the feature that $\Delta\Phi^{(14-12)} \equiv \Delta\phi_{\text{HH}}^{(14)0} - \Delta\phi_{\text{HH}}^{(12)0}$ is near zero for the experimental results of Ar. This is in contrast to the case of N₂, for which the sideband order dependence of $\Delta\phi_{\text{HH}}^{(2n)0}$ obtained by the calculation shows a similar curve as those of the experimental results (Fig. 5.3).

5 Discussions

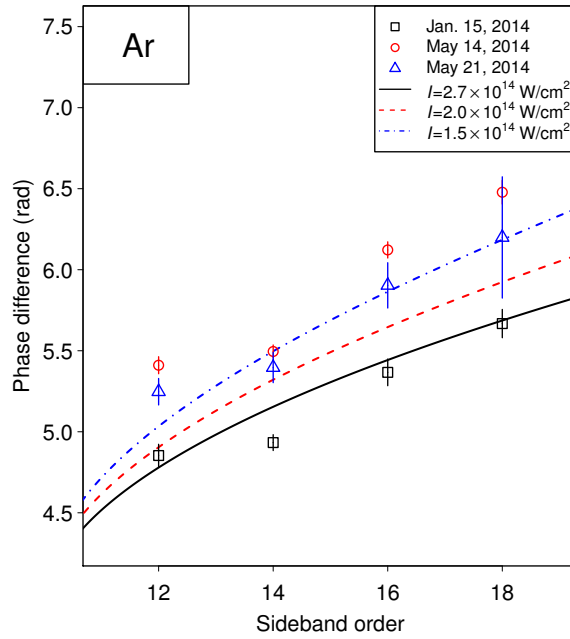


Figure 5.2: The experimental results for Ar shown in Fig. 4.7(b) together with the results of model calculation with the laser intensities of $2.7 \times 10^{14} \text{ W/cm}^2$ (solid curve), $2.0 \times 10^{14} \text{ W/cm}^2$ (dashed curve), and $1.5 \times 10^{14} \text{ W/cm}^2$ (dot-dashed curve).

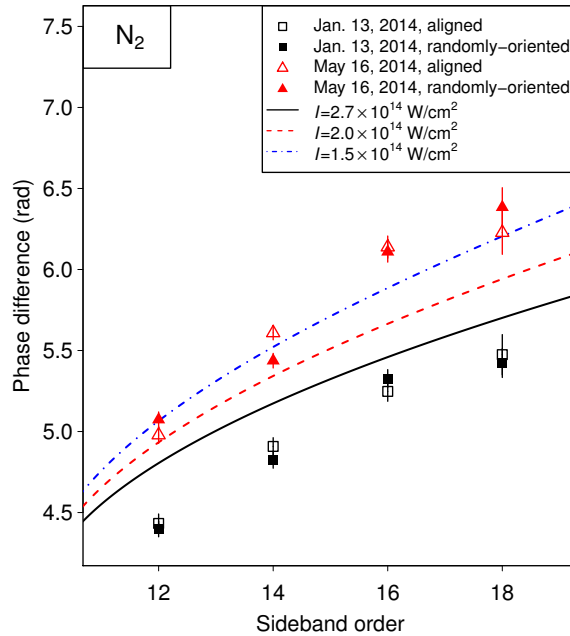


Figure 5.3: The experimental results for N_2 shown in Fig. 4.9 together with the results of model calculation with the laser intensities of $2.7 \times 10^{14} \text{ W/cm}^2$ (solid curve), $2.0 \times 10^{14} \text{ W/cm}^2$ (dashed curve), and $1.5 \times 10^{14} \text{ W/cm}^2$ (dot-dashed curve).

5.2 Two possible reasons for the day-by-day difference

First we consider the effect which can shift the overall phase differences $\Delta\phi_{\text{HH}}^{(2n)}$'s. In §4.1.2, we use the relation $\phi_{\text{probe}} = \omega_0\Delta t + \frac{\omega_0}{c}z$ [Eq. (4.5)] and $\phi_{\text{HH}}^{(2n\pm 1)} = \phi_{\text{HH}}^{(2n\pm 1)0} + \frac{(2n-1)\omega_0}{c}z$ [Eqs. (4.10) and (4.11)] between the phase $\phi_{\text{HH}}^{(2n\pm 1)0}$ of the $(2n \pm 1)$ th harmonics at the generation point and the phase $\phi_{\text{HH}}^{(2n\pm 1)}$ at the detection point which is the distance z away from the generation point (Fig. 4.4). The above discussion, however, neglect the dispersion of the medium gases for high-order harmonic generation and the slight optical path difference between the probe pulse and high-order harmonics. In the following we discuss their effects on the observed phase differences.

5.2.1 Effect of the dispersion of the gas

The importance of the medium dispersion is pointed out by Dinu *et al.* [49]. To take the dispersion into account, we consider a simple model in which Eqs. (4.5), (4.10), and (4.11) are replaced by

$$\phi_{\text{probe}} = \omega_0\Delta t + \frac{\omega_0}{c}z + n(\omega_0)\frac{\omega_0}{c}\Delta z, \quad (5.1)$$

$$\phi_{\text{HH}}^{(2n\pm 1)} = \phi_{\text{HH}}^{(2n\pm 1)0} + \frac{(2n \pm 1)\omega_0}{c}z + n((2n \pm 1)\omega_0)\frac{(2n \pm 1)\omega_0}{c}\Delta z, \quad (5.2)$$

where $n(\omega)$ is the refractive index at the angular frequency ω ,³ and Δz is the characteristic length of the medium. Then, the relation between the $\Delta\phi_{\text{HH}}^{(2n)0}$ and the fitting result ϕ [Eq. (4.12)] is changed into

$$\begin{aligned} \phi &\simeq +\phi_{\text{HH}}^{(2n-1)0} - \phi_{\text{HH}}^{(2n+1)0} + \Delta\phi_{\text{atom}}^{(2n)} \\ &\quad + 2n(\omega_0)\frac{\omega_0}{c}\Delta z + n((2n-1)\omega_0)\frac{(2n-1)\omega_0}{c}\Delta z - n((2n+1)\omega_0)\frac{(2n+1)\omega_0}{c}\Delta z \\ &= +\phi_{\text{HH}}^{(2n-1)0} - \phi_{\text{HH}}^{(2n+1)0} + \Delta\phi_{\text{atom}}^{(2n)} \\ &\quad - [(2n+1)n((2n+1)\omega_0) - 2n(\omega_0) - (2n-1)n((2n-1)\omega_0)]\frac{\omega_0\Delta z}{c}. \end{aligned} \quad (5.3)$$

To estimate the degree of the effect of dispersion on the phase differences, let us assume that the gas produces one free electron per atom, as in Ref. [49]. Then, the dielectric constant $\epsilon(\omega)/\epsilon_0$ becomes [137, §7.5]

$$\epsilon(\omega)/\epsilon_0 = 1 - \frac{\omega_{\text{P}}^2}{\omega^2}, \quad (5.4)$$

where ω_{P} is the plasma frequency defined by

$$\omega_{\text{P}}^2 = \frac{Ne^2}{\epsilon_0 m}. \quad (5.5)$$

The refractive index becomes

$$n(\omega) \simeq \sqrt{\epsilon(\omega)/\epsilon_0} = \sqrt{1 - \frac{\omega_{\text{P}}^2}{\omega^2}} \simeq 1 - \frac{1}{2} \frac{\omega_{\text{P}}^2}{\omega^2} = 1 - NA \frac{1}{\omega^2}, \quad (5.6)$$

³ To avoid confusion with the n for harmonic orders, we write n for the refractive index in roman type.

5 Discussions

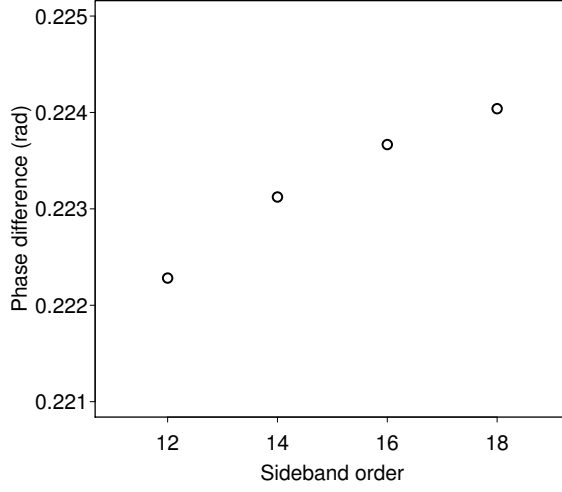


Figure 5.4: The correction term $N \frac{(2n)^2 - 3}{(2n)^2 - 1} \frac{A}{c\omega_0} \Delta z$ in Eq. (5.8) with $N = 1 \times 10^{18} \text{ cm}^{-3}$ and $\Delta z = 0.1 \text{ mm}$.

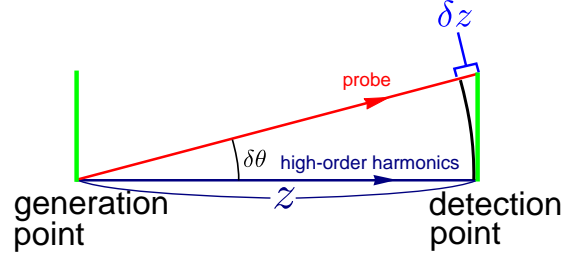


Figure 5.5: When the probe beam is inclined to the beam of the high-order harmonics, the optical path length becomes different between them.

where $A = e^2/2\epsilon_0 m$ is a constant. Then,

$$\begin{aligned}
 \phi &\simeq +\phi_{\text{HH}}^{(2n-1)0} - \phi_{\text{HH}}^{(2n+1)0} + \Delta\phi_{\text{atom}}^{(2n)} \\
 &\quad - 2NA \frac{1}{c\omega_0} \Delta z - NA \frac{1}{(2n-1)c\omega_0} \Delta z + NA \frac{1}{(2n+1)c\omega_0} \Delta z, \\
 &= -(\Delta\phi_{\text{HH}}^{(2n)0} - \Delta\phi_{\text{atom}}^{(2n)}) - N \frac{(2n)^2 - 3}{(2n)^2 - 1} \frac{A}{c\omega_0} \Delta z.
 \end{aligned} \tag{5.7}$$

Therefore,

$$\Delta\phi_{\text{HH}}^{(2n)0} \simeq -\phi + \Delta\phi_{\text{atom}}^{(2n)} - N \frac{(2n)^2 - 3}{(2n)^2 - 1} \frac{A}{c\omega_0} \Delta z. \tag{5.8}$$

This shows that the $\Delta\phi_{\text{HH}}^{(2n)0}$ has a correction term which linearly depends on the plasma density N and harmonic order $2n$. Figure 5.4 shows the correction term $N \frac{(2n)^2 - 3}{(2n)^2 - 1} \frac{A}{c\omega_0} \Delta z$ in Eq. (5.8). Based on the experimental condition shown in §3.2.1, we choose the parameters as $N = 1 \times 10^{18} \text{ cm}^{-3}$ and $\Delta z = 0.1 \text{ mm}$. The resulting correction is $\sim 0.2 \text{ rad}$, which is at the same order as the real difference $\sim 0.5 \text{ rad}$ appearing in Fig. 5.2. Although the correction brought by the dispersion effect is monotonically increased as a function of the sideband order, the change in the phase difference is very small ($< 2 \times 10^{-3} \text{ rad}$) over the observed sideband order. This is consistent with the fact that the results of the measurements obtained in different dates are similar in shape except for the overall shift. When the density of the gaseous medium changes the plasma density N also varies. As shown in Fig. 3.13, the density of the medium strongly depends on the distance from the nozzle exit. It is plausible that due to the small displacement of the focusing position of the driving pulse, the distance between the focus and the nozzle exit is different between the experiments done in January and those in May. The

5.2 Two possible reasons for the day-by-day difference

density of the medium will also change the degree of the coupling between the probe pulse and the driving pulse, which make the probe intensity change as a function of Δt (§4.1.2). This hypothesis gives an explanation for the observation that the modulation of the normalized sideband intensity behaves differently between the results in January [Fig. 4.6(a)] and those in May [Fig. 4.6(b)].

5.2.2 Effect of the misalignment

Another plausible cause for the day-by-day difference is the optical path difference between the probe pulse and high-order harmonics due to the slight change of the alignment. When the optical path length from the generation point to the detection point is z for the high-order harmonics, and that for the probe pulse is larger than z by δz [Fig. 5.5], Eq. (4.5) is replaced by

$$\phi_{\text{probe}} = \omega_0 \Delta t + \frac{\omega_0}{c} (z + \delta z). \quad (5.9)$$

In this case, the relation between the $\Delta\phi_{\text{HH}}^{(2n)0}$ and the fitting result ϕ [Eq. (4.12)] is changed into

$$\phi \simeq +\phi_{\text{HH}}^{(2n-1)0} - \phi_{\text{HH}}^{(2n+1)0} + \Delta\phi_{\text{atom}}^{(2n)} + 2\frac{\omega_0}{c}\delta z. \quad (5.10)$$

When the difference δz results from the misalignment of the probe beam from the high-order harmonics by the angle $\delta\theta$, $\delta z = \frac{z}{\cos\delta\theta} - z \simeq z\left(1 + \frac{(\delta\theta)^2}{2}\right) - z = z\frac{(\delta\theta)^2}{2}$ [Fig. 5.5], and the correction term becomes $2\frac{\omega_0}{c}\delta z = \frac{\omega_0}{c}z(\delta\theta)^2$. The distance z from the generation point to the detection point is ~ 0.9 m in our setup. Then the correction term $\frac{\omega_0}{c}z(\delta\theta)^2$ becomes 0.5 rad when the angle $\delta\theta$ is only $\sim 3 \times 10^{-4}$ rad. Therefore, even the slight change in the direction of the probe pulse due to the maintenance of the laser system can make a significant shift in the phase difference. Since the magnitude of the correction $\frac{\omega_0}{c}z(\delta\theta)^2$ does not depend on the harmonic order, the misalignment of the probe pulse simply leads to the overall shift in the phase differences.

5.2.3 Comparison among the measurements performed in series

Based on the above discussion, the absolute value of $\Delta\phi_{\text{HH}}^{(2n)0}$ can be compared among the measurements performed in series, because both the distance between the nozzle and the laser pulses and the optical path difference between the high-order harmonics and the probe pulse are considered to remain unchanged. In fact, when we plot in Fig. 5.6 the data measured in series in January their position relation is similar to that predicted by the model calculation shown in Fig. 5.1(b). For convenience we also plot the calculated result of Fig. 5.1(b) in Fig. 5.6. As stated in §4.2.3, the error in the results for Kr is larger than those for Ar and N₂ probably due to larger fluctuations in the density of Kr gas. Note that the error bars shown here indicate the error of the fitting, and the statistical fluctuations may be larger than them.

The phase differences of the harmonics generated in Kr are larger at all orders than those of Ar and N₂ both in the experimental data and the results obtained by the model calculation with the strong-field approximation. We assume that this difference can be attributed to the difference in the ionization potential I_P [52]: I_P of Ar and N₂ are close (15.76 eV and 15.58 eV, respectively), and

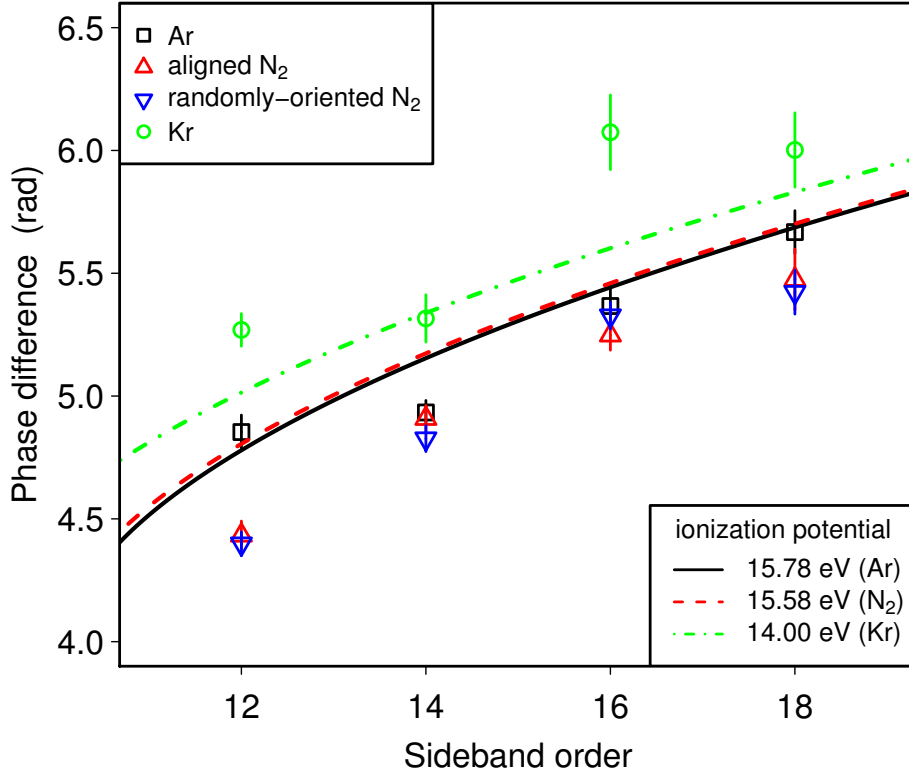


Figure 5.6: Points with bars: summary of the experimental results obtained in January, 2014. The results for Kr have larger errors possibly caused by the large fluctuation in the density of Kr gas and have limited reliability compared to those for Ar and N₂. Curves: the phase differences corresponding to the recombination times obtained by the model calculation with the strong-field approximation.

considerably higher than that of Kr (14.00 eV) [132]. In the Lewenstein model, the phase of the high-order harmonics is a linear function of the ionization potential I_p [Eq. (2.34)] and thus I_p affects the phase of the generated harmonics. This phenomenon was first pointed out in the experiment by Kanai *et al.* [52], in which the phase difference between He and Ne is observed by the mixed gas method. Our results obtained by the RABBIT method reinforce the validity of their interpretation. The results of N₂ and Ar is similar except for large difference in $\Delta\phi_{\text{HH}}^{(12)0}$. We discuss the origin of the difference in $\Delta\phi_{\text{HH}}^{(12)0}$ in the next section.

Figure 5.7 shows the results of another series of measurement conducted in June. We compare the results of Kr with those of CO₂, whose ionization potential (13.78 eV) is close to that of Kr (14.00 eV). The results are again similar except $\Delta\phi_{\text{HH}}^{(12)0}$. Note that in Fig. 4.12 the results for CO₂ obtained in May are largely displaced upward from the results obtained in June. This is consistent with the effect of dispersion given in Eq. (5.7), because as mentioned in §4.2.4 the density of the CO₂ in May might be rather different from other experiments due to the inappropriate timing of the pulsed valve.

5.3 The anomaly of the phase differences at the near-threshold region

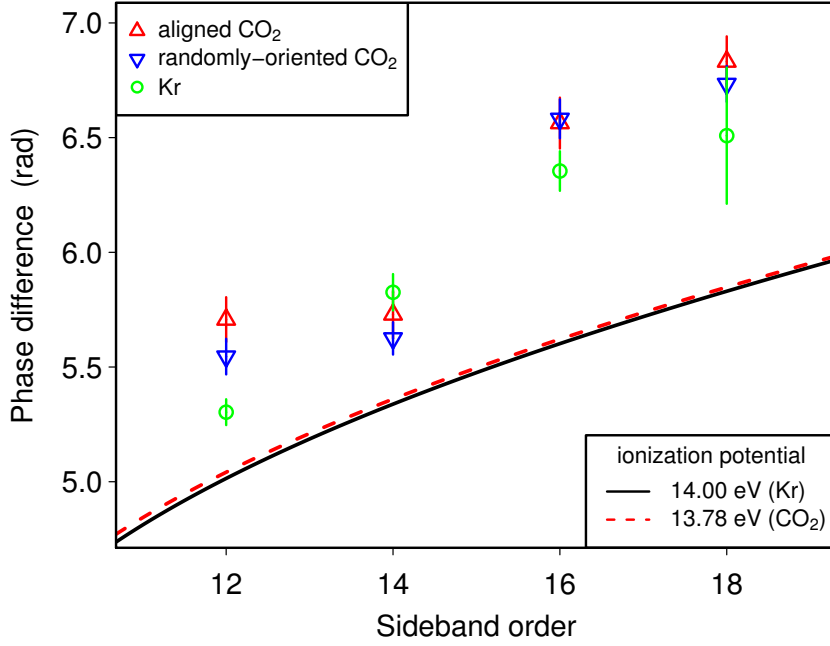


Figure 5.7: Points with bar: summary of the experimental results obtained in June, 2014. Curves: the phase differences corresponding to the recombination time obtained by the model calculation with the strong-field approximation.

5.3 The anomaly of the phase differences at the near-threshold region

5.3.1 Summary of the differences between $\Delta\phi_{\text{HH}}^{(12)0}$ and $\Delta\phi_{\text{HH}}^{(14)0}$

From the experimental results shown in §4.2, we find that the difference between $\Delta\phi_{\text{HH}}^{(12)0}$ and $\Delta\phi_{\text{HH}}^{(14)0}$ shows an interesting behavior: in the results for Ar and CO₂ $\Delta\phi_{\text{HH}}^{(12)0}$ is close to $\Delta\phi_{\text{HH}}^{(14)0}$, whereas $\Delta\phi_{\text{HH}}^{(12)0}$ is remarkably lower than $\Delta\phi_{\text{HH}}^{(14)0}$ in the results for N₂. For Kr the difference between $\Delta\phi_{\text{HH}}^{(12)0}$ and $\Delta\phi_{\text{HH}}^{(14)0}$ depends on the date of the measurement. For quantitative discussions, in Fig. 5.8 we summarize the differences $\Delta\Phi^{(14-12)} \equiv \Delta\phi_{\text{HH}}^{(14)0} - \Delta\phi_{\text{HH}}^{(12)0}$ for the media we investigated (“r.o.” in Fig. 5.8 stands for “randomly-oriented”). The error bars are calculated as the square root of the sum of the fitting error squared for $\Delta\phi_{\text{HH}}^{(12)0}$ and $\Delta\phi_{\text{HH}}^{(14)0}$. The difference is almost zero for Ar and CO₂ within the error bars. On the other hand, for N₂ the value of $\Delta\Phi^{(14-12)}$ is 0.4 ~ 0.6 rad. In the case of Kr, the value of $\Delta\Phi^{(14-12)}$ depends on the day of the measurements. To study the property of $\Delta\Phi^{(14-12)}$ of Kr, we plot in Fig. 5.9 the values of $\Delta\Phi^{(14-12)}$ as a function of the cutoff order. We find that $\Delta\Phi^{(14-12)}$'s of Kr are near zero when the cutoff is the 37th, but are above zero when the cutoff is the 31st or the 33rd. Since the cutoff order increases with the intensity of the driving pulse, the results of Fig. 5.9 suggest that $\Delta\Phi^{(14-12)}$ is dependent on the laser intensity.

Next, we compare the experimental results with the results of the model calculation with the strong-field approximation. Figure 5.10(a) shows the calculated phase differences of the high-order

5 Discussions

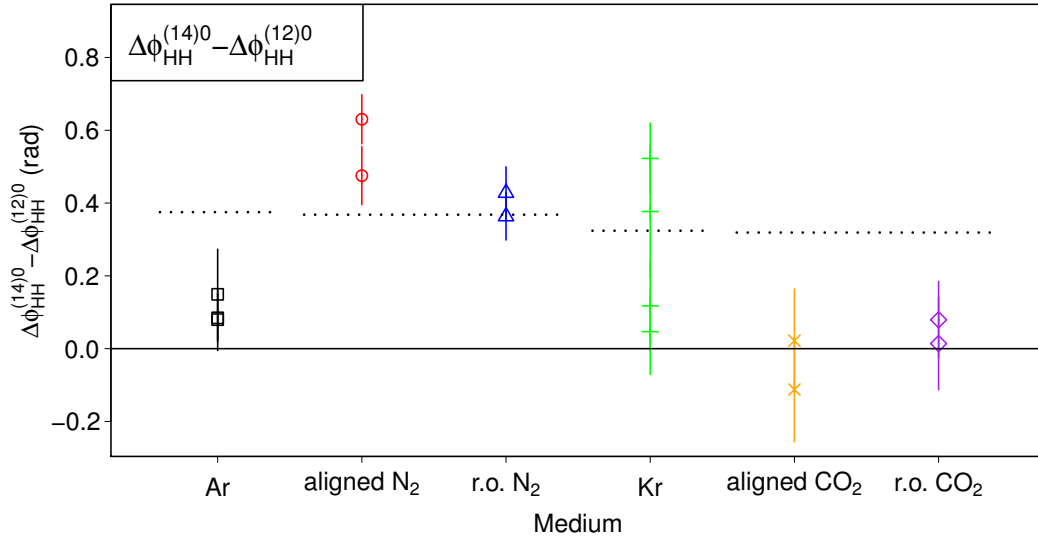


Figure 5.8: Summary of $\Delta\Phi^{(14-12)} \equiv \Delta\phi_{\text{HH}}^{(14)0} - \Delta\phi_{\text{HH}}^{(12)0}$. “r.o.” stands for “randomly-oriented”. The error bars are calculated as the square root of the sum of the fitting error squared of $\Delta\phi_{\text{HH}}^{(12)0}$ and $\Delta\phi_{\text{HH}}^{(14)0}$. Horizontal dotted lines show the values of $\Delta\Phi^{(14-12)}$ expected from the model calculation with the laser intensity of 2.7×10^{14} W/cm² shown in Fig. 5.1(b).

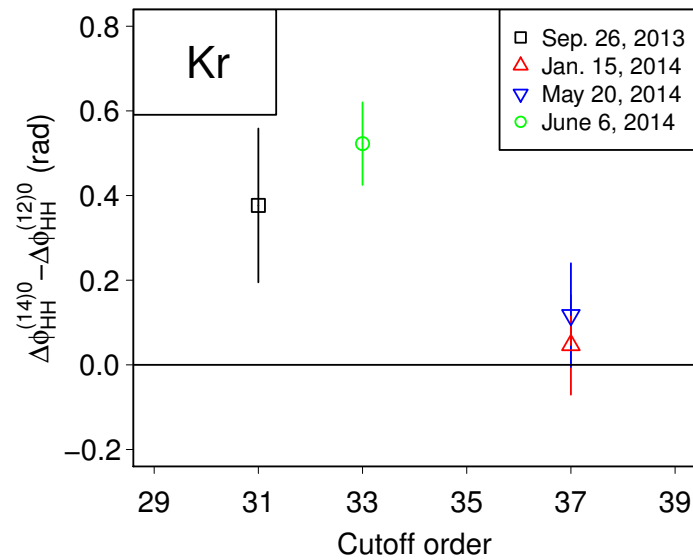


Figure 5.9: $\Delta\Phi^{(14-12)}$ of Kr as a function of the cutoff order.

5.3 The anomaly of the phase differences at the near-threshold region

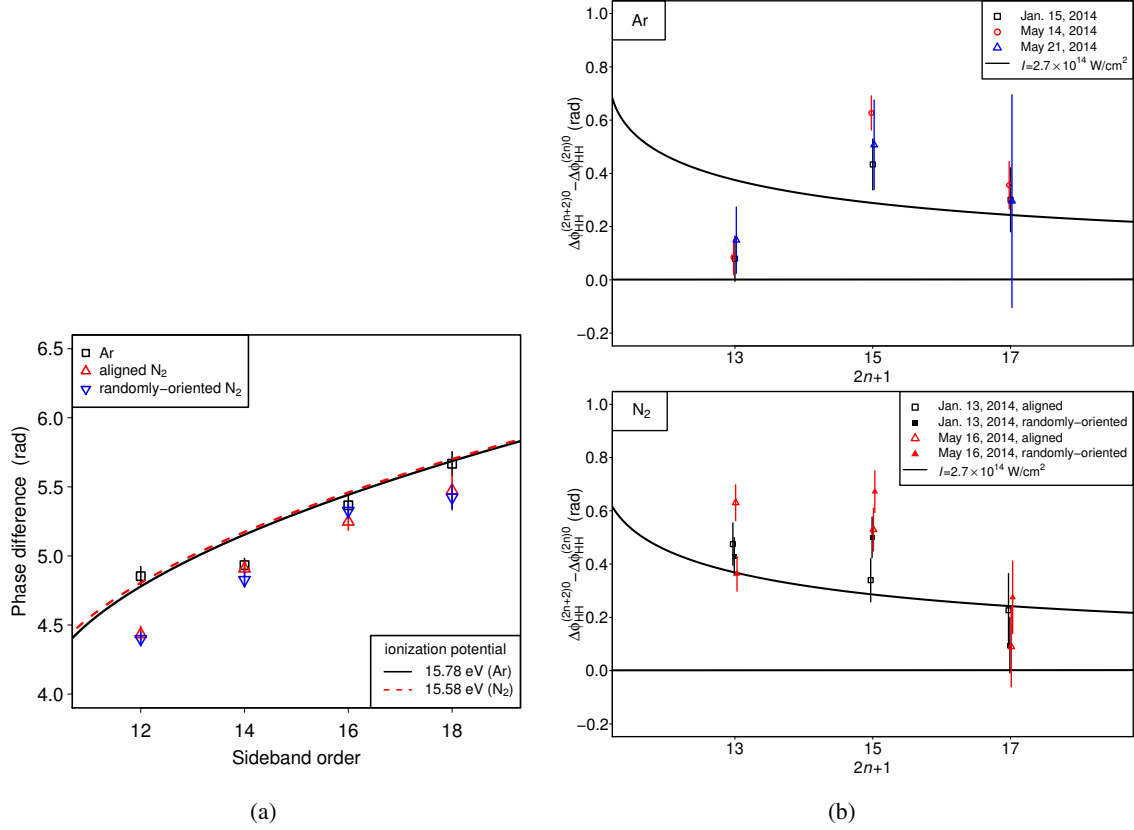


Figure 5.10: (a) Comparison between the results of the model calculation (curves) and experimental results (points with error bars). (b) $\Delta\phi_{\text{HH}}^{(2n+2)0} - \Delta\phi_{\text{HH}}^{(2n)0}$ for Ar (top) and N₂ (bottom) calculated from the model calculation (curves) and the experimental results (points with error bars). The error bars are calculated as the square root of the sum of the fitting error squared for $\Delta\phi_{\text{HH}}^{(2n+2)0}$ and $\Delta\phi_{\text{HH}}^{(2n)0}$.

harmonics generated in Ar and N₂ obtained from the model calculation in §5.1, together with the experimental results observed in January, 2014. The calculated results are monotonically increasing over the entire energy range shown in this figure, and does not reproduce the small $\Delta\Phi^{(14-12)} \equiv \Delta\phi_{\text{HH}}^{(14)0} - \Delta\phi_{\text{HH}}^{(12)0}$ in the result for Ar. In Fig. 5.10(b) we show $\Delta\phi_{\text{HH}}^{(2n+2)0} - \Delta\phi_{\text{HH}}^{(2n)0}$ for Ar (top) and N₂ (bottom) calculated from the model calculation (curves) and the experimental results (points with error bars). In both panels of Fig. 5.10(b) we also plot the results obtained from the experimental data in May, 2014 as well as those in January, 2014 and the error bars are calculated as the square root of the sum of the fitting error squared for $\Delta\phi_{\text{HH}}^{(2n+2)0}$ and $\Delta\phi_{\text{HH}}^{(2n)0}$. The $\Delta\phi_{\text{HH}}^{(2n+2)0} - \Delta\phi_{\text{HH}}^{(2n)0}$ obtained from the model calculation becomes larger when the order $2n$ becomes lower. However, in the experimental results for Ar $\Delta\Phi^{(14-12)} \equiv \Delta\phi_{\text{HH}}^{(14)0} - \Delta\phi_{\text{HH}}^{(12)0}$ is the smallest among the observed three $2n$'s. We also show in Fig. 5.8 by horizontal dotted lines the $\Delta\Phi^{(14-12)}$'s obtained by the model calculation.

Both of the two effects considered in the previous section, the effect of dispersion and that of the misalignment, are nearly independent of the harmonic order $2n$, and cannot cause the phenomena observed in the results of Ar that the difference between $\Delta\phi_{\text{HH}}^{(12)0}$ and $\Delta\phi_{\text{HH}}^{(14)0}$ is much smaller than

5 Discussions

differences in other sideband orders. In addition, the nonlinearity of the dispersion is predicted to be small in Ref. [49]. Therefore, we deduce that the smallness of $\Delta\Phi^{(14-12)} \equiv \Delta\phi_{\text{HH}}^{(14)0} - \Delta\phi_{\text{HH}}^{(12)0}$ comes from the single-atom property of Ar. Since the ionization potential I_p of Ar is 15.76 eV and the photon energy of the driving pulses is ~ 1.55 eV, the ionization threshold of Ar is $15.76/1.55 \simeq 10$ th harmonics and the 12th sideband is very near the ionization threshold. As introduced in §1.3, several phenomena are reported that cannot be explained by the strong-field approximation [62]. In the following, we investigate the possible causes of the anomaly in $\Delta\Phi^{(14-12)}$ by considering how the corrections of the strong-field approximation affect ionization, propagation, and recombination process.

5.3.2 Ionization

First we discuss the ionization process. According to the theory of Keldysh [138], the ionization by the intense laser field occurs by two kinds of process, the tunneling ionization and the multiphoton ionization, and the tunneling ionization is dominant when the parameter $\gamma = \omega_0 \sqrt{2I_p}/E^{\text{driving}}$ (so called the Keldysh parameter) is much smaller than 1 whereas the multiphoton ionization is dominant when $\gamma \gg 1$. In our experiment, the Keldysh parameter is $\gamma \simeq 0.7$ for Ar with the laser intensity $I \simeq 2.7 \times 10^{14} \text{W/cm}^2$. This value is lower than 1 but not very small, so multiphoton ionization will also occur to some extent. In Ref. [50] it is suggested that in the multiphoton ionization regime the phase difference $\Delta\phi_{\text{HH}}^{(2n)0}$ is strongly influenced by the resonant effects, which is not included in the strong-field approximation. According to Ref. [62] the contribution from some excited state is indicated in the high-order harmonic generation at the near-threshold region. The contribution of excited state to $\Delta\Phi^{(14-12)} \equiv \Delta\phi_{\text{HH}}^{(14)0} - \Delta\phi_{\text{HH}}^{(12)0}$ can explain the dependence of $\Delta\Phi^{(14-12)}$ on the laser intensity observed in our experiment (Fig. 5.9), because when the intensity varies, the fraction of the multiphoton ionization is changed and it will affect the phase difference of harmonics. However, our results of Fig. 5.9 shows that $\Delta\Phi^{(14-12)}$ approaches zero, which deviates from the prediction of strong field approximation, when the intensity of the laser field is stronger and reaches the tunneling ionization regime, where the effects of the excited states is less important than in the multiphoton-ionization regime. In fact, the effects of multiphoton ionization cannot be discussed only with a single parameter γ because its process depends largely on the structure of the excited states. Further theoretical and experimental investigations will be needed to clarify the effects of the multiphoton process on the phase of high-order harmonics.

5.3.3 Propagation

To investigate the effect of the Coulomb potential on the recombination time t_e , we calculate t_e with the classical trajectory Monte Carlo method [62, 139] (see Appendix A.7 for details.). We consider the one-dimensional classical trajectories of one electron in the soft-core potential

$$V(x) = -\frac{Z_e}{\sqrt{x^2 + \alpha^2}}, \quad (5.11)$$

5.3 The anomaly of the phase differences at the near-threshold region

with the laser field, and calculate the time when an electron with a positive energy (corresponding to the ionization) return to the origin $x = 0$ (corresponding to the recombination). As the initial distribution of the position x and momentum p we use the truncated Wigner distribution [139]: that is, we first calculate the quantum ground state, and based on this ground state we obtain the (x, p) distribution which can be allowed in the classical mechanics (see §A.7.2 for detail). Figure 5.11(b) shows the calculated recombination times for three potentials (Fig. 5.11(a)) with the same ionization energy $I_P = 15.58$ eV but different shapes, together with the result of the model calculation with the strong-field approximation. The intensity of the laser field is set as 2.7×10^{14} W/cm². By the right vertical axis we show the corresponding phase differences. Depending on the parameters of the soft-core potential, the slope changes over all the energy range rather than only the near-threshold region. Thus the effect of the Coulomb potential on the flight time of electrons does not seem to be a major reason for the observed difference in $\Delta\Phi^{(14-12)}$. To investigate the intensity dependence we also calculate the recombination time with the driving-pulse intensity of 2.3×10^{14} W/cm² and 2.0×10^{14} W/cm², whose results are shown in Figs. 5.11(c) and (d), respectively. When the intensity of the driving field varies, the results change in the same way both for the calculation with Coulomb potentials and for the calculation with the strong field approximation, and no remarkable dependence can be found at $\Delta\Phi^{(14-12)}$.

5.3.4 Recombination

The other possible reason may be the difference in the phase of the photorecombination dipole moment. According to the quantitative rescattering theory [59], the induced dipole $\tilde{x}(\omega)$ of atoms or molecules for high-order harmonic generation can be written as a product of the returning electron wave packet W and the photorecombination transition dipole moment d_{rec} : $\tilde{x}(\omega) \simeq Wd_{\text{rec}}$. Since the electric field of the high-order harmonics E_{HH} is related to the dipole moment $\tilde{x}(\omega)$ by $E_{\text{HH}} \propto \omega^2 \tilde{x}(\omega)$ [Eq. (2.14)], its phase $\arg[E_{\text{HH}}]$ can be resolved as

$$\arg[E_{\text{HH}}] \simeq \arg[\tilde{x}] + (\text{constant}) \simeq \arg[W] + \arg[d_{\text{rec}}] + (\text{constant}), \quad (5.12)$$

and the phase difference $\Delta\phi_{\text{HH}}^{(2n)0}$ becomes

$$\begin{aligned} \Delta\phi_{\text{HH}}^{(2n)0} &\equiv \phi_{\text{HH}}^{(2n+1)0} - \phi_{\text{HH}}^{(2n-1)0} = \arg[E_{\text{HH}}((2n+1)\omega_0)] - \arg[E_{\text{HH}}((2n-1)\omega_0)] \\ &\simeq \Delta \arg[W(2n\omega_0)] + \Delta \arg[d_{\text{rec}}(2n\omega_0)], \end{aligned} \quad (5.13)$$

where

$$\Delta \arg[W(\omega)] = \arg[W(\omega + \omega_0)] - \arg[W(\omega - \omega_0)], \quad (5.14)$$

$$\Delta \arg[d_{\text{rec}}(\omega)] = \arg[d_{\text{rec}}(\omega + \omega_0)] - \arg[d_{\text{rec}}(\omega - \omega_0)]. \quad (5.15)$$

In our model calculation used above, we only consider the recombination time of the electron, which corresponds to the term about the returning electron wavepacket $\Delta \arg[W(2n\omega_0)]$ in Eq. (5.13). However, when the phase of the photorecombination dipole moment $\arg[d_{\text{rec}}]$ also changes depending on the photon energy ω , it can influences the phase difference of the high-order harmonics.

5 Discussions

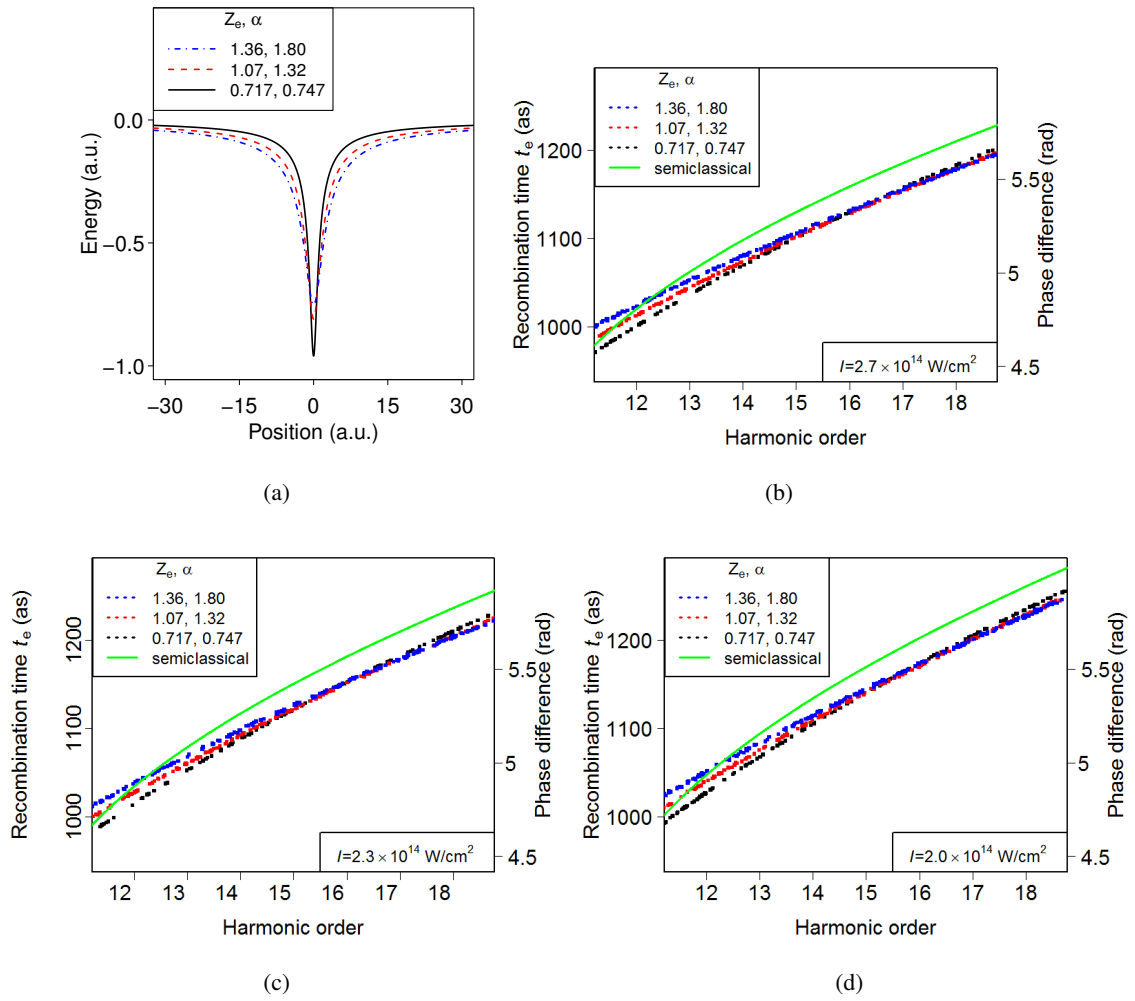


Figure 5.11: (a) three types of the soft-core potential used in the classical trajectory Monte Carlo calculation. (b)–(d) The recombination times calculated with the classical trajectory Monte Carlo calculation in three types of one-dimensional soft-core potentials [Eq. (5.11)]. The parameters for the soft-core potential are given in the legend. The intensity of the driving pulse is $2.7 \times 10^{14} \text{ W/cm}^2$, $2.3 \times 10^{14} \text{ W/cm}^2$ and $2.0 \times 10^{14} \text{ W/cm}^2$ for (b), (c), and (d), respectively.

5.3 The anomaly of the phase differences at the near-threshold region

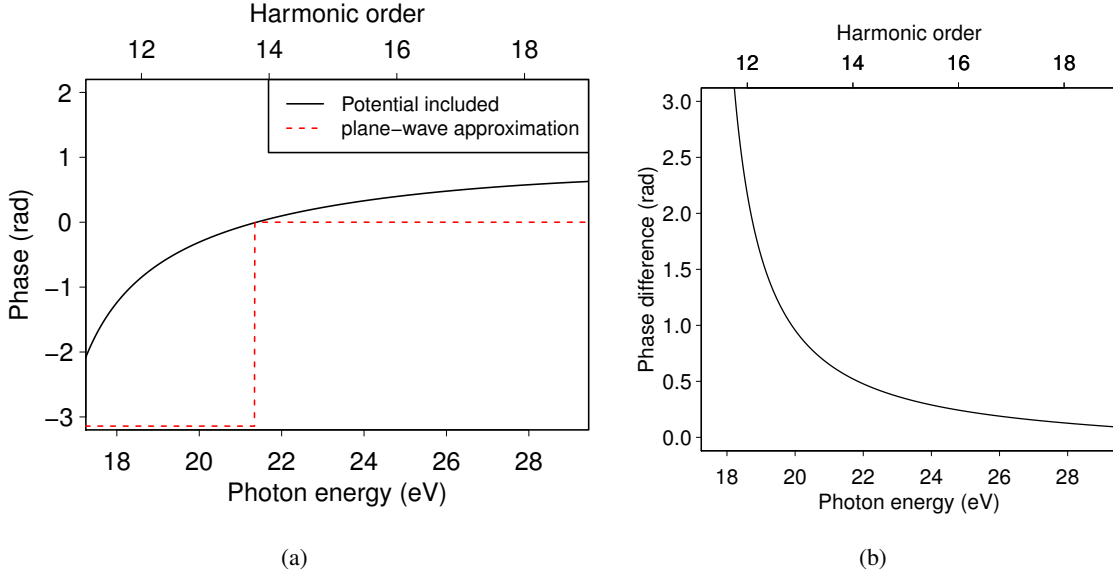


Figure 5.12: (a) Calculated phase of photorecombination transition dipole moment for Ar with the one-electron potential presented in Refs. [86, 89] (solid line) and with plane wave approximation (broken line). The energies corresponding to 12th, 14th, 16th and 18th sideband are shown by vertical lines. (b) $\Delta \arg [d_{\text{rec}}(\omega)] \equiv \arg [d_{\text{rec}}(\omega + \omega_0)] - \arg [d_{\text{rec}}(\omega - \omega_0)]$ obtained from $\arg [d_{\text{rec}}(\omega)]$ of Fig. 5.12(a).

In Fig. 5.12(a) we show by a solid line the phase of the photorecombination transition dipole moment for Ar calculated by reference to Ref. [59], with the one-electron potential presented in Refs. [86, 89] (the same one used in the calculation of $\Delta\phi_{\text{atom}}$ shown in Fig. 2.4(a)). See Appendix A.8 for the details of calculation. From this result we obtain $\Delta \arg [d_{\text{rec}}(\omega)] \equiv \arg [d_{\text{rec}}(\omega + \omega_0)] - \arg [d_{\text{rec}}(\omega - \omega_0)]$ [Eq. (5.15)], which is shown in Fig. 5.12(b). Due to the rapid phase change near the ionization threshold, $\Delta \arg [d_{\text{rec}}(12\omega_0)]$ is remarkably larger than those at other sideband orders. This rapid decrease in $\Delta \arg [d_{\text{rec}}(\omega)]$ around $12\omega_0$ can be a reason for small $\Delta\Phi^{(14-12)}$ of Ar because it can compensate the monotonic increase of the recombination time. We also show by the broken line in Fig. 5.12(a) the phase of the dipole moment calculated by using the returning electron wave packet uninfluenced by the Coulomb potential (plane-wave approximation). Its large derivation from the result including the effect of the potential means that the Coulomb potential plays a crucial role in the phase around this energy range.

There are several problems in the above discussions. First, the value of $\Delta\phi_{\text{HH}}^{(12)}$ in Fig. 5.12(b) (~ 2.2 rad) is too large to compensate the phase difference caused by the energy dependence of the recombination time, which is expected to be ~ 0.4 rad from our model calculation (Fig. 5.1(b)). This discrepancy is considered to come from the inaccuracy of the one-electron potential used in the calculation of $\arg[d_{\text{rec}}]$. The difference of $\Delta\Phi^{(14-12)}$ between Ar and N_2 may also be attributed to the different shapes of the potential, but the differences in the structures of the HOMO's must be taken into consideration for quantitative discussions because it can significantly affect the harmonic phase [51]. Another problem is that the recombination phase does not depend on the laser parameters

5 Discussions

and cannot explain the results that $\Delta\Phi^{(14-12)}$ of Kr depends on the laser intensity. The dependence on the laser intensity is thus considered to be from the ionization process stated in §5.3.2.

5.3.5 Errors caused by the fluctuations of experimental conditions

Before ending this section we discuss the errors of the measured phase differences. As stated above, the error bars in the figures for the measured phase differences show the errors associated with the least-square fitting of the sideband modulation by the function of Eq (4.8). However, there must be the error caused by the fluctuation of experimental conditions. For example, the fluctuation in the density of the gas and that in the pointing of the laser beam can change the phase differences through the mechanisms discussed in §5.2, and the actual errors of the measured data will be larger than those shown by the error bars. We also show in §5.2, however, that the change in the observed phase differences caused by both of these mechanisms is nearly independent of the harmonic order. In addition, in the present experiment we always observed all of the 12th–18th sidebands simultaneously. Therefore, we do not think that the difference between $\Delta\phi_{\text{HH}}^{(12)0}$ and $\Delta\phi_{\text{HH}}^{(14)0}$, which is the subject of this section, is seriously fluctuated by the fluctuation of experimental conditions compared to the error of the fitting.

5.4 Summary of the discussions

We conclude the above discussions as follows: as pointed out by Mairesse *et al.* [32], the monotonic increase of the phase difference comes from the dependence of the recombination time on the harmonic order, which is determined by the propagation process. However, although the model calculation of the recombination time predicts that $\Delta\phi_{\text{HH}}^{(12)0}$ is smaller than $\Delta\phi_{\text{HH}}^{(14)0}$ by ~ 0.4 rad, this is not consistent with our experimental results for Ar, CO₂ and some results of Kr, in which the difference $\Delta\Phi^{(14-12)} \equiv \Delta\phi_{\text{HH}}^{(14)0} - \Delta\phi_{\text{HH}}^{(12)0}$ is near zero (Fig. 5.8). The small $\Delta\Phi^{(14-12)}$ can be caused by the effect of the Coulomb potential on the recombination process: the rapid phase change around the 12th sideband order can make $\Delta\phi_{\text{HH}}^{(12)0}$ larger and close to $\Delta\phi_{\text{HH}}^{(14)0}$. On the other hand, unlike the case of Ar, $\Delta\Phi^{(14-12)}$ remains large in the results for N₂. In addition, since the recombination phase is independent of the laser parameters, this cannot produce the intensity dependence of $\Delta\Phi^{(14-12)}$ observed in the results for Kr. These problems imply the existence of other mechanisms to determine $\Delta\Phi^{(14-12)}$. One of them is the contribution of the excited states in the ionization process, which can be a cause of the intensity dependence in $\Delta\Phi^{(14-12)}$. The pump-probe experiment of Ref. [62] suggests that excited states contribute to the high-order harmonics generated in N₂, which is consistent with our difference between the $\Delta\Phi^{(14-12)}$ of N₂ and that of Ar. Another contributing mechanism may be the shape of the potential and the structure of the HOMO: they have a large influence on the phase of the recombination dipole moment. Further investigations are needed for quantitative discussions.

5.4 Summary of the discussions

Chapter 6

Conclusion

In this thesis, we have presented the experimental results of the phase differences of near-threshold high-order harmonics generated in Ar, N₂, Kr, and CO₂. In this chapter we summarize our study and present a future outlook.

6.1 Summary of the experiment

We used the RABBIT method (§2.3) to observe the phase differences between adjacent high-order harmonics. A “driving pulse” for high-order harmonic generation and a “probe pulse” of the RABBIT method were prepared by separating the output from the Ti:sapphire based chirped pulse amplifier with a drilled mirror (§3.1). The delay Δt between these two pulses was controlled with a piezoelectric positioning stage. The pulses entered the vacuum chamber (§3.2) and were focused onto a gas jet to generate high-order harmonics, after which the driving pulses were blocked. The generated high-order harmonics and the probe pulses were then focused by a toroidal mirror on an Ar gas jet for the RABBIT method. The produced photoelectrons were measured by using the velocity-map imaging technique (§3.3). From the obtained images we reconstructed the energy spectra of photoelectrons. (§§3.3.4–3.3.6). We extracted the phase differences by analyzing the signal intensities produced by two-color two-photon ionization of the high-order harmonics and the probe pulse (§4.1). Here, we removed the effects of the inevitable modulation of high-order harmonics by a new analysis method based on the theory of two-color two-photon ionization. When we observed the high-order harmonics generated in aligned molecules, we irradiated the sample with a pump pulse in advance and generated high-order harmonics when the molecules were aligned along the pump pulse polarization (§3.5).

6.2 Summary of the results and discussions

The observed phase differences $\Delta\phi_{\text{HH}}^{(2n)^0}$ were presented in §4.2. They monotonically increase as a function of the sideband order. This is consistent with the study by Mairesse *et al.* [32], in which the phase differences between adjacent harmonic orders are related to the recombination time of the electron (§2.2). However, we found two features which have not been discussed in earlier studies to

our knowledge. First one is that the absolute values of the results are shifted depending on the date of the measurement, i.e. some slight changes in the experimental conditions. We attribute this shift to the difference in the medium dispersion caused by the variation in the density of sample gases and the optical path difference between the high-order harmonics and the probe pulse due to the slight change of the alignment (§5.2). Both of these effects are nearly independent of the harmonic order in the observed energy range. The other feature is the difference of $\Delta\Phi^{(14-12)} \equiv \Delta\phi_{\text{HH}}^{(14)0} - \Delta\phi_{\text{HH}}^{(12)0}$ depending on the medium: $\Delta\Phi^{(14-12)}$'s in the results of Ar and CO₂ were almost zero, whereas they had a value of ~ 0.5 rad in the results of N₂. Moreover, $\Delta\Phi^{(14-12)}$'s for Kr was dependent on the driving pulse intensities. We deduced that the differences in the $\Delta\Phi^{(14-12)}$ come from some single atomic/molecular properties. By reference to the recent studies introduced in §1.3, we discussed in §5.3 the possible causes of the anomaly in $\Delta\Phi^{(14-12)}$'s with several numerical calculations. From this discussion we found that the $\Delta\Phi^{(14-12)}$'s can be influenced by the contribution of excited states to the ionization and the effect of the Coulomb potential on the recombination, both of which are out of the acceptable range of the strong-field approximation.

6.3 Outlook

Our results indicate that when near-threshold high-order harmonics are used in the imaging of molecular orbitals (§1.1), some corrections are needed to include the effects beyond the strong-field approximation. The detailed form of the correction is not clear from our experimental results and a deeper understanding of the near-threshold harmonics is required. One example of further investigations is the experiment with a longer-wavelength driving pulse. In the present experiment we used outputs from a Ti:sapphire laser with wavelength ~ 800 nm as a driving pulse. The energy interval of the generated high-order harmonics was ~ 3.1 eV, which is rather sparse for detailed investigations on the near-threshold region. In fact, the deviation from the model calculation only appears in the 12th sideband $\Delta\phi_{\text{HH}}^{(12)0}$ in the present experiment. When a longer-wavelength driving pulse is used, the spectra of the high-order harmonics become denser and provide richer information. On the other hand, our results suggest that the phase differences of the near-threshold harmonics can become a new probe of the structure of the excited states or the shape of the Coulomb potentials. This new probe will surely add further to the advantages of molecular imaging based on high-order harmonic generation.

Appendix

A.1 Detailed calculations in the saddle-point approximation

Here we present the detailed calculation in the saddle-point approximation that are omitted in § 2.1.2.

A.1.1 saddle points on t and t'

We derive the equations (2.25) and (2.26), which the stationary points $t_{\text{st}}^{(\pm)} \equiv (t_{\text{st}}^{\prime(\pm)}, t_{\text{st}}^{(\pm)})$ must satisfy. Since

$$\begin{aligned}
 S_{\text{st}}(t'; t) &= -\frac{t-t'}{2} \mathbf{p}_{\text{st}}^2(t'; t) + \frac{1}{2} \left[\int_{t'}^t \mathbf{A}^2(t'') dt'' \right] + I_p(t-t') \quad \{2.21\} \\
 \frac{\partial}{\partial t} \mathbf{p}_{\text{st}}(t'; t) &\stackrel{\text{Eq. (2.18)}}{=} \frac{\partial}{\partial t} \left[\frac{1}{t-t'} \int_{t'}^t \mathbf{A}(t'') dt'' \right] \\
 &= -\frac{1}{(t-t')^2} \left[\int_{t'}^t \mathbf{A}(t'') dt'' \right] + \frac{1}{t-t'} \mathbf{A}(t) \stackrel{\text{Eq. (2.18)}}{=} -\frac{1}{t-t'} [\mathbf{p}_{\text{st}}(t'; t) - \mathbf{A}(t)],
 \end{aligned} \quad (\text{A.1})$$

and

$$\begin{aligned}
 \frac{\partial}{\partial t'} \mathbf{p}_{\text{st}}(t'; t) &\stackrel{\text{Eq. (2.18)}}{=} \frac{\partial}{\partial t'} \left[\frac{1}{t-t'} \int_{t'}^t \mathbf{A}(t'') dt'' \right] \\
 &= \frac{1}{(t-t')^2} \left[\int_{t'}^t \mathbf{A}(t'') dt'' \right] - \frac{1}{t-t'} \mathbf{A}(t') \stackrel{\text{Eq. (2.18)}}{=} \frac{1}{t-t'} [\mathbf{p}_{\text{st}}(t'; t) - \mathbf{A}(t')],
 \end{aligned} \quad (\text{A.2})$$

$\partial \Theta_{(\pm)}/\partial t$ and $\partial \Theta_{(\pm)}/\partial t'$ can be calculated as

$$\begin{aligned}
 \frac{\partial \Theta_{(\pm)}}{\partial t} &= \omega \pm \left\{ -\frac{1}{2} \mathbf{p}_{\text{st}}^2(t'; t) + [\mathbf{p}_{\text{st}}(t'; t) - \mathbf{A}(t)] \cdot \mathbf{p}_{\text{st}}(t'; t) + \frac{1}{2} \mathbf{A}^2(t) + I_p \right\} \\
 &= \omega \pm \left\{ \frac{[\mathbf{p}_{\text{st}}(t'; t) - \mathbf{A}(t)]^2}{2} + I_p \right\},
 \end{aligned} \quad (\text{A.3})$$

and

$$\begin{aligned}
 \frac{\partial \Theta_{(\pm)}}{\partial t'} &= \pm \left\{ \frac{1}{2} \mathbf{p}_{\text{st}}^2(t'; t) - [\mathbf{p}_{\text{st}}(t'; t) - \mathbf{A}(t')] \cdot \mathbf{p}_{\text{st}}(t'; t) - \frac{1}{2} \mathbf{A}^2(t') - I_p \right\} \\
 &= \pm \left\{ -\frac{[\mathbf{p}_{\text{st}}(t'; t) - \mathbf{A}(t')]^2}{2} - I_p \right\},
 \end{aligned} \quad (\text{A.4})$$

A.1 Detailed calculations in the saddle-point approximation

respectively. Since by definition $\partial\Theta_{(\pm)}/\partial t|_{t=t_{\text{st}}^{(\pm)}} = 0$,

$$\frac{[\mathcal{P}_{\text{st}}(t'_{\text{st}}^{(\pm)}; t_{\text{st}}^{(\pm)}) - \mathcal{A}(t_{\text{st}}^{(\pm)})]^2}{2} + I_p \pm \omega = 0, \quad (\text{A.5})$$

$$\frac{[\mathcal{P}_{\text{st}}(t'_{\text{st}}^{(\pm)}; t_{\text{st}}^{(\pm)}) - \mathcal{A}(t'_{\text{st}}^{(\pm)})]^2}{2} + I_p = 0, \quad (\text{A.6})$$

which are Eqs. (2.25) and (2.26).

A.1.2 The saddle point approximation around the stationary points of the time

Below the detailed derivation of Eq. (2.27) is presented. We expand $\Theta_{(\pm)}(t'; t)$ using Taylor series around $\mathbf{t}_{\text{st}}^{(\pm)} \equiv (t'_{\text{st}}^{(\pm)}, t_{\text{st}}^{(\pm)})$ to the second order [73, § 3.8]:

$$\begin{aligned} & \Theta_{(\pm)}(t'; t) \\ &= \sum_{n=0}^{+\infty} \frac{1}{n!} \left[(t - t_{\text{st}}^{(\pm)}) \cdot \frac{\partial}{\partial \tilde{t}} \right]^n \Theta_{(\pm)}(\tilde{t}'; \tilde{t}) \Big|_{\tilde{t}=t_{\text{st}}^{(\pm)}} \\ &\simeq \Theta_{(\pm)}(t'_{\text{st}}^{(\pm)}; t_{\text{st}}^{(\pm)}) + (t - t_{\text{st}}^{(\pm)}) \cdot \frac{\partial}{\partial \tilde{t}} \Theta_{(\pm)}(\tilde{t}'; \tilde{t}) \Big|_{\tilde{t}=t_{\text{st}}^{(\pm)}} \\ &\quad + \frac{1}{2} (t - t_{\text{st}}^{(\pm)}) \cdot \left(\begin{array}{l} (t - t_{\text{st}}^{(\pm)}) \frac{\partial^2}{\partial \tilde{t}^2} \Theta_{(\pm)}(\tilde{t}'; \tilde{t}) \Big|_{\tilde{t}=t_{\text{st}}^{(\pm)}} + (t' - t'_{\text{st}}^{(\pm)}) \frac{\partial^2}{\partial \tilde{t} \partial \tilde{t}'} \Theta_{(\pm)}(\tilde{t}'; \tilde{t}) \Big|_{\tilde{t}=t_{\text{st}}^{(\pm)}} \\ (t - t_{\text{st}}^{(\pm)}) \frac{\partial^2}{\partial \tilde{t} \partial \tilde{t}'} \Theta_{(\pm)}(\tilde{t}'; \tilde{t}) \Big|_{\tilde{t}=t_{\text{st}}^{(\pm)}} + (t' - t'_{\text{st}}^{(\pm)}) \frac{\partial^2}{\partial \tilde{t}'^2} \Theta_{(\pm)}(\tilde{t}'; \tilde{t}) \Big|_{\tilde{t}=t_{\text{st}}^{(\pm)}} \end{array} \right) \\ &= \Theta_{(\pm)}(t'_{\text{st}}^{(\pm)}; t_{\text{st}}^{(\pm)}) + \frac{1}{2} (t - t_{\text{st}}^{(\pm)}, t' - t'_{\text{st}}^{(\pm)}) \Theta''_{(\pm)} \begin{pmatrix} t - t_{\text{st}}^{(\pm)} \\ t' - t'_{\text{st}}^{(\pm)} \end{pmatrix}, \end{aligned} \quad (\text{A.7})$$

where $\Theta''_{(\pm)}$ is a Hessian matrix of $\Theta_{(\pm)}(t'; t)$ at $\mathbf{t} = \mathbf{t}_{\text{st}}^{(\pm)}$:

$$\begin{aligned} \Theta''_{(\pm)} &\equiv \begin{pmatrix} \frac{\partial^2}{\partial t'^2} \Theta_{(\pm)}(t'; t) \Big|_{t=t_{\text{st}}^{(\pm)}} & \frac{\partial^2}{\partial t \partial t'} \Theta_{(\pm)}(t'; t) \Big|_{t=t_{\text{st}}^{(\pm)}} \\ \frac{\partial^2}{\partial t \partial t'} \Theta_{(\pm)}(t'; t) \Big|_{t=t_{\text{st}}^{(\pm)}} & \frac{\partial^2}{\partial t^2} \Theta_{(\pm)}(t'; t) \Big|_{t=t_{\text{st}}^{(\pm)}} \end{pmatrix} \\ &= \pm \begin{pmatrix} \frac{\partial^2}{\partial t'^2} S_{\text{st}}(t'; t) \Big|_{t=t_{\text{st}}^{(\pm)}} & \frac{\partial^2}{\partial t \partial t'} S_{\text{st}}(t'; t) \Big|_{t=t_{\text{st}}^{(\pm)}} \\ \frac{\partial^2}{\partial t \partial t'} S_{\text{st}}(t'; t) \Big|_{t=t_{\text{st}}^{(\pm)}} & \frac{\partial^2}{\partial t^2} S_{\text{st}}(t'; t) \Big|_{t=t_{\text{st}}^{(\pm)}} \end{pmatrix}. \end{aligned} \quad (\text{A.8})$$

A Appendix

By using this approximation,

$$\begin{aligned}
& +i \int_{-\infty}^{+\infty} dt \int_{t_0}^t dt' \left(\frac{\pi}{+i(t-t')/2 + \epsilon} \right)^{3/2} e^{+i\Theta_{(-)}(t';t)} [\mathbf{E}(t') \cdot \mathbf{d}(\mathbf{p}_{\text{st}}(t';t) - \mathbf{A}(t'))] \mathbf{d}^*(\mathbf{p}_{\text{st}}(t';t) - \mathbf{A}(t)) \\
& \simeq +i \int_{-\infty}^{+\infty} dt \int_{-\infty}^{+\infty} dt' \left(\frac{\pi}{+i(t-t')/2 + \epsilon} \right)^{3/2} e^{+i\Theta_{(-)}(t';t)} [\mathbf{E}(t') \cdot \mathbf{d}(\mathbf{p}_{\text{st}}(t';t) - \mathbf{A}(t'))] \mathbf{d}^*(\mathbf{p}_{\text{st}}(t';t) - \mathbf{A}(t)) \\
& \simeq +i \sum_{t_{\text{st}}^{(-)}} \left(\frac{\pi}{+i(t_{\text{st}}^{(-)} - t_{\text{st}}^{\prime(-)})/2 + \epsilon} \right)^{3/2} [\mathbf{E}(t_{\text{st}}^{\prime(-)}) \cdot \mathbf{d}(\mathbf{p}_{\text{st}}(t_{\text{st}}^{\prime(-)}; t_{\text{st}}^{(-)}) - \mathbf{A}(t_{\text{st}}^{\prime(-)}))] \mathbf{d}^*(\mathbf{p}_{\text{st}}(t_{\text{st}}^{\prime(-)}; t_{\text{st}}^{(-)}) - \mathbf{A}(t_{\text{st}}^{\prime(-)})) \\
& \quad \times e^{+i\Theta_{(-)}(t_{\text{st}}^{\prime(-)}; t_{\text{st}}^{(-)})} \int_{-\infty}^{+\infty} dt \int_{-\infty}^{+\infty} dt' \exp \left[+\frac{i}{2} (t - t_{\text{st}}^{(-)}, t' - t_{\text{st}}^{\prime(-)}) \Theta''_{(-)} \begin{pmatrix} t - t_{\text{st}}^{(-)} \\ t' - t_{\text{st}}^{\prime(-)} \end{pmatrix} \right] \\
& = +i \sum_{t_{\text{st}}^{(-)}} \left(\frac{\pi}{+i(t_{\text{st}}^{(-)} - t_{\text{st}}^{\prime(-)})/2 + \epsilon} \right)^{3/2} \mathbf{E}(t_{\text{st}}^{\prime(-)}) \cdot \mathbf{d}(\mathbf{p}_{\text{st}}(t_{\text{st}}^{\prime(-)}; t_{\text{st}}^{(-)}) - \mathbf{A}(t_{\text{st}}^{\prime(-)})) \mathbf{d}^*(\mathbf{p}_{\text{st}}(t_{\text{st}}^{\prime(-)}; t_{\text{st}}^{(-)}) - \mathbf{A}(t_{\text{st}}^{\prime(-)})) \\
& \quad \times e^{+i\Theta_{(-)}(t_{\text{st}}^{\prime(-)}; t_{\text{st}}^{(-)})} \sqrt{\frac{\pi}{-i\lambda_1^{(-)}/2}} \sqrt{\frac{\pi}{-i\lambda_2^{(-)}/2}} \\
& = \sum_{t_{\text{st}}^{(-)}} \frac{+i2\pi}{\sqrt{-\det \Theta''_{(-)}}} \left(\frac{\pi}{+i(t_{\text{st}}^{(-)} - t_{\text{st}}^{\prime(-)})/2 + \epsilon} \right)^{3/2} e^{+i\Theta_{(-)}(t_{\text{st}}^{\prime(-)}; t_{\text{st}}^{(-)})} \\
& \quad \times [\mathbf{E}(t_{\text{st}}^{\prime(-)}) \cdot \mathbf{d}(\mathbf{p}_{\text{st}}(t_{\text{st}}^{\prime(-)}; t_{\text{st}}^{(-)}) - \mathbf{A}(t_{\text{st}}^{\prime(-)}))] \mathbf{d}^*(\mathbf{p}_{\text{st}}(t_{\text{st}}^{\prime(-)}; t_{\text{st}}^{(-)}) - \mathbf{A}(t_{\text{st}}^{\prime(-)})),
\end{aligned} \tag{A.9}$$

where $\lambda_1^{(\pm)}$ and $\lambda_2^{(\pm)}$ are the eigenvalues of the matrix $\Theta''_{(\pm)}$ and

$$\det \Theta''_{(\pm)} \equiv \left(\frac{\partial^2}{\partial t^2} \Theta_{(\pm)}(t';t) \Big|_{t=t_{\text{st}}^{(\pm)}} \right) \left(\frac{\partial^2}{\partial t'^2} \Theta_{(\pm)}(t';t) \Big|_{t=t_{\text{st}}^{(\pm)}} \right) - \left(\frac{\partial^2}{\partial t \partial t'} \Theta_{(\pm)}(t';t) \Big|_{t=t_{\text{st}}^{(\pm)}} \right)^2 = \lambda_1^{(\pm)} \lambda_2^{(\pm)} \tag{A.10}$$

is the determinant of $\Theta''_{(\pm)}$ ¹. In the same way,

$$\begin{aligned}
& -i \int_{-\infty}^{+\infty} dt \int_{t_0}^t dt' \left(\frac{\pi}{-i(t-t')/2 + \epsilon} \right)^{3/2} e^{+i\Theta_{(+)}(t';t)} [\mathbf{E}(t') \cdot \mathbf{d}^*(\mathbf{p}_{\text{st}}(t';t) - \mathbf{A}(t'))] \mathbf{d}(\mathbf{p}_{\text{st}}(t';t) - \mathbf{A}(t)) \\
& \simeq \sum_{t_{\text{st}}^{(+)}} \frac{-i2\pi}{\sqrt{-\det \Theta''_{(+)}}} \left(\frac{\pi}{-i(t_{\text{st}}^{(+)} - t_{\text{st}}^{\prime(+)})/2 + \epsilon} \right)^{3/2} e^{+i\Theta_{(+)}(t_{\text{st}}^{\prime(+)}; t_{\text{st}}^{(+)})} \\
& \quad \times [\mathbf{E}(t_{\text{st}}^{\prime(+)}) \cdot \mathbf{d}^*(\mathbf{p}_{\text{st}}(t_{\text{st}}^{\prime(+)}; t_{\text{st}}^{(+)}) - \mathbf{A}(t_{\text{st}}^{\prime(+)}))] \mathbf{d}(\mathbf{p}_{\text{st}}(t_{\text{st}}^{\prime(+)}; t_{\text{st}}^{(+)}) - \mathbf{A}(t_{\text{st}}^{\prime(+)})).
\end{aligned} \tag{A.11}$$

Therefore, from Eq. (2.24),

$$\begin{aligned}
\tilde{x}_z(\omega, \theta, 0) & \simeq \sum_{t_{\text{st}}^{(-)}} \frac{+i2\pi}{\sqrt{-\det \Theta''_{(-)}}} \left(\frac{\pi}{+i(t_{\text{st}}^{(-)} - t_{\text{st}}^{\prime(-)})/2 + \epsilon} \right)^{3/2} e^{+i\Theta_{(-)}(t_{\text{st}}^{\prime(-)}; t_{\text{st}}^{(-)})} \\
& \quad \times [\mathbf{E}(t_{\text{st}}^{\prime(-)}) \cdot \mathbf{d}(\mathbf{p}_{\text{st}}(t_{\text{st}}^{\prime(-)}; t_{\text{st}}^{(-)}) - \mathbf{A}(t_{\text{st}}^{\prime(-)}))] \mathbf{d}^*(\mathbf{p}_{\text{st}}(t_{\text{st}}^{\prime(-)}; t_{\text{st}}^{(-)}) - \mathbf{A}(t_{\text{st}}^{\prime(-)})) \\
& + \sum_{t_{\text{st}}^{(+)}} \frac{-i2\pi}{\sqrt{-\det \Theta''_{(+)}}} \left(\frac{\pi}{-i(t_{\text{st}}^{(+)} - t_{\text{st}}^{\prime(+)})/2 + \epsilon} \right)^{3/2} e^{+i\Theta_{(+)}(t_{\text{st}}^{\prime(+)}; t_{\text{st}}^{(+)})} \\
& \quad \times [\mathbf{E}(t_{\text{st}}^{\prime(+)}) \cdot \mathbf{d}^*(\mathbf{p}_{\text{st}}(t_{\text{st}}^{\prime(+)}; t_{\text{st}}^{(+)}) - \mathbf{A}(t_{\text{st}}^{\prime(+)}))] \mathbf{d}(\mathbf{p}_{\text{st}}(t_{\text{st}}^{\prime(+)}; t_{\text{st}}^{(+)}) - \mathbf{A}(t_{\text{st}}^{\prime(+)})).
\end{aligned} \tag{A.12}$$

Thus we obtain Eq. (2.27).

¹ In Eq. (12) of [72], the sign of the determinant is opposite to the usual definition. We use in Eq. (A.10) the definition which is commonly used, so the sign before $\det \Theta''_{(-)}$ in Eq. (A.9) is opposite to that of Eq. (11) of [72].

A.1.3 Calculation of the determinant of the Hessian matrix $\det \Theta''_{(\pm)}$

We describe here the calculation process of the determinant of the Hessian matrix $\det \Theta''_{(\pm)}$ appeared in (2.28). By using $\mathbf{E} = -\frac{d}{dt}\mathbf{A}(t)$, $\partial\Theta_{(\pm)}/\partial t|_{t=t_{\text{st}}^{(\pm)}} = 0$, and Eqs. (A.1)–(A.6), the components of the matrix $\Theta''_{(\pm)}$ can be calculated as

$$\begin{aligned} \frac{\partial^2}{\partial t'^2}\Theta_{(\pm)}(t'; t)|_{t=t_{\text{st}}^{(\pm)}} &= \pm \left\{ \left[-\frac{1}{t_{\text{st}}^{(\pm)} - t'_{\text{st}}^{(\pm)}} [\mathbf{p}_{\text{st}}(t'_{\text{st}}^{(\pm)}; t) - \mathbf{A}(t_{\text{st}}^{(\pm)})] + \mathbf{E}(t_{\text{st}}^{(\pm)}) \right] \cdot [\mathbf{p}_{\text{st}}(t'_{\text{st}}^{(\pm)}; t) - \mathbf{A}(t_{\text{st}}^{(\pm)})] \right\} \\ &= \frac{2[\omega \pm I_p]}{t_{\text{st}}^{(\pm)} - t'_{\text{st}}^{(\pm)}} \pm \mathbf{E}(t_{\text{st}}^{(\pm)}) \cdot [\mathbf{p}_{\text{st}}(t'_{\text{st}}^{(\pm)}; t) - \mathbf{A}(t_{\text{st}}^{(\pm)})], \end{aligned} \quad (\text{A.13})$$

$$\begin{aligned} \frac{\partial^2}{\partial t \partial t'}\Theta_{(\pm)}(t'; t)|_{t=t_{\text{st}}^{(\pm)}} &= \pm \left\{ \left[\frac{1}{t_{\text{st}}^{(\pm)} - t'_{\text{st}}^{(\pm)}} [\mathbf{p}_{\text{st}}(t'_{\text{st}}^{(\pm)}; t) - \mathbf{A}(t'_{\text{st}}^{(\pm)})] \right] \cdot [\mathbf{p}_{\text{st}}(t'_{\text{st}}^{(\pm)}; t) - \mathbf{A}(t_{\text{st}}^{(\pm)})] \right\} \\ &= \pm \frac{[\mathbf{p}_{\text{st}}(t'_{\text{st}}^{(\pm)}; t) - \mathbf{A}(t'_{\text{st}}^{(\pm)})] \cdot [\mathbf{p}_{\text{st}}(t'_{\text{st}}^{(\pm)}; t) - \mathbf{A}(t_{\text{st}}^{(\pm)})]}{t_{\text{st}}^{(\pm)} - t'_{\text{st}}^{(\pm)}} \end{aligned} \quad (\text{A.14})$$

and

$$\begin{aligned} \frac{\partial^2}{\partial t'^2}\Theta_{(\pm)}(t'; t)|_{t=t_{\text{st}}^{(\pm)}} &= \pm \left\{ \left[-\frac{1}{t_{\text{st}}^{(\pm)} - t'_{\text{st}}^{(\pm)}} [\mathbf{p}_{\text{st}}(t'_{\text{st}}^{(\pm)}; t) - \mathbf{A}(t'_{\text{st}}^{(\pm)})] - \mathbf{E}(t'_{\text{st}}^{(\pm)}) \right] \cdot [\mathbf{p}_{\text{st}}(t'_{\text{st}}^{(\pm)}; t) - \mathbf{A}(t'_{\text{st}}^{(\pm)})] \right\} \\ &= \pm \frac{2I_p}{t_{\text{st}}^{(\pm)} - t'_{\text{st}}^{(\pm)}} \mp \mathbf{E}(t'_{\text{st}}^{(\pm)}) \cdot [\mathbf{p}_{\text{st}}(t'_{\text{st}}^{(\pm)}; t) - \mathbf{A}(t'_{\text{st}}^{(\pm)})]. \end{aligned} \quad (\text{A.15})$$

Therefore,

$$\begin{aligned} \det \Theta''_{(\pm)} &= \frac{4I_p [I_p \pm \omega]}{(t_{\text{st}}^{(\pm)} - t'_{\text{st}}^{(\pm)})^2} - \frac{2 [I_p \pm \omega]}{t_{\text{st}}^{(\pm)} - t'_{\text{st}}^{(\pm)}} \mathbf{E}(t'_{\text{st}}^{(\pm)}) \cdot [\mathbf{p}_{\text{st}}(t'_{\text{st}}^{(\pm)}; t) - \mathbf{A}(t'_{\text{st}}^{(\pm)})] \\ &\quad + \frac{2I_p}{t_{\text{st}}^{(\pm)} - t'_{\text{st}}^{(\pm)}} \mathbf{E}(t_{\text{st}}^{(\pm)}) \cdot [\mathbf{p}_{\text{st}}(t'_{\text{st}}^{(\pm)}; t) - \mathbf{A}(t_{\text{st}}^{(\pm)})] \\ &\quad - \left\{ \mathbf{E}(t_{\text{st}}^{(\pm)}) \cdot [\mathbf{p}_{\text{st}}(t'_{\text{st}}^{(\pm)}; t) - \mathbf{A}(t_{\text{st}}^{(\pm)})] \right\} \left\{ \mathbf{E}(t'_{\text{st}}^{(\pm)}) \cdot [\mathbf{p}_{\text{st}}(t'_{\text{st}}^{(\pm)}; t) - \mathbf{A}(t'_{\text{st}}^{(\pm)})] \right\} \\ &\quad - \frac{\left\{ [\mathbf{p}_{\text{st}}(t'_{\text{st}}^{(\pm)}; t) - \mathbf{A}(t'_{\text{st}}^{(\pm)})] \cdot [\mathbf{p}_{\text{st}}(t'_{\text{st}}^{(\pm)}; t) - \mathbf{A}(t_{\text{st}}^{(\pm)})] \right\}^2}{(t_{\text{st}}^{(\pm)} - t'_{\text{st}}^{(\pm)})^2}. \end{aligned} \quad (\text{A.16})$$

This gives Eq. (2.28).

A Appendix

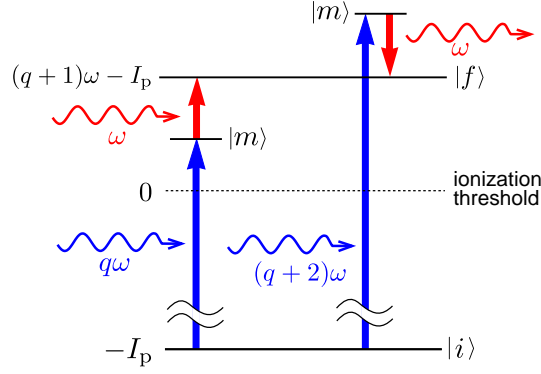


Figure A.1: Energy diagram of two-color two-photon ionization of an atom by XUV and IR fields. The kets $|i\rangle$, $|f\rangle$, and $|m\rangle$ stand for initial, final and intermediate states, respectively.

A.2 Derivation of the expression for the probability of two-color two-photon ionization

Here we describe the derivation of Eq.(2.64), which is used in the calculation of the sideband strength in the RABBIT method (§2.3.1).

Under the interaction $V = -E(z) \cdot z$, the first order of the time-evolution operator $\langle f | U^{(1)} | i \rangle$ [Eq. (2.62)] becomes

$$\begin{aligned}
 \langle f | U^{(1)} | i \rangle &= i \langle f | z | i \rangle \int_{t_i}^{t_f} d\tau \left[e^{-iE_f^0(t_f-\tau)} E(\tau) e^{-iE_i^0(\tau-t_i)} \right] \\
 &= i \langle f | z | i \rangle e^{-i(E_f^0 t_f - E_i^0 t_i)} \\
 &\quad \times \int_{t_i}^{t_f} d\tau \left\{ \sum_n \left[\mathcal{E}_X^{(2n+1)} e^{i[E_f^0 - E_i^0 - (2n+1)\omega_0]\tau} + \mathcal{E}_X^{(2n+1)*} e^{i[E_f^0 - E_i^0 + (2n+1)\omega_0]\tau} \right] \right. \\
 &\quad \left. + \mathcal{E}_I e^{i(E_f^0 - E_i^0 - \omega_0)\tau} + \mathcal{E}_I^* e^{i(E_f^0 - E_i^0 + \omega_0)\tau} \right\}. \tag{A.17}
 \end{aligned}$$

The energy of IR photon is much smaller than the ionization potential of the rare-gas atoms. Therefore, when the initial state i is the ground state and the final state f is in the continuum state, $E_f^0 - E_i^0 \pm \omega_0$ is large and the exponentials oscillate rapidly in the integration, which make the terms $\int_{t_i}^{t_f} e^{i(E_f^0 - E_i^0 \pm \omega_0)\tau} d\tau$ negligibly small. The same is true of the term $\int_{t_i}^{t_f} e^{i[E_f^0 - E_i^0 + (2n+1)\omega_0]\tau} d\tau$. Therefore,

$$\langle f | U^{(1)} | i \rangle \simeq i \langle f | z | i \rangle e^{-i(E_f^0 t_f - E_i^0 t_i)} \sum_n \mathcal{E}_X^{(2n+1)} \int_{t_i}^{t_f} d\tau e^{i[E_f^0 - E_i^0 - (2n+1)\omega_0]\tau}. \tag{A.18}$$

This term corresponds to one-photon absorption. For the same reason, the dominant term in the second order of the time-evolution operator $\langle f | U^{(2)} | i \rangle$ [Eq. (2.63)] is the ones which correspond to the process that the atom absorbs one XUV photon and absorb or emit one IR photon (see Fig. A.1). Since XUV field is much weaker than the IR field, the process of absorbing two XUV photon is

A.2 Derivation of the expression for the probability of two-color two-photon ionization

unlikely and can be neglected):

$$\begin{aligned}
& \langle f | U^{(2)} | i \rangle \\
& \simeq -e^{-i(E_f^0 t_f - E_i^0 t_i)} \sum_m \langle f | z | m \rangle \langle m | z | i \rangle \int_{t_i}^{t_f} d\tau \int_0^\tau d\tau' \\
& \times \left[\mathcal{E}_1 e^{i(E_f^0 - E_m^0 - \omega_0)\tau} \sum_n \mathcal{E}_X^{(2n+1)} e^{i[E_m^0 - E_i^0 - (2n+1)\omega_0]\tau'} + \mathcal{E}_1^* e^{i(E_f^0 - E_m^0 + \omega_0)\tau} \sum_n \mathcal{E}_X^{(2n+1)} e^{i[E_m^0 - E_i^0 - (2n+1)\omega_0]\tau'} \right. \\
& \quad \left. + \sum_n \mathcal{E}_X^{(2n+1)} e^{i[E_f^0 - E_m^0 - (2n+1)\omega_0]\tau} \mathcal{E}_1 e^{i(E_m^0 - E_i^0 - \omega_0)\tau'} + \sum_n \mathcal{E}_X^{(2n+1)} e^{i[E_f^0 - E_m^0 - (2n+1)\omega_0]\tau} \mathcal{E}_1^* e^{i(E_m^0 - E_i^0 + \omega_0)\tau'} \right] \\
& = -e^{-i(E_f^0 t_f - E_i^0 t_i)} \sum_m \sum_n \frac{\langle f | z | m \rangle \langle m | z | i \rangle}{E_i^0 + (2n+1)\omega_0 - E_m^0} \left\{ \mathcal{E}_1 \mathcal{E}_X^{(2n+1)} \int_{t_i}^{t_f} d\tau \left[e^{i[E_f^0 - E_i^0 - (2n+2)\omega_0]\tau} - e^{i(E_f^0 - E_m^0 - \omega_0)\tau} \right] \right. \\
& \quad \left. + \mathcal{E}_1^* \mathcal{E}_X^{(2n+1)} \int_{t_i}^{t_f} d\tau \left[e^{i(E_f^0 - E_i^0 - 2n\omega_0)\tau} - e^{i(E_f^0 - E_m^0 + \omega_0)\tau} \right] \right\} \\
& - i e^{-i(E_f^0 t_f - E_i^0 t_i)} \sum_m \sum_n \frac{\langle f | z | m \rangle \langle m | z | i \rangle}{E_i^0 + \omega_0 - E_m^0} \mathcal{E}_1 \mathcal{E}_X^{(2n+1)} \int_{t_i}^{t_f} d\tau \left[e^{i[E_f^0 - E_i^0 - (2n+2)\omega_0]\tau} - e^{i[E_f^0 - E_m^0 - (2n+1)\omega_0]\tau} \right] \\
& - i e^{-i(E_f^0 t_f - E_i^0 t_i)} \sum_m \sum_n \frac{\langle f | z | m \rangle \langle m | z | i \rangle}{E_i^0 - \omega_0 - E_m^0} \mathcal{E}_1^* \mathcal{E}_X^{(2n+1)} \int_{t_i}^{t_f} d\tau \left[e^{i(E_f^0 - E_i^0 - 2n\omega_0)\tau} - e^{i[E_f^0 - E_m^0 - (2n+1)\omega_0]\tau} \right].
\end{aligned} \tag{A.19}$$

If we define $\mathcal{M}_{f,m,i}^{(q)}$ as

$$\mathcal{M}_{f,m,i}^{(q)} \equiv \frac{\langle f | z | m \rangle \langle m | z | i \rangle}{E_i^0 + q\omega_0 - E_m^0}, \tag{A.20}$$

we can rewrite Eq. (A.19) as

$$\begin{aligned}
& \langle f | U^{(2)} | i \rangle \\
& \simeq -i e^{-i(E_f^0 t_f - E_i^0 t_i)} \sum_n \sum_m \left(\mathcal{M}_{f,m,i}^{(2n+1)} \left\{ \mathcal{E}_1 \mathcal{E}_X^{(2n+1)} \int_{t_i}^{t_f} d\tau \left[e^{i[E_f^0 - E_i^0 - (2n+2)\omega_0]\tau} - e^{i(E_f^0 - E_m^0 - \omega_0)\tau} \right] \right. \right. \\
& \quad \left. \left. + \mathcal{E}_1^* \mathcal{E}_X^{(2n+1)} \int_{t_i}^{t_f} d\tau \left[e^{i(E_f^0 - E_i^0 - 2n\omega_0)\tau} - e^{i(E_f^0 - E_m^0 + \omega_0)\tau} \right] \right\} \right. \\
& \quad \left. + \mathcal{M}_{f,m,i}^{(+1)} \mathcal{E}_1 \mathcal{E}_X^{(2n+1)} \int_{t_i}^{t_f} d\tau \left[e^{i[E_f^0 - E_i^0 - (2n+2)\omega_0]\tau} - e^{i[E_f^0 - E_m^0 - (2n+1)\omega_0]\tau} \right] \right. \\
& \quad \left. + \mathcal{M}_{f,m,i}^{(-1)} \mathcal{E}_1^* \mathcal{E}_X^{(2n+1)} \int_{t_i}^{t_f} d\tau \left[e^{i(E_f^0 - E_i^0 - 2n\omega_0)\tau} - e^{i[E_f^0 - E_m^0 - (2n+1)\omega_0]\tau} \right] \right) \\
& = -i e^{-i(E_f^0 t_f - E_i^0 t_i)} \sum_n \left\{ \sum_m \left[\mathcal{E}_1 \mathcal{E}_X^{(2n-1)} \left(\mathcal{M}_{f,m,i}^{(2n-1)} + \mathcal{M}_{f,m,i}^{(+1)} \right) + \mathcal{E}_1^* \mathcal{E}_X^{(2n+1)} \left(\mathcal{M}_{f,m,i}^{(2n+1)} + \mathcal{M}_{f,m,i}^{(-1)} \right) \right] \int_{t_i}^{t_f} d\tau e^{i(E_f^0 - E_i^0 - 2n\omega_0)\tau} \right. \\
& \quad + i e^{-i(E_f^0 t_f - E_i^0 t_i)} \sum_m \left(\sum_n \mathcal{E}_1 \mathcal{E}_X^{(2n+1)} \mathcal{M}_{f,m,i}^{(2n+1)} \right) \int_{t_i}^{t_f} d\tau e^{i(E_f^0 - E_m^0 - \omega_0)\tau} \\
& \quad + i e^{-i(E_f^0 t_f - E_i^0 t_i)} \sum_m \left(\sum_n \mathcal{E}_1^* \mathcal{E}_X^{(2n+1)} \mathcal{M}_{f,m,i}^{(2n+1)} \right) \int_{t_i}^{t_f} d\tau e^{i(E_f^0 - E_m^0 + \omega_0)\tau} \\
& \quad + i e^{-i(E_f^0 t_f - E_i^0 t_i)} \sum_m \left(\sum_n \mathcal{E}_1 \mathcal{E}_X^{(2n+1)} \mathcal{M}_{f,m,i}^{(+1)} \right) \int_{t_i}^{t_f} d\tau e^{i(E_f^0 - E_m^0 - (2n+1)\omega_0)\tau} \\
& \quad \left. + i e^{-i(E_f^0 t_f - E_i^0 t_i)} \sum_m \left(\sum_n \mathcal{E}_1^* \mathcal{E}_X^{(2n+1)} \mathcal{M}_{f,m,i}^{(-1)} \right) \int_{t_i}^{t_f} d\tau e^{i[E_f^0 - E_m^0 - (2n+1)\omega_0]\tau} \right.
\end{aligned} \tag{A.21}$$

A Appendix

By comparing Eqs. (A.18) and (A.21), we see that both $\langle f | U^{(1)} | i \rangle$ and $\langle f | U^{(2)} | i \rangle$ can be written in the form $\sum_l c_l \int_{t_i}^{t_f} d\tau e^{i\omega_l \tau}$, where $\omega_l \neq \omega_{l'}$ for $l \neq l'$, and the transition probability Eq. (2.61) can be represented as

$$\begin{aligned} W_{i \rightarrow f} &= \left| \sum_l c_l \int_{t_i}^{t_f} d\tau e^{i\omega_l \tau} \right|^2 \\ &= \sum_l |c_l|^2 \left| \int_{t_i}^{t_f} d\tau e^{i\omega_l \tau} \right|^2 + \sum_{l \neq l'} c_l c_{l'}^* \int_{t_i}^{t_f} d\tau e^{i\omega_l \tau} \int_{t_i}^{t_f} d\tau' e^{-i\omega_{l'} \tau'}. \end{aligned} \quad (\text{A.22})$$

If $|t_f - t_i|$ is sufficiently large, the integral $\int_{t_i}^{t_f} d\tau e^{i\omega \tau}$ becomes small except around $\omega = 0$. It follows that in the second term of the right-hand side of Eq. (A.22), at least one of the two integrals is small and this term therefore can be neglected:

$$W_{i \rightarrow f} \simeq \sum_l |c_l|^2 \left| \int_{t_i}^{t_f} d\tau e^{i\omega_l \tau} \right|^2. \quad (\text{A.23})$$

Moreover, when $|t_f - t_i|$ is large enough [24, § 12.5],

$$\begin{aligned} \left| \int_{t_i}^{t_f} d\tau e^{i\omega_l \tau} \right|^2 &= \left| \frac{e^{i\omega_l t_f} - e^{i\omega_l t_i}}{i\omega_l} \right|^2 \\ &= T^2 \frac{\sin^2(\omega_l T/2)}{(\omega_l T/2)^2} \quad (T \equiv t_f - t_i) \\ &\simeq 2\pi T \delta(\omega_l). \end{aligned} \quad (\text{A.24})$$

Therefore, when $\langle f | U^{(1)} | i \rangle + \langle f | U^{(2)} | i \rangle$ is written as $\sum_l c_l \int_{t_i}^{t_f} d\tau e^{i\omega_l \tau}$, the transition probability $W_{i \rightarrow f}$ is approximately written as

$$W_{i \rightarrow f} \simeq 2\pi T \sum_l |c_l|^2 \delta(\omega_l). \quad (\text{A.25})$$

A.2 Derivation of the expression for the probability of two-color two-photon ionization

By comparing this result with Eqs. (A.18) and (A.21), we get

$$\begin{aligned}
W_{i \rightarrow f} \simeq & 2\pi T \sum_n \left| \langle f | z | i \rangle \mathcal{E}_X^{(2n+1)} \right|^2 \delta(E_f^0 - E_i^0 - (2n+1)\omega_0) \\
& + 2\pi T \sum_n \left| \sum_m \left[\mathcal{E}_I \mathcal{E}_X^{(2n-1)} \left(\mathcal{M}_{f,m,i}^{(2n-1)} + \mathcal{M}_{f,m,i}^{(+1)} \right) \right. \right. \\
& \quad \left. \left. + \mathcal{E}_I^* \mathcal{E}_X^{(2n+1)} \left(\mathcal{M}_{f,m,i}^{(2n+1)} + \mathcal{M}_{f,m,i}^{(-1)} \right) \right] \right|^2 \\
& \quad \times \delta(E_f^0 - E_i^0 - 2n\omega_0) \\
& + 2\pi T \sum_m \left| \sum_n \mathcal{E}_I \mathcal{E}_X^{(2n+1)} \mathcal{M}_{f,m,i}^{(2n+1)} \right|^2 \delta(E_f^0 - E_m^0 - \omega_0) \\
& + 2\pi T \sum_m \left| \sum_n \mathcal{E}_I^* \mathcal{E}_X^{(2n+1)} \mathcal{M}_{f,m,i}^{(2n+1)} \right|^2 \delta(E_f^0 - E_m^0 + \omega_0) \\
& + 2\pi T \sum_m \left| \sum_n \mathcal{E}_I \mathcal{E}_X^{(2n+1)} \mathcal{M}_{f,m,i}^{(+1)} \right|^2 \delta(E_f^0 - E_m^0 - (2n+1)\omega_0) \\
& + 2\pi T \sum_m \left| \sum_n \mathcal{E}_I^* \mathcal{E}_X^{(2n+1)} \mathcal{M}_{f,m,i}^{(-1)} \right|^2 \delta(E_f^0 - E_m^0 - (2n+1)\omega_0).
\end{aligned} \tag{A.26}$$

The first and the second term of the right-hand side of Eq. (A.26) make peaks at $\omega_f = (2n+1)\omega_0$ and $2n\omega_0$ in the photoelectron spectrum, respectively. On the other hand, the delta functions in the other terms of Eq. (A.26) contain the energy of the intermediate state E_m , and if there is no resonance among intermediate states, these delta functions will vanish when the summation (or integration) over m is done. Therefore, the latter four terms of Eq. (A.26) are negligible compared to the first and the second term, and we finally get

$$\begin{aligned}
W_{i \rightarrow f} \simeq & 2\pi T \sum_n \left| \langle f | z | i \rangle \mathcal{E}_X^{(2n+1)} \right|^2 \delta(E_f^0 - E_i^0 - (2n+1)\omega_0) \\
& + 2\pi T \sum_n \left| \sum_m \left[\mathcal{E}_I \mathcal{E}_X^{(2n-1)} \left(\mathcal{M}_{f,m,i}^{(2n-1)} + \mathcal{M}_{f,m,i}^{(+1)} \right) + \mathcal{E}_I^* \mathcal{E}_X^{(2n+1)} \left(\mathcal{M}_{f,m,i}^{(2n+1)} + \mathcal{M}_{f,m,i}^{(-1)} \right) \right] \right|^2 \\
& \quad \times \delta(E_f^0 - E_i^0 - 2n\omega_0) \\
= & 2\pi T \sum_n \left| \langle f | z | i \rangle \mathcal{E}_X^{(2n+1)} \right|^2 \delta(E_f^0 - E_i^0 - (2n+1)\omega_0) \\
& + 2\pi T \sum_n \left| \left[\mathcal{E}_I \mathcal{E}_X^{(2n-1)} \left(\mathcal{M}_{(f,i)}^{(2n-1)} + \mathcal{M}_{(f,i)}^{(+1)} \right) + \mathcal{E}_I^* \mathcal{E}_X^{(2n+1)} \left(\mathcal{M}_{(f,i)}^{(2n+1)} + \mathcal{M}_{(f,i)}^{(-1)} \right) \right] \right|^2 \\
& \quad \times \delta(E_f^0 - E_i^0 - 2n\omega_0) \\
\stackrel{(2.57)}{=} & 2\pi T \sum_n \left| \langle f | z | i \rangle \right|^2 \mathcal{A}_X^{(2n+1)^2} \delta(E_f^0 - E_i^0 - (2n+1)\omega_0) \\
& + 2\pi T \sum_n \left| \left[\mathcal{E}_I \mathcal{E}_X^{(2n-1)} \left(\mathcal{M}_{(f,i)}^{(2n-1)} + \mathcal{M}_{(f,i)}^{(+1)} \right) + \mathcal{E}_I^* \mathcal{E}_X^{(2n+1)} \left(\mathcal{M}_{(f,i)}^{(2n+1)} + \mathcal{M}_{(f,i)}^{(-1)} \right) \right] \right|^2 \\
& \quad \times \delta(E_f^0 - E_i^0 - 2n\omega_0),
\end{aligned} \tag{A.27}$$

A Appendix

where

$$M_{(f,i)}^{(q)} \equiv \sum_m \mathcal{M}_{f,m,i}^{(q)} = \sum_m \frac{\langle f|z|m\rangle \langle m|z|i\rangle}{E_i^0 + q\omega_0 - E_m^0}. \quad (\text{A.28})$$

Thus Eq.(2.64) is obtained.

A.3 Calculation of the atomic phase

In this section we review and supplement the calculation presented by Toma and Muller [86] to show the procedure to calculate the atomic phase $\Delta\phi_{\text{atom}}^{(2n)}$ [Eq. (2.71)] appeared in §2.3. For convenience its definition is reproduced here:

$$\Delta\phi_{\text{atom}}^{(2n)} \stackrel{(2.71)}{\equiv} \arg\left(\sum_{i,f} \tilde{M}_{(f,i,+)}^{(2n+1)} (\tilde{M}_{(f,i,-)}^{(2n-1)})^*\right), \quad (\text{A.29})$$

where

$$\tilde{M}_{(f,i,\pm)}^{(2n\pm 1)} \stackrel{(2.67)}{\equiv} M_{(f,i)}^{(2n\mp 1)} + M_{(f,i)}^{(\pm 1)}, \quad (\text{A.30})$$

$$M_{(f,i)}^{(q)} \stackrel{(2.65)}{\equiv} \sum_m \frac{\langle f|z|m\rangle \langle m|z|i\rangle}{E_i^0 + q\omega_0 - E_m^0}. \quad (\text{A.31})$$

A.3.1 Separation of the radial part and the angular part

We assume that the electron is ionized from the highest orbital of the atom and other electrons remain the initial orbitals (single-active-electron approximation). We therefore represent the state of the atom by the state of the electron which is ionized. Let us consider that the initial state $|i\rangle$ of the rare-gas atom is the ground state: $|i\rangle = |n_i, l_i, m_i\rangle$, where n_i , l_i , and m_i are principal, angular momentum, and magnetic quantum number, respectively. For Ar $n_i = 3$, $l_i = 1$, and $m_i = \pm 1$ or 0.

Let us calculate the matrix element in which the final state is one of the continuum eigenstate of the system, $|f\rangle = |k_f, l_f, m_f\rangle$, where k_f corresponds to the magnitude of the wavevector of the ionized electron. From Eq. (A.31),

$$M_{(f,i)}^{(q)} \equiv \sum_m \frac{\langle k_f, l_f, m_f|z|m\rangle \langle m|z|n_i, l_i, m_i\rangle}{E_i^0 + q\omega_0 - E_m^0}. \quad (\text{A.32})$$

The intermediate state $|m\rangle$ runs both the bound states $|n_m, l_m, m_m\rangle$ and the continuum states $|k_m, l_m, m_m\rangle$. For simplicity, we define the integral-sum notation

$$\sum_{\tilde{k}_m} f(|\tilde{k}_m, l_m, m_m\rangle) \equiv \sum_{n_m} f(|n_m, l_m, m_m\rangle) + \int_{k_m} dk_m f(|k_m, l_m, m_m\rangle), \quad (\text{A.33})$$

where f is an arbitrary function of $|\tilde{k}_m, l_m, m_m\rangle$. Then,

$$\begin{aligned}
M_{(f,i)}^{(q)} &= \oint_{\tilde{k}_m} \sum_{l_m} \sum_{m_m} \frac{\langle k_f, l_f, m_f | z | \tilde{k}_m, l_m, m_m \rangle \langle \tilde{k}_m, l_m, m_m | z | n_i, l_i, m_i \rangle}{E_i^0 + q\omega_0 - E_m^0} \\
&= \oint_{\tilde{k}_m} \sum_{l_m} \sum_{m_m=-l_m}^{l_m} \frac{\int r^2 dr R_{k_f, l_f}^*(r) r R_{\tilde{k}_m, l_m}(r) \int r'^2 dr' R_{\tilde{k}_m, l_m}^*(r') r' R_{n_i, l_i}(r')}{E_i^0 + q\omega_0 - E_m^0} \\
&\quad \times \langle l_f, m_f | \cos \theta | l_m, m_m \rangle \langle l_m, m_m | \cos \theta | l_i, m_i \rangle \\
&= \oint_{\tilde{k}_m} \sum_{l_m} \sum_{m_m=-l_m}^{l_m} \frac{\int dr y_{k_f, l_f}^*(r) r y_{\tilde{k}_m, l_m}(r) \int dr' y_{\tilde{k}_m, l_m}^*(r') r' y_{n_i, l_i}(r')}{E_i^0 + q\omega_0 - E_m^0} \\
&\quad \times \langle l_f, m_f | \cos \theta | l_m, m_m \rangle \langle l_m, m_m | \cos \theta | l_i, m_i \rangle,
\end{aligned} \tag{A.34}$$

where $R_{k/n, l}(r)$ is the radial part of the spatial representation of $|k/n, l, m\rangle$ and $y_{k/n, l}(r) \equiv r R_{k/n, l}(r)$. The element $\langle l, m | \cos \theta | l', m' \rangle$ can be calculated analytically as (see Appendix A.4)

$$\langle l, m | \cos \hat{\theta} | l', m' \rangle = \delta_{mm'} \{ D_{l+1}^m \delta_{l+1, l'} + D_l^m \delta_{l-1, l'} \}, \tag{A.35}$$

where D_l^m is defined as [129]

$$D_l^m \equiv \sqrt{\frac{(l-m)(l+m)}{(2l-1)(2l+1)}}. \tag{A.36}$$

A.3.2 Summation over all the intermediate states

The problem is the calculation of the radial part in Eq. (A.34), which we write as

$$M_{|m\rangle} \equiv \oint_{\tilde{k}_m} \frac{\int dr y_{k_f, l_f}^*(r) r y_{\tilde{k}_m, l_m}(r) \int dr' y_{\tilde{k}_m, l_m}^*(r') r' y_{n_i, l_i}(r')}{E_i^0 + q\omega_0 - E_m^0}. \tag{A.37}$$

This integral diverges at $E_m^0 = E_i^0 + q\omega_0$. To avoid this divergence, a small imaginary part is added to the frequency of the fundamental as $\omega_0 \rightarrow \omega_0 + i\eta$ ($\eta > 0$). This corresponds to the situation where the amplitude of the field is zero when $t \rightarrow -\infty$ (see also [91, §4]). By using $\frac{1}{x-y \pm i\eta} = \text{P} \frac{1}{x-y} \mp i\pi \delta(x-y)$ [83, §5.18], where P means Cauchy's principal value, we separate $M_{|m\rangle}$ to its real and imaginary parts as

$$\lim_{\eta \rightarrow +0} M_{|m\rangle} = \text{Re}(M_{|m\rangle}) + i \text{Im}(M_{|m\rangle}), \tag{A.38}$$

$$\text{Re}(M_{|m\rangle}) \equiv \text{P} \oint_{\tilde{k}_m} \frac{\int dr y_{k_f, l_f}^*(r) r y_{\tilde{k}_m, l_m}(r) \int dr' y_{\tilde{k}_m, l_m}^*(r') r' y_{n_i, l_i}(r')}{E_i^0 + q\omega_0 - E_m^0}, \tag{A.39}$$

$$\text{Im}(M_{|m\rangle}) \equiv -\pi \int dr y_{k_f, l_f}^*(r) r y_{\tilde{k}_m^0, l_m}(r) \int dr' y_{\tilde{k}_m^0, l_m}^*(r') r' y_{n_i, l_i}(r'), \tag{A.40}$$

where \tilde{k}_m^0 is the wavenumber corresponding to the energy satisfying $E_m^0 = E_i^0 + q\omega_0$.

To sum over all the intermediate states in Eq. (A.39), Ref. [86] introduces the technique called Dalgarno–Lewis method, which is shown below.

A Appendix

First, $y_{\tilde{k}_m, l_m}(r)$ is an eigenfunction of the Hamiltonian

$$H_{l_m} \equiv -\frac{1}{2} \frac{d^2}{dr^2} + V(r) + \frac{l_m(l_m + 1)}{2r^2}. \quad (\text{A.41})$$

By using this Hamiltonian,

$$\begin{aligned} \text{Re}(M_{|m\rangle}) &\equiv \text{P} \sum_{\tilde{k}_m} \frac{\int dr y_{k_f, l_f}^*(r) r y_{\tilde{k}_m, l_m}(r) \int dr' y_{\tilde{k}_m, l_m}^*(r') r' y_{n_i, l_i}(r')}{E_i^0 + q\omega_0 - E_m^0} \\ &= \text{P} \sum_{\tilde{k}_m} \int dr y_{k_f, l_f}^*(r) r \frac{1}{E_i^0 + q\omega_0 - H_{l_m}} y_{\tilde{k}_m, l_m}(r) \int dr' y_{\tilde{k}_m, l_m}^*(r') r' y_{n_i, l_i}(r') \\ &= \text{P} \int dr \int dr' y_{k_f, l_f}^*(r) r \frac{1}{E_i^0 + q\omega_0 - H_{l_m}} \left[\sum_{\tilde{k}_m} y_{\tilde{k}_m, l_m}(r) y_{\tilde{k}_m, l_m}^*(r') \right] r' y_{n_i, l_i}(r') \quad (\text{A.42}) \\ &\simeq \text{P} \int dr \int dr' y_{k_f, l_f}^*(r) r \frac{1}{E_i^0 + q\omega_0 - H_{l_m}} \delta(r - r') r' y_{n_i, l_i}(r') \\ &= \text{P} \int dr y_{k_f, l_f}^*(r) r \frac{1}{E_i^0 + q\omega_0 - H_{l_m}} r y_{n_i, l_i}(r). \end{aligned}$$

In the above calculation, the completeness relation

$$\sum_{\tilde{k}_m} y_{\tilde{k}_m, l_m}(r) y_{\tilde{k}_m, l_m}^*(r') = \delta(r - r') \quad (\text{A.43})$$

is used (this relation holds because $y_{\tilde{k}_m, l_m}(r)$ is an eigenfunction of the Hamiltonian H_{l_m} [eq. (A.41)] and the sum and integral $\sum_{\tilde{k}_m}$ runs over all eigenfunctions of H_{l_m} .)

Now, we define an auxiliary wavefunction $\Psi(r)$, which satisfies

$$(E_i^0 + q\omega_0 - H_{l_m}) \Psi(r) = r y_{n_i, l_i}(r). \quad (\text{A.44})$$

With this wavefunction, we can rewrite Eq. (A.42) as

$$M_{|m\rangle} = \int dr y_{k_f, l_f}^*(r) r \Psi(r). \quad (\text{A.45})$$

We use the filtering technique presented in [86, §4] for this integral because both $y_{k_f, l_f}^*(r)$ and $\Psi(r)$ are oscillation functions.

□ **extended Numerov method** To solve Eq. (A.44), we extend the Numerov method [140] to inhomogeneous equations. First, Eq. (A.44) can be written as

$$\left(\frac{d^2}{dr^2} + f(r) \right) \Psi(r) = g(r), \quad (\text{A.46})$$

where

$$f(r) = 2 \left[E_i^0 + q\omega_0 - \frac{l_m(l_m + 1)}{2r^2} - V(r) \right], \quad (\text{A.47})$$

$$g(r) = 2r y_{n_i, l_i}(r). \quad (\text{A.48})$$

A.4 Matrix elements of spherical harmonics, $\cos \theta$ and $\cos^2 \theta$

When the functions $\Psi(r)$, $f(r)$, $g(r)$ are discretized as

$$r_n \equiv r_0 + n\Delta r, \quad (\text{A.49})$$

$$\Psi_n \equiv \Psi(r_n), \quad (\text{A.50})$$

$$f_n \equiv f(r_n), \quad (\text{A.51})$$

$$g_n \equiv g(r_n), \quad (\text{A.52})$$

the differential equation (A.46) leads to the recurrence formula (the proof is similar to the one for usual Numerov method)

$$\Psi_{n+1} = \frac{\left(2 - \frac{5\Delta r^2}{6} f_n\right) \Psi_n - \left(1 + \frac{\Delta r^2}{12} f_{n-1}\right) \Psi_{n-1} + \frac{\Delta r^2}{12} (g_{n+1} + 10g_n + g_{n-1})}{1 + \frac{\Delta r^2}{12} f_{n+1}}. \quad (\text{A.53})$$

Since the inhomogeneous part of Eq. (A.46) goes to zero when $r \rightarrow 0$, the auxiliary wavefunction $\Psi(r)$ obeys the same boundary condition as the radial wavefunctions obeys [141, § 35]: $\lim_{r \rightarrow 0} \Psi(r) = 0$. The initial slope $\lim_{r \rightarrow 0} \Psi'(r)$ is determined by the method described in [86, §2].

A.4 Matrix elements of spherical harmonics, $\cos \theta$ and $\cos^2 \theta$

Integrals of products of three spherical harmonics $\langle Y_{JM} | Y_{jm} | Y_{J'M'} \rangle$ can be represented in terms of Clebsch–Gordan coefficients [71, § 12.9]:

$$\begin{aligned} \langle Y_{JM} | Y_{jm} | Y_{J'M'} \rangle &\equiv \int_0^{2\pi} d\phi \int_0^\pi \sin \theta d\theta Y_{JM}(\theta, \phi)^* Y_{jm}(\theta, \phi) Y_{J'M'}(\theta, \phi) \\ &= \sqrt{\frac{(2j+1)(2J'+1)}{4\pi(2J+1)}} \langle J'M', jm | JM \rangle \langle J'0, j0 | J0 \rangle. \end{aligned} \quad (\text{A.54})$$

Clebsch–Gordan coefficients $\langle J'M', jm | JM \rangle$ is related to the Wigner's 3- j symbol as [142, § 5.10]

$$\langle J'M', jm | JM \rangle = (-1)^{J'-j+m} \sqrt{2J+1} \begin{pmatrix} J' & j & J \\ M' & m & -M \end{pmatrix}. \quad (\text{A.55})$$

With this relation, Eq. (A.54) becomes²

$$\langle Y_{JM} | Y_{jm} | Y_{J'M'} \rangle = (-1)^m \sqrt{\frac{(2j+1)(2J'+1)(2J+1)}{4\pi}} \begin{pmatrix} J' & j & J \\ M' & m & -M \end{pmatrix} \begin{pmatrix} J' & j & J \\ 0 & 0 & 0 \end{pmatrix}. \quad (\text{A.56})$$

The Wigner's 3- j symbol can be calculated by using `gs1_sf_coupling_3j` function in the GNU Scientific Library (GSL) [75]³. Note that $\langle Y_{JM} | Y_{jm} | Y_{J'M'} \rangle$ is nonzero only when all of the following conditions hold: [71, § 12.9]

$$\left\{ \begin{array}{l} |J - J'| \leq j \leq J + J', \\ M = m + M', \\ J' + j + J \text{ is an even integer.} \end{array} \right. \quad (\text{A.57})$$

² Equation (A.56) differs in its sign from Eq. (3.119) of Ref. [143, § 3.9] because the integrand of Eq. (A.56) is $Y_{JM}^* Y_{jm} Y_{J'M'}$ while the integrand in Ref. [143, § 3.9] is $Y_{JM} Y_{jm} Y_{J'M'}$.

³Note that the arguments of `gs1_sf_coupling_3j` function are given in half-integer units. See the manual of GSL [75, § 7.8.1].

A Appendix

□ $\cos \theta$ From Eq. (A.56) and

$$Y_{1,0} = \sqrt{\frac{3}{4\pi}} \cos \theta, \quad (\text{A.58})$$

we can calculate the matrix element of $\cos \theta$ as

$$\begin{aligned} \langle J, M | \cos \theta | J', M' \rangle &= \sqrt{\frac{4\pi}{3}} \langle Y_{JM} | Y_{1,0} | Y_{J'M'} \rangle \\ &= \sqrt{(2J'+1)(2J+1)} \begin{pmatrix} J' & 1 & J \\ M' & 0 & -M \end{pmatrix} \begin{pmatrix} J' & 1 & J \\ 0 & 0 & 0 \end{pmatrix} \\ &= \delta_{MM'} \left\{ D_{J+1}^M \delta_{J+1, J'} + D_J^M \delta_{J-1, J'} \right\}, \end{aligned} \quad (\text{A.59})$$

where D_J^M is defined as $D_J^M \equiv \sqrt{\frac{(J-M)(J+M)}{(2J-1)(2J+1)}}$ [129].

□ $\cos^2 \theta$ From Eq. (A.59) we readily obtain

$$\begin{aligned} \langle J, M | \cos^2 \theta | J', M' \rangle &= \sum_{J'', M''} \langle J, M | \cos \theta | J'', M'' \rangle \langle J'', M'' | \cos \theta | J', M' \rangle \\ &= \delta_{MM'} \left\{ \left[(D_J^M)^2 + (D_{J+1}^M)^2 \right] \delta_{J, J'} + D_{J+1}^M D_{J+2}^M \delta_{J+2, J'} + D_{J-1}^M D_J^M \delta_{J-2, J'} \right\}. \end{aligned} \quad (\text{A.60})$$

A.5 Calculation of the density matrix of molecules at the thermal equilibrium

Here we derive the expression of the density matrix (3.40) for molecular rotational states appeared in § 3.5.2. The density matrix for the system with a temperature T_{rot} is given by [144]

$$\hat{\rho}_{\text{eq}}(t=0) = \frac{e^{-\hat{H}_0/(k_B T_{\text{rot}})}}{\text{Tr} e^{-\hat{H}_0/(k_B T_{\text{rot}})}}. \quad (\text{A.61})$$

where \hat{H}_0 is the Hamiltonian of the system. For a rigid-rotor with the rotational constant B , the Hamiltonian of the rotational states becomes $B\hat{J}^2$. The trace in Eq. (A.61) runs over all possible states of the system. If a molecule can belong to all the rotational states $\{|J, M\rangle | J = 0, \dots, +\infty, M = -J, \dots, J\}$, Eq. (A.61) becomes

$$\begin{aligned} \hat{\rho}_{\text{eq}}(t=0) &= \frac{e^{-\hat{H}_0/(k_B T_{\text{rot}})}}{\sum_{J=0}^{+\infty} \sum_{M=-J}^J \langle J, M | e^{-\hat{H}_0/(k_B T)} | J, M \rangle} \sum_{J_0=0}^{+\infty} \sum_{M_0=-J_0}^{J_0} |J_0, M_0\rangle \langle J_0, M_0| \\ &= \sum_{J_0=0}^{+\infty} \sum_{M_0=-J_0}^{J_0} \frac{e^{-BJ_0(J_0+1)/(k_B T_{\text{rot}})}}{\sum_{J=0}^{+\infty} \sum_{M=-J}^J e^{-BJ(J+1)/(k_B T_{\text{rot}})}} |J_0, M_0\rangle \langle J_0, M_0|. \end{aligned} \quad (\text{A.62})$$

However, when the molecule contains identical nuclei, some of the rotational states may be excluded by the following reason [93, § 10.5]: from the relation between spin and statistics [141, § 61], an interchange of two identical particles with integral spin unchanges the wavefunction, while that with

A.5 Calculation of the density matrix of molecules at the thermal equilibrium

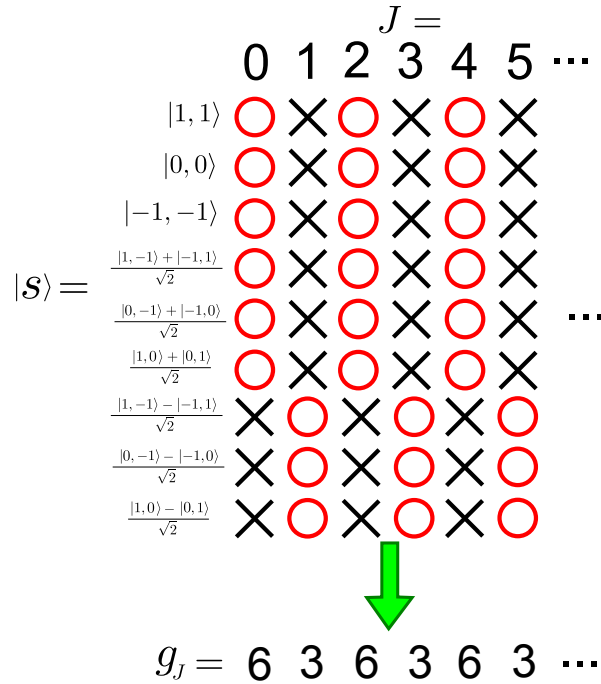


Figure A.2: Calculation of the degeneracy g_J for $^{14}\text{N}_2$. Since nucleus ^{14}N has spin $I = 1$, the interchange of two ^{14}N must unchange the overall wavefunction. The sum of two spin-1 state can have nine possible spin states, of which 6 states are symmetric and 3 are antisymmetric to the interchange of the spin state. To conserve the symmetry, J have only even integers for symmetric spin states and only odd integers for antisymmetric spin states. Therefore, the degeneracy g_J is 6 for even J and 3 for odd J .

half-integral spin only changes sign. Let us consider a linear molecule which is symmetric about the rotation center. For this molecule, the interchange of the two identical nuclei is equivalent to a series of operation: (1)the rotation of the whole molecule by π , (2)inversion of the electronic wavefunction about the center, followed by reflection of it in a plane perpendicular to the rotational axis, and (3)permutation of the nuclear spin state. Because of the equivalence of these two processes, the operation (1)–(3) unchanges the wavefunction when the nuclei have integer spin and changes sign when they have half-integer spin. The rotational wavefunction $|J, M\rangle$ is multiplied by $(-1)^J$ by the operation(1), Operations (2) and (3) give the change of sign depending on the symmetry of the electronic wavefunction and that of the the spin state of the nuclei, respectively. Therefore, J must have only odd or even values, depending on the electronic and nuclear states.

For the calculation of molecular alignment, it is not convenient to restrict the rotational states which molecules can belong to. In the following we show that for symmetric molecules the density matrix can also be written as the sum of all the $|J, M\rangle$'s like Eq. (3.40).

Here we consider only one electronic state, so the values which J can take are determined by the spin state $|s\rangle$ of the nuclei. Let $\mathcal{R}_{|s\rangle}$ denotes the set of possible J 's under the nuclear spin state $|s\rangle$. We neglect the spin-spin interaction between nuclei. Then, the Hamiltonian \hat{H}_0 for a nuclear spin state

A Appendix

can be regarded as an identity operator **1**:

$$\hat{H}_0 = B\hat{J}^2 \otimes \mathbf{1}. \quad (\text{A.63})$$

When we write the tensor product of $|J, M\rangle$ and $|s\rangle$ as $|J, M, s\rangle$, the numerator of the density operator (A.61) is expanded as

$$\begin{aligned} e^{-\hat{H}_0/(k_B T_{\text{rot}})} &= e^{-\hat{H}_0/(k_B T_{\text{rot}})} \sum_{|s\rangle} \sum_{J \in \mathcal{R}_{|s\rangle}} \sum_{M=-J}^J |J, M, s\rangle \langle J, M, s| \\ &= \sum_{|s\rangle} \sum_{J \in \mathcal{R}_{|s\rangle}} \sum_{M=-J}^J e^{-BJ(J+1)/(k_B T_{\text{rot}})} |J, M, s\rangle \langle J, M, s| \end{aligned} \quad (\text{A.64})$$

Let us write the number of the spin state $|s\rangle$ which allows the rotational state to have a value J as g_J (see Fig. A.2 for an example for $^{14}\text{N}_2$). g_J corresponds to the degeneracy of the state $|J, M\rangle$. Using g_J , we can interchange the sum over $|s\rangle$ and that over J , and expand the range of J to all the integers:

$$\begin{aligned} e^{-\hat{H}_0/(k_B T_{\text{rot}})} &= \sum_{|s\rangle} \sum_{J \in \mathcal{R}_{|s\rangle}} \sum_{M=-J}^J e^{-BJ(J+1)/(k_B T_{\text{rot}})} |J, M, s\rangle \langle J, M, s| \\ &= \sum_{J=0}^{+\infty} g_J \sum_{|s\rangle} \sum_{M=-J}^J e^{-BJ(J+1)/(k_B T_{\text{rot}})} |J, M, s\rangle \langle J, M, s| \\ &= \sum_{J=0}^{+\infty} g_J \sum_{M=-J}^J e^{-BJ(J+1)/(k_B T_{\text{rot}})} |J, M\rangle \langle J, M| \otimes \sum_{|s\rangle} |s\rangle \langle s| \\ &= \sum_{J=0}^{+\infty} g_J \sum_{M=-J}^J e^{-BJ(J+1)/(k_B T_{\text{rot}})} |J, M\rangle \langle J, M| \otimes \mathbf{1}. \end{aligned} \quad (\text{A.65})$$

In the same way, the denominator of (A.61) can be calculated as

$$\begin{aligned} \text{Tr} e^{-\hat{H}_0/(k_B T_{\text{rot}})} &= \sum_{|s\rangle} \sum_{J \in \mathcal{R}_{|s\rangle}} \sum_{M=-J}^J \langle J, M, s| e^{-\hat{H}_0/(k_B T_{\text{rot}})} |J, M, s\rangle \\ &= \sum_{|s\rangle} \sum_{J \in \mathcal{R}_{|s\rangle}} \sum_{M=-J}^J e^{-BJ(J+1)/(k_B T_{\text{rot}})} \langle J, M, s|J, M, s\rangle \\ &= \sum_{J=0}^{+\infty} g_J \sum_{|s\rangle} \sum_{M=-J}^J e^{-BJ(J+1)/(k_B T_{\text{rot}})} \langle J, M, s|J, M, s\rangle \\ &= \sum_{J=0}^{+\infty} g_J \sum_{M=-J}^J e^{-BJ(J+1)/(k_B T_{\text{rot}})} \langle J, M|J, M\rangle \cdot \sum_{|s\rangle} \langle s|s\rangle \\ &= \sum_{J=0}^{+\infty} g_J \sum_{M=-J}^J e^{-BJ(J+1)/(k_B T_{\text{rot}})} \langle J, M|J, M\rangle. \end{aligned} \quad (\text{A.66})$$

Therefore, Eq. (A.61) becomes

$$\hat{\rho}_{\text{eq}}(t=0) = \sum_{J_0=0}^{+\infty} \sum_{M_0=-J_0}^{+J_0} \frac{g_{J_0} \exp[-BJ_0(J_0+1)/(k_B T_{\text{rot}})]}{\sum_{J, M} g_J \exp[-BJ(J+1)/(k_B T_{\text{rot}})]} |J_0, M_0\rangle \langle J_0, M_0| \otimes \mathbf{1}. \quad (\text{A.67})$$

The identity operator for the spin state is not necessary to be concerned in the usual calculation of the molecular alignment, so we consider only the density matrix operating on the rotational state, which is the one presented in Eq. (3.40).

A.6 Calculation of the Abel transform of the basis in the BASEX method

Here we give the derivation of Eq. (3.20) in § 3.3.5.3. By using the binomial theorem and the formula [145, Eq. (7.4.4)]

$$\int_0^{+\infty} t^{2n} e^{-at^2} = \frac{1 \cdot 3 \dots (2n-1)}{2^{n+1} a^n} \sqrt{\frac{\pi}{a}}, \quad (\text{A.68})$$

$\chi_k(x) \equiv 2 \int_{|x|}^{+\infty} \frac{r\rho_k(r)}{\sqrt{r^2-x^2}} dr$ [Eq. (3.19)] can be calculated as

$$\begin{aligned} \chi_k(x) &\equiv 2 \int_{|x|}^{+\infty} \frac{r\rho_k(r)}{\sqrt{r^2-x^2}} dr \\ &= 2 \int_0^{+\infty} \rho_k(\sqrt{u^2+x^2}) du \quad (\sqrt{r^2-x^2} \equiv u) \\ &\stackrel{(3.16)}{=} 2 \left(\frac{e}{k^2}\right)^{k^2} \int_0^{+\infty} \left[\left(\frac{u}{\sigma}\right)^2 + \left(\frac{x}{\sigma}\right)^2\right]^{k^2} \exp\left[-\left(\frac{u}{\sigma}\right)^2 - \left(\frac{x}{\sigma}\right)^2\right] du \\ &= 2 \left(\frac{e}{k^2}\right)^{k^2} e^{-(x/\sigma)^2} \int_0^{+\infty} \sum_{l=0}^{k^2} \frac{(k^2)!}{l!(k^2-l)!} \left(\frac{u}{\sigma}\right)^{2l} \left(\frac{x}{\sigma}\right)^{2(k^2-l)} e^{-(u/\sigma)^2} du \\ &\stackrel{(3.16)}{=} 2\rho_k(x) \sum_{l=0}^{k^2} \left(\frac{x}{\sigma}\right)^{-2l} \frac{(k^2)!}{l!(k^2-l)!} \int_0^{+\infty} \left(\frac{u}{\sigma}\right)^{2l} e^{-(u/\sigma)^2} du \quad (\text{A.69}) \\ &= 2\sigma\rho_k(x) \left[\int_0^{+\infty} e^{-t^2} dt + \sum_{l=1}^{k^2} \left(\frac{x}{\sigma}\right)^{-2l} \frac{(k^2)!}{l!(k^2-l)!} \int_0^{+\infty} t^{2l} e^{-t^2} dt \right] \quad (u/\sigma \equiv t) \\ &= 2\sigma\rho_k(x) \left\{ \sqrt{\pi} + \sum_{l=1}^{k^2} \left(\frac{x}{\sigma}\right)^{-2l} \frac{(k^2)!}{l!(k^2-l)!} \left[\left(\frac{1}{2}\right) \cdot \left(\frac{3}{2}\right) \cdot \dots \cdot \left(\frac{2l-1}{2}\right) \right] \sqrt{\pi} \right\} \\ &= 2\sqrt{\pi}\sigma\rho_k(x) \left[1 + \sum_{l=1}^{k^2} \left(\frac{x}{\sigma}\right)^{-2l} \prod_{m=1}^l \frac{(k^2+1-m)(m-1/2)}{m} \right]. \end{aligned}$$

Thus Eq. (3.20) is proved.

A.7 Note on classical trajectory Monte Carlo method

This is a note for the classical trajectory Monte Carlo (CTMC) method used for the calculation shown in Fig 5.11(b) of §5.3.3. This note is based on Ref. [139], CTMC was first presented in Ref. [146] and also used in the work of Soifer *et al.* [62]. We only consider one-dimensional problem in a symmetric potential.

A Appendix

A.7.1 classical theory

The classical Hamiltonian for an electron in a potential $V(x)$ and a laser field $F(t)$ is written as

$$H(x, p) = H_0(x, p) + xF(t), \quad (\text{A.70})$$

$$H_0(x, p) = \frac{p^2}{2} + V(x). \quad (\text{A.71})$$

The classical behavior of the position x and the momentum p of the electron can be obtained by solving the Hamilton equations

$$\frac{\partial x(t)}{\partial t} = \frac{\partial H(x, p)}{\partial p} = p_i(t) \quad (\text{A.72})$$

$$\frac{\partial p_i(t)}{\partial t} = -\frac{\partial H(x, p)}{\partial x} = -\frac{\partial V(x)}{\partial x} - F(t) \quad (\text{A.73})$$

with the fourth order Runge-Kutta method [133, § 17.1].

A.7.2 Wigner distribution with cutoff

In Ref. [62, 139], the initial distribution of the position x and the momentum p of an electron is given by the Wigner phase-space distribution associated with the classical energy [147].

A standard Wigner distribution is [147].

$$\rho_W(x, p) = \frac{1}{2\pi} \int d\chi e^{-i p \chi} \psi_0^*(x - \chi/2) \psi_0(x + \chi/2) \quad (\text{A.74})$$

where $\psi_0(x)$ is the ground state of the laser-field-free quantum Hamiltonian

$$\hat{H}_0(x, p) = -\frac{1}{2} \frac{d^2}{dx^2} + V(x). \quad (\text{A.75})$$

The energy distribution is obtained from this (x, p) distribution as

$$f_W(E) = \iint dx dp \rho_W(x, p) \delta(H_0(x, p) - E). \quad (\text{A.76})$$

By using the relation [146]

$$\int_{-\infty}^{+\infty} g(x) \delta(f(x)) = \sum_{f(x_0)=0} \left| \frac{df(x)}{dx} \right|_{x=x_0}^{-1} g(x_0), \quad (\text{A.77})$$

the $\delta(H_0(x, p) - E)$ in Eq. (A.76) becomes

$$\begin{aligned} \delta(H_0(x, p) - E) &= \sum_{p_0=\pm \sqrt{2[E-V(x)]}} \left(\left| \frac{\partial H_0}{\partial p} \right|_{p=p_0} \right)^{-1} \delta(p - p_0) \\ &= \sum_{p_0=\pm \sqrt{2[E-V(x)]}} \frac{1}{|p_0|} \delta(p - p_0) \end{aligned} \quad (\text{A.78})$$

Then,

$$\begin{aligned}
f_W(E) &= \iint dx dp \sum_{p_0 = \pm \sqrt{2[E-V(x)]}} \rho_W(x, p) \frac{1}{|p_0|} \delta(p - p_0) \\
&= \int dx \sum_{p_0 = \pm \sqrt{2[E-V(x)]}} \frac{1}{|p_0|} \rho_W(x, p_0) \\
&= \frac{1}{2\pi} \int_{-\infty}^{+\infty} dx \sum_{p_0 = \pm \sqrt{2[E-V(x)]}} \frac{1}{|p_0|} \int_{-\infty}^{+\infty} d\chi e^{-ip_0\chi} \psi_0^*(x - \chi/2) \psi_0(x + \chi/2),
\end{aligned} \tag{A.79}$$

and we obtain⁴

$$\begin{aligned}
f_W(E) &= \frac{2}{\pi} \int_{E-V(x)>0} dx \frac{1}{\sqrt{2[E-V(x)]}} \\
&\quad \times \int d\chi \cos(2\chi \sqrt{2[E-V(x)]}) \psi_0^*(x - \chi) \psi_0(x + \chi).
\end{aligned} \tag{A.80}$$

□ **truncated energy distribution** The $f_W(E)$ derived from quantum mechanics includes a region where $f < 0$, which is not suitable for classical calculation. In Ref. [139] the distribution is truncated at a cutoff E_0^+ as

$$f_{Wt}(E) = \begin{cases} 0 & (E < E_{\min} \text{ or } E > E_0^+) \\ f_W(E)/N_W & (E_{\min} \leq E < E_0^+). \end{cases} \tag{A.81}$$

E_{\min} and N_W in Eq. (A.81) are defined by the following equations:

$$\left\{ \begin{aligned} \int_{E_{\min}}^{E_0^+} f_{Wt}(E) dE &= 1, \\ \int_{E_{\min}}^{E_0^+} f_{Wt}(E) E dE &= E_0, \\ \frac{\int_{E_{\min}}^{E_0^+} f_W(E) E dE}{\int_{E_{\min}}^{E_0^+} f_W(E) dE} &= E_0, \\ \int_{E_{\min}}^{E_0^+} f_W(E) dE &= N_W. \end{aligned} \right. \tag{A.82}$$

In Ref. [139] the energy cutoff E^+ is defined based on the corresponding principle:

$$\iint_{E \leq E_0^+} dx dp = 2\pi \tag{A.83}$$

(note that in atomic units, $\hbar = 1$). The condition $E \leq E_0^+$ is equivalent to $\frac{p^2}{2} + V(x) \leq E_0^+$, that is, $|p| \leq \sqrt{2} \sqrt{E_0^+ - V(x)}$. Since $|p|$ is a real value, $V(x) \leq E_0^+$. If we define $x_0 > 0$ as the position such

⁴The integrand in this integral diverges at $E = V(x)$, so the double-exponential integral method [148] is needed for numerical calculation.

A Appendix

that $V(\pm x_0) = E_0^+$,

$$\begin{aligned} \iint_{E \leq E_0^+} dx dp &= \int_{-x_0}^{x_0} \left[\int_{-\sqrt{2}\sqrt{E_0^+ - V(x)}}^{\sqrt{2}\sqrt{E_0^+ - V(x)}} dp \right] dx \\ &= 4\sqrt{2} \int_0^{x_0} \sqrt{E_0^+ - V(x)} dx. \end{aligned} \quad (\text{A.84})$$

Thus, E_0^+ can be obtained by solving

$$\begin{cases} \int_0^{x_0} \sqrt{E_0^+ - V(x)} dx = \frac{\pi}{2\sqrt{2}}, \\ V(\pm x_0) = E_0^+. \end{cases} \quad (\text{A.85})$$

□ **(x, p) distribution** The (x, p) distribution $\rho_{\text{Wt}}(x, p)$ is obtained from the truncated energy distribution $f_{\text{Wt}}(E)$ as

$$\begin{aligned} \rho_{\text{Wt}}(x, p) &= \int_{E_{\min}}^{E_0^+} dE f_{\text{Wt}}(E) \rho_{\text{M}}(E; x, p) \\ &= \int_{E_{\min}}^{E_0^+} dE f_{\text{Wt}}(E) \kappa(E) \delta(H_0(x, p) - E) \\ &= \begin{cases} f_{\text{W}}(H_0(x, p)) \kappa(H_0(x, p)) / N_{\text{W}} & (E_{\min} \leq H_0(x, p) \leq E_0^+) \\ 0 & (\text{otherwise}) \end{cases} \end{aligned} \quad (\text{A.86})$$

Here, $\rho_{\text{M}}(E; x, p)$ is a microcanonical density

$$\begin{aligned} \rho_{\text{M}}(E; x, p) &= \kappa(E) \delta(H_0(x, p) - E) \\ &\stackrel{\text{Eq. (A.78)}}{=} \kappa(E) \sum_{p_0 = \pm \sqrt{2[E - V(x)]}} \frac{1}{|p_0|} \delta(p - p_0) \\ &= \begin{cases} \kappa(E) \frac{\delta(p - \sqrt{2[E - V(x)]}) + \delta(p + \sqrt{2[E - V(x)]})}{\sqrt{2[E - V(x)]}} & (E > V(x)) \\ 0 & (E \leq V(x)) \end{cases} \end{aligned} \quad (\text{A.87})$$

where $\kappa(E)$ is a normalization constant which satisfies $\iint dx dp \rho_{\text{M}}(E; x, p) = 1$. Since

$$\begin{aligned} 1 &= \iint dx dp \kappa(E) \sum_{p_0 = \pm \sqrt{2[E - V(x)]}} \frac{1}{|p_0|} \delta(p - p_0) \\ &= 2\kappa(E) \int_{E > V(x)} dx \frac{1}{\sqrt{2[E - V(x)]}}, \end{aligned} \quad (\text{A.88})$$

we get

$$\kappa(E) = \frac{1}{2} \left[\int_{E > V(x)} dx \frac{1}{\sqrt{2[E - V(x)]}} \right]^{-1}. \quad (\text{A.89})$$

By reference to Ref. [149], we use the ‘‘Mersenne Twister’’ [150] as a generator of random numbers, and obtain the distribution $\rho_{\text{Wt}}(x, p)$ by using the rejection method [133, § 7.3.6]

A.7.3 Scaling

From the Hamiltonian (A.75),

$$\left(-\frac{1}{2} \frac{d^2}{dx^2} + V(x)\right) \psi(x) = E \psi(x). \quad (\text{A.90})$$

If we change $x \rightarrow x/\rho^2$,

$$\left(-\frac{\rho^2}{2} \frac{d^2}{dx^2} + V(x/\rho)\right) \psi(x/\rho) = E \psi(x/\rho), \quad (\text{A.91})$$

and therefore

$$\left(-\frac{1}{2} \frac{d^2}{dx^2} + \frac{1}{\rho^2} V(x/\rho)\right) \psi(x/\rho) = \frac{E}{\rho^2} \psi(x/\rho). \quad (\text{A.92})$$

From the above equations, when we find a potential which gives the eigenstate $\psi(x)$ with energy E we can get the state with its energy $\rho^{-2}E$ by setting the potential as $\rho^{-2}V(x/\rho)$. This property is useful when we look for a set of potentials which have the same ionization potential but different shapes.

A.7.4 Softcore potential

Let us consider a one-dimensional scaled hydrogen with a soft-core potential

$$V(x) = -\frac{Z_e}{\sqrt{x^2 + \alpha^2}}, \quad (\text{A.93})$$

where $\alpha^2 = 2/Z_e^2$ is a soft-core parameter and Z_e is the effective charge corresponding to the ionization potential I_p as

$$Z_e = \sqrt{2I_p}. \quad (\text{A.94})$$

$\psi_0(x)$ for $\alpha^2 = 2/Z_e^2$ can be written analytically as [151]

$$\psi(x) = \left(1 + Z_e \sqrt{x^2 + \frac{2}{Z_e^2}}\right) e^{-Z_e \sqrt{x^2 + \frac{2}{Z_e^2}}}, \quad (\text{A.95})$$

with its eigenvalue $E_0 = -Z_e^2/2 = -I_p$. Since $x_0 = \sqrt{\frac{Z_e^2}{E_0^+} - \alpha^2}$, the cutoff of the truncated energy distribution becomes [Eq.(A.85)]

$$\int_0^{\sqrt{\frac{Z_e^2}{E_0^+} - \alpha^2}} \sqrt{E_0^+ + \frac{Z_e}{\sqrt{x^2 + \alpha^2}}} dx = \frac{\pi}{2\sqrt{2}}. \quad (\text{A.96})$$

A.8 Calculation of the recombination transition dipole moment of atoms

This is the note for the calculation of the photorecombination transition dipole moment for an Ar atom shown in Fig. 5.12(a) in §5.3.4. This note is based on the paper by Le *et al.* [59].

A Appendix

A.8.1 The stationary continuum state

In preparation for the calculation of the transition dipole moment, we first consider the stationary continuum state with the energy E and the angular momentum quantum number l :

$$\langle \mathbf{r} | \Psi_{El} \rangle = R_{El}(r) Y_{lm}(\Omega_{\mathbf{r}}). \quad (\text{A.97})$$

Let us define the normalized radial wavefunction $y_{El}(r)$ as

$$y_{El}(r) \equiv r R_{El}(r). \quad (\text{A.98})$$

This function is a solution of the differential equation

$$\left\{ \frac{d^2}{dr^2} + 2 \left[E - \frac{l(l+1)}{2r^2} - V(r) \right] \right\} y_{El}(r) = 0, \quad (\text{A.99})$$

which satisfies the following boundary condition at $r \rightarrow +\infty$ [39, 55]

$$y_{El}(r) \simeq C [F_l(\eta; kr) \cos \delta_l + G_l(\eta; kr) \sin \delta_l]. \quad (\text{A.100})$$

Here, $F_l(\eta; kr)$ and $G_l(\eta; kr)$ are Coulomb functions [145, § 14] which satisfy

$$F_l(\eta; \rho) \underset{\rho \rightarrow +\infty}{\sim} \sin \left(\rho - \eta \ln(2\rho) - \frac{\pi l}{2} + \sigma_l \right), \quad (\text{A.101})$$

$$G_l(\eta; \rho) \underset{\rho \rightarrow +\infty}{\sim} \cos \left(\rho - \eta \ln(2\rho) - \frac{\pi l}{2} + \sigma_l \right), \quad (\text{A.102})$$

where

$$\sigma_l \equiv \arg \Gamma(l+1+i\eta) \quad (\text{A.103})$$

is a Coulomb phase. The δ_l in Eq. (A.100) is a phase shift due to the non-Coulomb potential, which can be determined as [152]

$$\delta_l = \arctan \left(\frac{(y'/y)F - F'}{G' - (y'/y)G} \right). \quad (\text{A.104})$$

A.8.2 The transition dipole moment from a continuum state to a bound state

Let us consider a state of an electron $|\Psi_{\mathbf{k}}^+\rangle$ which recombines with the parent ion and has the wavevector \mathbf{k} far from the parent ion. The spatial representation of $|\Psi_{\mathbf{k}}^+\rangle$ satisfies the out-going wave boundary condition [59, 153]⁵

$$\langle \mathbf{r} | \Psi_{\mathbf{k}}^+ \rangle = \frac{1}{4\pi} \frac{1}{\sqrt{k}} \sum_{l=0}^{+\infty} i^l (2l+1) \exp[i(\sigma_l + \delta_l)] \frac{y_{El}(r)}{r} P_l(\cos \theta), \quad (\text{A.105})$$

⁵It may sound strange that the recombining electron satisfying not the ‘‘in-coming’’ wave boundary condition but the ‘‘out-going’’ wave boundary condition. The name of the ‘‘out-going’’ wave boundary condition comes from the elastic scattering problem, in which an electron with a given wavevector \mathbf{k} is scattered by a potential and the spherical wave ‘‘out-goes’’ from the potential.

A.8 Calculation of the recombination transition dipole moment of atoms

where θ is the angle between \mathbf{r} and \mathbf{k} , $y_{El}(r)$ is the normalized radial wavefunction defined in Eq. (A.98), and σ_l and δ_l are the phase determined by Eqs. (A.103) and (A.104), respectively. By using the addition theorem for spherical harmonics [71, §12.8], we get

$$\langle \mathbf{r} | \Psi_{\mathbf{k}}^+ \rangle = \frac{1}{\sqrt{k}} \sum_{l=0}^{+\infty} \sum_{m=-l}^l i^l \exp[i(\sigma_l + \delta_l)] \frac{y_{El}(r)}{r} Y_{lm}(\Omega_{\mathbf{r}}) Y_{lm}^*(\Omega_{\mathbf{k}}). \quad (\text{A.106})$$

From the spherical symmetry of the atom, its bound state can be written as $\langle \mathbf{r} | \Psi_i \rangle = \frac{y_{m_b l_b}(r)}{r} Y_{l_b m_b}(\Omega_{\mathbf{r}})$. Therefore, the dipole moment $\langle \Psi_i | \mathbf{r} \cdot \mathbf{n} | \Psi_{\mathbf{k}}^+ \rangle$ becomes

$$\begin{aligned} & \langle \Psi_i | \mathbf{r} \cdot \mathbf{n} | \Psi_{\mathbf{k}}^+ \rangle \\ &= \frac{1}{\sqrt{k}} \sum_{l=0}^{+\infty} \sum_{m=-l}^l i^l \exp[i(\sigma_l + \delta_l)] \int dr r^3 \frac{y_{m_b l_b}(r)}{r} Y_{l_b m_b}^*(\Omega_{\mathbf{r}}) (\mathbf{r} \cdot \mathbf{n}) \frac{y_{El}(r)}{r} Y_{lm}(\Omega_{\mathbf{r}}) Y_{lm}^*(\Omega_{\mathbf{k}}). \end{aligned} \quad (\text{A.107})$$

Since $\mathbf{r} \cdot \mathbf{n} = r \cos \theta$ and $Y_{lm}^*(\Omega_{\mathbf{k}}) = Y_{lm}^*(0, \phi) = \sqrt{\frac{2l+1}{4\pi}} \delta_{m,0}$ [71, §12.6], we obtain

$$\begin{aligned} \langle \Psi_i | \mathbf{r} \cdot \mathbf{n} | \Psi_{\mathbf{k}}^+ \rangle &= \frac{1}{\sqrt{4\pi k}} \sum_{l=0}^{+\infty} i^l \sqrt{2l+1} \exp[i(\sigma_l + \delta_l)] \int dr r^3 \frac{y_{m_b l_b}(r)}{r} Y_{l_b m_b}^*(\Omega_{\mathbf{r}}) r \cos \theta \frac{y_{El}(r)}{r} Y_{l0}(\Omega_{\mathbf{r}}) \\ &= \frac{1}{\sqrt{4\pi k}} \sum_{l=0}^{+\infty} i^l \sqrt{2l+1} \exp[i(\sigma_l + \delta_l)] \mathcal{R}_{l_b l} \int d\Omega_{\mathbf{r}} Y_{l_b m_b}^*(\Omega_{\mathbf{r}}) \cos \theta Y_{l0}(\Omega_{\mathbf{r}}), \end{aligned} \quad (\text{A.108})$$

where

$$\mathcal{R}_{l_b l} \equiv \int_0^{+\infty} dr y_{m_b l_b}(r) r y_{El}(r). \quad (\text{A.109})$$

Substituting $\int d\Omega_{\mathbf{r}} Y_{l_b m_b}^*(\Omega_{\mathbf{r}}) \cos \theta Y_{lm}(\Omega_{\mathbf{r}}) = \delta_{m, m_b} (D_{l_b}^{m_b} \delta_{l_b-1, l} + D_{l_b+1}^{m_b} \delta_{l_b+1, l})$ (see Appendix §A.4), we obtain

$$\begin{aligned} \langle \Psi_i | \mathbf{r} \cdot \mathbf{n} | \Psi_{\mathbf{k}}^+ \rangle &= \delta_{m_b, 0} \frac{1}{\sqrt{4\pi k}} \left\{ i^{l_b-1} \sqrt{2l_b-1} \exp[i(\sigma_{l_b-1} + \delta_{l_b-1})] \mathcal{R}_{l_b l_b-1} D_{l_b}^{m_b} \right. \\ &\quad \left. + i^{l_b+1} \sqrt{2l_b+3} \exp[i(\sigma_{l_b+1} + \delta_{l_b+1})] \mathcal{R}_{l_b l_b+1} D_{l_b+1}^{m_b} \right\} \\ &= i^{l_b-1} \delta_{m_b, 0} \frac{1}{\sqrt{4\pi(2l_b+1)k}} \\ &\quad \times \left\{ \exp[i(\sigma_{l_b-1} + \delta_{l_b-1})] \mathcal{R}_{l_b l_b-1} l_b \right. \\ &\quad \left. - \exp[i(\sigma_{l_b+1} + \delta_{l_b+1})] \mathcal{R}_{l_b l_b+1} (l_b + 1) \right\}. \end{aligned} \quad (\text{A.110})$$

The transition dipole about the recombination with the $3p_z$ orbital of Ar ($l_b = 1, m_b = 0$) [59, §II.C] is

$$\langle \Psi_i | \mathbf{r} \cdot \mathbf{n} | \Psi_{\mathbf{k}}^+ \rangle = \frac{1}{\sqrt{3\pi k}} \left\{ \frac{\exp[i(\sigma_0 + \delta_0)]}{2} \mathcal{R}_{1,0} - \exp[i(\sigma_2 + \delta_2)] \mathcal{R}_{1,2} \right\}. \quad (\text{A.111})$$

A Appendix

The $y_{n_b, l_b}(r)$ and $y_{E_l}(r)$ are required for the calculation of $\mathcal{R}_{l_b, l}$ [Eq.(A.109)]. These radial wavefunction can be obtained by numerically integrating the Schrödinger equation with the Numerov method [140] and considering the appropriate boundary conditions [152].

A.8 Calculation of the recombination transition dipole moment of atoms

Bibliography

- [1] S. Wilson, ed., "Handbook of molecular physics and quantum chemistry," (Wiley, 2003) Chap. 1.
- [2] L. M. Brown, A. Pais, and A. B. Pippard, eds., "Twentieth century physics," (Institute of Physics Publishing, American Institute of Physics Press, 1995) Chap. 2.
- [3] S. Weinberg, *The Discovery of Subatomic Particles*, revised ed. (Cambridge University Press, 2003) (Japanese translation by Saburo Homma is published by Chikuma Shobo).
- [4] R. S. Mulliken, "Spectroscopy, molecular orbitals, and chemical bonding," *Science* **157**, 13 (1967).
- [5] K. Fukui, "Role of frontier orbitals in chemical reactions," *Science* **218**, 747 (1982).
- [6] W. H. Eugen Schwarz, "Measuring orbitals: Provocation or reality?" *Angew. Chem., Int. Ed.* **45**, 1508 (2006).
- [7] A. Szabo and N. S. Ostlund, *Modern Quantum Chemistry: Introduction to Advanced Electronic Structure Theory*, new ed. (Dover Publications, 1996).
- [8] R. G. Parr and W. Yang, *Density-Functional Theory of Atoms and Molecules* (Oxford University Press, 1989).
- [9] A. A. Granovsky, "Firefly version 8.0," <http://classic.chem.msu.su/gran/firefly/index.html>.
- [10] M. W. Schmidt, K. K. Baldridge, J. A. Boatz, S. T. Elbert, M. S. Gordon, J. H. Jensen, S. Koseki, N. Matsunaga, K. A. Nguyen, S. Su, T. L. Windus, M. Dupuis, and J. A. Montgomery, "General atomic and molecular electronic structure system," *J. Comput. Chem.* **14**, 1347 (1993).
- [11] M. Suenaga, "Facio: new computational chemistry environment for PC GAMESS," *J. Comput. Chem. Jpn.* **4**, 25 (2005).
- [12] M. Suenaga, "Development of GUI for GAMESS / FMO calculation," *J. Comput. Chem. Jpn.* **7**, 33 (2008).

BIBLIOGRAPHY

- [13] E. Weigold and I. McCarthy, *Electron Momentum Spectroscopy* (Plenum Publishing Corporation, 1999).
- [14] S. Patchkovskii, Z. Zhao, T. Brabec, and D. M. Villeneuve, "High harmonic generation and molecular orbital tomography in multielectron systems," *J. Chem. Phys.* **126**, 114306 (2007).
- [15] C. Brion, G. Cooper, Y. Zheng, I. Litvinyuk, and I. McCarthy, "Imaging of orbital electron densities by electron momentum spectroscopy - a chemical interpretation of the binary ($e, 2e$) reaction," *Chem. Phys.* **270**, 13 (2001).
- [16] M. Takahashi, "Development of molecular frame ($e, 2e$) spectroscopy by means of a triple coincidence technique," *BUTSURI* **61**, 90 (2006), (in Japanese).
- [17] X. Lu, M. Grobis, K. H. Khoo, S. G. Louie, and M. F. Crommie, "Spatially mapping the spectral density of a single c_{60} molecule," *Phys. Rev. Lett.* **90**, 096802 (2003).
- [18] J. Repp, G. Meyer, S. M. Stojković, A. Gourdon, and C. Joachim, "Molecules on insulating films: Scanning-tunneling microscopy imaging of individual molecular orbitals," *Phys. Rev. Lett.* **94**, 026803 (2005).
- [19] L. Gross, N. Moll, F. Mohn, A. Curioni, G. Meyer, F. Hanke, and M. Persson, "High-resolution molecular orbital imaging using a p-wave STM tip," *Phys. Rev. Lett.* **107**, 086101 (2011).
- [20] J. Itatani, J. Levesque, D. Zeidler, H. Niikura, H. Pepin, J. C. Kieffer, P. B. Corkum, and D. M. Villeneuve, "Tomographic imaging of molecular orbitals," *Nature (London)* **432**, 867 (2004).
- [21] H. Stapelfeldt, "Electrons frozen in motion," *Nature (London)* **432**, 809 (2004).
- [22] J. Itatani, "Molecular orbital imaging using high harmonics," *OYO BUTURI* **78**, 118 (2009), (in Japanese).
- [23] F. Rosca-Pruna and M. J. J. Vrakking, "Experimental observation of revival structures in picosecond laser-induced alignment of i_2 ," *Phys. Rev. Lett.* **87**, 153902 (2001).
- [24] R. W. Boyd, *Nonlinear Optics*, 3rd ed. (Academic Press, 2008).
- [25] P. B. Corkum, "Plasma perspective on strong field multiphoton ionization," *Phys. Rev. Lett.* **71**, 1994 (1993).
- [26] M. Lewenstein, P. Balcou, M. Y. Ivanov, A. L'Huillier, and P. B. Corkum, "Theory of high-harmonic generation by low-frequency laser fields," *Phys. Rev. A* **49**, 2117 (1994).
- [27] M. Lewenstein, P. Salières, and A. L'Huillier, "Phase of the atomic polarization in high-order harmonic generation," *Phys. Rev. A* **52**, 4747 (1995).
- [28] P. Antoine, A. L'Huillier, M. Lewenstein, P. Salières, and B. Carré, "Theory of high-order harmonic generation by an elliptically polarized laser field," *Phys. Rev. A* **53**, 1725 (1996).

BIBLIOGRAPHY

- [29] P. Salières, B. Carre, L. Le Deroff, F. Grasbon, G. G. Paulus, H. Walther, R. Kopold, W. Becker, D. B. Milosevic, A. Sanpera, and M. Lewenstein, “Feynman’s path-integral approach for intense-laser-atom interactions,” *Science* **292**, 902 (2001).
- [30] S. Patchkovskii, Z. Zhao, T. Brabec, and D. M. Villeneuve, “High harmonic generation and molecular orbital tomography in multielectron systems: Beyond the single active electron approximation,” *Phys. Rev. Lett.* **97**, 123003 (2006).
- [31] H. Niikura, F. Legare, R. Hasbani, A. D. Bandrauk, M. Y. Ivanov, D. M. Villeneuve, and P. B. Corkum, “Sub-laser-cycle electron pulses for probing molecular dynamics,” *Nature (London)* **417**, 917 (2002).
- [32] Y. Mairesse, A. de Bohan, L. J. Frasinski, H. Merdji, L. C. Dinu, P. Monchicourt, P. Breger, M. Kovacev, R. Taieb, B. Carre, H. G. Muller, P. Agostini, and P. Salieres, “Attosecond synchronization of high-harmonic soft x-rays,” *Science* **302**, 1540 (2003).
- [33] S. Baker, J. S. Robinson, C. A. Haworth, H. Teng, R. A. Smith, C. C. Chirila, M. Lein, J. W. G. Tisch, and J. P. Marangos, “Probing proton dynamics in molecules on an attosecond time scale,” *Science* **312**, 424 (2006).
- [34] A. H. Zewail, “Femtochemistry: Atomic-scale dynamics of the chemical bond,” *J. Phys. Chem. A* **104**, 5660 (2000).
- [35] N. L. Wagner, A. Wüest, I. P. Christov, T. Popmintchev, X. Zhou, M. M. Murnane, and H. C. Kapteyn, “Monitoring molecular dynamics using coherent electrons from high harmonic generation,” *Proc. Natl. Acad. Sci. USA* **103**, 13279 (2006).
- [36] H. J. Wörner, J. B. Bertrand, D. V. Kartashov, P. B. Corkum, and D. M. Villeneuve, “Following a chemical reaction using high-harmonic interferometry,” *Nature (London)* **466**, 604 (2010).
- [37] S. Haessler, J. Caillat, W. Boutu, C. Giovanetti-Teixeira, T. Ruchon, T. Auguste, Z. Diveki, P. Breger, A. Maquet, B. Carré, R. Taïeb, and P. Salières, “Attosecond imaging of molecular electronic wavepackets,” *Nature Phys.* **6**, 200 (2010).
- [38] B. K. McFarland, J. P. Farrell, P. H. Bucksbaum, and M. Guhr, “High harmonic generation from multiple orbitals in n₂,” *Science* **322**, 1232 (2008).
- [39] A. Messiah, *Quantum Mechanics* (Dover Publications, 1999).
- [40] C. Vozzi, M. Negro, F. Calegari, G. Sansone, M. Nisoli, S. De Silvestri, and S. Stagira, “Generalized molecular orbital tomography,” *Nature Phys.* **7**, 822 (2011).
- [41] T. Kanai, S. Minemoto, and H. Sakai, “Quantum interference during high-order harmonic generation from aligned molecules,” *Nature (London)* **435**, 470 (2005).

- [42] P. M. Paul, E. S. Toma, P. Breger, G. Mullot, F. Auge, P. Balcou, H. G. Muller, and P. Agostini, "Observation of a train of attosecond pulses from high harmonic generation," *Science* **292**, 1689 (2001).
- [43] H. Muller, "Reconstruction of attosecond harmonic beating by interference of two-photon transitions," *Appl. Phys. B: Lasers Opt.* **74**, s17 (2002).
- [44] S. Haessler, B. Fabre, J. Higuët, J. Caillat, T. Ruchon, P. Breger, B. Car'è, E. Constant, A. Maquet, E. Mével, P. Salières, R. Taïeb, and Y. Mairesse, "Phase-resolved attosecond near-threshold photoionization of molecular nitrogen," *Phys. Rev. A* **80**, 011404 (2009).
- [45] R. López-Martens, K. Varjú, P. Johnsson, J. Mauritsson, Y. Mairesse, P. Salières, M. B. Gaarde, K. J. Schafer, A. Persson, S. Svanberg, C.-G. Wahlström, and A. L'Huillier, "Amplitude and phase control of attosecond light pulses," *Phys. Rev. Lett.* **94**, 033001 (2005).
- [46] S. Haessler, J. Caillat, and P. Salières, "Self-probing of molecules with high harmonic generation," *J. Phys. B: At., Mol. Opt. Phys.* **44**, 203001 (2011).
- [47] P. Salières, A. Maquet, S. Haessler, J. Caillat, and R. Taïeb, "Imaging orbitals with attosecond and ångström resolutions: toward attochemistry?" *Rep. Prog. Phys.* **75**, 062401 (2012).
- [48] Z. Diveki, R. Guichard, J. Caillat, A. Camper, S. Haessler, T. Auguste, T. Ruchon, B. Carré, A. Maquet, R. Taïeb, and P. Salières, "Molecular orbital tomography from multi-channel harmonic emission in N₂," *Chem. Phys.* **414**, 121 (2013).
- [49] L. C. Dinu, H. G. Muller, S. Kazamias, G. Mullot, F. Augé, P. Balcou, P. M. Paul, M. Kovačev, P. Breger, and P. Agostini, "Measurement of the subcycle timing of attosecond XUV bursts in high-harmonic generation," *Phys. Rev. Lett.* **91**, 063901 (2003).
- [50] S. A. Aseyev, Y. Ni, L. J. Frasinski, H. G. Muller, and M. J. J. Vrakking, "Attosecond angle-resolved photoelectron spectroscopy," *Phys. Rev. Lett.* **91**, 223902 (2003).
- [51] W. Boutu, S. Haessler, H. Merdji, P. Breger, G. Waters, M. Stankiewicz, L. J. Frasinski, R. Taieb, J. Caillat, A. Maquet, P. Monchicourt, B. Carre, and P. Salières, "Coherent control of attosecond emission from aligned molecules," *Nature Phys.* **4**, 545 (2008).
- [52] T. Kanai, E. J. Takahashi, Y. Nabekawa, and K. Midorikawa, "Destructive interference during high harmonic generation in mixed gases," *Phys. Rev. Lett.* **98**, 153904 (2007).
- [53] Y. Mairesse, D. Zeidler, N. Dudovich, M. Spanner, J. Levesque, D. M. Villeneuve, and P. B. Corkum, "High-order harmonic transient grating spectroscopy in a molecular jet," *Phys. Rev. Lett.* **100**, 143903 (2008).
- [54] X. X. Zhou, X. M. Tong, Z. X. Zhao, and C. D. Lin, "Role of molecular orbital symmetry on the alignment dependence of high-order harmonic generation with molecules," *Phys. Rev.*

BIBLIOGRAPHY

- [A 71, 061801 \(2005\)](#), copyright (C) 2009 The American Physical Society; Please report any problems to prola@aps.org.
- [55] J. R. Taylor, *Scattering Theory: The Quantum Theory of Nonrelativistic Collisions* (Dover Publications, 2006).
- [56] M. Lein, N. Hay, R. Velotta, J. P. Marangos, and P. L. Knight, “Interference effects in high-order harmonic generation with molecules,” [Phys. Rev. A **66**, 023805 \(2002\)](#).
- [57] M. Y. Ivanov, T. Brabec, and N. Burnett, “Coulomb corrections and polarization effects in high-intensity high-harmonic emission,” [Phys. Rev. A **54**, 742 \(1996\)](#).
- [58] O. Smirnova, M. Spanner, and M. Ivanov, “Analytical solutions for strong field-driven atomic and molecular one- and two-electron continua and applications to strong-field problems,” [Phys. Rev. A **77**, 033407 \(2008\)](#).
- [59] A.-T. Le, R. R. Lucchese, S. Tonzani, T. Morishita, and C. D. Lin, “Quantitative rescattering theory for high-order harmonic generation from molecules,” [Phys. Rev. A **80**, 013401 \(2009\)](#).
- [60] T.-M. Yan, S. V. Popruzhenko, M. J. J. Vrakking, and D. Bauer, in *Multiphoton Processes and Attosecond Physics*, Springer Proceedings in Physics No. 125, edited by K. Yamanouchi and M. Katsumi (Springer Berlin Heidelberg, 2012) pp. 221–230.
- [61] N. H. Burnett, C. Kan, and P. B. Corkum, “Ellipticity and polarization effects in harmonic generation in ionizing neon,” [Phys. Rev. A **51**, R3418 \(1995\)](#).
- [62] H. Soifer, P. Botheron, D. Shafir, A. Diner, O. Raz, B. D. Bruner, Y. Mairesse, B. Pons, and N. Dudovich, “Near-threshold high-order harmonic spectroscopy with aligned molecules,” [Phys. Rev. Lett. **105**, 143904 \(2010\)](#).
- [63] K. Miyazaki and H. Takada, “High-order harmonic generation in the tunneling regime,” [Phys. Rev. A **52**, 3007 \(1995\)](#).
- [64] V. P. Krainov, H. R. Reiss, and B. M. Smirnov, in *Radiative Processes in Atomic Physics* (John Wiley & Sons, Inc., 1997) Appendix I: Atomic Units and Measures of Intensity.
- [65] C. C. Chirilă and M. Lein, “Strong-field approximation for harmonic generation in diatomic molecules,” [Phys. Rev. A **73**, 023410 \(2006\)](#).
- [66] Y. Han and L. B. Madsen, “Comparison between length and velocity gauges in quantum simulations of high-order harmonic generation,” [Phys. Rev. A **81**, 063430 \(2010\)](#).
- [67] M. O. Scully and M. S. Zubairy, *Quantum Optics*, 1st ed. (Cambridge University Press, 1997).
- [68] D. Bauer, D. B. Milošević, and W. Becker, “Strong-field approximation for intense-laser-atom processes: The choice of gauge,” [Phys. Rev. A **72**, 023415 \(2005\)](#).

BIBLIOGRAPHY

- [69] K. Kato, *High-order harmonic generation from aligned molecules with 800-nm and 1300-nm femtosecond pulses*, Master's thesis, The University of Tokyo (2011).
- [70] R. P. Feynman and A. R. Hibbs, *Quantum mechanics and path integrals*, emended ed. (Dover Publications, 2010).
- [71] G. B. Arfken and H. J. Weber, *Mathematical Methods for Physicists*, sixth ed. (Academic Press, 2005).
- [72] G. Sansone, C. Vozzi, S. Stagira, and M. Nisoli, "Nonadiabatic quantum path analysis of high-order harmonic generation: Role of the carrier-envelope phase on short and long paths," *Phys. Rev. A* **70**, 013411 (2004).
- [73] H. F. Davis and A. D. Snider, *Introduction to Vector Analysis*, 6th ed. (William C. Brown Publishers, 1995).
- [74] M. Lewenstein, K. C. Kulander, K. J. Schafer, and P. H. Bucksbaum, "Rings in above-threshold ionization: A quasiclassical analysis," *Phys. Rev. A* **51**, 1495 (1995).
- [75] "GNU scientific library – reference manual," http://www.gnu.org/software/gsl/manual/html_node/index.html.
- [76] P. Salières, A. L'Huillier, and M. Lewenstein, "Coherence control of high-order harmonics," *Phys. Rev. Lett.* **74**, 3776 (1995).
- [77] P. Antoine, A. L'Huillier, and M. Lewenstein, "Attosecond pulse trains using high-order harmonics," *Phys. Rev. Lett.* **77**, 1234 (1996).
- [78] P. Balcou, P. Salières, A. L'Huillier, and M. Lewenstein, "Generalized phase-matching conditions for high harmonics: The role of field-gradient forces," *Phys. Rev. A* **55**, 3204 (1997).
- [79] M. Bellini, C. Lyngå, A. Tozzi, M. B. Gaarde, T. W. Hänsch, A. L'Huillier, and C.-G. Wahlström, "Temporal coherence of ultrashort high-order harmonic pulses," *Phys. Rev. Lett.* **81**, 297 (1998).
- [80] O. Svelto, *Principles of Lasers*, 5th ed. (Springer-Verlag, 2009).
- [81] R. W. Boyd, "Intuitive explanation of the phase anomaly of focused light beams," *J. Opt. Soc. Am.* **70**, 877 (1980).
- [82] R. Santra and A. Gordon, "Three-step model for high-harmonic generation in many-electron systems," *Phys. Rev. Lett.* **96**, 073906 (2006).
- [83] K. Cahill, *Physical Mathematics* (Cambridge University Press, 2013).
- [84] N. Wagner, X. Zhou, R. Lock, W. Li, A. Wüest, M. Murnane, and H. Kapteyn, "Extracting the phase of high-order harmonic emission from a molecule using transient alignment in mixed samples," *Phys. Rev. A* **76**, 061403 (2007).

BIBLIOGRAPHY

- [85] T. Kanai, E. J. Takahashi, Y. Nabekawa, and K. Midorikawa, "Observing molecular structures by using high-order harmonic generation in mixed gases," *Phys. Rev. A* **77**, 041402 (2008).
- [86] E. S. Toma and H. G. Muller, "Calculation of matrix elements for mixed extreme-ultraviolet–infrared two-photon above-threshold ionization of argon," *J. Phys. B: At., Mol. Opt. Phys.* **35**, 3435 (2002).
- [87] H. G. Muller, "Tunneling excitation to resonant states in helium as main source of superponderomotive photoelectrons in the tunneling regime," *Phys. Rev. Lett.* **83**, 3158 (1999).
- [88] K. L. Ishikawa, E. J. Takahashi, and K. Midorikawa, "Single-attosecond pulse generation using a seed harmonic pulse train," *Phys. Rev. A* **75**, 021801 (2007).
- [89] H. G. Muller, "Numerical simulation of high-order above-threshold-ionization enhancement in argon," *Phys. Rev. A* **60**, 1341 (1999).
- [90] K. Klünder, J. M. Dahlström, M. Gisselbrecht, T. Fordell, M. Swoboda, D. Guénot, P. Johnson, J. Caillat, J. Mauritsson, A. Maquet, R. Taïeb, and A. L'Huillier, "Probing single-photon ionization on the attosecond time scale," *Phys. Rev. Lett.* **106**, 143002 (2011).
- [91] J. M. Dahlström, A. L'Huillier, and A. Maquet, "Introduction to attosecond delays in photoionization," *J. Phys. B: At., Mol. Opt. Phys.* **45**, 183001 (2012).
- [92] J. W. Cooper, "Photoionization from outer atomic subshells. a model study," *Physical Review* **128**, 681 (1962).
- [93] P. W. Atkins and R. Friedman, *Molecular quantum mechanics*, 5th ed. (Oxford University Press, 2011).
- [94] R. Szipöcs, K. Ferencz, C. Spielmann, and F. Krausz, "Chirped multilayer coatings for broadband dispersion control in femtosecond lasers," *Opt. Lett.* **19**, 201 (1994).
- [95] A. Stingl, M. Lenzner, C. Spielmann, F. Krausz, and R. Szipöcs, "Sub-10-fs mirror-dispersion-controlled ti:sapphire laser," *Opt. Lett.* **20**, 602 (1995).
- [96] D. Strickland and G. Mourou, "Compression of amplified chirped optical pulses," *Opt. Commun.* **56**, 219 (1985).
- [97] P. Maine, D. Strickland, P. Bado, M. Pessot, and G. Mourou, "Generation of ultrahigh peak power pulses by chirped pulse amplification," *IEEE J. Quantum Electron.* **24**, 398 (1988).
- [98] E. Hecht, *Optics*, 4th ed. (Addison-Wesley, Reading, Mass., 2002).
- [99] P. Tournois, "Acousto-optic programmable dispersive filter for adaptive compensation of group delay time dispersion in laser systems," *Opt. Commun.* **140**, 245 (1997).
- [100] E. Treacy, "Optical pulse compression with diffraction gratings," *IEEE J. Quantum Electron.* **5**, 454 (1969).

BIBLIOGRAPHY

- [101] J. Peatross, J. L. Chaloupka, and D. D. Meyerhofer, "High-order harmonic generation with an annular laser beam," *Opt. Lett.* **19**, 942 (1994).
- [102] J. A. R. Samson and D. L. Ederer, eds., *Vacuum ultraviolet spectroscopy I*, Experimental methods in the physical sciences, Vol. 31 (Academic Press, 1998).
- [103] M. Born and E. Wolf, *Principles of Optics: Electromagnetic Theory of Propagation, Interference and Diffraction of Light*, 7th ed. (Cambridge University Press, 1999).
- [104] E. D. Palik, ed., *Handbook of Optical Constants of Solids* (Academic Press, 1985).
- [105] J. Levesque, Y. Mairesse, N. Dudovich, H. Pépin, J.-C. Kieffer, P. B. Corkum, and D. M. Villeneuve, "Polarization state of high-order harmonic emission from aligned molecules," *Phys. Rev. Lett.* **99**, 243001 (2007).
- [106] X. Zhou, R. Lock, N. Wagner, W. Li, H. C. Kapteyn, and M. M. Murnane, "Elliptically polarized high-order harmonic emission from molecules in linearly polarized laser fields," *Phys. Rev. Lett.* **102**, 073902 (2009).
- [107] J. Vac. Sci. Technol., "Graphic symbols in vacuum technology," *J. Vac. Sci. Technol.* **4**, 139 (1967).
- [108] J. A. R. Samson and D. L. Ederer, eds., *Vacuum ultraviolet spectroscopy II*, Experimental methods in the physical sciences, Vol. 32 (Academic Press, 1998).
- [109] G. Scoles, D. Bassi, U. Buck, and D. C. Laine, *Atomic and Molecular Beam Methods: Volume I* (Oxford University Press, USA, 1988).
- [110] D. H. Levy, "The spectroscopy of very cold gases," *Science* **214**, 263 (1981).
- [111] U. Even, J. Jortner, D. Noy, N. Lavie, and C. Cossart-Magos, "Cooling of large molecules below 1 k and He clusters formation," *J. Chem. Phys.* **112**, 8068 (2000).
- [112] B. J. Whitaker, ed., *Imaging in Molecular Dynamics: Technology and Applications* (Cambridge University Press, 2007).
- [113] W. C. Wiley and I. H. McLaren, "Time-of-Flight mass spectrometer with improved resolution," *Rev. Sci. Instrum.* **26**, 1150 (1955).
- [114] A. T. J. B. Eppink and D. H. Parker, "Velocity map imaging of ions and electrons using electrostatic lenses: Application in photoelectron and photofragment ion imaging of molecular oxygen," *Rev. Sci. Instrum.* **68**, 3477 (1997).
- [115] D. J. Manura and D. A. Dahl, *SIMION (R) 8.0 User Manual* (Scientific Instrument Services, Inc., 2008).
- [116] D. W. Chandler and P. L. Houston, "Two-dimensional imaging of state-selected photodissociation products detected by multiphoton ionization," *J. Chem. Phys.* **87**, 1445 (1987).

BIBLIOGRAPHY

- [117] D. W. Chandler, J. W. Thoman Jr., M. H. M. Janssen, and D. H. Parker, "Photofragment imaging: The 266 nm photodissociation of CH₃I," *Chem. Phys. Lett.* **156**, 151 (1989).
- [118] D. W. Chandler, M. H. M. Janssen, S. Stolte, R. N. Strickland, J. W. Thoman, and D. H. Parker, "Photofragment imaging: the 266-nm photolysis of CD₃I," *J. Phys. Chem.* **94**, 4839 (1990).
- [119] H. Nanjo, *Development of two-dimensional ion imaging system and its application to the observation of aligned molecules*, Master's thesis, The University of Tokyo (2002), (in Japanese).
- [120] H. Tanji, *Three-dimensional orientation of neutral molecules with combined electrostatic and elliptically polarized laser fields*, Master's thesis, The University of Tokyo (2005).
- [121] J. L. Wiza, "Microchannel plate detectors," *Nucl. Instr. and Meth.* **162**, 587 (1979).
- [122] Hamamatsu Photonics K.K., "MCP assembly selection guide," http://www.hamamatsu.com/resources/pdf/etd/MCPassy_TMCP0001E10.pdf.
- [123] M. Haidekker, "Advanced biomedical image analysis," (Wiley, 2010) Chap. 9.1.
- [124] L. Montgomery Smith, D. R. Keefer, and S. Sudharsanan, "Abel inversion using transform techniques," *J. Quant. Spectrosc. Radiat. Transf.* **39**, 367 (1988).
- [125] V. Dribinski, A. Ossadtchi, V. A. Mandelshtam, and H. Reisler, "Reconstruction of Abel-transformable images: The gaussian basis-set expansion Abel transform method," *Rev. Sci. Instrum.* **73**, 2634 (2002).
- [126] R. C. Aster, B. Borchers, and C. H. Thurber, *Parameter estimation and inverse problems.*, 2nd ed. (Academic Press, 2012).
- [127] B. Friedrich and D. Herschbach, "Alignment and trapping of molecules in intense laser fields," *Phys. Rev. Lett.* **74**, 4623 (1995).
- [128] S. Mukamel, *Principles of Nonlinear Optical Spectroscopy* (Oxford Univ Pr on Demand, 1999).
- [129] B. J. Sussman, J. G. Underwood, R. Lausten, M. Y. Ivanov, and A. Stolow, "Quantum control via the dynamic Stark effect: Application to switched rotational wave packets and molecular axis alignment," *Phys. Rev. A* **73**, 053403 (2006).
- [130] G. Sansone, E. Benedetti, F. Calegari, C. Vozzi, L. Avaldi, R. Flammini, L. Poletto, P. Villoresi, C. Altucci, R. Velotta, S. Stagira, S. De Silvestri, and M. Nisoli, "Isolated single-cycle attosecond pulses," *Science* **314**, 443 (2006).
- [131] C. T. Lynch, *CRC Handbook of Materials Science: Volume II: Metals, Composites, and Refractory Materials* (CRC Press, 1975).

BIBLIOGRAPHY

- [132] “NIST computational chemistry comparison and benchmark database,” NIST Standard Reference Database Number 101, Release 16a, August 2013, Editor: Russell D. Johnson III, <http://cccbdb.nist.gov/>.
- [133] W. H. Press, S. A. Teukolsky, W. T. Vetterling, and B. P. Flannery, *Numerical Recipes: The Art of Scientific Computing*, 3rd ed. (Cambridge Univ Press, 2007).
- [134] K. Kato, S. Minemoto, and H. Sakai, in *International Conference on Ultrafast Phenomena*, edited by M. Chergui, D. Jonas, E. Riedle, R. Schoenlein, and A. Taylor (Oxford University Press, 2010) pp. 56–58.
- [135] A. L’Huillier, M. Lewenstein, P. Salières, P. Balcou, M. Y. Ivanov, J. Larsson, and C. G. Wahlström, “High-order harmonic-generation cutoff,” *Phys. Rev. A* **48**, R3433 (1993).
- [136] G. V. Marr and J. B. West, “Absolute photoionization cross-section tables for helium, neon, argon, and krypton in the VUV spectral regions,” *Atomic Data and Nuclear Data Tables* **18**, 497 (1976).
- [137] J. D. Jackson, *Classical Electrodynamics*, 3rd ed. (John Wiley & Sons, 1998).
- [138] L. V. Keldysh, “Ionization in the field of a strong electromagnetic wave,” *Sov. Phys. JETP*, **20**, 1307 (1965).
- [139] P. Botheron and B. Pons, “One-electron atom in a strong and short laser pulse: Comparison of classical and quantum descriptions,” *Phys. Rev. A* **80**, 023402 (2009).
- [140] J. L. M. Q. Gonzalez and D. Thompson, “Getting started with Numerov’s method,” *Comput. Phys.* **11**, 514 (1997).
- [141] L. D. Landau and L. M. Lifshitz, *Quantum Mechanics (Non-Relativistic Theory)*, 3rd ed. (Butterworth-Heinemann, 1981).
- [142] M. Tinkham, *Group Theory and Quantum Mechanics* (Dover Publications, 2003).
- [143] R. N. Zare, *Angular Momentum: Understanding Spatial Aspects in Chemistry and Physics*, 1st ed. (Wiley-Interscience, 1988).
- [144] R. P. Feynman, “Statistical mechanics: A set of lectures,” (Westview Press, 1998) Chap. 2.
- [145] M. Abramowitz and I. A. Stegun, eds., *Handbook of Mathematical Functions: With Formulas, Graphs, and Mathematical Tables* (Dover Publications, 1965).
- [146] R. Abrines and I. C. Percival, “Classical theory of charge transfer and ionization of hydrogen atoms by protons,” *Proc. Phys. Soc.* **88**, 861 (1966).
- [147] D. Eichenauer, N. Grün, and W. Scheid, “Classical trajectory calculations for $H^+ - H$ collisions with the Wigner function as initial phase space distribution,” *J. Phys. B: At. Mol. Phys.* **14**, 3929 (1981).

BIBLIOGRAPHY

- [148] H. Takahasi and M. Mori, “Double exponential formulas for numerical integration,” [Publ. Res. Inst. Math. Sci.](#) **9**, 721 (1973).
- [149] M. Suzuki, *Development of a hexapole focuser for controlling molecular orientation*, Master’s thesis, The University of Tokyo (2011), (in Japanese).
- [150] M. Matsumoto and T. Nishimura, “Mersenne twister: A 623-dimensionally equidistributed uniform pseudo-random number generator,” [ACM Trans. Model. Comput. Simul.](#) **8**, 3 (1998).
- [151] W.-C. Liu and C. W. Clark, “Closed-form solutions of the Schrödinger equation for a model one-dimensional hydrogen atom,” [J. Phys. B: At., Mol. Opt. Phys.](#) **25**, L517 (1992).
- [152] F. Salvat, J. M. Fernández-Varea, and W. Williamson, “Accurate numerical solution of the radial Schrödinger and Dirac wave equations,” [Comput. Phys. Commun.](#) **90**, 151 (1995).
- [153] U. Fano and A. R. P. Rau, *Atomic Collisions and Spectra* (Academic Press, 1986).